
Electronic Thesis and Dissertation Repository

9-25-2018 2:30 PM

Layer-by-Layer Construction Strategies Towards Efficient CZTS Solar Cells

Matthew J. Turnbull
The University of Western Ontario

Supervisor
Ding, Zhifeng
The University of Western Ontario

Graduate Program in Chemistry
A thesis submitted in partial fulfillment of the requirements for the degree in Doctor of Philosophy
© Matthew J. Turnbull 2018

Follow this and additional works at: <https://ir.lib.uwo.ca/etd>

 Part of the [Analytical Chemistry Commons](#), and the [Physical Chemistry Commons](#)

Recommended Citation

Turnbull, Matthew J., "Layer-by-Layer Construction Strategies Towards Efficient CZTS Solar Cells" (2018). *Electronic Thesis and Dissertation Repository*. 5735.
<https://ir.lib.uwo.ca/etd/5735>

This Dissertation/Thesis is brought to you for free and open access by Scholarship@Western. It has been accepted for inclusion in Electronic Thesis and Dissertation Repository by an authorized administrator of Scholarship@Western. For more information, please contact wlsadmin@uwo.ca.

Abstract

Solar energy has very high potential for ensuring the world's energy requirements for the long-term future. Earth-abundant materials like $\text{Cu}_2\text{ZnSnS}_4$ (CZTS) are especially desirable, with a non-toxic, low-cost nature, though the quaternary nature allows for a lot of crystal structure variability, and thus underwhelming performance. This Ph.D. thesis is devoted to deepening the understanding of the CZTS material formation, and the processes that can be used to control it, to construct a low-cost, high efficiency CZTS-based solar cell. The layer-by-layer approach presented within this thesis shows great potential for rectifying the problem. CZTS nanocrystal (NC) stoichiometric control was achieved, and led to reproducible structure formation within the films (Chapter 2). Structural correlations to photoresponse for these films were established by means of synchrotron spectroscopies, and increased charge-carrier flux out of the NC film (Chapter 3). Refinement of the NC stoichiometry (Chapter 4) enhanced these results, and extended the structural correlations. CdS addition to the CZTS film to form the p-n junction was investigated, and confirmed water intercalations in the film arising during CdS deposition. Mild thermal treatments were found to purify the films, and lead to further amplification of the charge-carrier flux (Chapter 5).

The CZTS/CdS films were found to not have the desired enhancement to the overall photoresponse due to surface oxides, and poor alignment in the valence/conduction bands of the materials interface. It was discovered that acetic acid etching of the CZTS layer prior to CdS addition removed the oxides, and drastically improved the charge-carrier flux (Chapter 6). In fact, the band structure was aligned favorably to create an ideal p-n junction. The band structure diagram was well established, and the electron flow in the conduction band overlap was confirmed to be favored. The full device was built by combining all refinement processes, and adding ZnO and Al-doped ZnO window layers with atomic layer deposition (Chapter 7). A high open-circuit potential of 0.85 V, and competitive device efficiency of 8.5% were achieved. The layer-by-layer approach is thus proven throughout this thesis to be a highly effective strategy and anticipated to guide intelligent solar cell designs and fabrications.

Keywords

Cu₂ZnSnS₄ (CZTS); Nanocrystals; Synchrotron Spectroscopy; Crystal Lattice Defects; X-ray Absorption Fine Structure (XAFS); X-ray Absorption Near Edge Structure (XANES); Extended X-ray Absorption Fine Structure (EXAFS); Photoelectrochemistry; X-ray Photoelectron Spectroscopy (XPS); Heterojunction; Interfacial Chemistry; Band Structure; Photovoltaic Materials; Thin-Film Solar Cells; Photovoltaic Efficiency.

Dedication

To my father, *Stacy Turnbull*,

who taught me that everything is possible, if you are willing to try.

To my grandfather, *Joseph Myos*,

who taught me the true value of family.

And to my mother, *Helen Turnbull*,

for being my guide throughout the many crazy turns life takes.

Co-Authorship Statement

Prof. Zhifeng Ding was the corresponding author on the papers presented within this thesis. Dr. Ding was responsible for the supervision of Matthew J. Turnbull throughout his graduate studies, and was the primary editor for all works presented herein. Dr. Ding also finalized all manuscript submissions. This thesis contains material presented in four publications, and two manuscripts read for submission, all of which had contributions from co-authors.

Matthew J. Turnbull was the primary author of the published works presented in Chapters 2, 3, 4, and 5. Matthew was also the primary author of the manuscripts ready for submission, presented in Chapters 6, and 7. He was responsible for most of the experimental and theoretical work in each Chapter, as well as the writing and revision of all drafts.

Throughout this work, data that was acquired or analyzed by – or jointly with – co-authors, is summarized below:

Chapter 2: Turnbull, M.J.; Khoshmashrab, S.; Wang, Z.; Harbottle, R.; Sham, T.K.; Ding, Z. Controlling $\text{Cu}_2\text{ZnSnS}_4$ Photocatalytic Ability Through Alterations in Sulfur Availability. *Catal. Today*, **2016**, 260, 119-125.

Saghar Khoshmashrab fabricated some of the samples, and was a collaborating Masters student working alongside Matthew in developing compositional controls for the CZTS nanocrystals. Dr. Zhiqiang Wang accompanied Matthew and Dr. Ding to the Advanced Photon Source synchrotron facility (APS). He trained Matthew on the operation of the 20-BM beamline, and provided valuable oversight throughout the trip. Robert Harbottle helped Matthew to design a consistent method for measuring optical band gaps through UV-vis spectroscopy. Dr. Tsun-Kong Sham trained Matthew in the use of synchrotron radiation, and supervised the submission of the successful proposal for time at the APS. Dr. Sham also directed Matthew regarding resources concerning the synchrotron, both print and human, and provided feedback on the synchrotron-based sections of the paper.

Chapter 3: Turnbull, M.J.; Vaccarello, D.; Yiu, Y.M.; Sham, T.K.; Ding, Z. Identifying Barriers to Charge-Carriers in the Bulk and Surface Regions of $\text{Cu}_2\text{ZnSnS}_4$ Nanocrystal Films by X-ray Absorption Fine Structure (XAFS). *J. Chem. Phys.*, **2016**, 145, 204702-12.

Dr. Daniel Vaccarello provided a few of the samples used in this manuscript, and accompanied Matthew to the APS. Dr. Vaccarello also drew the photoelectrochemical schematic, and CZTS unit cell images used in the final version of the manuscript. Dr. Yun-Mui Yiu supervised Matthew's treatment of the EXAFS data, and performed the FEFF9 modeling with Matthew. She was also involved in reviewing the final manuscript. Dr. Sham was responsible for supervising the submission of the successful proposal for time at the APS, and was involved in reviewing the final manuscript.

Chapter 4: Turnbull, M.J.; Khoshmashrab, S.; Yiu, Y.M.; Ding, Z. Resolving the Effects of Compositional Change on Structures in $\text{Cu}_2\text{ZnSnS}_4$ Nanocrystals by X-ray Absorption Fine Structure. *Can. J. Chem.*, **2018**, 96, 785-794.

Saghar Khoshmashrab was responsible for the fabrication of the samples analyzed within this manuscript. Dr. Yun-Mui Yiu reviewed Matthew's treatment of the EXAFS data, and was involved in the reviewing of the final manuscript.

Chapter 5: Turnbull, M.J.; Vaccarello, D.; Wong, J.; Yiu, Y.M.; Sham, T.K.; Ding, Z. Probing the CZTS/CdS Heterojunction Utilizing Photoelectrochemistry and X-ray Absorption Spectroscopy. *J. Chem. Phys.*, **2018**, 148, 134702-9.

Dr. Daniel Vaccarello did some preliminary work on the CZTS/CdS heterojunction at the Canadian Light Source synchrotron facility (CLS) in collaboration with Matthew. This work provided the foundation for this studies that lead to this manuscript. Jonathan Wong was an undergraduate student working with Dr. Vaccarello, and provided all the samples for the preliminary investigation. Dr. Yun-Mui Yiu taught Matthew the EXAFS analysis, and was involved in reviewing the final manuscript. Dr. Tsun-Kong Sham provided the expertise for preparing the samples prior to visiting the APS.

Chapter 6: Turnbull, M.J.; Yiu, Y.M.; Goldman, M.; Sham, T.K.; Ding, Z. Favorable Bond and Band Structure of $\text{Cu}_2\text{ZnSnS}_4$ and CdS Films and Their Photovoltaic Junctions. *Manuscript ready for submission.*

Dr. Yun-Mui Yiu performed the DFT calculations, and generated the DOS used in this manuscript. She also was involved in reviewing the final manuscript. Maxwell Goldman collaborated with Matthew in generating the CasaXPS-generated fits based on the DOS

provided by Dr. Yiu. Maxwell was also involved in the revision of the XPS sections of the manuscript. Dr. Sham was involved in preparing Matthew to visit the CLS, and was involved in the final revisions.

Chapter 7: Turnbull, M.J.; Gupta, J.; Goldman, M.; Yiu, Y.M.; Ding, Z. Layer-by-Layer Construction Strategies towards CZTS-Based Solar Cell Devices. *Manuscript ready for submission.*

Jaya Gupta was an undergraduate student working with Matthew, and fabricated the CZTS and CdS layers used for the device testing, under the supervision of, and using the procedures provided by Matthew. Maxwell Goldman again provided the CasaXPS-generated fits, and was involved in the revision process. Dr. Yun-Mui Yiu was involved in reviewing the final manuscript. She also ran the DFT calculations presented in Chapter 6, making this work possible.

Acknowledgments

I would like to take this moment to thank my supervisor, Dr. Zhifeng Ding, for his tireless dedication to his craft, and his relentless pursuit of excellence. He has been a constant force throughout my time here, driving me to excel in all my academic pursuits. Dr. Ding has always given me the opportunity to explore new methods, and pursue my own research ideas. He has also always given me the opportunity to collaborate with many different people within the department of chemistry at Western, and at both the CLS and APS synchrotron centers. I will forever remember the lessons he taught me.

Many thanks to all of the, facilities, funding partners and agencies who made this work possible. I would like to thank the staff at Surface Science Western, Western Nanofabrication Facility, the Chemistry electronic shop, the Glass Blowing Shop, the Canadian Light Source, and the Advanced Photon Source. Sector-20 facilities at the Advanced Photon Source, and research at these facilities, were supported by the US Department of Energy—Basic Energy Sciences, the Canadian Light Source and its funding partners, the University of Washington, and the Advanced Photon Source. Use of the Advanced Photon Source, an Office of Science User Facility operated for the US Department of Energy (DOE) Office of Science by Argonne National Laboratory, was supported by the US DOE under Contract No. DE-AC02-06CH11357.

I'd also like to thank all of those who have helped offer guidance and support along this journey. These include: Dr. Tsun-Kong Sham, Dr. Yun-Mui Yiu, Zou Finfrock, Brad Kobe, Dr. Xiaoyu Cui, Dr. Dongniu Wang, Dr. Yang Song, Dr. François Lagugné-Labarthe, Dr. Mark Biesinger, Michael S. Pape, Dr. Martin Stillman, Dr. David Shoosmith, Dr. James Noël, Dr. Keith Griffiths, Dr. Styliani Conostas, Dr. Mark Workentin, Dr. Viktor Staroverov, Dr. Paul Ragogna, Dr. Michael Kerr, Dr. Kim Baines, Dr. Johanna Blacquiere, Dr. Joe Gilroy, Sandy Holtslag, Rob Harbottle, Robin Hall, Dr. Chris Levy, Dr. Paul Boyle, John Vanstone, Jon Aukema, Dr. Todd Simpson, Barakat Misk, and Yves Rambour.

Over the years in the Ding group, I have had the pleasure of working with some truly exceptional people, and have enjoyed friendships with many of them outside of the lab. I would like to say thank you to Dr. Jane Stockmann, Dr. Kalen Swanick, Dr. Daniel

Vaccarello, Dr. Amy Tapley, Dr. Michelle Li, Dr. Lorenzo Perini, Dr. Shuijian He, Dr. Ruizhong Zhang, Dr. Xuejin Wang, Kyle Jeffs, Sara Khoshmashrab, Dr. Fraser Filice, Jonathan Adsetts, Brandon Yang, and all of the many visiting scholars, undergraduates, and researchers who have made the Ding group such a tight-knit community. It has truly been a pleasure working with each of you. To my friends in the Shoesmith, Sham, Noël, Stillman, and Lagugn -Labarhet labs, thank you for sharing in this journey with me. I look forward to continued friendships with all of you. I would like to particularly thank Dr. Greg Wallace for his calming presence through the years. Your visits through the wardrobe were always appreciated. I would also like to thank Maxwell Goldman, for never failing to put a smile on my face. Cheers to the both of you!

I would like to give a special thank you to my friend, J. Andrew Lanz-O'Brien. You've been here since I began this crazy journey as an undergraduate, back in 2007, and we've had many exceptional times since. I think, after all this, it's time for another Franko's Pizza, or three. I would also like to give a special thank you to James Stubbs. You've been my constant lunch buddy, occasional tennis and swimming partner, and never-ending pain in my backside in our fantasy hockey league. Thanks for always being there for me, but know that I will beat you one of these years!

Finally, I'd like to thank my family, Helen, Joseph, and Rosemarie Turnbull. You guys have always been there for me, willing to lend a hand, offer advice, or just be there when I needed you. You've sat up with me during the late nights, seen me at my worst, and helped me get myself back together after those years that end in a 4. I look forward to many more family game nights, tennis matches, and adventures! Truly, thank you. To Mary Turnbull, who always made sure I had someone nearby, especially when I was 16 and here alone, to Anne Myos, who has never wavered in her dedication to all of her family, and to the rest of my extended family, thank you for the support through these years. I will never forget it.

Table of Contents

Abstract	i
Keywords	ii
Dedication	iii
Co-Authorship Statement.....	iv
Acknowledgments.....	vii
Table of Contents	ix
List of Tables	xiv
List of Figures	xv
List of Abbreviations, Symbols, and Nomenclature.....	xxii
Chapter 1	1
1 General Introduction	1
1.1 The Energy Problem	1
1.2 Renewable Energy Sources.....	1
1.3 Harnessing Solar Energy.....	2
1.3.1 The Photovoltaic Effect	2
1.3.2 Extraction of Charge Carriers	3
1.3.3 Photovoltaic Devices	5
1.3.4 $\text{Cu}_2\text{ZnSnS}_4$	6
1.4 Methods of Analysis	7
1.4.1 Photoelectrochemical Measurements.....	7
1.4.2 Synchrotron-Based X-ray Absorption Fine Structure.....	8
1.5 Scope of the Thesis	11
1.6 References.....	12
Chapter 2	15

2	Controlling CZTS Photocatalytic Ability through Alterations in Sulfur Availability.	15
2.1	Introduction.....	15
2.2	Experimental.....	17
2.2.1	Synthesis and Film Formation	17
2.2.2	Characterization	17
2.3	Results and Discussion	18
2.3.1	Structural Properties.....	18
2.3.2	Extended X-ray Absorption Fine Structure (EXAFS).....	22
2.3.3	Photocatalysis	25
2.4	Conclusions.....	29
2.5	References.....	30
	Chapter 3.....	32
3	Identifying Barriers to Charge-Carriers in the Bulk and Surface Regions of $\text{Cu}_2\text{ZnSnS}_4$ Nanocrystal Films by XAFS	32
3.1	Introduction.....	32
3.2	Experimental.....	33
3.2.1	Fabrication	33
3.2.2	Characterization	34
3.3	Results and Discussion	36
3.3.1	Photoelectrochemical Measurements.....	36
3.3.2	X-ray Diffraction	41
3.3.3	XANES	44
3.3.4	EXAFS.....	48
3.4	Conclusions.....	55
3.5	References	56
	Chapter 4.....	59

4	Resolving the Effects of Compositional Change on Structures in $\text{Cu}_2\text{ZnSnS}_4$ Nanocrystals by X-ray Absorption Fine Structure.....	59
4.1	Introduction.....	59
4.2	Experimental.....	61
4.2.1	Nanocrystal Fabrication.....	61
4.2.2	Synchrotron Analysis.....	62
4.3	Results and Discussion.....	63
4.3.1	Composition.....	63
4.3.2	XANES.....	66
4.3.3	EXAFS.....	74
4.4	Conclusions.....	83
4.5	References.....	84
	Chapter 5.....	87
5	Probing the CZTS/CdS Heterojunction Utilizing Photoelectrochemistry and X-ray Absorption Spectroscopy.....	87
5.1	Introduction.....	87
5.2	Experimental.....	89
5.2.1	Fabrication.....	89
5.2.2	Characterization.....	90
5.3	Results and Discussion.....	91
5.3.1	Photoelectrochemical Measurements.....	91
5.3.2	XANES Analysis.....	93
5.3.3	EXAFS Analysis.....	97
5.3.4	Identification of the Short Zn-Nearest Neighbor Bond.....	100
5.3.5	IR-Spectroscopy.....	101
5.4	Conclusion.....	102
5.5	References.....	103

Chapter 6.....	108
6 Favorable Bond and Band Structures of $\text{Cu}_2\text{ZnSnS}_4$ and CdS Films and Their Photovoltaic Junctions	108
6.1 Introduction.....	108
6.2 Experimental.....	110
6.2.1 Fabrication	110
6.2.2 Characterization	111
6.3 Results and Discussion	113
6.3.1 Insight into CZTS Structure.....	113
6.3.2 CZTS Band Structure.....	120
6.3.3 CdS Band Structure.....	124
6.3.4 CZTS/CdS Interface.....	125
6.3.5 Constructing the Band Diagram.....	128
6.4 Conclusions.....	132
6.5 References.....	133
Chapter 7.....	137
7 Constructing the Efficient CZTS Solar Cell	137
7.1 Introduction.....	137
7.2 Experimental.....	138
7.2.1 Solar Cell Fabrication	138
7.2.2 Characterization	139
7.3 Results and Discussion	140
7.3.1 CZTS/CdS Interface.....	140
7.3.2 Solar Cell Band Structure	145
7.3.3 Full Device Performance	149
7.4 Conclusion	152

7.5 References.....	153
Chapter 8.....	156
8 Concluding Remarks and Outlook.....	156
8.1 Conclusions.....	156
8.2 Outlook and Project Future.....	159
8.3 References.....	161
Abstract A – Copyrights	162
Curriculum Vitae	166

List of Tables

Table 2.1 Sulfur Content Associated with TU and MPP and its Effects on Final NC
Composition..... 19

Table 3.1 Elemental ratios for each sample as determined through EDX averages of 25 films.
..... 40

Table 3.2 Metal coordination and bond lengths of the model kesterite CZTS. 52

Table 3.3 Metal coordination and bond lengths determined through EXAFS data fitting.
Samples with limited scatter associated with certain bonds have been indicated with ---. 53

Table 4.1 Elemental ratios for each sample as determined through EDX averages of 25 films.
The range for the Cu ratio is shown in Samples 1 through 3, while the range for the Zn ratio
is shown in Samples 3 through 5. Deviation within the presented ratios was calculated to \pm
0.02..... 64

Table 4.2 Area under the peak displayed in each of the derivative spectra, measured as a peak
area ratio relative to Sample 3. Total peak area is listed beside each ratio in brackets. 69

Table 4.3 EXAFS fitting parameters for Samples 1-3 at metal center. Each bond length has
an error of $\pm 0.02 \text{ \AA}$ or less, and are fairly close across all samples, as expected. Energy
shifts (ϵ_0) were held constant for all scattering paths, and were less than 3.5 eV in all cases. 75

Table 4.4 EXAFS fitting parameters for Sample 4 and 5 at metal center. Parameters and
error margins are the same as in Table 4.3. 76

Table 6.1 Fitting parameters using FEFF8 code and Artemis software for each of (A) Cu, (B)
Zn, and (C) Sn metal centers. The first neighboring S atom has been split to show the two
different bond lengths separately in each of the parameter sets. 117

List of Figures

Figure 1.1 Increasing atom number increases the number of energy levels, to a point where they appear to be continuous, forming an energy band. 3

Figure 1.2 Schematic diagram of the p-n junction band structure, and electron flow after E_F equilibration occurs..... 4

Figure 1.3 Schematic representation of the typical thin film device structure. 5

Figure 1.4 The unit cell for the kesterite crystal structure of CZTS. 6

Figure 1.5 Schematic view of the PECM setup. The electrochemical process that is occurring is shown in the inset above the Xenon Lamp. 7

Figure 1.6 An example XAFS spectrum, taken at the Cu(I) K-edge, highlighting the individual XANES and EXAFS regions..... 9

Figure 1.7 A stylized FT of the EXAFS signal, or radial distance space (r-space) plot. 10

Figure 2.1 Effects of changing sulfur-source on Cu / Zn stoichiometry. The grey region indicates compositions that was extrapolated. 20

Figure 2.2 Powder XRD comparisons of three distinct stoichiometries..... 21

Figure 2.3 SR fluorescence yield of the CZTS NCs a) Normalized Sn K-edge XAFS and b) radial distances..... 23

Figure 2.4 Photocatalysis of MV^{2+} to MV^+ resulting from photon absorbance observed in M1. Control measures were taken in the dark, as indicated by the dotted line. 26

Figure 2.5 PECM comparison of each of the four altered stoichiometries. M2 and M3 show high resistivity, while M4 and M5 show little resistivity, as denoted by the decreased slope of the line and low current density in light off conditions. 27

Figure 2.6 Changes to the optical band gap induced by stoichiometric changes, +/- 0.03 eV. 28

Figure 3.1 PECM results for the 5 samples, showing the light-on condition (top solid line) under alternative light illumination. Samples 1, 2, and 5 in A, B, and E, respectively, show high photoresponse to light exposure, indicating a high density of charge-carriers leaving the surface. Samples 3 and 4 (C and D) show low current density regardless of conditions, indicating a low density of charge-carriers. Four photoelectrochemical reaction steps are illustrated in F: photo-generation of an electron-hole pair, electron transfer (ET) to the MV^{2+} , electron-hole recombination (Rec) and product separation (PS). 37

Figure 3.2 XRD spectra of Samples 1-5 showing deviations in the (220) and (312) peaks. Due to the high counts used, there is some contribution to the spectrum from the aluminum tray, marked (*). The standard kesterite CZTS peaks (JCPDS 26-0575) have been shown for reference. 41

Figure 3.3 Crystal planes for the (A) (112), (B) (220), and (C) (312) planes in CZTS. Red spheres are Cu, blue are S, black are Zn, and green are Sn. SEM images of (D) the NCs and (E) the film structure of Sample 1. The Cu atoms have two distinct crystallographic positions. The first has been marked with “1”, and occurs at the (0,0,0) position, while the second has been marked with “2”, and occurs at $(0, \frac{1}{2}, \frac{3}{4})$ in the kesterite phase. The first forms a horizontal lattice of Cu and Sn. The second forms a horizontal lattice of Cu and Zn. The Zn atoms have one crystallographic position, analogous to the second indicated Cu position. .. 42

Figure 3.4 XANES spectra for the A) Zn, B) Cu, and C) Sn K-edge showing similar crystal structure between samples. 44

Figure 3.5 Contributions to the XANES come from the scattering dominated by multiple pathways of low kinetic energy photoelectrons (black), while EXAFS come from the interference of outgoing and back scattering pathways at the absorbing atom as the kinetic energy of the photoelectron increases and single scattering pathway becomes dominant (constructive and destructive interference of the black, red, and blue waves). Additional scattering atoms would contribute from above and below the plane shown. 46

Figure 3.6 Radial distributions of Cu (top) and Zn (bottom) obtained by the FEFF simulations of the Cu and Zn K-edge EXAFS in the stoichiometric CZTS kesterite crystal. 49

Figure 3.7 The magnitude of the FT of the EXAFS data for A) Zn, B) Cu, and C) Sn K-edges, and the corresponding three shell fit (dashed line) in the window region – 1.0 to 6 Å for Cu, 1.1 to 6 Å for Zn, and 1.2 to 6 Å for Sn. Sample 1 is imaged red, Sample 2 black, Sample 3 green, Sample 4 blue, and Sample 5 purple. The solid lines show the experimental data..... 50

Figure 4.1 The CZTS crystal structure as A) a perfectly stoichiometric kesterite structure and B) a kesterite structure exhibiting two Zn-on-Cu antisites, denoted with a red circle, and a Cu vacancy, denoted with a purple circle..... 61

Figure 4.2 Photoelectrochemical measurements for each of the 5 samples. 65

Figure 4.3 Cu K-edge XANES spectra showing changes in the Cu/(Zn+Sn) ratio (red < green < purple), and changes in the Zn/Sn ratio (blue < green < blue). Vertical lines (maroon and grey) are shown at peak locations of 8,982.6 eV and 8,986.3 eV respectively. Samples are ordered by sample number, with Sample 1 (red) being at the top, and Sample 5 being at the bottom (blue). Derivative of the XANES spectra is shown in the inset (top left). 66

Figure 4.4 Zn K-edge XANES spectra showing changes in the Cu/(Zn+Sn) ratio (red < green < purple), and changes in the Zn/Sn ratio (blue < green < blue). A vertical line (grey) is shown to denote the main peak at 9,665.1 eV. Samples are ordered by sample number, with Sample 1 (red) being at the top, and Sample 5 being at the bottom (blue). Derivative of the XANES spectra is shown in the inset (top left). 71

Figure 4.5 Sn K-edge XANES spectra showing changes in the Cu/(Zn+Sn) ratio (red < green < purple), and changes in the Zn/Sn ratio (blue < green < blue). A vertical line (grey) is shown to denote the main peak at 29,212.0 eV. Samples are ordered by sample number, with Sample 1 (red) being at the top, and Sample 5 being at the bottom (blue). Derivative of the XANES spectra is shown in the inset (top left). 72

Figure 4.6 Cu EXAFS for each sample in k-space A), and R-space B). The k-space spectra are divided by periodic grey lines every 1.7 Å⁻¹ beginning at 2.7 Å⁻¹ for ease of comparison. Each R-space spectrum has been overlain with its corresponding fit (dashed line) using the Artemis software package. Samples are ordered by sample number, with Sample 1 (red) being at the top, and Sample 5 being at the bottom (blue), with fitting mismatch factors of

0.020, 0.021, 0.019, 0.023, and 0.021 respectively. The rest of the parameters are presented in Table 4.3 and Table 4.4. 77

Figure 4.7 Zn EXAFS for each sample in k-space A), and R-space B). The k-space spectra are divided by periodic grey lines every 1.6 \AA^{-1} beginning at 2.7 \AA^{-1} for ease of comparison. Each R-space spectrum has been overlain with its corresponding fit (dashed line) using the Artemis software package. Samples are ordered by sample number, with Sample 1 (red) being at the top, and Sample 5 being at the bottom (blue), with fitting mismatch factors of 0.015, 0.010, 0.019, 0.005, and 0.021 respectively. The rest of the parameters are presented in Table 4.3 and Table 4.4. 80

Figure 4.8 Sn EXAFS for each sample in k-space A), and R-space B). The k-space spectra are divided by periodic grey lines every 1.6 \AA^{-1} beginning at 2.8 \AA^{-1} for ease of comparison. Each R-space spectrum has been overlain with its corresponding fit (dashed line) using the Artemis software package. Samples are ordered by sample number, with Sample 1 (red) being at the top, and Sample 5 being at the bottom (blue), with fitting mismatch factors of 0.054, 0.035, 0.040, 0.079, and 0.056 respectively. The rest of the parameters are presented in Table 4.3 and Table 4.4. 82

Figure 5.1 PECM result for the CZTS film, and effects of CdS addition, with and without post-processing. Left untreated, addition of CdS layer reduces current density, particularly at low negative potentials, and shows increased recombination, as seen through the sharp decrease in photoresponse following initial excitation. Post-processing via annealing restores previous current densities. 92

Figure 5.2 Metal K-edge XANES for each of the metal centers found in CZTS and CZTS-CdS films. Crystal structure as denoted by the change in immediate post-edge oscillations shows Zn center to be especially vulnerable to deformations caused by CdS addition. Annealing creates more distinct oscillations at the Cu and Zn centers. Note the absence of a Cd spectrum for the CZTS film. 94

Figure 5.3 The magnitude of the EXAFS data FT for the Cu, Zn, Sn, and Cd metal sites in a CZTS film (trace a), a CZTS-CdS film (trace b), and an annealed CZTS-CdS film (trace c). 98

Figure 5.4 Fitting of the first shell Zn EXAFS. The curve was based on the FEFF fit of the CZTS kesterite crystal. The extra scattering pathway was added to account for the first major peak which is of a low Z atom origin.	100
Figure 5.5 IR spectra for as-deposited CZTS (red), CZTS-CdS (black), and annealed CZTS-CdS (green).	102
Figure 6.1 Metal K-edge XAFS spectra for the (A) Cu, (B) Zn, and (C) Sn metal centers in the CZTS film (black), alongside the corresponding theoretical spectra for a pure CZTS kesterite (Chapter 1.3.4). The experimental spectra have been offset for better visual comparison. Fitting of the radial distance space (R-space), Fourier Transform (FT) of the EXAFS signals, is shown for (D) Cu, (E) Zn, and (F) Sn metal centers, respectively. All fittings used a k^3 weighting to maximize signal in the high k-ranges. Full fitting parameters are provided in Supporting Information.	114
Figure 6.2 High resolution core level XPS for each of the (A) $Zn^{2+} 2p_{3/2}$, (B) $Cu^+ 2p_{3/2}$, (C) $Sn^{4+} 3d_{5/2}$, and (D) $S^{2-} 2p_{3/2}$ & $2p_{1/2}$ in the CZTS film, and their corresponding best fit (blue dashed line). The sulfur spectrum has been further curve-fit into its known components (Brown: Cu_2S , Pink: ZnS , Blue: SnS_2), confirming the known metal ratios with which the sulfur atoms combine. The SR-XPS (E) for the CZTS valence band overlays the CZTS density of states as determined using GGA. Linear extrapolation of the leading edge marks the valence band energy (E_{VB}).	121
Figure 6.3 The $Cu 2p_{3/2}$ and Cu LLM peaks for the CZTS sample. The binding energy for the $Cu 2p_{3/2}$ is for similar for the different Cu oxidation states, but can be distinguished by the Modified Auger Parameter (MAP). Cu^{2+} has a MAP of 1,851.2 eV, and Cu^+ has a MAP of 1,849.2 eV. In this way, it was determined that only Cu^+ was present in the CZTS samples.	122
Figure 6.4 High resolution core level XPS for each of the (A) $Cd^{2+} 3d_{5/2}$, (B) $S^{2-} 2p_{3/2}$ and $2p_{1/2}$ in the CdS film, and their corresponding best fit (blue dashed line). The SR-XPS for (C) the CdS valence band overlays the CdS density of states as calculated using GGA. Linear extrapolation of the leading edge marks the E_{VB}	124

Figure 6.5 Comparison of the SR-XPS VB spectra of the interface at different CdS layer depths, to bulk CZTS and CdS. The measured E_{VB} of the interface is distinct, and the partial DOS of both bulk CZTS and CdS blend together to create a very broad band from 0 – 8 eV. 126

Figure 6.6 High resolution core level XPS of the CZTS-CdS interface for each of the (A) $Zn^{2+} 2p_{3/2}$, (B) $Cu^+ 2p_{3/2}$, (C) $Sn^{4+} 3d_{5/2}$, (D) $Cd^{2+} 3d_{5/2}$, and (E) $S^{2-} 2p_{3/2}$ and $2p_{1/2}$ in the CZTS-CdS interface, and the SR-XPS for the valence band (F). The corresponding best fit is overlaid in blue. Linear extrapolation of the leading edge marks the E_{VB} 127

Figure 6.7 Optical band gap as measured via Tauc Plot conversion of the UV-vis absorbance spectrum of (A) CZTS, and (B) CdS. 129

Figure 6.8 Band diagram schematic of the CZTS layer, CdS layer, and CZTS-CdS interface, with energy values included for each. The band gap region of the interface has been expanded for enhanced viewing, and thus the energy scale for the CL beneath it has been truncated, as indicated by the double hashed lines. 130

Figure 7.1 PECMs of A) CZTS only, and B) CZTS with CdS on top. Cleaning the CZTS surface (black) using a glacial acetic acid etch leads to increased current density relative to analogous films of uncleaned CZTS (red). 140

Figure 7.2 Valence band spectra of the A) etched, and B) non-etched CZTS film via SR-XPS. Linear extrapolation of the leading edge marks the valence band energy (E_{VB}). 143

Figure 7.3 The A) Tauc plots of the UV-vis absorbance showing the optical band gap for all films in the full device, and B) the VB energy (E_{VB}) for each of the films placed above the CZTS layer. 146

Figure 7.4 Energy band diagram for the full solar cell device A) using the etched CZTS film, and B) using the non-etched CZTS film. The relative Fermi level location has been marked as E_F 148

Figure 7.5 J-V curve for a champion device using (A) an etched CZTS film, and (B) a non-etched CZTS film. The current (I_{mp}) and potential (V_{mp}) at maximum power are indicated by dashed green lines, and used to calculate the Fill Factor (FF)..... 149

Figure 7.6 J-V curve of the large-sized CZTS device fabricated with the A) etched, and B) non-etched, CZTS. The current (I_{mp}) and potential (V_{mp}) at maximum power are indicated by dashed green lines, and used to calculate the Fill Factor (FF)..... 151

Figure 8.1 CZTS full device structure, with heterogeneous distribution of metals within the CZTS layer. Gaps and pinholes are also readily visible within the same layer. 159

List of Abbreviations, Symbols, and Nomenclature

$\Delta\mu(k)$	mean free path
$\Delta\mu_o(E)$	the jump in the absorption coefficient at the threshold energy
$\mu(E)$	measured absorption coefficient
$\mu_o(E)$	smooth background function for the abs. of an isolated atom
σ_i^2	mean squared displacement
$\varphi(k)$	effective scattering phase shift
$\chi(E)$	the EXAFS fine-structure function
$\chi(k)$	the EXAFS oscillations, a function of photoelectron wave number
$[\text{Cu}'_{\text{Zn}} + \text{Zn}'_{\text{Cu}}]^0$	Cu-on-Zn and Zn-on-Cu antisite pair
acac	acetylacetonate
APS	Advanced Photon Source
BC	back contact
CB	conduction band
CLS	Canadian Light Source
Cu'_{Zn}	Cu-on-Zn antisite defect
CIGS	$\text{CuIn}_x\text{Ga}_{(1-x)}\text{S}(\text{e})_2$
CIS	$\text{CuInS}(\text{e})_2$
CZTS	$\text{Cu}_2\text{ZnSnS}_4$
DFT	density functional theory

DOS	density of states
DWF	Debye-Waller factor
E_0	energy threshold
EB_{CB}	energy barrier between conduction bands
EB_{VB}	energy barrier between valence bands
E_F	Fermi level
E_g	energy band gap
E_{VB}	energy gap from the valence band to the Fermi level
EDX	energy dispersive X-ray spectroscopy
EXAFS	extended X-ray absorption fine structure
$F_i(k)$	effective scattering amplitude
FT	Fourier transform
FTO	fluorine-doped tin oxide coated soda lime glass
GGA	generalized gradient approximation
I_0	incident photon flux
I_{mp}	potential at maximum power, for a full device solar cell
I_{sc}	short circuit current
kWh	kilowatt-hour
MAP	modified Auger parameter
m_e	effective mass of an electron

MO	molecular orbital
MPP	2-mercapto-5-n-propylpyrimidine
MV	methyl viologen
NCs	nanocrystals
N_i	degeneracy of path
PECM	photoelectrochemical measurements
PS	electron-hole separation
R_0	initial path length
Rec	electron-hole recombination
S_0^2	passive electron reduction factor
SCR	space charge region
SEM	scanning electron microscopy
$Sn_{Cu}^{\bullet\bullet}$	Sn-on-Zn antisite defect
$Sn_{Zn}^{\bullet\bullet}$	Sn-on-Zn antisite defect
SR	synchrotron radiation
SSP	single scattering path
TU	thiourea
UV-vis	ultraviolet-visible spectroscopy
VB	valence band
V'_{Cu}	Cu-vacancy defect

V_{mp}	potential at maximum power, for a full device solar cell
V_{oc}	open circuit potential
V_{Zn}''	Zn-vacancy defect
XAFS	X-ray absorption fine structure
XANES	X-ray absorption near edge spectroscopy
XPS	X-ray photoelectron spectroscopy
XRD	X-ray diffraction
Zn_{Cu}^{\bullet}	Zn-on-Cu antisite defect

Chapter 1

1 General Introduction

Energy is perhaps the most important resource in modern society. We use energy to heat and light our homes, power our cars, cook and store food, and even to communicate with each other. With an ever growing population, the demand for energy is only increasing, which leads to increased costs, an unsettling trend that many in society are unable to afford. Both short and long term economic strategy require low-cost energy sources.¹ Unfortunately, the technology to implement such strategy is not yet available, and is a priority for many nations.¹⁻² The source of such energy remains largely controversial, leading to the proposal of multiple solutions to the problem.

1.1 The Energy Problem

Fossil fuels account for the majority of our current energy production, despite being costly to our population health and detrimental to the environment.¹ They are relatively inexpensive, but are rapidly being depleted. Fossil fuels produce nitrous oxides that adversely affect our health, and carbon dioxide that harms the environment.^{1, 3-4} . Additionally, the cost of fossil fuels is rising.¹ With an eye on the future, the time has come to replace fossil fuels with long term renewable energy solutions.

1.2 Renewable Energy Sources

Nuclear energy is one of the most common alternatives energy sources in use today. Nuclear is environmentally controversial, provides vast amounts of energy, and has been a part of the energy strategy of developed nations for some time.¹⁻³ This has led to improvements in nuclear plant safety over the years, and significant improvements in the disposal of spent nuclear wastes.⁵ Despite its success as an alternate energy source, nuclear energy produces large quantities of radioactive waste, which we have yet to find a solution to.^{1,5} It is therefore a useful alternative energy source, but not necessarily the best one.

In theory, the solution to this energy problem is in renewable resources, though they are typically far more expensive. Hydroelectric has high start-up costs, is limited to damnable areas on rivers, and the damming process is harmful to the environment.¹⁻² Wind energy has high capital cost and requires vast amounts of land, while geothermal energy is only accessible in limited locations.¹ Solar energy is a renewable resource that is not limited to specific areas. It is readily available, with enough solar energy striking the US annually to meet their annual needs 1000 times over.¹ Unfortunately, current solar technology lacks the ability to harness it effectively or efficiently.^{1,6} Furthermore, the consumer cost per kilowatt-hour (kWh) is too high at around \$0.15 / kWh as of 2017.² For this technology to become readily adopted, this needs to be reduced to around \$0.05 / kWh.¹⁻² All proposed strategies for achieving this rely on continued improvements to the devices themselves, in materials, efficiencies, and fabrication procedures. The environmental cost of the devices needs to be factored into this as well. The environmental impact of solar technology during operation is negligible; however, modern device fabrication produces a lot of CO₂ and excess heat.⁷⁻⁸ There must therefore be a concerted effort to focus on developing efficient devices using low-cost materials, and environmentally green fabrication processes that limit CO₂ production.

1.3 Harnessing Solar Energy

1.3.1 The Photovoltaic Effect

All photovoltaic devices function on the same principle for solar radiation capture. Photons from the sun strike the surface of the device and are absorbed and an electron excited from an absorbing layer. In a singular atom, a valence electron would be excited to a higher energy level, with each energy level being distinct and well separated from the other. As more atoms are grouped together, each one has its own set of molecular orbitals (MOs) that contribute to the available energy levels, bringing the orbitals closer together. This results in the compacting of MO, as shown in Figure 1.1. With enough atoms, the orbitals blend together to form energy bands. The bonding orbitals form the valence band (VB), and the antibonding orbitals form the conduction band (CB).⁹ Now, when the photon strikes the surface, an electron is promoted from the VB into the CB.

The gap between the VB and CB – the energy band gap (E_g) – determines the photon energy required to achieve this promotion.¹⁰

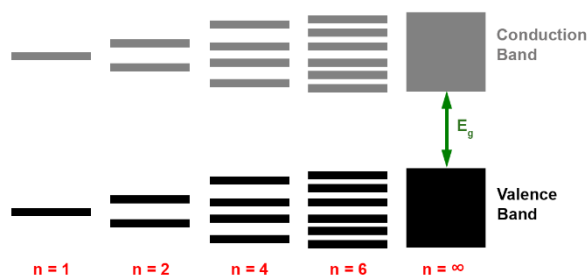


Figure 1.1 Increasing atom number increases the number of energy levels, to a point where they appear to be continuous, forming an energy band.

1.3.2 Extraction of Charge Carriers

Semiconductors can be broken down into types based on the position of the VB and CB relative to the Fermi level (E_F).¹¹⁻¹² The E_F corresponds to the average energy of the electrons within the material, at absolute zero temperature, and will exist somewhere within the energy forbidden region of E_g .¹¹ This will be dependent on the distributions of electrons, and positively charged ions in the crystal lattice – termed “holes” – throughout the film. In a purely crystalline semiconductor, the electrons and holes will be evenly distributed, causing E_F to be located in the center of E_g . These are termed intrinsic, or i-type, semiconductors. Any impurities within a material, be it structural abnormalities / crystal defects, or distinct atom additions to the material, will alter the number of available charge carriers, causing E_F to shift. If the impurity results in a region of relative increased electron density, E_F is raised closer to the CB, and the material is termed an n-type semiconductor. If the impurity creates a relative increase in holes, E_F will be located closer to the VB, and the material is termed a p-type semiconductor. The type of semiconductor determines how charge-carrier flow will occur within the material, and is critical to extracting energy from the initial photoabsorption. The process is fully illustrated in Figure 1.2, using $\text{Cu}_2\text{ZnSnS}_4$ (CZTS) as the p-type semiconductor, and CdS as the n-type. The CZTS and CdS each have different absolute E_F prior to coming in contact with each other. When brought into contact, the electrochemical potentials will

equilibrate, meaning electrons will flow from the material with a higher E_F (the n-type material) to that with a lower E_F (the p-type). This leaves behind a region of uncompensated positive ions in the n-type lattice, and generates a region of uncompensated electrons in the p-type material. The area in which this occurs is indicated by the dashed green lines in Figure 1.2, and is called the space charge region (SCR).

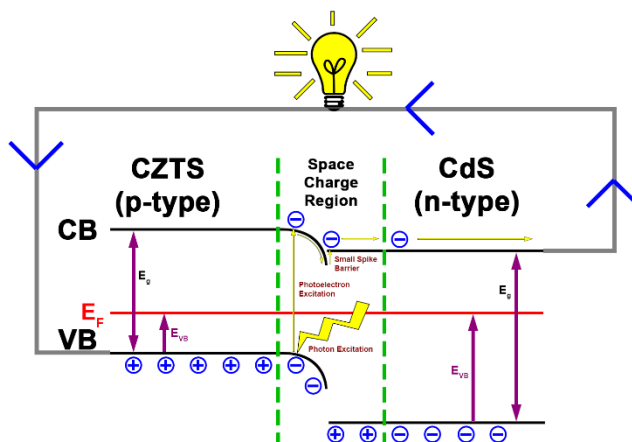


Figure 1.2 Schematic diagram of the p-n junction band structure, and electron flow after E_F equilibration occurs.

Within a p-type material, holes are the majority charge-carriers, while electrons are the majority charge-carriers in an n-type material (both are shown as charges underneath the VB in Figure 1.2). Within the SCR, this is reversed by the equilibration of E_F , and the charge imbalance sets up an electric field, or internal bias, as well as causes a band bending to occur in the CB and VB, equivalent to the charge-redistribution. Then photons absorbed by the material cause photo-excitation of electrons within the CZTS, and the internal bias will help sweep those electrons within the SCR from the CB of the CZTS into that of the CdS.¹³ This means that both the electric field, and the band bending, help drive separation of the charge-carriers, and transfer them from one CB to the other. Depending on the band energies, the gap at the CB interface can be spike-like, as shown in Figure 1.2, where a small energy barrier must be overcome by the electron as it moves into the CdS, or a cliff-like drop down into the CdS CB. A spike-like barrier creates a large barrier to holes, and thus limits electron-hole recombination at the

interface. A small energy barrier can be easily overcome by the internal bias, and as it helps keep electrons from recombining, is advantageous alignment. If this barrier is too high though, (> 0.4 eV), the barrier will be too large for the electrons to easily overcome, and cause large decreases in short circuit current, I_{sc} . A cliff causes the electron to undergo energy decay, reducing the potential that can be generated across the different layers. This will decrease the SCR, thereby decrease the open circuit potential, V_{oc} , and increase the likelihood of recombination through trap-assisted energy levels that could form between the two bands due to non-homogeneity in either film.

1.3.3 Photovoltaic Devices

The full device includes both absorber and buffer layers that create the p-n junction, plus the window layers that allow light to pass through to the absorber layer, and help facilitate electron transfer out of the cell. The complete device structure is shown in Figure 1.3.

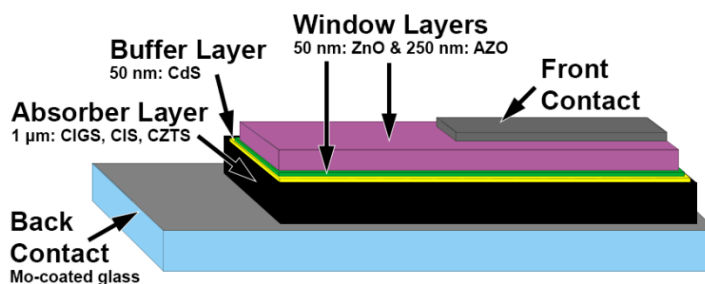


Figure 1.3 Schematic representation of the typical thin film device structure.

These devices make use of minimal metal material to generate the p-n junction, and can employ a variety of different absorber layers, such as $\text{CuIn}_x\text{Ga}_{(1-x)}\text{S(e)}_2$ (CIGS) or CuInS(e)_2 (CIS).¹⁴⁻¹⁵ CIGS based cells have seen efficiencies as high as 19.2%, but these benefits are countered by the scarcity and toxicity of the required indium, selenium, and gallium components.¹⁵ CuInS_2 (CIS) was developed to reduce the costs by removing the expensive gallium and selenium elements.¹⁶ Unfortunately, CIS is less efficient at around 14% and, with indium requirements, it remains costly.¹⁷ Both materials do not satisfy the long-term goals, as the material costs are high, and not abundant.

1.3.4 $\text{Cu}_2\text{ZnSnS}_4$

CZTS is therefore an ideal derivative of the above mention layers. It eliminates costly elements and makes use of only earth-abundant elements, though at the expense of efficiency.¹⁸⁻¹⁹ While CIGS and CIS both adopt a chalcopyrite structure, CZTS has a more complex quaternary structure, and can have several different crystal phases, defects, or impurities.⁶ CZTS is a p-type semiconductor with a tunable direct energy band gap of 1.4-1.5 eV and a high absorption coefficient $> 10^4 \text{ cm}^2$, with device efficiencies of 9.5% for pure sulfide CZTS, and 12.6% when using a sulfur/selenium mix.²⁰⁻²¹

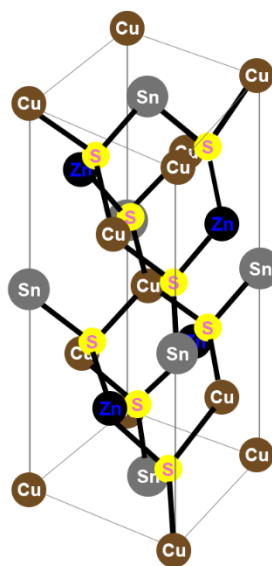


Figure 1.4 The unit cell for the kesterite crystal structure of CZTS.

Ideal CZTS NCs are of kesterite (Figure 1.4) crystal structure – of the space group $I\bar{4}$ – with a relatively Cu-poor and Zn-rich composition;²²⁻²⁴ however, fabricated CZTS can form an alternate stannite structure – of the space group $I\bar{4}2m$ – and both crystal structures can form in Cu-rich, Zn-poor compositions. The fabrication of the desired crystal structures requires careful control of the conditions and the starting ratios; this becomes a challenge during fabrication, as the final compositions do not correspond directly to the initial starting ratios, and uniformity of the film is very difficult to achieve.²⁵⁻²⁷ To combat this, several techniques were used throughout this thesis to

separately measure the charge-carriers, and the crystal structure, and create meaningful ties between the two.

1.4 Methods of Analysis

1.4.1 Photoelectrochemical Measurements

The complex nature of the full solar device makes it especially difficult to study, due to the many films and interfaces involved. This necessitated a method for examining the CZTS layer for responsiveness to photon stimulus, without introducing the CdS layer, and thus without completing the p-n junction. A pseudo-junction was therefore created by immersing the CZTS layer, attached to the back contact (BC), in a solution medium to create a Schottky junction, and electrochemically measure the kinetics at the surface of the CZTS.¹¹ The BC was connected to the electrode, standardizing contact area to ensure reproducibility between samples. The cast CZTS films were then immersed in a methyl viologen electrolyte solution of 0.05 M MV^{2+} and 0.1 M potassium chloride. Using a three-electrode system, potential is measured via the film electrode and a saturated calomel electrode, while current was measured via the film electrode and a platinum counter electrode to obtain PECMs. By passing a linear potential sweep from 0.0 to -0.4 V at a scan rate of 5 mV/s, photocatalytic current was collected. Figure 1.5 gives a full schematic of this setup, while the Figure 1.5 inset outlines the reduction of MV^{2+} to MV^+ , which serves as a measure of the current density associated with the CZTS layer.

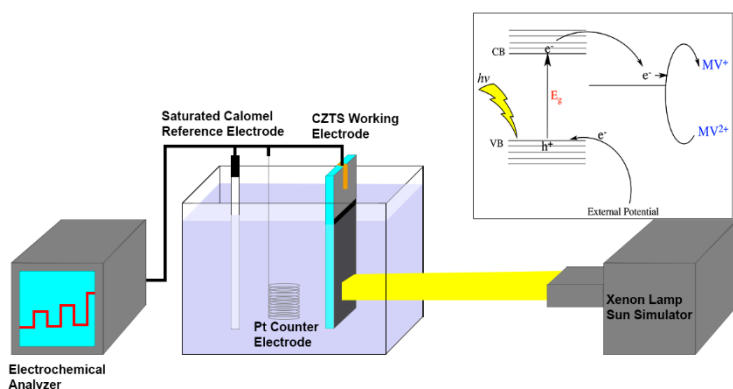


Figure 1.5 Schematic view of the PECM setup. The electrochemical process that is occurring is shown in the inset above the Xenon Lamp.

The greater the difference between the current density in light-on and light-off scenarios, the better the CZTS layer for photoconversion and thus for potential use in photovoltaics. On exposure to light, the creation of a photogenerated electron-hole pair occurs, with the electron transfer to the MV solution via the scheme outlined herein.



Ideal films require good absorption via (1.1), with limited to no decay through (1.2), with preferential electron transfer through (1.3). Films that show enhanced product separation – (1.5) – and limited recombination of charges – (1.4) – will maximize photocatalysis.

1.4.2 Synchrotron-Based X-ray Absorption Fine Structure

The tuning of the materials to maximize the photoresponse required very detailed structural analysis. Synchrotron Radiation (SR) a method for producing highly collimated light, and is a very powerful way to achieve this. This radiation is tunable from IR to hard X-rays. They have a very high brilliance, have tunable polarizability, and have a high flux. This makes them very useful in probing materials. For solar energy materials, while SR is typically reserved for the detection of secondary phases and disordered atoms,²⁸⁻³² the use of X-ray absorption near edge structures (XANES) and extended X-ray absorption fine structures (EXAFS) can probe the local and extended environments of a target atom, respectively.³³ Together, XANES and EXAFS make up an XAFS spectrum. Each XAFS is a measure of the change in absorption coefficient (μ) relative to the absorption of an isolated atom, or background, μ_0 , shown as (1.6).³⁴

$$\chi(E) = \frac{\mu(E) - \mu_0(E)}{\Delta\mu_0(E)} \quad (1.6)$$

The resultant spectrum gives an oscillatory pattern as shown in Figure 1.6.

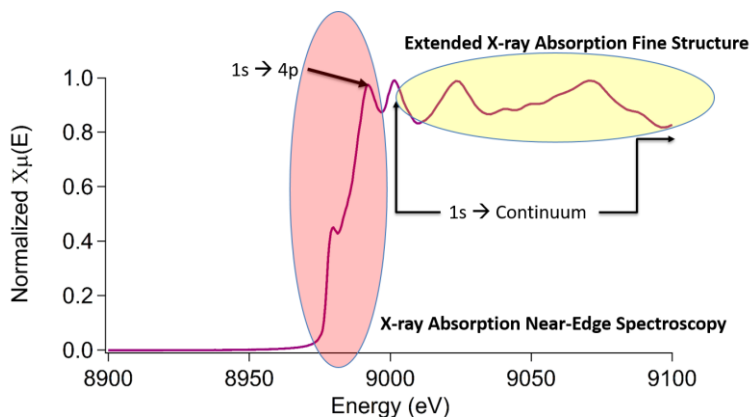


Figure 1.6 An example XAFS spectrum, taken at the Cu(I) K-edge, highlighting the individual XANES and EXAFS regions.

The EXAFS portion can then be isolated, and transformed into the photoelectron momentum vector k space.³⁴⁻³⁵ To do that, the EXAFS of the photo-electron is converted via (1.7), and plotted against wavenumber.

$$k = \sqrt{\frac{2m_e(E - E_0)}{\hbar^2}} \quad (1.7)$$

The oscillations in this type of a plot decay rapidly with respect to increasing wavenumber due to the multiple-scatter pathways involved in EXAFS. To accommodate this, additional weight or value can be added to later oscillations by multiplying (k) by a power of k ; this is usually seen as being k^2 or k^3 (squaring or cubing (1.7)).³⁶ Due to the presence of heavy atoms and the potential for defect-induced multiple-scatter pathways within the CZTS, a k^3 factor was used throughout the thesis to prevent the decay in the oscillations pertaining to the second and third shell scattering atoms. The k -space plot can be converted using a Fourier transform (FT) to give the radial distance space (r -space), seen in Figure 1.7.

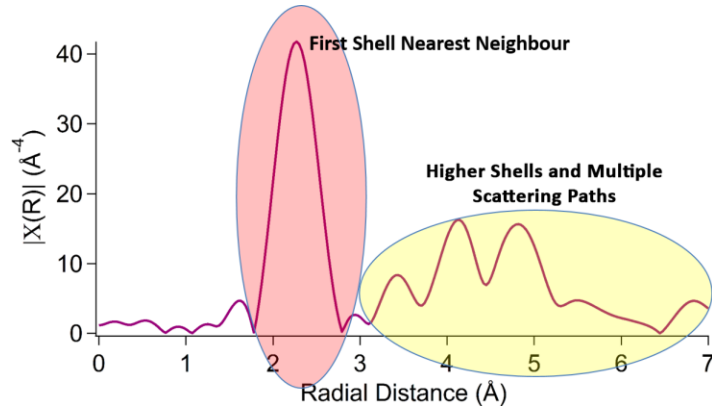


Figure 1.7 A stylized FT of the EXAFS signal, or radial distance space (r-space) plot.

The R-space plot is based on the modulation of the absorption coefficient relative to a free atom, the EXAFS, rather than a true radial distribution function, and so is described by the EXAFS Equation, $\chi(k) = \sum_i \chi_i(k)$, which can be expanded to **(1.8)**.

$$\chi_i(k) = \text{Im} \left(\frac{(N_i S_0^2) F_i(k)}{k R_i^2} \exp(i(2kR_i + \varphi_i(k))) \exp(-2\sigma_i^2 k^2) \exp\left(\frac{-2R_i}{\lambda(k)}\right) \right) \quad (1.8)$$

where $R_i = R_0 + \Delta R$. From equation 6, the values of $F_i(k)$, the effective scattering amplitude of the neighboring atom, $\varphi_i(k)$, the effective scattering phase shift (including both the absorber and the back scatterer), and $\lambda(k)$, the mean free path, are determined theoretically during the analysis, while R_0 , the initial path length to the neighboring atom, together with the remaining parameters are determined by fitting the data with a model, using equation 8. These include N_i , the path degeneracy (coordination number), S_0^2 , the passive electron reduction factor due to a small but unavoidable many body effect, σ_i^2 , the mean squared displacement of half-path length, $E - E_0$, the energy shift, and ΔR , the change in half-path length.^{33, 36-38} The deconvolution of these parameters therefore yields quantitative structural information³³ that, combined with the qualitative information in the XANES,³⁹ can be coupled with the PECM to provide a structural explanation for the photoresponses observed.

1.5 Scope of the Thesis

The work presented in this thesis focuses primarily on the layer-by-layer analysis of each layer and interfaces in a CZTS-based photovoltaic device (the full device), leading to the low-cost fabrication of a working, full device. The goal is to produce a working device with comparable efficiencies to literature, using low-cost fabrication techniques. Due to the importance of the absorber layer, and the structural ambiguity associated with the quaternary kesterite CZTS, emphasis was placed on reconciling its structural, optical, and charge-carrier properties. Unless otherwise stated, all procedures and handling was conducted in an open-air environment, in an effort to keep fabrication costs low, and remain within the scope of long-term international goals.

The CZTS layer is the most important layer to fabricate with controlled uniformity. As such, the reproducibility and control of the crystallinity are of primary concern throughout. In Chapter 2, the focus is on establishing a crystal structure CZTS nanocrystals (NCs) that maximizes photoresponse through specific stoichiometric control of the metal ratios. This formed the base photoelectron excitation portion of Figure 2. The presence of charge-carrier traps limits bulk transfer, and therefore is the primary limiting factor in this transfer. SR-XAFS was used to control the formation of these traps in Chapter 3, and allow more of the photon-excited electrons to reach the CZTS surface. Chapter 4 takes this a step further, to fully link composition with photoresponse, and allow for intelligent design of the material to fit with the CdS.

With the CZTS layer characterization well established, Chapter 5 explores the addition of the CdS barrier, to complete the scheme shown in Figure 2. Unexpectedly, charge-carrier traps were introduced during the deposition process, and lead to slow bulk electron movement, diminishing the SCR and leading to drastically reduced photoresponse. Removal of these traps through thermal annealing allowed the electrons to once again flow through the SCR, and be extracted from the cell; however, the band positioning was not optimized, and so the extraction was not ideal. By studying the surface states of each film, and the SCR about the interface, the bands were tuned to produce the optimal cliff like structure, as shown in Figure 2, and maximize the internal bias of the SCR to transfer electrons through the interface, and into the bulk CdS (Chapter 6). With the bands

aligned, and controlled stoichiometry, full device efficiencies were measured to great success, with the small spike-like barrier helping to maintain a high V_{oc} , and producing competitive efficiencies (Chapter 7). The final chapter (Chapter 8) summarizes the results, and offers next steps in the further enhancement of this promising device.

1.6 References

1. Dresselhaus, M. S.; Thomas, I. L., *Nature* **2001**, *414*, 332.
2. Cook, J. J.; Ardani, K. B.; Margolis, R. M.; Fu, R. *Cost-Reduction Roadmap for Residential Solar Photovoltaics (PV), 2017-2030*; United States, 2018.
3. Vaillancourt, K.; Labriet, M.; Loulou, R.; Waaub, J. P., *Energy Policy* **2008**, *36*, 2296.
4. Kabir, E.; Kumar, P.; Kumar, S.; Adelodun, A. A.; Kim, K. H., *Renew. Sust. Energ. Rev.* **2018**, *82*, 894.
5. Wu, L. D.; Qin, Z.; Shoesmith, D. W., *Corros. Sci.* **2014**, *84*, 85.
6. Siebentritt, S.; Schorr, S., *Prog. Photovoltaics* **2012**, *20*, 512.
7. Shah, A.; Torres, P.; Tscharnner, R.; Wyrsh, N.; Keppner, H., *Science* **1999**, *285*, 692.
8. Song, D. Y.; Cho, E. C.; Conibeer, G.; Flynn, C.; Huang, Y. D.; Green, M. A., *Sol. Energy Mater. Sol. Cells* **2008**, *92*, 474.
9. Lowdin, P. O., *J. Appl. Phys.* **1962**, *33*, 251.
10. Sarma, D. D.; Shanthi, N.; Barman, S. R.; Hamada, N.; Sawada, H.; Terakura, K., *Phys. Rev. Lett.* **1995**, *75*, 1126.
11. Bard, A. J.; Faulkner, L. R., *Electrochemical Methods: Fundamentals and Applications, 2nd Edition*; John Wiley & Sons, 2000.
12. Kaur, K.; Kumar, N.; Kumar, M., *J. Mater. Chem. A* **2017**, *5*, 3069.
13. Sah, C. T.; Noyce, R. N.; Shockley, W., *Proc. Inst. Radio Eng.* **1957**, *45*, 1228.
14. Ye, H.; Park, H. S.; Akhavan, V. A.; Goodfellow, B. W.; Panthani, M. G.; Korgel, B. A.; Bard, A. J., *J. Phys. Chem. C* **2010**, *115*, 234.
15. Ramanathan, K.; Keane, J.; Noufi, R. In *Properties of high-efficiency CIGS thin-film solar cells*, Photovoltaic Specialists Conference, 2005. Conference Record of the Thirty-first IEEE, 3-7 Jan. 2005; 2005; pp 195.
16. Tapley, A.; Vaccarello, D.; Hedges, J.; Jia, F.; Love, D. A.; Ding, Z., *Phys. Chem. Chem. Phys.* **2013**, *15*, 1431.
17. Kushiya, K., *Sol. Energy Mater. Sol. Cells* **2014**, *122*, 309.
18. Guo, Q.; Ford, G. M.; Yang, W. C.; Walker, B. C.; Stach, E. A.; Hillhouse, H. W.; Agrawal, R., *J. Am. Chem. Soc.* **2010**, *132*, 17384.

19. Khalkar, A.; Lim, K. S.; Yu, S. M.; Patole, S. P.; Yoo, J. B., *Electron. Mater. Lett.* **2014**, *10*, 43.
20. Kato, T.; Sakai, N.; Sugimoto, H. In *Efficiency improvement of Cu₂ZnSn(S,Se)₄ submodule with graded bandgap and reduced backside ZnS segregation*, Photovoltaic Specialist Conference (PVSC), 2014 IEEE 40th, 8-13 June 2014; 2014; pp 0844.
21. Yan, C.; Sun, K.; Huang, J.; Johnston, S.; Liu, F.; Veettil, B. P.; Sun, K.; Pu, A.; Zhou, F.; Stride, J. A.; Green, M. A.; Hao, X., *ACS Energy Lett.* **2017**, *2*, 930.
22. Mitzi, D. B.; Gunawan, O.; Todorov, T. K.; Wang, K.; Guha, S., *Sol. Energy Mater. Sol. Cells* **2011**, *95*, 1421.
23. Zhou, H.; Song, T. B.; Hsu, W. C.; Luo, S.; Ye, S.; Duan, H. S.; Hsu, C. J.; Yang, W.; Yang, Y., *J. Am. Chem. Soc.* **2013**, *135*, 15998.
24. Sun, H.; Sun, K.; Huang, J.; Yan, C.; Liu, F.; Park, J.; Pu, A.; Stride, J. A.; Green, M. A.; Hao, X., *ACS Appl. Energy Mater.* **2017**, *1*, 154.
25. Gu, Y. C.; Shen, H. P.; Ye, C.; Dai, X. Z.; Cui, Q.; Li, J. B.; Hao, F.; Hao, X. J.; Lin, H., *Adv. Funct. Mater.* **2018**, *28*, 1703369.
26. Kaur, K.; Sood, M.; Kumar, N.; Nazari, H. H.; Gudavalli, G. S.; Dhakal, T. P.; Kumar, M., *Sol. Energy Mater. Sol. Cells* **2018**, *179*, 22.
27. Sun, K. L.; Yan, C.; Huang, J. L.; Sun, K. W.; Sun, H.; Jiang, L. X.; Deng, X. F.; Stride, J.; Hao, X. J.; Liu, F. Y., *J. Alloys Compd.* **2018**, *750*, 328.
28. Just, J.; Luzenkirchen-Hecht, D.; Frahm, R.; Schorr, S.; Unold, T., *Appl. Phys. Lett.* **2011**, *99*, 262105.
29. Di Benedetto, F.; d'Acapito, F.; Bencistà, I.; Luca, A. D.; Fornaciai, G.; Frizzera, S.; Innocenti, M.; Montegrossi, G.; Pardi, L. A.; Romanelli, M., *Phys. Status Solidi C* **2013**, *10*, 1055.
30. Di Benedetto, F.; Cinotti, S.; Guerri, A.; De Luca, A.; Lavacchi, A.; Montegrossi, G.; Carla, F.; Felici, R.; Innocenti, M., *ECS Trans.* **2013**, *58*, 59.
31. Hartman, K.; Newman, B. K.; Johnson, J. L.; Du, H.; Fernandes, P. A.; Chawla, V.; Bolin, T.; Clemens, B. M.; Cunha, A. F.; Teeter, G.; Scarpulla, M. A.; Buonassisi, T. In *Detection of ZnS Phases in CZTS Thin Films by EXAFS*, Photovoltaic Specialists Conference (PVSC), Seattle, WA, IEEE, Ed. IEEE: Seattle, WA, 2011.
32. Mendis, B. G.; Shannon, M. D.; Goodman, M. C.; Major, J. D.; Claridge, R.; Halliday, D. P.; Durose, K., *Prog. Photovoltaics* **2014**, *22*, 24.
33. Zhang, P., *J. Phys. Chem. C* **2014**, *118*, 25291.
34. Teo, B. K., *EXAFS: Basic Principles and Data Analysis*; Springer: Berlin, 1986.
35. Newville, M., *Rev. Mineral. Geochem.* **2014**, *78*, 33.
36. Ravel, B.; Newville, M., *J. Synchrotron Radiat.* **2005**, *12*, 537.
37. Ravel, B., *J. Synchrotron Radiat.* **2015**, *22*, 1258.

38. Chevrier, D. M.; Zeng, C.; Jin, R.; Chatt, A.; Zhang, P., *J. Phys. Chem. C* **2014**, *119*, 1217.
39. Stöhr, J., *NEXAFS Spectroscopy*; Springer: Berlin, Germany, 1992.

Chapter 2

2 Controlling CZTS Photocatalytic Ability through Alterations in Sulfur Availability

$\text{Cu}_2\text{ZnSnS}_4$ (CZTS) nanocrystals (NCs) were made via a one-pot solvothermal method with various amounts of available free-sulfur and a fixed amount of sulfur bound to 2-mercapto-5-n-propylpyrimidine (MPP). Varying the sulfur availability yields CZTS NCs of different stoichiometry, from which five distinct samples were analyzed for consistency both microscopically and macroscopically. As revealed by X-ray absorption fine structure investigation, samples fabricated in the presence of decreased free-sulfur showed decreased CZTS character, with sporadic compositions and no long term order; however, when fabricated in the presence of no free-sulfur, sulfur from the degraded MPP was found incorporated into the CZTS structure. These NCs showed improved long-term order over standard synthetic procedure. The catalysis of methyl viologen (MV) from MV^{2+} to MV^+ state by CZTS under light irradiation was used as the probe to test the photovoltaic nature. The photocatalysis was enhanced in the films made from NCs fabricated without available free-sulfur. This enhancement is consistent with the measured band gaps, with more ordered NCs showing a band gap that better matches the most intense regions of the solar spectrum.

2.1 Introduction

Semiconductor NCs for use in thin film photovoltaics have shown great promise as a source for renewable solar energy, especially those such as CZTS that contain only cost-effective and non-toxic elements.¹⁻⁴ Our solvothermal process for CZTS production has been shown to be an effective way of fabricating the NCs at low-cost.⁵⁻⁷ The resultant NCs show a high consistency in composition and structure, producing predominantly the ideal kesterite structure with few secondary phases, though the relationship of the starting materials ratio against final compositions is not clear.⁷⁻⁸ Systematic improvements to the NC quality, the NC films, and ultimately the device efficiency require correlation between the changes made in starting material and the final NC outcome.

This chapter is a version of previously published work in Catal. Today, 2016, 260, 119-125.

Ideal CZTS NCs are of kesterite crystal structure – of the space group $I\bar{4}$ – with a relatively Cu-poor and Zn-rich composition;^{5, 9-10} however, fabricated CZTS can form an alternate stannite structure – of the space group $I\bar{4}2m$ – and both crystal structures can form in Cu-rich, Zn-poor compositions. The fabrication of the desired crystal structures requires careful control of the conditions and the starting ratios; this becomes a challenge when using solution phase synthesis as the final compositions do not correspond directly to the initial starting ratios.⁹⁻¹¹ Present work has focused on exploring this trend, and determining the effects of changes in starting conditions on the final NCs. Particular attention is paid to the delivery of sulfur to the system.

Crystal structure and related photoactivity have been previously reported with respect to the effects of Cu-poor, Cu-stoichiometric, and Cu-rich NCs fabricated solvothermally. The effects of these changes were studied on the photocatalytic conversion of MV from the oxidized MV^{2+} to the reduced MV^+ .^{5, 7} While promising, tighter control over NC formation would result in long term improved order, and thus tighter films. To achieve this, alterations in sulfur content were investigated with respect to sulfur presence in both free and organic capping-ligand-bound forms as a method for controlling the fabrication environment. Sulfur-containing precursors are known to aid in producing more uniform films,¹ which is suggestive of highly conserved NC structure. By changing the sulfur content, and the method by which sulfur is supplied, it is anticipated that long-term NC order can be achieved.

CZTS composition was studied using energy dispersive X-ray spectroscopy (EDX), and compared against precursor sulfur-content to determine the relationship between sulfur availability and NC composition. Distinct samples were selected for analysis by powder X-ray diffraction (XRD), and X-ray absorption fine structure (XAFS), to determine local and long-range crystal structure, and to elucidate the effect of sulfur addition on the final NC structures. NCs were then deposited in a thin-film. The films were tested by measuring the catalytic conversion of MV^{2+} to MV^+ in the format of photoelectrochemical measurements (PECM). Higher catalytic conversion is indicative of higher photovoltaic response and thus allows for the determination of improvements in the absorber layer for use in solar cell devices. Band gap analysis using ultraviolet-

visible spectroscopy (UV-vis) was performed to ensure the top-performing NCs having ideal band gap for future devices. XAFS is another powerful tool in addition to other synchrotron radiation (SR) spectroscopy techniques for energy materials.¹²⁻¹³

2.2 Experimental

2.2.1 Synthesis and Film Formation

CZTS NCs were synthesized in a modified one-pot solvothermal process as published elsewhere.⁷ Metal precursor salts of copper(II) acetylacetonate (acac) (Sigma-Aldrich 97%), and tin(II) chloride (Alfa Aesar 98%), with zinc(II) acac (Sigma-Aldrich 95%) substituted for zinc (II) chloride (Sigma-Aldrich 98%), were briefly dissolved in benzyl alcohol (BA) (Sigma-Aldrich 99.8%) at 160 °C. MPP was added to the solution along with 0.2 M thiourea (TU) (Fluka 99.0%) in BA. The MPP and TU concentrations were varied specifically in this work to alternate the free-S and S in ligand form. The reaction vial was then heated at 180 °C for 10 minutes to decompose TU and allow S to react with the metal precursors, and to facilitate ligand-S association to the metals precursors. The resulting dispersed CZTS NCs were cooled down, and then transferred into centrifuge tubes for separation using a Thermo Scientific Sorveall Legend Micro 21 centrifuge at 12.0×10^3 times gravity for 6 minutes. The liquid was removed and the particles were washed and dispersed in solvents such as acetone, isopropanol, and ethanol using a 1510 Branson Sonicator at 40 kHz for a minimum of 5 minutes. The washed NCs were then allowed to air dry for no less than 30 minutes. For NC compositional studies, the dried crystals were stored under normal atmospheric conditions in a dry environment for additional 24 hours to remove trace amounts of solvent prior to analyzing. For dropcasting, NCs were redispersed in acetone before being dropcast in a predetermined surface area of 10 mm^2 on molybdenum-coated glass. The glass functions as the back contact (BC), which were pretreated by immersing in 2% Hellmanex for 2 min and rinsing with ethanol, isopropanol, and deionized water prior to use.

2.2.2 Characterization

Structural and compositional analyses were performed using EDX with scanning electron microscopy (SEM), XRD, and XAFS using SR. A Hitachi S-4500 field emission

microscope with a 100 kV EDX system was used for EDX/SEM. An Inel CPS Powder Diffractometer with an Inel XRG 3000 Cu X-ray generator with an Intel CPS 120 detector provided the XRD data. Sn K-edge extended X-ray absorption fine structure (EXAFS) measurements were performed at the APS@CLS 20-BM beamline of the Advanced Photon Source (APS) at Argonne National Laboratory, Argonne, IL. Thin uniform NC samples were prepared on Kapton tape, and the tape was folded to a thickness of about 1-2 absorption lengths ($1/\mu$ where μ is the absorption coefficient). A Si (111) monochromator and a 400 μm vertical slit was used over a 29.0 to 30.1 keV range. The detection mode was fluorescence X-ray yield recorded using a 13-element Canberra detector. The samples were placed at 45° with respect to the incident photons, and the fluorescence detector was placed at 90° with respect to the incident photons. The detector count rate was kept below 50,000 counts to prevent detector saturation. All spectra were normalized to the incident photon flux, I_0 . Reference Sn foil (EXAFS Materials Inc.) with a thickness of 50 μm , used for energy calibration, was measured in transmission mode downstream of the sample between two ion chambers filled with an 85:20 sccm N_2/Ar mixture. Athena and Artemis software packages were used, and fluorescence yield was plotted over the corrected energy range by normalizing the pre-edge to zero and the post-edge to unity. Normalized spectra were converted using the Fourier Transform (FT) with k^2 weighting from $k = 2.0$ to 6.5 \AA^{-1} to obtain the R space.¹⁴

CZTS NCs were analyzed for current density generated by its photocatalytical conversion of MV^{2+} to MV^+ by PECMs,^{5-8, 15-16} described in Chapter 1.4.1. CZTS band gaps were determined through UV-vis absorption by means of a Varian Cary 50 spectrometer using 20 mM CZTS dispersions in acetone. The scans were carried out at a rate of 1 nm/s from 1100 to 400 nm, and the resulting absorption converted to generate a plot relating the absorption coefficient to the wavelength energy, known as a Tauc plot.

2.3 Results and Discussion

2.3.1 Structural Properties

Fabricated NCs were characterized to determine their crystal phase and electronic properties for optimization prior to their photocatalysis measurements. Initial

optimization was focused on the composition to obtain a correlation between reactant ratios and the resultant NC composition with respect to the sulfur content. Contributions to the sulfur content came from both thiourea and MPP capping ligand, though the extent of the contribution from the capping ligand is not well known. Table 2.1 outlines the effects of decreasing thiourea content on the final NC stoichiometries by focusing on specific permutations of the reduction.

Table 2.1 Sulfur Content Associated with TU and MPP and its Effects on Final NC Composition

Sample	Initial Element Ratio	Final Element Ratio in
	Cu:Zn:Sn:TU:MPP (mol)	CZTS Cu:Zn:Sn:S
M1	1.7 : 1.6 : 1.0 : 3.3 : 7.7	2.1 : 1.3 : 1.0 : 4.2
M2	1.7 : 1.6 : 1.0 : 2.5 : 7.7	2.2 : 0.8 : 1.0 : 4.7
M3	1.7 : 1.6 : 1.0 : 1.6 : 7.7	2.1 : 0.7 : 1.0 : 5.5
M4	1.7 : 1.6 : 1.0 : 0.8 : 7.7	1.7 : 1.6 : 1.0 : 4.0
M5	1.7 : 1.6 : 1.0 : 0.0 : 7.7	1.9 : 1.1 : 1.0 : 4.0

Initial reductions in TU from sample M1 to M3 showed an inverse relationship with final sulfur, with a 50% decrease in TU resulted in an increase in sulfur content by 30%, which can be attributed to more complexation between metal precursors and sulfur in MPP, similar to sulfurization of co-sputtered metallic and sulfur-containing precursor films.¹ With decreased availability of free S from TU, the number of metal-sulfur complexes associated with free S will be decreased due to decreasing sulfur presence, reducing the available CZTS nucleation sites. This again appears similar to that in sulfurization process of co-sputtered metallic and sulfur-containing precursor films.¹ The above S reduction also allows for additional complexation between the metal and the capping ligand to occur. This in turn leads to additional capping ligand presence within the final product as a result of increased MPP-metal bonds, and thus an increase in sulfur content

is observed in the final NCs.¹⁷ The resultant decrease in Zn content is likely an effect of additional Cu-on-Zn type antisite defects (Cu'_{Zn}).^{4, 18-19} The fact that Zn being the most chalcogenide-reactive of the metal precursors, followed by Sn, increases the chance for free sulfur to quickly bind in place of MPP-sulfur, which limits the availability of Zn and Sn for incorporation within the crystal lattice, leading to the respective relative increased Cu and S content observed. The incorporation of the Cu'_{Zn} antisite is of low enough energy that it seems favorable over the dissociation of the other metals from the capping ligand. This trend holds until the free sulfur available from thiourea drops below the stoichiometric sulfur in the final CZTS NCs. All metal precursors are expected to predominantly be bound to the sulfur of the capping ligand. The ratio between Sn and S is particularly significant because the Sn position remains relatively constant between different crystal structures of CZTS in comparison to the S position.

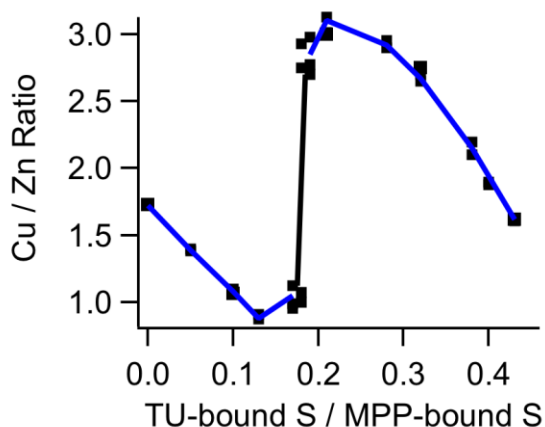


Figure 2.1 Effects of changing sulfur-source on Cu / Zn stoichiometry. The grey region indicates compositions that was extrapolated.

A series of samples were tested to determine the compositional relationship between Cu/Zn and sulfur source, normalized based on the Sn content (Figure 2.1). Low TU leads to the formation of Zn-rich and Cu-poor NCs, while high TU leads Zn-poor and Cu-rich NCs to form. This holds true up to the TU/MPP ratio of 0.18, where an inflection is observed. This inflection point shows a wide range of Cu/Zn ratios, from as low as 1.2 to as high as 2.9, but does not show intermediate ratios – the recognized ideal for CZTS.

This inflection is consistent with reduced TU, to the point where TU alone no longer can supply enough S to account for all produced CZTS. Given the known production of CZTS with only MPP-sulfur present, in the absence of thiourea, the MPP must be a viable source of sulfur. Further, the reaction visually occurs slower, taking twice the time to observe the black color indicative of CZTS formation. This occurs due to the higher decomposition temperature of MPP, which begins around 200 °C.¹⁶ Though the reaction is never heated to temperatures above which MPP decomposes, we clearly see some decomposition in the absence of free-S. This suggests that the formation of CZTS using MPP-sulfur does occur, though at a significantly slower rate when compared to that using free sulfur from thiourea. This leads to the increase in Zn and Sn availability for incorporation in the final NCs, yielding a more controllable synthetic process.

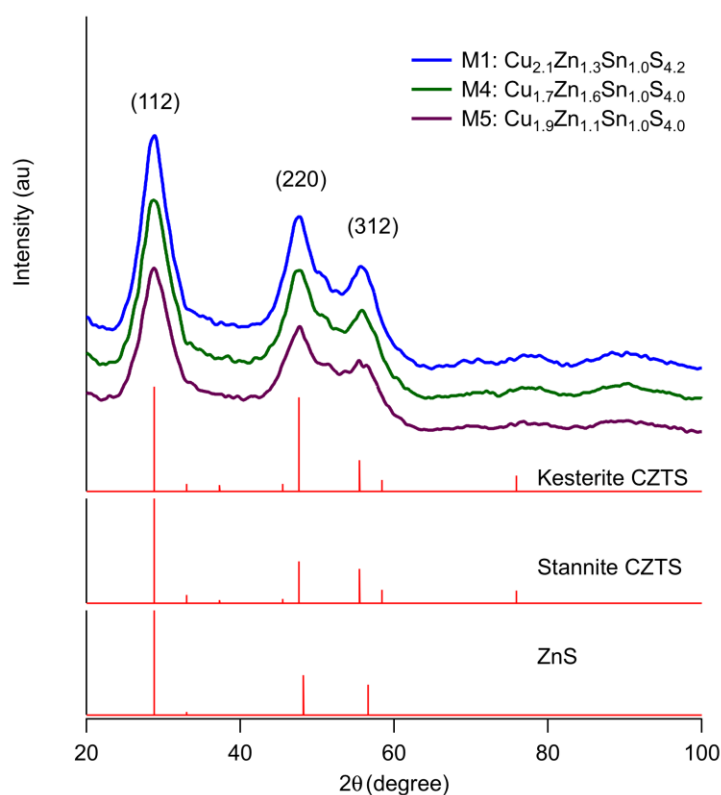


Figure 2.2 Powder XRD comparisons of three distinct stoichiometries.

The resultant NC crystal structure was examined using powder XRD, Figure 2.2. Patterns were taken for compositionally different samples to understand the effect on

long term crystal order. Despite the various compositional differences, the XRD patterns in Figure 2.2 show remarkably similar structural details. The XRD diffraction peaks at the (112), (220), and (312) planes correspond to the expected kesterite CZTS planes (JCPDS 26-0575) for all samples, and show a tetragonal unit cell with parameters $a = b = 5.40 \text{ \AA}$, and $c = 10.7 \text{ \AA}$, with 90° internal angles. These correspond well with literature values of $a = b = 5.40 \text{ \AA}$, and $c = 10.8 \text{ \AA}$.²⁰ This suggests a lack of secondary phase formation during synthesis, the confirmation of which can be seen in Figure 2.2. The peaks characterizing common secondary phases are not present to the extent of detection of the instrument.^{9, 21-22} When coupled to the observed peak broadness, NC compositional changes are more likely indicative of small local structure deviations and defects rather than whole structural changes to the NCs. These deviations are commonly attributed to Cu and Zn defects.¹⁸

2.3.2 Extended X-ray Absorption Fine Structure (EXAFS)

The extended and local structure of the NCs were examined using SR-EXAFS (Figure 2.3), which allows for the examination of the NCs for local structural abnormalities and reconcile the described structural properties with the crystal structure.⁵ Cu and Zn occupy lattice positions where the second shell nearest neighbors are various due to antisite defects, whereas the Sn environment is relatively constant. The Sn K-edge XAFS (Figure 2.3A) are identical in all samples, with little deviation in the threshold energy (E_0), which indicates a singular oxidation state (Sn^{4+} according to the XRD result in Figure 2.2) and chemical environment of Sn across all the samples. This confirms that the long range order of the NCs is maintained, and that the Sn local environment is invariant, as expected. This suggests that each Sn site experiences equal scattering from nearest neighbors, indicating a high degree of similarity among neighboring S atoms. This suggests that any defects are aperiodic. These defects would thus be unobserved in diffraction patterns due to the symmetric constraints imposed, which is consistent with the presented XRD data. The Sn radial distance (Figure 2.3B) provides explanation for the local structure deviations.

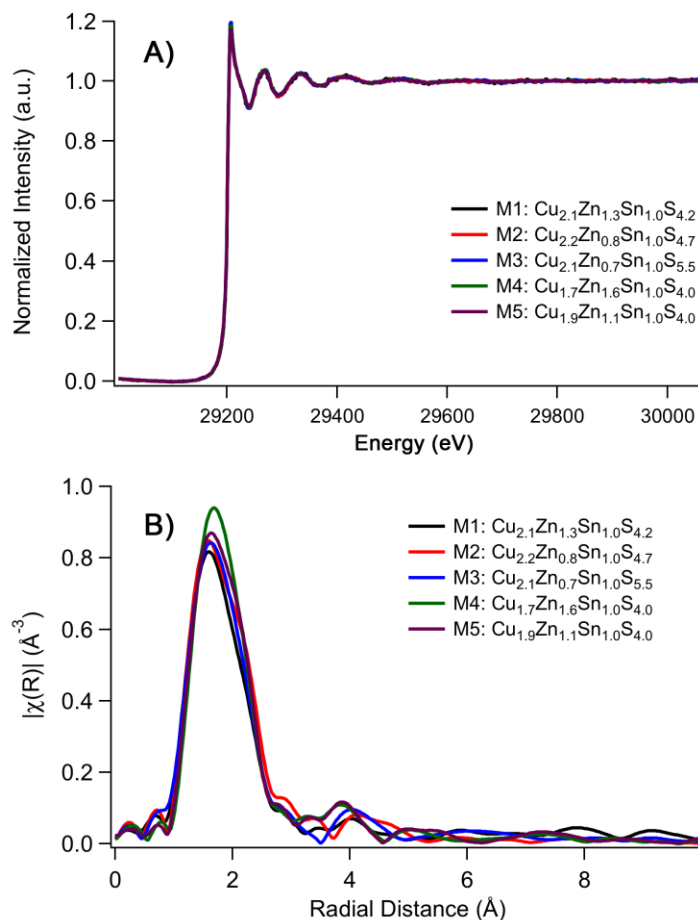


Figure 2.3 SR fluorescence yield of the CZTS NCs a) Normalized Sn K-edge XAFS and b) radial distances.

Due to the unresolved positional nature of the Cu and Zn as describe above, the Sn sites were selected for EXAFS analysis to help correlate changes in the spectra with the associated variations in the sulfur content. The radial distribution maximum corresponds to the average Sn-S inter atomic distance plus a phase correction factor (an identical negative value for constant absorber, Sn and back scattered S). Thus to the first approximation, the difference in the radial distribution represents the difference in the Sn-S bond between samples. Relative to samples made in the presence of high TU content – which corresponds to the M1 sample – there is a small increase in Sn radial distance in the samples with little-to-no TU content – which corresponds to the M3 through M5 samples. This suggests a correlation between Sn radial distance and the reduction in free sulfur during synthesis. This further corresponds to the inclusion of additional MPP-

bound S in the lattice, as is suggested compositional changes (Table 2.1), and is further suggested by the peak intensity, which is proportional to coordination number and the Debye-Waller factor (DWF, a measure of the root mean square displacement due to thermal motion; the smaller the DWF factor, the more order the environment). Since the coordination number is supposed to be constant in all samples, the peak intensity then correlates to better long-range order.²³⁻²⁴ A larger amplitude also indicates fewer defects, with more consistent NC packing.

The increased bond strength is consistent with the removal of excess free-S, which would contribute to additional negative charge carriers on the metals, and thus a weaker initial association between individual CZTS components. This allows for additional point defects and local deformation between metals,²⁵ resulting in the long term disorder observed in M1 through M3. The long term radial distance between M4 and M5 are highly consistent to each other; this is particularly noticeable in the peaks at 4 and 7.2Å. Where high free-S samples show highly inconsistent long term radial distance, M4 and M5 deviate from each other only around the 5.5Å region, likely indicative of a Cu'_{Zn} defect.²⁰ This data corresponds well to the observed trends associated with changes to the TU:MPP ratio. Initial decreases in TU show similar peak positions, but contain a small shoulder peak, indicative of the non-equal Sn bond in M2. Given that Sn is known to be bonded solely to S,¹⁵ this shoulder peak is indicative of a secondary S bond. This could be attributed to MPP-bound S rather than free S, or to the presence of lattice distortions that incorporate extra additional sulfur in the tetrahedral holes. Compositional data suggests the former to be more likely given that the overall S content increase in M2 is relatively small. This indicates the S environments are dissimilar, confirming presence of MPP-bound S and free-S in the NCs. Additionally, stronger bonds between Sn and S are due to some Cu'_{Zn} antisite defects.²⁰ The continued reduction of TU from starting material causes a small increase in radial distance relative to the M1, indicating a small relaxation in the Sn-S bond. This is consistent with the increased sulfur content of M3, as more sulfur fills the unused tetrahedral holes, resulting in a 1.0:5.5 ratio of Sn:S. In the transition to the second relationship, the increase in peak height is indicative of stronger bonds and more uniform crystal structure.²⁰ The enhanced peak suggests an increased uniformity within the second shell, which leads to the sharper and more defined

secondary peaks in the spectra. Both M4 and M5 show a high degree of similarity through several shells, which indicates a level of control in the crystal structure formation as a result of the predominant sulfur source being MPP-bound. The slower release of sulfur into the reaction appears to favor the formation of Zn-rich Cu-poor stoichiometry in highly conserved crystal structures. This is outlined in the Cu / (Zn + Sn) ratio. The ratios determined for M1 through M3 are all >1, yielding the expected Cu rich films.¹⁴ Observation of NCs synthesized via MPP-decomposition controlled S release show a drastic decrease in the ratio, from 0.65 for M4 to 0.90 for M5. This Zn-rich and Cu-poor configuration is known to be ideal for fabrication of high efficiency solar cells, suggesting that a slow sulfur release mechanism could be advantageous in the synthesis of this material.^{3, 26-27}

2.3.3 Photocatalysis

It is plausible that the changes in composition and crystal structure have a profound impact on the effectiveness of the NCs as photoabsorbing layers. By measuring the photoinduced catalytic abilities of the individual absorbing layers, the changes in composition can be reconciled with photoabsorbing ability.^{15, 28} Figure 2.4 demonstrates a typical PECM. On excitation, the electron transfer to MV^{2+} occurs at the surface, indicated by the sharp rise in the current density. The surface composition is thus of great importance to the catalytic response, with more uniformity resulting in increased performance,²⁸ with less electron scavengers present to drive equations 2 and 4.²⁹ This is of note in the initial spike, followed by the small decay in current density seen in the light on scenario of Figure 2.4, as outlined by Khoshmashrab *et al.*⁵

Increased product separation increases the photocatalysis of MV^{2+} to MV^+ . Using M1 as a standard, alternate compositions were tested to compare the compositional trends to their resultant current densities, and thus form optimized absorber layers for use in fabricating CZTS-based solar cells. Figure 2.5 outlines these effects. Initial decreases in the free-S content reduce the effective photocatalysis of MV^{2+} to the point of completely diminishing any photo-response by M3, therefore the photocurrent density. This is consistent with published literature, suggesting that increasing defects to a large degree, leads to an increase in “traps” for the electron that leads to increased recombination. This

means in the presence of excess sulfur, any photogenerated electrons are unable to escape the film to participate in the catalysis. This suggests that the increase in S:Sn of 0.5 from M1 to M2 affects an increases in decomposition and in electron-hole recombination, reducing the desired electron transfer.

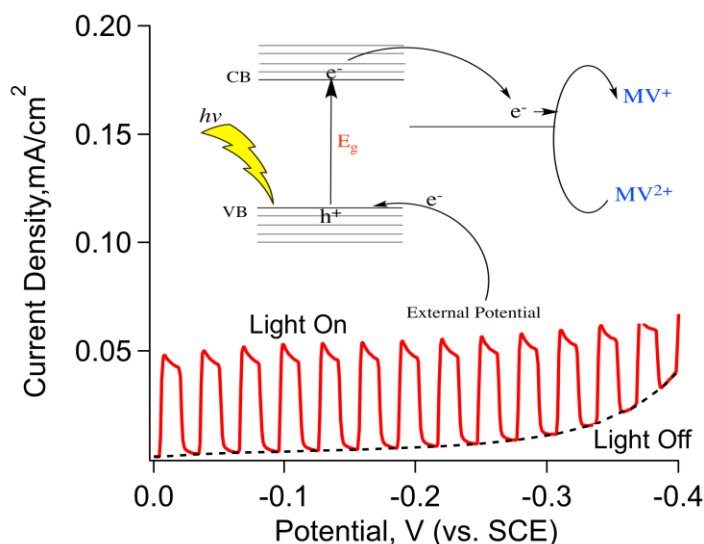


Figure 2.4 Photocatalysis of MV^{2+} to MV^+ resulting from photon absorbance observed in M1. Control measures were taken in the dark, as indicated by the dotted line.

This is seen by the decrease in effective current density from 0.045 mA/cm^2 in M1 to 0.035 mA/cm^2 in M2. The films made predominantly with MPP-bound S show good photoresponse, consistent with highly ordered CZTS films, but only the film made in the absence of free-S show enhancement of the photocatalysis process. Measures of the current density associated with M4 are equivalent to M1 at 0.045 mA/cm^2 , whereas M5 consistently reaches 0.055 mA/cm^2 . This improved photocatalysis associated with the films fabricated from little-to-no free sulfur suggests that there is a detrimental effect of excess free-S on the final NCs. Unfortunately, the excess free-S is required, as indicated by the poor performance of the M2 and M3 samples grown in more stoichiometric free-S quantities. This can be attributed to the instability of the CZTS precursor solution.⁴ Initial decreases in TU reduce the free-S content, leading to a destabilization of the precursor solution and resulting in some secondary phase formation.

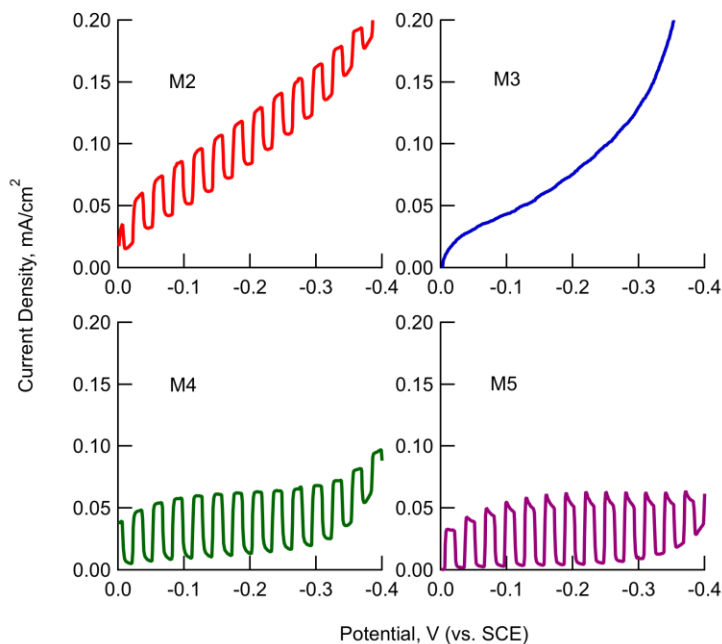


Figure 2.5 PECM comparison of each of the four altered stoichiometries. M2 and M3 show high resistivity, while M4 and M5 show little resistivity, as denoted by the decreased slope of the line and low current density in light off conditions.

As the free-S decreases, the MPP-bound S begins to play a more prominent role in the formation of CZTS, which appears to reduce this instability and leads to more regular films, likely the result of decreased secondary phase formation. Similar trends have been reported in conjunction with TU in studies involving annealing or film structure, suggesting that TU is indeed adversely affecting the observed photoresponse here.^{4, 30} This is corroborated by the enhancements seen in the photocatalysis from the films produced with only MPP-bound S. The MPP-bound S appears to offer similar benefits to those seen when using long-chain organic capping ligands to control the synthesis,² but without requiring high temperature annealing to remove the unwanted carbon residue, thus avoiding any adverse Sn loss associated with SnS loss at high temperature.³¹ Controlling the rate of S-infusion to the metal precursors yield improved catalytic results consistent with the improved NC composition and local defect structure. This can also be

associated with the band gap of the NCs. Figure 2.6 outlines the changes in optical band gap resulting from the changed composition and structure.

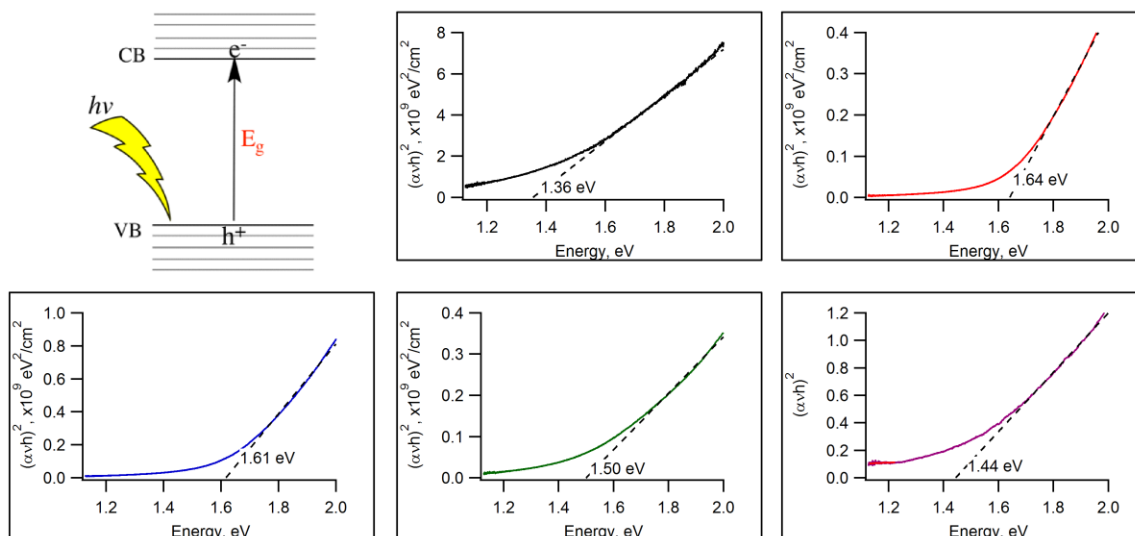


Figure 2.6 Changes to the optical band gap induced by stoichiometric changes, +/- 0.03 eV.

It is ideal for the band gap to be 1.45 – 1.51 eV corresponding to the most intense region of the solar spectrum³. The reference films made with excess free-S show a lower than ideal band gap, potentially indicating a more stannite structure.^{7, 32} Initial decreases in available free-S lead to higher than ideal band gaps, which could be attributed to the additional S within the structure and thus a decrease in the p-type character.⁴ This is difficult to probe, given techniques such as XRD lack the ability to probe local structure, and a soft X-ray SR source is required to probe the S k-edge; however, the presence of additional S has been shown through EDX, and the additional negative charge content is contrary to the formation of local positive charge required for p-type formation. This adverse effect is reversed as free-S content is decreased further. As the available free-S decreases to lower levels and eventually removed from synthesis, the band gap gradually shifts back to lower regions, though higher than that of the M1 film, and within the desired absorbance region. This correlates well with the observed stoichiometry changes, with the Cu-poor and Zn-rich films showing ideal band gaps, while Cu-rich films show lower than ideal band gaps. This makes sense, given the propensity for increases to the

band gap as a result of decreases in copper.³³ The samples without any free-S showed decreased band gaps associated with lower Cu, while maintaining a higher crystallinity and thus a greater photogenerated catalysis due to the lack of compounding factors resulting from the presence of excess sulfur.

2.4 Conclusions

CZTS NCs growth through solution phase, one-pot, solvothermal synthesis shows dependence on different sulfur environments. Altering the free-S availability shows initial reductions in CZTS formation, with large deviations from stoichiometric in the final NC composition; however, on further reduction below Sn concentration in solution, MPP-bound S begins to play a role, mitigating any loss of stability in the precursor solution and resulting in highly conserved CZTS NCs. This trend continues, even in the presence of no free-S. The catalytic conversion of MV^{2+} to MV^+ also follows a similar trend, with large decreases in catalytic conversion observed in decreasing free-S availability, with increased and even enhanced conversion in films made in the presence of very little free-S, or exclusively MPP-bound S. This suggests that the slow-release of S through MPP degradation offers enhanced control over the NC formation, and thus greater control over final stoichiometry and long-term crystallinity. Both of these conditions are desired characteristics for eventual CZTS solar cell device fabrication.

The sulfur source and availability also contribute to the band gap of the fabricated CZTS. Initial decreases in free-S were inversely proportional with the increased band gap, which is consistent with the decreased catalytic conversion. The high band gap achieves less photo-excitation, converting less of the solar spectrum and thus converts less MV^{2+} . As MPP-bound S begins to play more of a role, the band gap begins declining back towards the optimal gap, with the NCs fabricated solely based on MPP-bound S corresponding better with the most intense portion of the solar spectrum than any other combination. The slow-release mechanism offered through MPP-degradation appears favorable to free-S association of metal ions for solution-phase synthesis of CZTS NCs.

2.5 References

1. Platzter-Björkman, C.; Scragg, J.; Flammersberger, H.; Kubart, T.; Edoff, M., *Sol. Energy Mater. Sol. Cells* **2012**, *98*, 110.
2. Kim, Y.; Woo, K.; Kim, I.; Cho, Y. S.; Jeong, S.; Moon, J., *Nanoscale* **2013**, *5*, 10183.
3. Guo, Q.; Ford, G. M.; Yang, W. C.; Walker, B. C.; Stach, E. A.; Hillhouse, H. W.; Agrawal, R., *J. Am. Chem. Soc.* **2010**, *132*, 17384.
4. Park, S. N.; Sung, S. J.; Son, D. H.; Kim, D. H.; Gansukh, M.; Cheong, H.; Kang, J. K., *R. Soc. Chem. Adv.* **2014**, *4*, 9118.
5. Khoshmashrab, S.; Turnbull, M. J.; Vaccarello, D.; Nie, Y. T.; Martin, S.; Love, D. A.; Lau, P. K.; Sun, X. H.; Ding, Z. F., *Electrochim. Acta* **2015**, *162*, 176.
6. Vaccarello, D.; Hedges, J.; Tapley, A.; Love, D. A.; Ding, Z., *J. Electroanal. Chem.* **2015**, *738*, 35.
7. Vaccarello, D.; Tapley, A.; Ding, Z., *R. Soc. Chem. Adv.* **2013**, *3*, 3512.
8. Tapley, A.; Vaccarello, D.; Hedges, J.; Jia, F.; Love, D. A.; Ding, Z., *Phys. Chem. Chem. Phys.* **2013**, *15*, 1431.
9. Zhou, H. P.; Hsu, W. C.; Duan, H. S.; Bob, B.; Yang, W. B.; Song, T. B.; Hsu, C. J.; Yang, Y., *R. Soc. Chem. Energ. Environ. Sci.* **2013**, *6*, 2822.
10. Mitzi, D. B.; Gunawan, O.; Todorov, T. K.; Wang, K.; Guha, S., *Sol. Energy Mater. Sol. Cells* **2011**, *95*, 1421.
11. Katagiri, H.; Jimbo, K.; Maw, W. S.; Oishi, K.; Yamazaki, M.; Araki, H.; Takeuchi, A., *Thin Solid Films* **2009**, *517*, 2455.
12. Liu, X.; Yang, W.; Liu, Z., *Adv. Mater.* **2014**, *26*, 7710.
13. Sham, T. K., *Adv. Mater.* **2014**, *26*, 7896.
14. Ravel, B.; Newville, M., *J. Synchrotron Radiat.* **2005**, *12*, 537.
15. Ye, H.; Park, H. S.; Akhavan, V. A.; Goodfellow, B. W.; Panthani, M. G.; Korgel, B. A.; Bard, A. J., *J. Phys. Chem. C* **2010**, *115*, 234.
16. Tapley, A.; Hart, C.; Vaccarello, D.; Love, D. A.; Ding, Z., *J. Electrochem. Soc.* **2014**, *161*, H725.
17. Huang, W.; Li, Q.; Chen, Y.; Xia, Y.; Huang, H.; Dun, C.; Li, Y.; Carroll, D. L., *Sol. Energy Mater. Sol. Cells* **2014**, *127*, 188.
18. Chen, S. Y.; Yang, J. H.; Gong, X. G.; Walsh, A.; Wei, S. H., *Phys. Rev. B* **2010**, *81*, 245204.
19. Schorr, S., *Sol. Energy Mater. Sol. Cells* **2011**, *95*, 1482.
20. Espinosa-Faller, F. J.; Conradson, D. R.; Riha, S. C.; Martucci, M. B.; Fredrick, S. J.; Vogel, S.; Prieto, A. L.; Conradson, S. D., *J. Phys. Chem. C* **2014**, *118*, 26292.

21. Redinger, A.; Berg, D. M.; Dale, P. J.; Siebentritt, S., *J. Am. Chem. Soc.* **2011**, *133*, 3320.
22. Yang, H.; Jauregui, L. A.; Zhang, G.; Chen, Y. P.; Wu, Y., *Nano Lett.* **2012**, *12*, 540.
23. Koza, M. M.; Leithe-Jasper, A.; Rosner, H.; Schnelle, W.; Mutka, H.; Johnson, M. R.; Grin, Y., *Phys. Rev. B* **2014**, *89*, 014302.
24. Maradudin, A. A.; Flinn, P. A., *Phys. Rev.* **1963**, *129*, 2529.
25. Erslev, P. T.; Young, M. R.; Li, J. V.; Siah, S. C.; Chakraborty, R.; Du, H.; Lad, R. J.; Buonassisi, T.; Teeter, G., *Sol. Energy Mater. Sol. Cells* **2014**, *129*, 124.
26. Haight, R.; Shao, X. Y.; Wang, W.; Mitzi, D. B., *Appl. Phys. Lett.* **2014**, *104*, 033902.
27. Xu, P.; Chen, S. Y.; Huang, B.; Xiang, H. J.; Gong, X. G.; Wei, S. H., *Physical Review B* **2013**, *88*, 045427.
28. Amara, A.; Ferdi, A.; Drici, A.; Bernède, J. C.; Morsli, M.; Guerioune, M., *Catal. Today* **2006**, *113*, 251.
29. Todorova, N.; Giannakopoulou, T.; Pomoni, K.; Yu, J. G.; Vaimakis, T.; Trapalis, C., *Catal. Today* **2015**, *252*, 41.
30. Wen, X.; Luo, W.; Zou, Z., *J. Mater. Chem. A* **2013**, *1*, 15479.
31. Scragg, J. J.; Ericson, T.; Kubart, T.; Edoff, M.; Platzer-Björkman, C., *Chem. Mater.* **2011**, *23*, 4625.
32. Malerba, C.; Biccari, F.; Ricardo, C. L. A.; Valentini, M.; Chierchia, R.; Müller, M.; Santoni, A.; Esposito, E.; Mangiapane, P.; Scardi, P.; Mittiga, A., *J. Alloys Compd.* **2014**, *582*, 528.
33. Caballero, R.; Victorov, I.; Serna, R.; Cano-Torres, J. M.; Maffiotte, C.; Garcia-Llamas, E.; Merino, J. M.; Valakh, M.; Bodnar, I.; León, M., *Acta Mater.* **2014**, *79*, 181.

Chapter 3

3 Identifying Barriers to Charge-Carriers in the Bulk and Surface Regions of $\text{Cu}_2\text{ZnSnS}_4$ Nanocrystal Films by XAFS

Solar cell performance is most affected by the quality of the light absorber layer. For thin-film devices, this becomes a two-fold problem of maintaining a low-cost design with well-ordered nanocrystal structure. The use of $\text{Cu}_2\text{ZnSnS}_4$ (CZTS) nanocrystals (NCs) as the light absorber films forms an ideal low-cost design, but the quaternary structure makes it difficult to maintain a well-ordered layer without the use of high-temperature treatments. There is little understanding of how CZTS NC structures affect the photoconversion efficiency, the charge-carriers, and therefore the performance of the device manufactured from it. To examine these relationships, the measured photoresponse from the photo-generation of charge-carrier electron-hole pairs was compared against the crystal structure, as short-range and long-range crystal orders for the films. The photoresponse simplifies the electronic properties into three basic steps that can be associated with changes in energy levels within the band structure. These changes result in the formation of barriers to charge-carrier flow. The extent of these barriers were determined using synchrotron-based X-ray absorbance fine structure (XAFS) to probe the individual metal centers in the film, and comparing these to molecular simulations of the ideal extended X-ray absorption fine structure (EXAFS) scattering. This allowed for the quantification of bond lengths, and thus an interpretation of the distortions in the crystal lattice. The various characteristics of the photoresponse was then correlated to the crystallographic order, and used to gain physical insight into barriers to charge-carriers in the bulk and surface regions of CZTS films.

3.1 Introduction

Using NCs to fabricate the absorber layer poses its challenges in the form of film uniformity. Not only are the NCs required to be highly conserved throughout, but the film itself needs a uniform deposition to prevent physical barriers to charge-carrier

This chapter is a version of previously published work in J. Chem. Phys., 2016, 145, 204702-12.

mobility.¹⁻⁴ Using electrophoretic deposition, these films can be fabricated to size-exclusive, well-packed specifications, which provides the required uniform film.⁵⁻⁶ The effectiveness of these films is thus governed by the degree of similarity across all NCs.^{1,7} This makes the individual differences between the NCs of a particular group and will be the primary influence on the charge carrier separation, and thus the key to improved absorber layer design.

There is little understanding of how CZTS NC structures affect the photoconversion efficiency, the charge-carriers, and therefore the performance of manufactured devices. Xiao, and Goddard III reported DFT simulations on predicting roles of defects on band offsets and energetics at CIGS (Cu(In,Ga)Se₂/CdS) solar cell interfaces, and their implications for improving performance.⁸ Analysis of the CZTS NC structures in this fashion would have similar benefits for improving performance of CZTS solar cells.

In this Chapter, fluorescence yield XAFS were employed to investigate the local structure of various stoichiometry CZTS films.⁹⁻¹⁰ Its dependency on the distance between atoms in the structure, including the vibrational variance was elucidated. As such, the measured EXAFS was then used to provide extensive qualitative and quantitative information of a sample. These were translated into an evaluation of the relative Zn-, Cu-, and Sn-mesh across the film, and the degree to which that mesh is distorted from the perfectly crystalline, uniform structure.²² Given that sulfur is the nearest neighbor to each metal atom, a first shell analysis of the extended X-ray absorption fine structure (EXAFS) was used to generate a full structural analysis of the NC structure. When compared against the FEFF-simulated EXAFS of CZTS, a fully constructed structural break-down of the film can be determined.¹¹⁻¹² This can then be used to draw conclusions with regards to small changes seen using photoelectrochemistry, therefore to identify barriers to the charge-carriers.

3.2 Experimental

3.2.1 Fabrication

CZTS NCs were fabricated solvothermally as previously reported by our group,²⁹⁻³⁰ using the methods reported in Chapter 2.2.1. Individual samples were prepared by making

small deviations in the precursor salt ratios to produce samples with a range of Zn/Sn and $Cu/(Zn + Sn)$ ratios between 1.64 and 0.72, and between 1.24 and 0.87, respectively. Based on stoichiometric CZTS, both Zn/Sn and $Cu/(Zn + Sn)$ should have ratios of 1:1. Samples of high Zn content were made with additional Zn precursor to yield Zn/Sn ratios greater than 1. Reduced Zn precursor gave rise to Zn/Sn ratios less than one. Likewise, increasing the Cu precursor produced higher $Cu/(Zn + Sn)$ ratios. Resultant NCs were dried in vacuum and stored under argon prior to analysis to avoid possible oxidative damage. Compositional analysis of the prepared CZTS NCs was performed using a Hitachi S-4500 field emission microscope with a 100 kV energy dispersive X-ray spectroscopy (EDX) Quartz XOne system. Films were fabricated by dispersing dried NCs with differing compositions in isopropanol to 2 g/L, and electrophoretically depositing the dispersion onto fluorine-doped tin oxide-coated glass (FTO),³ using a Keithly 2400 source meter. The depositions were made using a constant 0.24 mA/cm² current for 40 s.

3.2.2 Characterization

Photoelectrochemical measurements (PECMs) were carried out to access the light absorbing film quality as reported elsewhere.¹³⁻¹⁵ and described in Chapter 1.4.4. These electrochemical characteristics were then correlated against crystal structures, determined by an Inel CPS Powder Diffractometer with an Inel XRG 3000 Cu X-ray generator and an Inel CPS 120 detector.

These films were then further examined for short-range disorder using synchrotron-based XAFS. XAFS measurements were performed at the CLS@APS 20-BM beamline of the Advanced Photon Source (APS) at Argonne National Laboratory, Argonne, IL. K-edge absorption was measured for Cu, Zn, and Sn, quantified by fitting analysis, and compared against FEFF simulations of stoichiometric kesterite-phase CZTS.^{9, 16}

The samples were prepared on Kapton tape, and the tape was folded to achieve a uniform NC thickness of 0.5 mm. A 400 μm vertical slit was used over 8.78 to 9.52 keV for the Cu-edge, 9.46 to 10.4 keV for the Zn-edge, and 29.0 to 30.1 keV for the Sn-edge. The detection mode was in fluorescence yield recorded using a 13-element Canberra Ge

detector. The samples were placed at 45° with respect to the incident beam, and the fluorescence detector was placed at 90° with respect to the incident beam. The detector count rate was kept below 50,000 counts per element to prevent detector saturation, and scans were duplicated to ensure 2,000,000 total counts per scan to ensure excellent statistics. All spectra were normalized to the incident photon flux, I_0 . Cu, Zn, and Sn reference foils (EXAFS Materials Inc.) with a thickness of 7.5, 10, and 50 μm , respectively were used for energy calibration, and were measured in transmission mode downstream of the sample between two ion chambers filled with an 85:20 N_2/Ar mixture. With the software packages of Athena and Artemis, fluorescence yield was plotted over the corrected energy range by normalizing the pre-edge to zero and the post-edge to unity.²² The normalized energy spectra were examined, and the momentum component was isolated.

This was analyzed using Athena, Artemis as well as FEFF9 software packages. The oscillations in this type of a plot decay rapidly with respect to increasing wavenumber due to the multiple-scatter pathways involved in EXAFS. To accommodate this, additional weight or value can be added to later oscillations by multiplying (k) by a power of k ; this is usually seen as being k^2 or k^3 . Due to the presence of heavy atoms and the potential for defect-induced multiple-scatter pathways, a k^3 factor was used to prevent the decay in the oscillations pertaining to the second and third shell scattering atoms. The k -space plot was then converted using a Fourier transform (FT) and over a wavenumber range of 2.5 to 12 in the k -space to isolate discrete oscillations caused by atoms of different distances from the central absorber using a Hanning window.^{9-10, 17} The lower window limit was chosen to reflect the region of relative stability in the background function, while the upper limit was set to eliminate the regions of high noise that could introduce artifacts to the model. The k -space curve is then inverse Fourier transformed back to the Real-space plot. Using Artemis with FEFF8, and FEFF9 software, a multi-shell fit was obtained for all samples at the Cu, Zn, and Sn K-edge, using the stoichiometric kesterite CZTS from the crystallographic information file generated using VESTA.³³ Fitting parameters allowed deviations within the model, determined to be within a realistic value range. This was done to allow for the deviations predicted through XRD, and XANES, while maintaining the integrity of the model. These fittings

were used to overlap the peaks and thus quantify the bond distances in our experimental EXAFS. The fitting was refined to measure deviations from a model, and reported to within 0.01 Å. The complete theoretical spectra were further compared across the samples to determine the relative closeness of our samples to the theoretically pure kesterite structure.

3.3 Results and Discussion

3.3.1 Photoelectrochemical Measurements

Photoresponse was measured for each film immersed in a 0.05 M methyl viologen (MV^{2+}) to examine the change in charge-carrier flow caused by light. This allows for direct correlations to be made among the quality of the NCs, the layered film, and the final photoresponse.¹⁹⁻²⁰ Any imperfection in the NCs or in the film will contribute charge-carrier traps to the device, increasing bulk resistance in the absorber layer and ultimately decreases the efficiency.^{3, 7}

Five samples of different compositions, encompassing high and low Cu and Zn permutations, were examined to identify the current density associated with each without exposure to light, Figure 3.1. On exposure to light, the current density increases due to photo-generated electron-hole pairs transitioning to the MV^{2+} solution (Figure 3.1).

A sample will be considered high-performance CZTS in this Chapter if it produces a current density increase of greater than 0.05 mA/cm². These high performance samples were compared against high Cu and high Zn controls – both known as low-performance NCs – in an effort to identify factors that contribute to reduced performance in final devices. The effects of each are quantified in the resultant PECMs (Figure 3.1).

Sample 1 (Figure 3.1A) shows the greatest current density of 0.15 mA/cm². This high-performance sample shows that under illumination, there is an initial increase in current density with increasing potential, forming the upper level of the diffusion-controlled region, though the slow increase in total current density suggests the possibility of shallow-traps, which will be discussed later.²¹ Under chopped light, this same pattern is

seen, with illumination causing an immediate rise from the dark current, with a photoresponse of 0.15 mA/cm^2 .

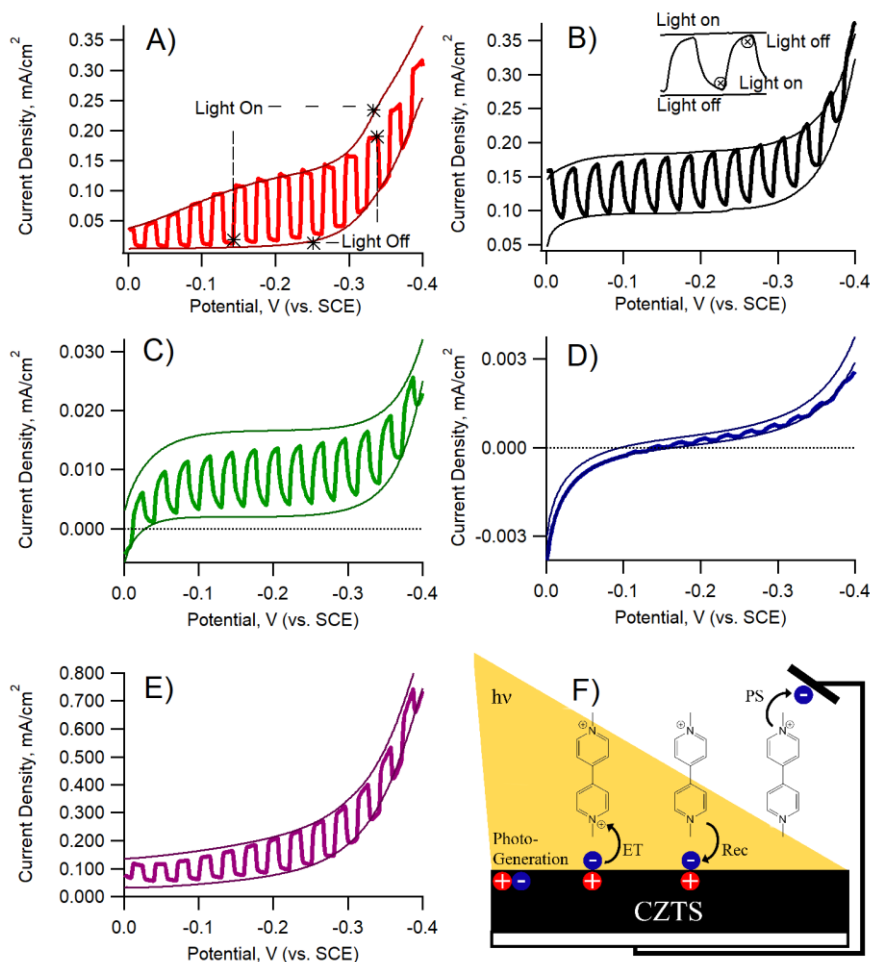


Figure 3.1 PECM results for the 5 samples, showing the light-on condition (top solid line) under alternative light illumination. Samples 1, 2, and 5 in A, B, and E, respectively, show high photoresponse to light exposure, indicating a high density of charge-carriers leaving the surface. Samples 3 and 4 (C and D) show low current density regardless of conditions, indicating a low density of charge-carriers. Four photoelectrochemical reaction steps are illustrated in F: photo-generation of an electron-hole pair, electron transfer (ET) to the MV²⁺, electron-hole recombination (Rec) and product separation (PS).

This immediate response is significant, as it suggests a high mobility of charge-carriers through the bulk, with few traps in the bulk to inhibit that mobility. This can be contrasted with Sample 2 (Figure 3.1B). Here, the photoresponse is again high-performance at 0.10 mA/cm^2 , and shows a stable upper-level to the diffusion-controlled region, suggesting fewer surface states and low-level traps inhibiting the charge-carriers. The difference is seen in the transients, highlighted in the inset for Figure 3.1B. The response to sudden illumination is slow rising, barely reaching the upper level before the light is chopped, and the signal drops. This slow response to changing light stimulus is indicative of slow diffusion of charges through the bulk of the film, increasing the opportunity for recombination sites within the bulk.²² Furthermore, the high dark current is indicative of hole-injection from the valence band, adding additional opportunity for recombination sites. Sample 3 (Figure 3.1C) shows this to an even greater extent. This sample was specifically designed as a high-Cu control sample, so the photoresponse is limited at 0.015 mA/cm^2 . High Cu shows reduced bulk transport, indicating systemic defects throughout the film, and the presence of deep charge-carrier traps. Sample 4 (Figure 3.1D) is the high Zn control sample, which shows very little photoresponse of 0.0005 mA/cm^2 . Whether this yields defects in the bulk is hard to determine with such limited photoresponse; however, excessive Zn content clearly confers no advantage to the film. Under slow-release sulfur conditions during fabrication, the resultant films Sample 5 (Figure 3.1E) shows much the same characteristics as Figure 3.1A, though with a higher low limit dark current.

There is also a correlation between the charge carriers leaving the film and the measured photoresponse. In p-type semiconductors, such as CZTS, electrons serve as the minority carriers, meaning there will be a measurable increase in the number of electrons relative to holes following the creation of an electron-hole pair under illumination. As depicted in Figure 3.1F, the photo-generated electron transfers to the methyl viologen on illumination. The electron on the reduced form, MV^+ , can then recombine with the hole left behind in the film (Rec in Figure 3.1F), or fully separate to complete the circuit (PS in Figure 3.1F). Those with the highest photoresponse will have high PS and low Rec. Increases in PS result from high charge-carrier mobility, while increases in Rec result from electron tunneling into the CZTS VB, or through low charge-carrier mobility.²¹⁻²²

In each of the spectra in Figure 3.1, there is a sloping increase in the current density, regardless of light, that begins around -0.3 V in all samples save for sample 5 (Figure 3.1E). This increase corresponds with a shift from a rectifying (Schottky) junction to a non-rectifying (Ohmic) junction.²³⁻²⁵ This is also known as the breakdown voltage, which is the point at which the junction deteriorates, allowing current to flow freely through the film. Under these conditions, pseudo-space charge region breaks down, creating a rapid accumulation of charge, reducing the observed photoresponse. The point at which this transition occurs is well conserved throughout the samples indicating a high degree of conservation within the valence band (VB).²⁶⁻²⁷ The diffusion-controlled region corresponds to the hole-injection limited by diffusion of charge carriers.⁴¹⁻⁴² At higher potentials, the surface barrier shrinks, allowing more charge-carriers to cross the barrier, causing a breakdown of the junction.^{27, 30} This breakdown is more pronounced in Sample 5 (Figure 3.1E) than in any of the other samples, suggesting a small VB deviation resulting in better overlap with the solution and increased conductivity in the film.³¹ This becomes even more pronounced at the high end of the diffusion-controlled region, where rapid drop off in photoresponse is the result of higher bleed-back in dark current compared to hole diffusion, resulting in a high degree of recombination.²⁷ This can severely limit eventual device performance;³² however, the band alignment between CZTS that occurs in solution phase will be significantly reduced under a solid-solid interface situation, as will be the case in any device fabricated with CZTS. This reduces the implications of this breakdown at higher potentials, given that they will already be reduced naturally further down the fabrication process.

In order to examine the defects responsible for the observed phenomena, an accurate depiction of the elemental composition of each sample is required. To that effect, photoresponse can be compared as a function of individual defect structures within the film. Samples were analyzed via EDX to determine elemental ratios for the Cu, Zn, and Sn content, with the results summarized in Table 3.1. These ratios tend to show a good relation with long-range crystal order, acting as good predictors for device performance. The above indicators are most commonly attributed to deviations in the Cu and Zn positions, and Zn and Sn positions through antisite defect formation.¹² These defects are indicated by Kröger-Vink notation, which uses the notation M_S^C . Here, M represents the

atomic species or vacancy (denoted “V” for vacancy) that currently occupies the lattice site in question, S represents the atom that should occupy the site if it were a perfect crystal lattice, and C represents the charge difference at that location that results from the defect indicated by M and S. A negative charge difference is indicated by a ’ (apostrophe) symbol, and each positive by a • symbol.³³⁻³⁴

Table 3.1 Elemental ratios for each sample as determined through EDX averages of 25 films.

Sample	$Cu/(Zn + Sn)$	Zn/Sn	Defining Features
Sample 1	0.87 +/- 0.03	1.13 +/- 0.04	High-performance, ZnCl ₂ precursor
Sample 2	0.99 +/- 0.03	0.90 +/- 0.03	High-performance, ZnCl ₂ precursor
Sample 3	1.24 +/- 0.02	0.72 +/- 0.02	Control – High Cu content
Sample 4	0.98 +/- 0.02	1.64 +/- 0.02	Control – High Zn content
Sample 5	0.87 +/- 0.04	0.90 +/- 0.03	High-performance, Zn(acac) ₂ low sulfur

Each defect contributes an additional energy level to the local band structure, and can be additive or destructive to the p-type nature of the films. Shallow defects will be close in energy to the CB, with an energy difference less than ambient thermal energy. This allows shallow defects to act as additional regions within the CB, aiding in charge-carrier mobility. Deep defects add energy levels between the CB and VB that can be accessed by charge-carriers, but require more than ambient thermal energy for charge-carriers to escape from.^{19,35} For this reason, shallow defects will contribute beneficially to the CZTS films, whereas deep defects will adversely affect it.³⁵ This has been shown to be effective through the addition of dopants, but would be ideally build into the fabrication process.^{31,36} In the case of CZTS, high Cu content will lead to a Cu'_{Zn} defect. This is a shallow-level acceptor defect that acts as a trap for charge-carriers, and thus is non-ideal. This defect is likely the cause of the low photoresponse seen in Sample 3 (Figure 3.2C). To the opposite effect, higher Zn content will reduce the shallow-level Cu'_{Zn} defect, and

promote Zn_{Cu}^{\bullet} donor sites, and a vacancy at the Cu site, V_{Cu}' acceptors.^{1,37} The shallow donor and acceptor sites will lead to enhanced photoresponse, as seen in Sample 1 (Figure 3.1A); however, too much additional Zn contributes excessive distortion to the crystal structure, and no longer functions as an absorber layer as seen in Sample 4 (Figure 3.1D). For this reason, the highest efficiency CZTS reported herein show elemental ratios of $Cu/(Zn + Sn) = 0.87$ and $Zn/Sn = 1.13$, which agrees well with literature values of 0.8 and 1.2, respectively.^{2,38} Since this arises due to the lack of presence of deep-donor levels, which are created by the $Sn_{Zn}^{\bullet\bullet}$ defects. These defects where Cu or Sn replaces Zn have a higher probability of forming under lower Zn conditions, suggesting that Sample 5 (Figure 3.1E), and to a lesser extent, Sample 2 (Figure 3.1B), have inherent fabrication flaws that produce excess $Sn_{Zn}^{\bullet\bullet}$ defects that are significantly hindering their performance through deep-donor level formations. These proposed defects were examined further using XRD and EXAFS to identify key points required to reduce their effects on future subsequent layer depositions.

3.3.2 X-ray Diffraction

Through XRD, each of the films were examined against the others to identify the crystal planes which deviate from sample to sample.

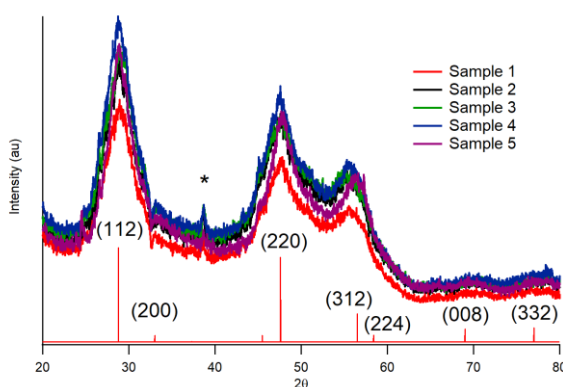


Figure 3.2 XRD spectra of Samples 1-5 showing deviations in the (220) and (312) peaks. Due to the high counts used, there is some contribution to the spectrum from the aluminum tray, marked (*). The standard kesterite CZTS peaks (JCPDS 26-0575) have been shown for reference.

To eliminate interference of the Sn within the FTO, samples were placed on an aluminum tray rather than FTO. Relatively similar crystallinity can be seen in Figure 3.2. The planes corresponding to these XRD peaks, and the images of the tested films are illustrated in Figure 3.3. The major peak at (112) is highly conserved throughout the samples, but show minor deviations in the peaks at (220) and (312). This indicates a distinct difference in defect structure between samples, identified by the small shifts seen between each of the latter peaks.

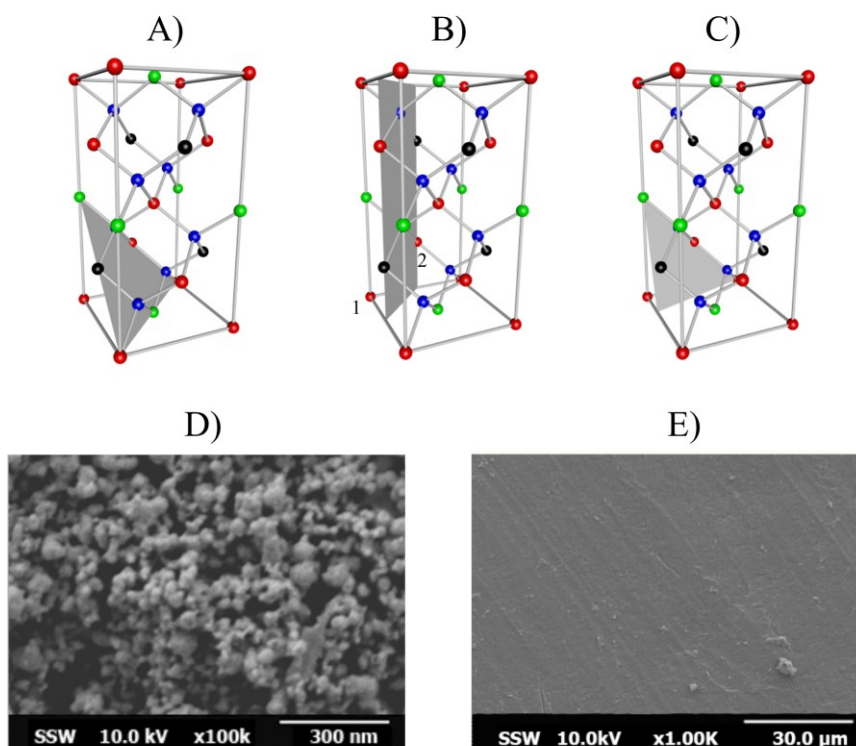


Figure 3.3 Crystal planes for the (A) (112), (B) (220), and (C) (312) planes in CZTS. Red spheres are Cu, blue are S, black are Zn, and green are Sn. SEM images of (D) the NCs and (E) the film structure of Sample 1. The Cu atoms have two distinct crystallographic positions. The first has been marked with “1”, and occurs at the (0,0,0) position, while the second has been marked with “2”, and occurs at $(0, \frac{1}{2}, \frac{3}{4})$ in the kesterite phase. The first forms a horizontal lattice of Cu and Sn. The second forms a horizontal lattice of Cu and Zn. The Zn atoms have one crystallographic position, analogous to the second indicated Cu position.

The conserved nature of the first peak confirms the shift is the effect of individual, non-conserved defects rather than periodic stacking defects.³⁹ These defects will put strains on individual planes, creating the potential for charge-carrier traps, and allowing for the identification of specific strains.³⁹ Since the (112) plane, Figure 3.3A, is highly conserved in the XRD patterns in Figure 3.2, it is unlikely to have any major differences in the overall tension or compression stresses that lead to lattice distortions.⁴⁰⁻⁴² However, in both the (220) and (312) planes, Figure 3.3A and B, Sample 4 is shifted right, indicating a compression stress is added in both of these planes.³⁹ This correlates well to EDX data, as increases in Zn content would lead to Cu vacancies, or additional Zn^{2+} in place of Cu^+ sites, resulting in compression stress on both the vertical lattice parameter – and thus the (220) plane – and on the lateral cross, distorting the crystal structure from basic tetragonal shape. This shift would not affect the (112) plane, as any deviations would be similarly conserved throughout both sides, and averaged across multiple NCs, but would show deviations in the (312) plane based on the level of distortion.⁴² The deviation in Sample 4 is most severe in the (220) plane, and Sample 3 in the (312) plane, indicating that defects resulting from excess Cu factor more into lateral lattice distortions, while excess Zn leads to vertical compression of the NCs. This can be used to examine the high-performance samples, and determine their distortions that contribute to the observed PECMs. Vertically, all three samples show peaks in the same region as Sample 4, with no shift from the expected peak values.^{16, 41} Laterally, there is a much wider range, with samples 1 and 2 shifted left, though not to the same extent as Sample 4. Sample 5 matches literature.⁴¹ This suggests a compression stress on the (312) plane of Samples 1 and 2, likely in the form of a Cu vacancy for Sample 1 – due to near-stoichiometric composition – and a Zn in a Cu position (a Zn_{Cu}^{\bullet} antisite defect) in Sample 2. Is it also possible that Sample 1 has multiple $[Cu'_{Zn} + Zn_{Cu}^{\bullet}]^0$ defect pairs, which would explain the bulk recombination sites seen in the PECMs.³⁵ Furthermore, the presence of Zn_{Cu}^{\bullet} in Sample 2 increases the charge in the CZTS, likely leading to excessive capping at the surface of the NCs. This is the likely source of surface trapping seen in the PECM for Sample 2. Sample 5 appears to be more balanced, with no significant shift from the expected CZTS peaks. Despite this, the overall current density of Sample 5 is no greater than that of Sample 1, and in similar region to that of Sample 2.

This suggests that the lack of free-S used in the synthesis has some limiting factors on the final photocurrent. The films were studied using SEM to corroborate the presence of defects as the source of these deviations, as opposed to structures within the film. The films show high consistency with little variation between samples. The presence of the NCs throughout the film (Figure 3.3D), and the uniform structure of the full film (Figure 3.3E), suggest the surface morphology contributes negligibly to the deviations observed. The determination of the extent of this, and of the aforementioned defects, requires in-depth analysis of local structure for each individual atom.

3.3.3 XANES

K-edge XANES spectra for each metal were measured in order to assess deviations in the local environment around the absorbing atom, Figure 3.4.

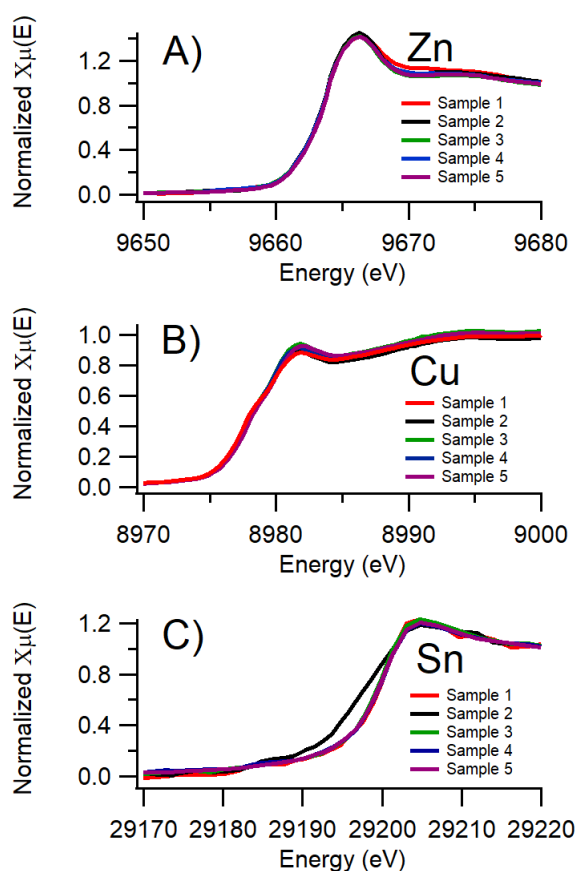


Figure 3.4 XANES spectra for the A) Zn, B) Cu, and C) Sn K-edge showing similar crystal structure between samples.

As suggested by XRD, the local environments for all three metal atoms show minor deviations between samples, as seen in Figure 3.4, with a few notable exceptions. The Zn spectra (Figure 3.4A) shows no pre-edge structure. This suggests a decrease in, or weaker association between the Zn and S orbitals. This is consistent with previous work,¹³⁻¹⁵ and gives further prominence to the importance of Zn as an active site within the CZTS film. The lack of deviation in the edge step is suggestive of a highly conserved oxidation state at the Zn sites, much the same as in the Cu spectra (Figure 3.4B). This is expected given charge-transfer processes, and thus the chemical environment, must be conserved to maintain any significant photoresponse.⁴³⁻⁴⁴ The edge step is seen in at 9,659 eV. Minor deviations in the post-edge region are seen in Sample 1, which shows a slight blue-shift towards higher electron density in the first shell.^{9, 17, 45-46} This deviation in Sample 1 corresponds to an increase in electron density at the Zn-S region of the crystal, which is consistent with increased Zn content and thus increased Zn_{Cu}^{\bullet} defects as predicted by the EDX results in Table 3.1. Increased Zn_{Cu}^{\bullet} defects would result in increased shallow-level defects and thus electron density, contributing to the ease at which they are removed – lower energy peaks – from the crystal. The additional empty energy level existing just below the CB in the crystal requires less energy to promote an electron to that level, resulting in a minor shift in electron density to the Zn sites, which is observed in the XANES spectra. In the case of the high-Zn Sample 4, the lack of this deviation suggests that the explanation is too simple. This can be rectified by coupling the Zn_{Cu}^{\bullet} with the V'_{Cu} or Cu'_{Zn} antisite as predicted for Sample 1 by the PECMs (Figure 3.1). The $[Cu'_{Zn} + Zn_{Cu}^{\bullet}]^0$ pair would result in increased broadening in the XANES due to various distribution of these defects, though the short core hole lifetime may also be contributing and thus reducing the strength of the argument without accounting for the EXAFS. In the Cu rich Sample 3, the relative distribution of the Zn will be less periodic, and a noted decrease in V'_{Cu} would be expected. This would contribute to the lack of deviation seen throughout the other samples. Furthermore, the Cu XANES shows a very slight, but predictable blue shift in Sample 1 (Figure 3.4B), as would be expected as a corollary to the blue shift in the Zn due to the predicted coupling. We also see the blue shift in the Cu XANES for Sample 5, but not in Sample 2 or 4, suggesting that there is an increased electron density around Cu, but not Zn, and that the V'_{Cu} defect is more

dominant in Sample 5. This corresponds well with atomic radii arguments. The Zn^{2+} ion with an atomic radius of 60 pm is larger than the Sn^{4+} ion with 55 pm but equal in size to the Cu^+ ion.⁵⁶ This size difference results in unequal electron densities within the defect site that are not present in the Zn-Cu defects. The reduced electron density associated with the defect site of Zn should thus result in a shift in the Zn peaks; however, instead show blue shifts in the Cu. This suggests that the Zn-S bond is readjusting to redistribute electrons from the Cu-S to the Zn-S, resulting in an unchanged electronic environment around the Zn, while altering that around Cu.^{1, 35, 47-48} This would result in minor deviations at the late XANES and EXAFS oscillations, which would manifest in the metal-sulfur bond-lengths. These observations agree very well with a schematic of the Zn absorber illustrated in Figure 3.5.

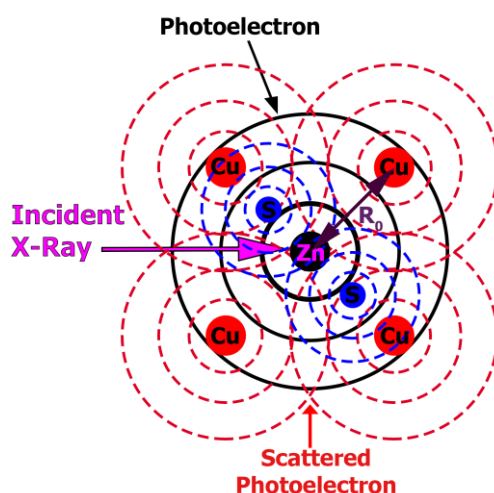


Figure 3.5 Contributions to the XANES come from the scattering dominated by multiple pathways of low kinetic energy photoelectrons (black), while EXAFS come from the interference of outgoing and back scattering pathways at the absorbing atom as the kinetic energy of the photoelectron increases and single scattering pathway becomes dominant (constructive and destructive interference of the black, red, and blue waves). Additional scattering atoms would contribute from above and below the plane shown.

The XANES photoelectrons should, in theory, be near identical due to the lack of deviation in the underlying structure. Defect groups will not contribute to these spectra because they do not significantly change the oxidation state or overall geometry and coordination of the crystal, and thus the photoelectron wave will remain unchanged from sample to sample.

In the Cu spectra (Figure 3.4B), a pre-edge structure can be seen in all samples at 8978 eV, indicating a transition from a Cu 1s to a low-lying valence state.^{9, 17, 49} This can include the dipole-forbidden Cu transition $1s \rightarrow 3d$, or the dipole-allowed Cu transition $1s \rightarrow 4p$.⁴⁹⁻⁵⁰ In the case of CZTS, it is expected that Cu is in the full 3-d orbital Cu^+ form rather than its Cu^{2+} , leading to the expectation that only the dipole-allowed transition, or transition to the hybrid orbitals resulting from the Cu^+ 3d and S^{2-} 4p mixing, is occurring, producing unoccupied states with some 3d character.^{9, 49, 51} The intensity of the pre-edge feature confirms this. In dipole-forbidden transitions (quadruple allowed in this case) the pre-edge features would be sensitive to small symmetry variations due to variations in the mixing of the 3d and 4p orbitals, whereas would be mostly independent for dipole-allowed transitions.^{49, 52} This confirms that the changes at the Cu sites are not resulting from oxidation state changes, or localized secondary phase formations, but from crystal lattice defect structure. The edge itself and near-edge regions are well conserved. The edge energy is seen at 8,979 eV, with the post edge features mirrored in all five samples. This suggests a lack of any major distortions in the photoelectron being detected (Figure 3.4), and thus a lack of major distortions around the Cu centers.

In the Sn XANES spectra (Figure 3.4C) deviations appear in the Sn edge-step only in Sample 2. The increased in unoccupied electron density of states around Sn in this case could be caused through lattice distortions around the Sn site, resulting in a deviation from the perfect tetrahedral coordination.^{46, 53-54} In Samples 1, and 3-5, the edge step is seen at 29,200 eV, whereas Sample 2 shows it at 29,197 eV. This distortion is likely an aggregation of additional electron density around the Sn^{4+} site, suggesting a possible reduction in the oxidation state of Sn.^{35, 48} Given that this is not seen in the XRD (Figure 3.2), and the major structure of Sample 2 remains CZTS, this is indicative of a Sn-based defect. As previously determined from the Zn edge (Figure 3.4A), the Zn appears

unaffected, suggesting some redistribution of electrons in the presence of reduced Cu^+ content. This redistribution appears to allocate more electron density to Sn, suggesting a loosening of the Sn-S bond, or alternatively, an unequal distribution of the Cu and Zn associated defects. This appears to show some deep-level defect structure inhibiting charge-carrier mobility, which would explain the decrease in photoresponse seen between Sample 1 (Figure 3.1A) and Sample 2 (Figure 3.1B).

3.3.4 EXAFS

The deviations noted through XRD and XANES ultimately suggest a deviation in bond lengths throughout the different samples, which distort the uniformity of the NCs in films, and contributes to the defect structure noted. This explains the balance that must be struck between introducing beneficial defect structure to NCs, and distorting the film to the point of limiting bulk charge-carrier diffusion, as seen in the PECMs. The exact structural deviations were calculated using EXAFS fit to the multiple-scatter models generated through Artemis and FEFF9 software.

The atomic number of Cu and Zn differ from each other by 1 and their FEFF fit parameters can be approximated as indistinguishable if within a certain crystal lattice. We have run FEFF9 simulations of the Cu and Zn K-edge EXAFS in the stoichiometric CZTS kesterite crystal. Their radial distributions are shown in Figure 3.6 on the next page. It is well-known that the first shell illustrated in Figure 3.6 is attributed to the Cu-S and Zn-S radial distances (Figure 3.3), respectively. The second peaks in Figure 3.6 are ascribed to the Cu-to-Cu and Zn-to-Zn radial distances. The Cu atoms in two distinct crystallographic positions 2a (0,0,0) and 2c (0, $\frac{1}{2}$, $\frac{1}{4}$),⁵⁵ have a similar Cu-to-Cu radial distance, which is very different from that of uniquely positioned Zn-to-Zn, Figure 3.3 and Figure 3.5. For a better fit, we have treated Cu and Zn as different atomic shells. Please note that, the K-edges of Cu and Zn are at about 8,979 eV and 9,659 eV, respectively. This is corroborated by our PECMs (Figure 3.1) and elemental composition (Table 3.1), which eliminate certain possible configurations, limiting the possible interchanges at this shell (as outlined by Makinson *et al.*).³⁹

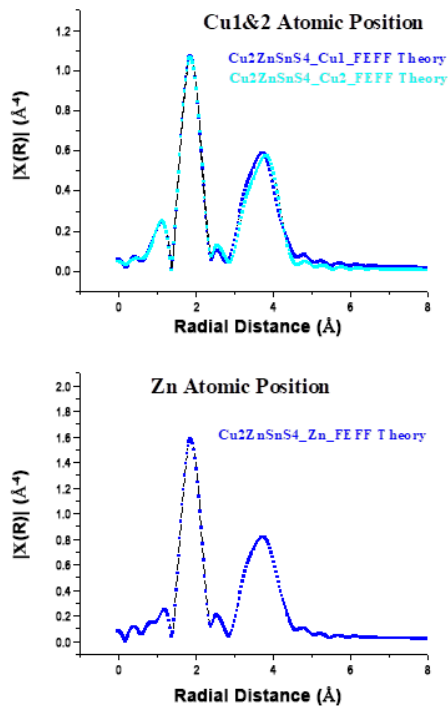


Figure 3.6 Radial distributions of Cu (top) and Zn (bottom) obtained by the FEFF simulations of the Cu and Zn K-edge EXAFS in the stoichiometric CZTS kesterite crystal.

It also keeps our second-shell analysis of both Cu and Zn independent of each other. These account for scatter from the simple and multiple scatter pathways caused by neighboring atoms through the crystal structure, Figure 3.3. This would correspond to the constructive and destructive interference of all of the multiple scatter waves produced. The atoms above and below this plane would also contribute, and give a sense of local area order, as seen in Figure 3.7.

In each set of data in Figure 3.7, the fitting allows for the quantification of the radial distance between neighboring atoms in the absorber. In the Zn spectra, there are significant shifts in the peak maximum, suggesting that Zn bonds to S are contribute heavily to the structural defects. This correlates well with literature,⁵⁶ indicating that in CZTS NC-based films, the Zn plays a significant role in the total performance. As illustrated in Figure 3.5 at the Zn-edge, the EXAFS would have contributions from the photoelectron (black) and both sets of scatterers (Cu red, and S blue).

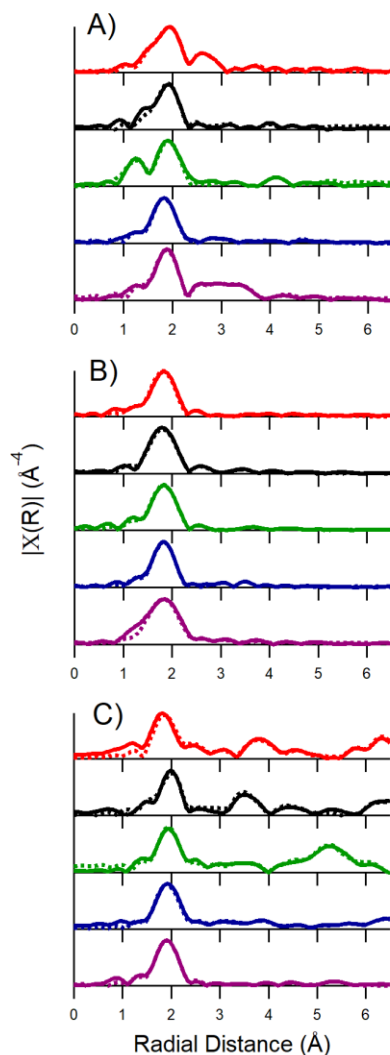


Figure 3.7 The magnitude of the FT of the EXAFS data for A) Zn, B) Cu, and C) Sn K-edges, and the corresponding three shell fit (dashed line) in the window region – 1.0 to 6 Å for Cu, 1.1 to 6 Å for Zn, and 1.2 to 6 Å for Sn. Sample 1 is imaged red, Sample 2 black, Sample 3 green, Sample 4 blue, and Sample 5 purple. The solid lines show the experimental data.

This indicates a highly conserved interference between the Zn and S scattering pattern in Figure 3.5, and between a Sn and S scattering pattern (Sn does not appear in the plane shown in Figure 3.5, but would scatter from above). The changing peak positions seen in Figure 3.7A would correlate with small changes in the S positions in Figure 3.5. The shorter radial distances would result in shorter Zn-S distances, and thus change the

interference patterns observed. The blue rings in Figure 3.5 would interfere differently with both the Zn absorber and the Cu rings, which explains the variation seen in the second and third shell in Figure 3.7A. These peaks are muted due to the high DWF (Debye-Waller Factor) associated with EXAFS measurements in ambient temperature. The DWF also correlates with a small static disorder (slightly different bond lengths due to distortion). This can be correlated to the defects noted previous, and thus predicted by XANES and EDX data.

The number of shallow Zn_{Cu}^{\bullet} defects changes between Samples, altering the atomic distance between Zn and S. These bonds are shortest in Sample 1 and 5, confirming the previous analysis that the shallow antisite defect resulting from Zn replacing Cu is found in the high-performance samples. This bond length is also shorter than that of the stoichiometric model. In the presence of too much excess Zn (Sample 4), the bond elongates, confirming the increased lattice distortion that corresponds with the loss of the beneficial effects.

The Cu EXAFS spectra (Figure 3.7B) for the 5 samples show very minor deviations in the Cu-S distance, indicated by the first major spectral peak, the interaction in Figure 3.5 between a red and a blue scattering centers. This suggests that while the Zn-S bond length changes between samples, the Cu-S distance remains constant, and thus the Cu-Zn distance contracts in high performance samples. Each measured atomic distance is within 0.02 Å of each other; however, in each case, the bond distance is 0.04 Å to 0.06 Å smaller than that predicted by the FEFF9 model. This is consistent with the XANES data (Figure 3.4B) that suggests highly conserved local structure around Cu, regardless of the composition, with deviations resulting from defects rather than crystallographic changes.⁵⁷ This phenomenon is maintained well throughout all of the high performance samples in literature.^{10, 13-14} Even at the extended shells, there is a high degree of conservation among the Cu sites in terms of their neighboring crystallographic sites. The only noticeable deviation occurs in the peak broadness. The broadening of peaks in Cu R-space in Sample 2 (black) and 5 (purple) is indicative of minor, non-conserved deviations in the radial distance, which can be traced back to the Zn_{Cu}^{\bullet} and Cu'_{Zn} defects respectively predicted by the PECMs and XANES, given that temperature was held

constant throughout. This increases the likelihood of shallow defects contributing to the increased PS (Figure 3.1F) and thus increased photoresponse seen in Sample 1 in Figure 3.1A, and that of deep donor defects contributing to the decreased charge-carrier mobility seen in Sample 2 in Figure 3.1B. As in the XANES spectra, there is decreased peak broadening in the Cu spectra for Samples 3 (green) and 4 (blue), confirming the postulate that at very high or very low Cu concentrations, there is not enough to pose significant structural abnormalities within formed CZTS. This confirms the relationship determined through XANES, but further quantifies the extent to which these defects occur; Sample 5 in particular appears to have a significant contribution from high electron-density Cu-S bonds.^{10, 58} This broadening is not observed in the Zn and Sn spectra.

The deviations are even more pronounced in the Sn-S bonds in Figure 3.7C. Unlike in the other two metal centers, the high-performance Sample 1 shows a distance that matches that of the model, while the other samples all show increased Sn-S bond distance. This is most pronounced in Sample 2. This corroborates the postulates made from the PECM data in Figure 3.1 that suggested the presence of lattice distortions resulting in excess contribution from the Sn centers, and thus the deep-trap Sn_{Zn}^{\bullet} defect. This also explains the deviations seen in the second and third shells in the Sn spectra, as lattice distortions at the Sn sites would lead to electronic rearrangements in the band structure that could impact the scattering pathway primarily contributing to the radial distribution function. The model kesterite CZTS bond lengths have been tabulated in Table 3.2.

Table 3.2 Metal coordination and bond lengths of the model kesterite CZTS.

	Metal Edge	1 st Shell (Å)	Bond Length to 2 nd (Metal) and 3 rd (S) (Å)			
		S	Cu	Zn	Sn	S
Model Kesterite CZTS	Cu	2.33	3.80	3.80	3.81	4.21
	Zn	2.34	3.80	3.80	3.80	4.23
	Sn	2.33	3.81	3.80	3.80	4.21

Table 3.3 Metal coordination and bond lengths determined through EXAFS data fitting. Samples with limited scatter associated with certain bonds have been indicated with ---.

	Metal Edge	1 st Shell (Å)	Bond Length to 2 nd (Metal) and 3 rd (S) (Å)			
		S	Cu	Zn	Sn	S
Sample 1	Cu	2.27 ± 0.02	3.65 ± 0.03	3.66 ± 0.02	3.63 ± 0.03	4.15 ± 0.08
	Zn	2.32 ± 0.02	3.67 ± 0.04	3.66 ± 0.03	3.68 ± 0.05	4.20 ± 0.09
	Sn	2.33 ± 0.02	3.62 ± 0.04	3.68 ± 0.04	3.68 ± 0.04	4.17 ± 0.09
Sample 2	Cu	2.28 ± 0.02	3.55 ± 0.04	3.88 ± 0.04	3.71 ± 0.05	4.27 ± 0.09
	Zn	2.32 ± 0.03	3.90 ± 0.05	---	3.95 ± 0.05	4.06 ± 0.10
	Sn	2.45 ± 0.03	3.68 ± 0.04	3.94 ± 0.05	4.01 ± 0.05	4.79 ± 0.09
Sample 3	Cu	2.29 ± 0.02	3.74 ± 0.03	3.74 ± 0.04	3.38 ± 0.04	4.35 ± 0.09
	Zn	2.35 ± 0.02	3.91 ± 0.04	4.27 ± 0.05	4.07 ± 0.04	4.45 ± 0.08
	Sn	2.39 ± 0.02	3.96 ± 0.03	4.03 ± 0.04	4.01 ± 0.04	---
Sample 4	Cu	2.28 ± 0.02	3.83 ± 0.05	3.84 ± 0.05	3.71 ± 0.05	---
	Zn	2.30 ± 0.03	3.84 ± 0.05	3.81 ± 0.06	3.85 ± 0.05	4.45 ± 0.10
	Sn	2.40 ± 0.02	3.67 ± 0.05	4.21 ± 0.05	3.94 ± 0.05	4.43 ± 0.11
Sample 5	Cu	2.29 ± 0.02	3.56 ± 0.04	3.68 ± 0.04	3.87 ± 0.02	---
	Zn	2.33 ± 0.03	3.69 ± 0.05	3.68 ± 0.05	3.61 ± 0.05	4.26 ± 0.10
	Sn	2.40 ± 0.03	3.98 ± 0.04	3.92 ± 0.05	4.01 ± 0.04	---

All calculated bond lengths have been tabulated in Table 3.3 for improved comparison of the values calculated for atoms beyond the first shell. From Table 3.2 and Table 3.3, the second and third shell deviations continue the patterns seen in the first shell albeit with larger uncertainties. The high-performance Sample 1 shows short bonds relative to the model structure, both in metal-to-metal distance and in metal-to-sulfur distance at the third shell, confirming the compact nature predicted through XRD in Figure 3.2. Further, we see that the metal-to-metal bonds are relatively regular, as is the case in the model. This confers a degree of order to Sample 1 films not obtained in any of the other samples. It also matches the prediction from the Zn and Cu spectra in Figure 3.7A and Figure 3.7B, with Sample 1 showing reduced Zn-S and Cu-Zn bond lengths compared to the stoichiometric model. The Cu and Zn second-shell neighbors are treated separately, given that their radial distributions underlying the model are not identical, and thus are not identical within the fitting (Figure 3.6). The greatest distance deviations are seen in the Sn distances, where the model predicts Sn-Cu vs Sn-Zn bonds to differ by only 0.01 Å. These distances in Sample 1 and Sample 5, both high-performance CZTS, deviate by 0.06 Å, which suggests defect-dependent ordering within the samples. In Samples 2 and 4, this deviation are 0.26 Å and 0.54 Å, confirming the XANES and XRD conclusions that long-range order is not highly conserved in these samples. In Sample 3, this same deviation is measured as 0.07 Å in the Sn spectrum (Figure 3.7C), but is 0.65 Å when the Sn-Cu distance is calculated using the Cu spectrum (Figure 3.7A). This is the only instance where two different absorbers yield significantly different results, suggesting that the lattice distortions and deep-level charge-carrier traps present in Sample 3 are Cu and Sn related, and very non-periodic, likely contributing to the low carrier mobility in the PECM Figure 3.1C. This deviation likely results from imperfect position capture, and thus the changing bond length confirms the non-conserved bond length throughout the film. This can be seen to a lesser extent in Sample 4 at the Sn-Zn distance, suggesting the same in regards to that sample.

The third shell distance accentuate this non-periodic nature the most despite larger uncertainty. This now includes the entire scatter pattern depicted in Figure 3.5 with respect to Zn, plus contributions above and below the depicted plane. In the high-performance Sample 1, and to a lesser extent Sample 5, all three metal absorbers are

matched to similar third-shell distances, corroborating the long range order present in these films. This distance conservation breaks down in Samples 2, 3, and 4 as more lattice distortions and non-conserved defects are introduced. The presence of these defects, and the contributions of deep-level charge-carrier traps reduces their effectiveness as a solar energy absorber.

3.4 Conclusions

The fabrication of low-cost, high-efficiency devices using CZTS as the light absorber layer is highly dependent on the nature and efficiency of the underlying crystal structure. CZTS films with high $Cu/(Zn + Sn)$ ratio contain lateral lattice distortions due to unequal Cu'_{Zn} antisite defects. This leads to slower charge transport through the bulk CZTS layer due to deep charge-carrier traps. Conversely, films with a very high Zn/Sn ratio contain vertical lattice compressions and significant lateral distortions that drastically hinder the separation of charge-carriers. Both extremes are unacceptable in final device structure, but offer context for structural features with greater photoresponse. By keeping the $Cu/(Zn + Sn)$ ratio close to 0.87 and the Zn/Sn ratio close to 1.15, CZTS NCs can be fabricated with beneficial shallow defects that promote charge-carrier generation and extraction from the CZTS film. This also appears to have the benefit of tighter crystal structures, promoting a more rigid and uniform NC structure and thus film structure for reducing recombination sites. Deviations from these ratios contribute to deep defect sites that act as charge-carrier traps and reduce the film effectiveness.

Both the XANES and EXAFS data confirm defects and the resulting preferential local distortion as the source of changes observed photoelectrochemically rather than secondary phases or major crystallographic deviations. In particular, high efficiency CZTS NCs show shallow $Zn\bullet_{Cu}$ and V'_{Cu} defects, contributing additively to the observed photoresponse. The deep-trap $Sn\bullet\bullet_{Zn}$ and shallow Cu'_{Zn} defects detract from the photoresponse, and appear limited in the high efficiency films. The EXAFS spectra also suggest the potential for size-effects within the NCs, which offers the potential for enhanced charge-carrier transport. The smaller NCs with shallow defects are the key to low-cost, high-efficiency CZTS solar cells, and to creating an ideal p-n junction.

3.5 References

1. Chen, S.; Wang, L. W.; Walsh, A.; Gong, X. G.; Wei, S. H., *Appl. Phys. Lett.* **2012**, *101*, 223901.
2. Todorov, T. K.; Tang, J.; Bag, S.; Gunawan, O.; Gokmen, T.; Zhu, Y.; Mitzi, D. B., *Adv. Energy Mater.* **2013**, *3*, 34.
3. Winkler, M. T.; Wang, W.; Gunawan, O.; Hovel, H. J.; Todorov, T. K.; Mitzi, D. B., *Energy Environ. Sci.* **2014**, *7*, 1029.
4. Mitzi, D. B.; Gunawan, O.; Todorov, T. K.; Wang, K.; Guha, S., *Sol. Energ. Mat. Sol. Cells* **2011**, *95*, 1421.
5. Kornhuber, K.; Kavalakkatt, J.; Lin, X.; Ennaoui, A.; Lux-Steiner, M. C., *RSC Adv.* **2013**, *3*, 5845.
6. Perini, L.; Vaccarello, D.; Martin, S.; Jeffs, K.; Ding, Z., *J. Electrochem. Soc.* **2016**, *163*, H3110.
7. Walsh, A.; Chen, S.; Gong, X. G.; Wei, S. H.; Ihm, J.; Cheong, H. In *Crystal Structure and Defect Reactions in the Kesterite Solar Cell Absorber Cu₂ZnSnS₄ (CZTS): Theoretical Insights*, AIP Conf. Proc., 2011; p 63.
8. Xiao, H.; Goddard III, W. A., *J. Chem. Phys.* **2014**, *141*, 094701.
9. Teo, B. K., *EXAFS: Basic Principles and Data Analysis*; Springer-Verlag Berlin Heidelberg: New York, 1986, p 349.
10. Ravel, B., *J. Synchrotron Radiat.* **2015**, *22*, 1258.
11. Ravel, B.; Newville, M., *J. Synchrotron Radiat.* **2005**, *12*, 537.
12. Maradudin, A. A.; Flinn, P. A., *Phys. Rev.* **1963**, *129*, 2529.
13. Turnbull, M. J.; Khoshmashrab, S.; Wang, Z. Q.; Harbottle, R.; Sham, T. K.; Ding, Z. F., *Catal. Today* **2016**, *260*, 119.
14. Vaccarello, D.; Tapley, A.; Ding, Z., *RSC Adv.* **2013**, *3*, 3512.
15. Khoshmashrab, S.; Turnbull, M. J.; Vaccarello, D.; Nie, Y. T.; Martin, S.; Love, D. A.; Lau, P. K.; Sun, X. H.; Ding, Z. F., *Electrochim. Acta* **2015**, *162*, 176.
16. Ahmed, S.; Reuter, K. B.; Gunawan, O.; Guo, L.; Romankiw, L. T.; Deligianni, H., *Adv. Energy Mater.* **2012**, *2*, 253.
17. Teo, B. K.; Joy, D. C., *EXAFS Spectroscopy: Techniques and Applications*; Plenum Press: New York, 1981.
18. Momma, K.; Izumi, F., *J. Appl. Crystallogr.* **2011**, *44*, 1272.
19. Katagiri, H.; Jimbo, K.; Maw, W. S.; Oishi, K.; Yamazaki, M.; Araki, H.; Takeuchi, A., *Thin Solid Films* **2009**, *517*, 2455.
20. Katagiri, H.; Jimbo, K.; Yamada, S.; Kamimura, T.; Maw, W. S.; Fukano, T.; Ito, T.; Motohiro, T., *Appl. Phys. Express* **2008**, *1*, 041201.
21. Nozik, A. J.; Memming, R., *J. Phys. Chem.* **1996**, *100*, 13061.

22. Espinosa-Faller, F. J.; Conradson, D. R.; Riha, S. C.; Martucci, M. B.; Fredrick, S. J.; Vogel, S.; Prieto, A. L.; Conradson, S. D., *J. Phys. Chem. C* **2014**, *118*, 26292.
23. Liang, S.; Sheng, H.; Liu, Y.; Huo, Z.; Lu, Y.; Shen, H., *J. Cryst. Growth* **2001**, *225*, 110.
24. Saha, S. K.; Guchhait, A.; Pal, A. J., *Phys. Chem. Chem. Phys.* **2012**, *14*, 8090.
25. McDonnell, S.; Addou, R.; Buie, C.; Wallace, R. M.; Hinkle, C. L., *ACS Nano* **2014**, *8*, 2880.
26. Haight, R.; Barkhouse, A.; Gunawan, O.; Shin, B.; Copel, M.; Hopstaken, M.; Mitzi, D. B., *Appl. Phys. Lett.* **2011**, *98*, 253502.
27. Sah, C. T.; Noyce, R. N.; Shockley, W., *Proc. Inst. Radio Eng.* **1957**, *45*, 1228.
28. He, J. J.; Lindström, H.; Hagfeldt, A.; Lindquist, S. E., *J. Phys. Chem. B* **1999**, *103*, 8940.
29. Lin, M. E.; Xue, G.; Zhou, G. L.; Greene, J. E.; Morkoç, H., *Appl. Phys. Lett.* **1993**, *63*, 932.
30. Cao, Y.; Denny, M. S.; Caspar, J. V.; Farneth, W. E.; Guo, Q.; Ionkin, A. S.; Johnson, L. K.; Lu, M.; Malajovich, I.; Radu, D.; Rosenfeld, H. D.; Choudhury, K. R.; Wu, W., *J. Am. Chem. Soc.* **2012**, *134*, 15644.
31. Korala, L.; McGoffin, J. T.; Prieto, A. L., *ACS Appl Mater Interfaces* **2016**, *8*, 4911.
32. Zhang, Y.; Wang, Y.; Zhang, J.; Xi, L.; Zhang, P.; Zhang, W., *J. Chem. Phys.* **2016**, *144*, 194706.
33. Meethong, N.; Kao, Y. H.; Speakman, S. A.; Chiang, Y. M., *Adv. Funct. Mater.* **2009**, *19*, 1060.
34. Kröger, F. A.; Vink, H. J., Relations between the Concentrations of Imperfections in Crystalline Solids. In *Solid State Physics*, Frederick, S.; David, T., Eds. Academic Press: 1956; Vol. Volume 3, pp 307.
35. Chen, S. Y.; Gong, X. G.; Walsh, A.; Wei, S. H., *Appl. Phys. Lett.* **2010**, *96*, 021902.
36. Tiwari, D.; Koehler, T.; Lin, X. Z.; Harniman, R.; Griffiths, I.; Wang, L.; Cherns, D.; Klenk, R.; Fermin, D. J., *Chem. Mater.* **2016**, *28*, 4991.
37. Wei, S. H.; Zhang, S. B., *J. Phys. Chem. Solids* **2005**, *66*, 1994.
38. Todorov, T. K.; Reuter, K. B.; Mitzi, D. B., *Adv. Mater.* **2010**, *22*, E156.
39. Makinson, J. D.; Lee, J. S.; Magner, S. H.; De Angelis, R. J., *Adv. X-Ray Anal.* **2000**, *42*, 407
40. Valakh, M. Y.; Dzhagan, V. M.; Babichuk, I. S.; Fontane, X.; Perez-Rodriquez, A.; Schorr, S., *JETP Lett.* **2013**, *98*, 255.
41. Tiong, V. T.; Bell, J.; Wang, H., *Beilstein J. Nanotechnol.* **2014**, *5*, 438.

42. Balzar, D.; Ramakrishnan, P. A.; Hermann, A. M., *Phys. Rev. B* **2004**, *70*, 092103.
43. Siah, S. C.; Jaramillo, R.; Chakraborty, R.; Erslev, P. T.; Sun, C. J.; Weng, T. C.; Toney, M. F.; Teeter, G.; Buonassisi, T., *IEEE J. Photovolt.* **2015**, *5*, 372.
44. Chernenkaya, A.; Morherr, A.; Backes, S.; Popp, W.; Witt, S.; Kozina, X.; Nepijko, S. A.; Bolte, M.; Medjanik, K.; Ohrwall, G.; Krellner, C.; Baumgarten, M.; Elmers, H. J.; Schonhense, G.; Jeschke, H. O.; Valenti, R., *J. Chem. Phys.* **2016**, *145*, 034702.
45. Toyama, T.; Konishi, T.; Tsuji, R.; Maenishi, R.; Arata, A.; Yudate, S.; Shirakata, S., *Phys. Status Solidi C* **2015**, *12*, 721.
46. Gracia, L.; Longo, V. M.; Cavalcante, L. S.; Beltrán, A.; Avansi, W.; Li, M. S.; Mastelaro, V. R.; Varela, J. A.; Longo, E.; Andrés, J., *J. Appl. Phys.* **2011**, *110*, 043501.
47. Carter, C. B.; Norton, M. G., *Ceramic Materials: Science and Engineering*; Springer Science & Business Media: New York, 2013, p 766.
48. Romero, M. J.; Du, H.; Teeter, G.; Yan, Y.; Al-Jassim, M. M., *Phys. Rev. B* **2011**, *84*, 165324.
49. Getty, K.; Delgado-Jaime, M. U.; Kennepohl, P., *Inorg. Chim. Acta* **2008**, *361*, 1059.
50. Tomson, N. C.; Williams, K. D.; Dai, X.; Sproules, S.; DeBeer, S.; Warren, T. H.; Wieghardt, K., *Chem. Sci.* **2015**, *6*, 2474.
51. McKeown, D. A., *Phys. Rev. B: Condens. Matter* **1992**, *45*, 2648.
52. Housecroft, C. E.; Sharpe, A. G., *Inorganic Chemistry*, 2 ed.; Pearson Education Limited: Harlow, 2005; Vol. 2, p 949.
53. Blokhin, E.; Kotomin, E.; Kuzmin, A.; Purans, J.; Evarestov, R.; Maier, J., *Appl. Phys. Lett.* **2013**, *102*, 112913.
54. Bessiere, A.; Lecointre, A.; Priolkar, K. R.; Gourier, D., *J. Mater. Chem.* **2012**, *22*, 19039.
55. Hall, S. R.; Szymanski, J. T.; Stewart, J. M., *Can. Mineral.* **1978**, *16*, 131.
56. Hartman, K.; Newman, B. K.; Johnson, J. L.; Hui, D.; Fernandes, P. A.; Chawla, V.; Bolin, T.; Clemens, B. M.; da Cunha, A. F.; Teeter, G.; Scarpulla, M. A.; Buonassisi, T. In *Detection of ZnS Phases in CZTS Thin-Films by EXAFS*, IEEE Phot. Spec. Conf., 19-24 June 2011; IEEE: 2011; pp 002506.
57. Li, Q.; Qiao, L.; Chen, R.; Ma, Z.; Si, R.; Yao, Y.; Wu, K., *Phys. Chem. Chem. Phys.* **2016**, *18*, 2784.
58. Roberts, D. R.; Ford, R. G.; Sparks, D. L., *J. Colloid Interface Sci.* **2003**, *263*, 364.

Chapter 4

4 Resolving the Effects of Compositional Change on Structures in $\text{Cu}_2\text{ZnSnS}_4$ Nanocrystals by X-ray Absorption Fine Structure

Renewable energy sources, and solar energy in particular, are a high impact research topic in the push for sustainable, long-term energy alternatives to fossil fuels. $\text{Cu}_2\text{ZnSnS}_4$ (CZTS) is one of the attractive, cost-effective materials that meets these needs. The quaternary nature makes the structure prone to defects and crystal alignment disorder. Some of these defects create advantageous electronic effects through antisite substitutions of Zn_{Cu} . Others, such as Sn for Zn replacements, are detrimental. Synchrotron-based X-ray absorbance fine structure (XAFS) analysis was used to identify specific patterns in the antisite contributions to the structure of low- cost CZTS films that produced the highest photoresponse in each of our samples. Correlations were found between the $\text{Cu}/(\text{Zn}+\text{Sn})$ ratio and advantageous antisite formations, though at the cost of increased alignment disorder. Similarly, the Zn/Sn ratio showed relationships between both advantageous and disadvantageous antisite and vacancy pairs. Variations in the local surroundings for each metal center were confirmed through X-ray absorption near-edge structures (XANES). Extended X-ray absorption fine structures (EXAFS), verified through FEFF fitting of the EXAFS, confirmed the patterns in crystal alignment disorder, and the effects each antisite had on the overall crystal structure. The precision and unique nature of such synchrotron techniques offers opportunities to identify these trends at each metal center, providing guidance to balance negative and positive structural components during fabrication. Each minor change in stoichiometry has been shown to affect several interactions within the structure.

4.1 Introduction

Each synthetic method for producing CZTS has different characteristic structural relationships. Its quaternary nature often makes for complex associations and randomness in the crystal structure that can create both advantageous and

This chapter is a version of previously published work in Can. J. Chem., 2018, 96, 785-794.

disadvantageous microstructures and substructures within the film.¹ Previous work has shown maximal photoresponse within small compositional ranges, though the exact range appears to be dependent on the method of synthesis.²⁻⁵ Using a facile, low-temperature solvothermal method, the maximal photocurrent range appears to be relatively large. This occurs due to the increased number of antisite substitutions and disordered sites associated with low-temperature fabrication. Such a trade-off between cost-effective fabrication and highly controlled structural congruency, necessitates the intense probing of the various structures that produce high photoresponse.⁶⁻⁷ Focusing on those permutations with high short circuit current will allow for the selecting and controlling of specific structures in high-performing layers that will compliment and extend the charge carrier management through the device, ultimately leading to better open circuit potentials and useful device efficiencies.

Synchrotron radiation (SR) is an especially potent tool for probing small structural changes at the atomic level.⁸⁻¹⁰ SR provides X-rays of high brilliance, in a highly focused beam.¹⁰⁻¹¹ Combined with the ability to specifically target individual metal centers, SR allows for the detection of small changes to the substructure and atomic alignment of local regions of the CZTS films.¹² Previous work has identified many different defect structures that form in CZTS films, and how they contribute to the overall photoresponse of the layer.^{2, 5} These defects, including antisite substitutions and atomic vacancies, are associated with stoichiometric regions that correspond with different photoresponses. Using X-ray absorption near-edge spectroscopy (XANES) and extended X-ray absorption fine structure (EXAFS), the changes in antisite structure within the narrow stoichiometric band that produces high photoresponse can be isolated for many different stoichiometries.^{9, 13} These are important when dealing with low-cost fabrications.

CZTS nanocrystals (NCs) that are produced without high-temperature or high-energy post-processing steps tend to contain deviations from the perfect crystal, as shown in Figure 4.1.⁵ The antisite substitutions shown in Figure 4.1B (red circle) occur when an atom, Zn as shown, occupies a crystal position that is typically filled with a different atom. Vacancies, as shown in Figure 4.1B (purple circle), also can occur. These deviations from the ‘perfect’ crystal contribute to the disorder in the films. In some

cases, these antisites can create beneficial effects on the overall photoresponse, whereas others contribute to lattice strain and disorder, both of which can hinder the photoresponse.

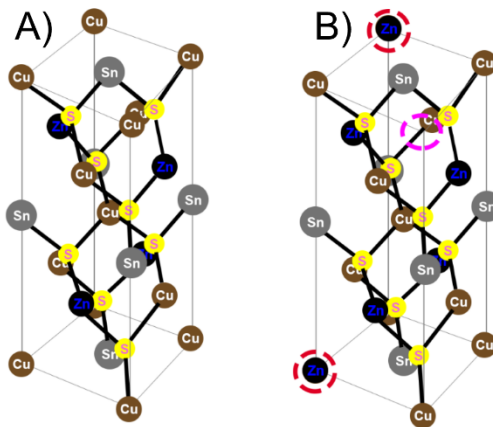


Figure 4.1 The CZTS crystal structure as A) a perfectly stoichiometric kesterite structure and B) a kesterite structure exhibiting two Zn-on-Cu antisites, denoted with a red circle, and a Cu vacancy, denoted with a purple circle.

Through exact fabrication, specific metal ratios were synthesized within a stoichiometric range that produces the highest photoresponse, and the antisite structures of each were characterized. Further work is required in the step-wise optimization of the CZTS NCs, for eventual fabrication of low-cost solar cells based on a CZTS light-absorber layer.

4.2 Experimental

4.2.1 Nanocrystal Fabrication

CZTS NCs were synthesized via a previously reported one-pot solvothermal method,¹⁴ as presented in Chapter 2.2.1. This method produced NCs with high photoresponses, provided the Cu/(Zn+Sn) ratio was between 0.9 and 1.0, and the Zn/Sn ratio was between 0.9 and 1.1. Herein, the elemental compositions are purposely tuned within these regions to produce minor variations in the metal ratios while maintaining maximum photoresponse. Cu-, Zn, and Sn-metal precursor salts (Sigma-Aldrich) were dissolved in benzyl alcohol (BA) at 160 °C for 2 minutes. The temperature was raised to 180 °C, and 0.2 mol/L thiourea (Sigma-Aldrich, $\geq 99.0\%$) in BA was added, followed by 0.1 mol/L 2-

mercapto-5-n-propylpyrimidine in BA. This mixture was held at temperature for 10 minutes. Resultant NCs were washed in acetone three times, and centrifuged from solution at 12.0×10^3 times gravity using a Thermo Scientific Sorveall Legend Micro 21 centrifuge.

Sample composition was determined using energy dispersive X-ray spectroscopy (EDX). A Hitachi S-4500 field emission microscope with a 100 kV EDX system was used. Samples were stored under argon in sealed containers until examined at the synchrotron facilities.

4.2.2 Synchrotron Analysis

XAFS measurements were performed at the CLS@APS 20-BM beamline at the Advanced Photon Source (APS) in the Argonne National Laboratory in Argonne, IL. The stored NCs were encapsulated in Kapton tape to a thickness that produced a strong edge jump ($\Delta\mu_0 > 0.5$). Multiple measurements were collected at room temperature for each sample to ensure reproducibility of fine structure oscillations, reduce artifacts, and improve the resolution. The Cu, Zn, and Sn K-edges were probed using an unfocused beam, which has a spot size of 30 mm x 1 mm, and an energy resolution of about 2 eV. It should be noted that the observed deviations are expected to be very small relative to the photon resolution and 1s lifetime of each of the elements; therefore, multiple passes were made at each sample, and multiple locations within each sample were scanned, to ensure reproducibility, and averaged to improve the resolution. A Si (111) monochromator with a harmonic rejection mirror, and vertical slit height of 3.5 mm were used for the Cu and Zn edges. The mirror was removed, and the vertical slit height was reduced to 400 μm , for the Sn edge. Data were collected in transmission mode using ionization chamber detection, and samples placed 45° to the incident photons. The incident chamber was filled with 100% N_2 when measuring the Cu and Zn edges, and 100% Ar when measuring the Sn edge. The transmission and reference chambers were filled with 90% N_2 , and 10% Ar by weight throughout. For the Cu and Zn K-edge measurements, the incident beam was detuned 15% at 9.8 keV, and a harmonic rejection (HR) mirror was placed at a grazing angle within the beam to reflect the fundamental energy towards the sample,

while reflecting any harmonic X-rays away. For the Sn K-edge, the beam was detuned 15% at 29.5 keV. The HR mirror was not required during Sn measurements.

Data processing was carried out using the Athena software package.¹⁵ Spectra were normalized to unity against the incident photon flux, I_0 , and calibrated against a reference foil (EXAFS Materials Inc.) using the first inflection point of the derivative spectra.¹³ Derivative spectra were then smoothed using a 7 point, 4th order Savitzky-Golay algorithm. The standards used included a 7.5 μm thick copper foil, a 10 μm Zn foil, and a 50 μm Sn foil. The treated data were transferred to k-space, using a range of 3 – 12 for Cu, and 3 – 14 for Zn and Sn data. These were then fit using the Artemis software package, and using the FEFF8 computational software.¹⁵ Fittings were based around a kesterite-phase CZTS unit cell (JCPDS card 26-0575) at room temperature, as calculated from the crystallographic information file generated using VESTA.¹⁶ Coordination number was fixed according to the theoretical value from the kesterite crystal structure. The amplitude reduction factor was fixed at 0.70 for the Cu K-edge, 0.90 for the Zn K-edge, and 1.00 for the Sn K-edge EXAFS fitting, with each determined by measuring the metal reference foil and fitting the metal-metal bond distance.²¹ Energy corrections to the measured energy threshold were applied uniformly to all atoms within a fit to ensure phase transferability between the experimental and theoretical EXAFS signal. Interatomic distance and thermal vibrations were allowed to adjust separately, to allow for expected antisites within the structure. In this manner, the total free running parameters for the fittings were reduced, allowing for the extended multi-shell fitting. Defects are indicated by Kröger-Vink notation, as described in Chapter 3.3.1.

4.3 Results and Discussion

4.3.1 Composition

The compositional integrity of the CZTS layer ultimately determines the effectiveness of the absorbing layer. This integrity is comprised of the ratios of the elements present, of their local arrangement about each other, and of the extent to which that arrangement is facsimiled through a long-range film. CZTS NC-based films of similar composition were tested to determine the extent to which compositional integrity hinders electron flow.

Intense focus was paid to the effects of minor changes in the Cu and Zn content. This was used to refine the composition of the NCs, and limit resistance within the absorber layer.

Samples were analyzed via EDX to quantify the composition. Results are summarized in Table 4.1.

Table 4.1 Elemental ratios for each sample as determined through EDX averages of 25 films. The range for the Cu ratio is shown in Samples 1 through 3, while the range for the Zn ratio is shown in Samples 3 through 5. Deviation within the presented ratios was calculated to ± 0.02 .

Sample	(Cu : Zn : Sn : S) Ratio	$\frac{Cu}{(Zn + Sn)}$	$\frac{Zn}{Sn}$
1	1.8 : 1.0 : 1.0 : 4.4	0.89	1.0
2	2.0 : 1.0 : 1.0 : 4.5	0.99	1.0
3	1.9 : 1.0 : 1.0 : 4.4	0.95	1.0
4	2.0 : 1.1 : 1.0 : 4.4	0.95	1.1
5	1.8 : 0.9 : 1.0 : 4.5	0.95	0.9

Each of the samples presented show small metal ratio deviations relative to each other. These ratio changes were consistently measured across each of the 25 films that made up each sample set; however, photoelectrochemical measurements were unable to detect a deviation in the resulting photoresponse. Each NC-based film consistently produced 0.148 ± 0.007 mA/cm². Measurements for each sample can be found in Figure 4.2. These measurements are taken as a linear sweep voltammogram, during which a high powered Xe-lamp ‘light source’ is switched on and off, creating the pulse-like sequence, with higher current readings seen under illumination, and lower currents seen in the dark. Photoresponse is then a measure of the maximum photocurrent (current measured in the ‘light on’ scenario), subtracting the dark current (current measured in the ‘light off’

scenario). As such, the deviations in metal ratio can be attributed to local antisites or vacancies within the film, as opposed to deviations pervasive throughout. The nature of these local structures will have a more significant impact on the solid-solid interface of the final device, and requires characterization in order to optimize the CZTS layer for use in full devices. Two trends were observed via the presented ratios. Samples 1, 2, and 3 hold the Zn/Sn ratio constant within error, while altering the Cu/(Zn+Sn) ratio. Samples 3, 4, and 5 hold a constant Cu/(Zn+Sn) ratio, while varying the Zn/Sn ratio. It should be noted that all samples constitute a Cu-poor, Zn-rich state relative to the stoichiometric CZTS ratios, which matches well with reported high photocurrent samples.^{4, 7, 18}

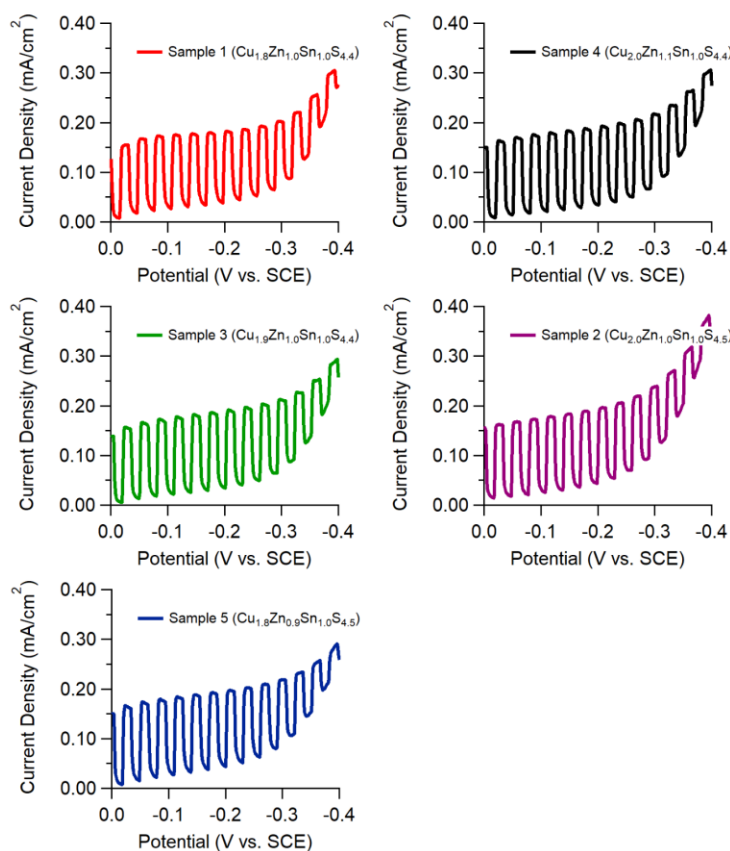


Figure 4.2 Photoelectrochemical measurements for each of the 5 samples.

Minor changes in the Zn/Sn ratio appear to correlate inversely to the amount of sulfur found in each sample. A higher ratio (Sample 4) can be seen to have less sulfur presence than samples of lower Zn/Sn ratio (Sample 5). Conversely, changes in the Cu/(Zn+Sn) ratio correlate directly with the sulfur content of the sample, though to a lesser degree.

The higher Cu sample (Sample 2) shows a slight increase in sulfur relative to that of the lower Cu ratio of Sample 1. The importance of such will be explored further in the EXAFS section.

4.3.2 XANES

Each metal K-edge was examined to identify changes in the local environment resulting from the changes in chemical composition. Given that large deviations would be expected to have significant impact on the photoresponse, it is expected that only minor deviations will be present at all edges. Figure 4.3 shows the Cu K-edge for both ranges, slightly offset vertically for improved visualization.

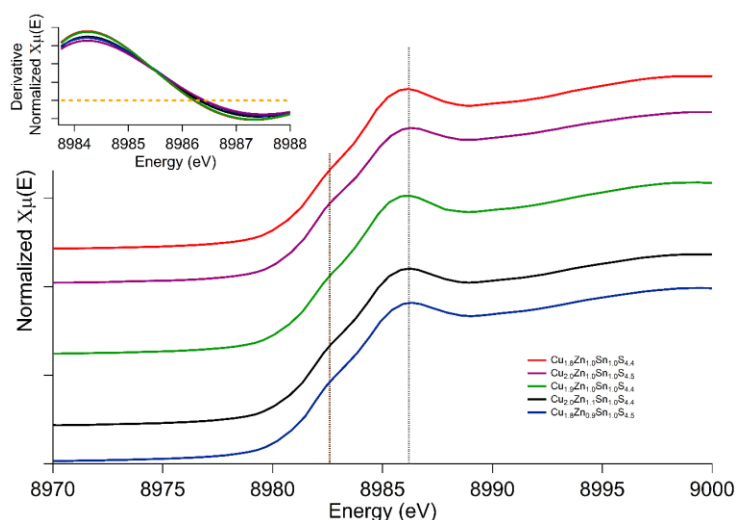


Figure 4.3 Cu K-edge XANES spectra showing changes in the Cu/(Zn+Sn) ratio (red < green < purple), and changes in the Zn/Sn ratio (blue < green < blue). Vertical lines (maroon and grey) are shown at peak locations of 8,982.6 eV and 8,986.3 eV respectively. Samples are ordered by sample number, with Sample 1 (red) being at the top, and Sample 5 being at the bottom (blue). Derivative of the XANES spectra is shown in the inset (top left).

Analysis of all spectra shows highly similar absorption edges, with very similar features. The Cu pre-edge region, below 8,980 eV, is completely devoid of features. This region arises from dipole-forbidden, quadrupole-allowed $1s \rightarrow 3d$ excitations.^{9, 13} These transitions occur with far less frequency than dipole-allowed transitions, leading to

weaker absorbance.¹⁹ As such, they are highly sensitive to any minor disruption to the electric fields around the metal center.²⁰ This means that it will show features related to the spin state, centrosymmetry, and ligand-field effects.¹³ In all the spectra shown in Figure 4.3, there is a complete lack of a pre-edge peak, which indicates that these transitions are not available. This means that either the Cu centers have a full d-shell, or the centrosymmetry is highly conserved about the metal center. In CZTS, the Cu should be bound in a tetrahedral geometry, wherein the 4p orbitals will have t_2 symmetry, and the 3d orbitals will have t_2 and e symmetry. This should allow significant mixing of the symmetry-paired orbitals. Given the complete lack of a pre-edge, the center must therefore be in the $3d^{10}$ state. This is consistent in Figure 4.3, regardless of the metal ratios, and is indicative of both a Cu^+ metal center, and a highly conserved ligand field around the Cu-centers, regardless of the metal ratio.

The Cu rising-edge contains additional information arising from the dipole-allowed $1s \rightarrow 4p$ transitions. These transitions are a lot stronger, making the features in the rising-edge much stronger than the pre-edge features. Changes in geometric layout, as well as oxidation state, and orbital overlap between the metal center and surrounding atoms, will all contribute to changes in the rising-edge features. As seen in Figure 4.3, all samples share a common peak at 8,982.6 eV, followed by a slightly shifted main absorption peak in the 8,986 eV region. This gives the appearance of p-orbitals are split into a single, and double degeneracy as seen in 3-coordinate Cu^+ compounds; however, that should then lead to a double peak, or large broadening in the main peak, as expressed in the literature.²⁰⁻²³ Therefore, this explanation does not fit. Furthermore, the peak at 8,982.6 eV is more of a shoulder, rather than a distinct absorption. According to literature, such features are common among 4-coordinate Cu^+ compounds bound to sulfur, due to higher covalent strength contributing to shake-down transitions.^{20, 24-26} This explanation fits far better than the 3-coordinate explanation, although these features could also arise from Cu^{2+} centers.²⁰ The latter option was discounted due to the lack of a pre-edge peak around 8,979 eV, and lack of higher energy features around 8,990 eV, that would be present in a Cu^{2+} situation.²³ This leaves the conclusion that the copper centers in a tetrahedral geometry, in the Cu^+ oxidation state. This would supply the consistent ligand field strength indicated by the lack of pre-edge features.

The location of the main absorption peak remains within 0.3 eV with changes in the Cu and Zn ratios, as seen in the derivative of the XANES spectra (Figure 4.3 inset); however, given the core-hole lifetime and photon resolution, these changes must be acknowledged as being extremely small. The use of multiple passes and multiple film locations all yielding the same shifts suggest that these changes are present, and thus have been interpreted as such. The $1s \rightarrow 4p$ transition noted at 8,982.6 eV is identical in all samples, it can be easily interpreted that these shifts signify minor changes in the ligand field strength around the center. These peaks are also in the $1s \rightarrow 4p$ region, which signifies an unequal distribution of the p-orbitals.^{13, 23, 26} The known metal ratio deviations, coupled with the clear differentiation in the zero crossing of the derivative spectra, provide compelling evidence of the subtle nature of the changes to the overall structure in the film. This would ultimately appear to contradict the previously discussed features, and so was discounted as an option. Instead, these small changes must be considered the result of changes in ligand arrangement, and in metal-ligand overlap.^{13, 23, 26} As seen in the second grey marker in Figure 4.3, this peak occurs at 8,986.2 eV in Sample 1 (red), 8,986.4 eV in Sample 2 (purple), and 8,986.2 eV in Sample 3 (green). This is a very small shift, and therefore likely associated with very small changes structurally. Fundamentally, the effects of changes in the ligand arrangement, or metal-ligand overlap, would manifest as a shift in the peak position relative to the edge onset, as the molecular orbital energy levels change slightly due to both electron and orbital redistribution.^{9, 13, 27} These come about from small structural changes in the ligands surrounding the absorber atom, and constitute changes in the charge transfer from ligand to metal center.^{9, 13} In the case of CZTS, the ligands would equate to the sulfur atoms bound to other metals. The primary bond between the Cu absorber, and sulfur, would not change; however, the other metals to which that S atom is bound do not remain static. Small deviations in these secondary bounds are enough to explain the observed changes in electronic structure. As such, the noted deviations must arise from substitutions in the crystal lattice that lead to changes in the metals bound to the sulfur atom, which is bound to the absorbing Cu center. Therefore, the above noted changes must be caused by changes in shallow Zn_{Cu}^{\bullet} antisites (Zn replacing Cu in the crystal lattice, as shown in the red circle of Figure 4.1B).^{3, 5, 28-29} These create slight charge mis-matches throughout the

film, as the Zn^{2+} center holds an additional charge relative to the Cu^+ . This creates an advantageous shallow donor level just below the conduction band that promotes high photoresponse. The formation of this antisite is known to favor the formation of a Cu'_{Zn} antisite that pairs to the Zn^{\bullet}_{Cu} , creating a $[Cu'_{Zn} + Zn^{\bullet}_{Cu}]^0$ antisite pair. In the presence of excess Zn relative to Cu, although some pairing does occur, there will be additional Zn^{\bullet}_{Cu} antisites relative to Cu'_{Zn} .^{2, 18, 29} This would then alter the charge distribution on the sulfur atoms, which in turn is leading to the small changes seen in the Cu XANES. Sample 2 (Figure 4.3) shows the largest peak value, and has the smallest peak area in the derivative spectra and therefore the greatest charge transfer to Cu (Table 4.2), because it is very close to stoichiometric, and thus lacks the Zn^{\bullet}_{Cu} antisite.

Table 4.2 Area under the peak displayed in each of the derivative spectra, measured as a peak area ratio relative to Sample 3. Total peak area is listed beside each ratio in brackets.

Sample	Area Under Cu Peak	Area Under Zn Peak	Area Under Sn Peak
1	1.02 (0.43)	1.01 (1.12)	0.99 (0.87)
2	0.96 (0.41)	1.03 (1.14)	1.05 (0.93)
3	1.00 (0.42)	1.00 (1.10)	1.00 (0.88)
4	0.98 (0.41)	1.00 (1.11)	1.02 (0.90)
5	0.99 (0.42)	1.00 (1.11)	1.03 (0.91)

Sample 3 has the lowest energy value in the main absorption peak, suggesting that it has more of these antisites than the other samples. Sample 1 was expected to have an even lower peak position and more antisites, but instead the peak energy is identical to that of Sample 3, and has a slightly larger peak area under the derivative spectra indicating decreased charge transfer from S to Cu (Table 4.2). This leads to the conclusion that the increase in Zn content relative to Cu initially forms antisite Zn^{\bullet}_{Cu} , but eventually produces more V'_{Cu} . There is therefore a threshold at which a vacancy at the Cu site

forms predominantly.^{3, 29} This would manifest as a pocket of excess negative charge, which would alter the local field strength around those sulfurs, and thus around the remaining Cu centers. Sample 1 has crossed that threshold.

This trend remains when holding Cu ratios constant, and instead increasing the Sn content relative to the Zn (Figure 4.3). In that case, the principle absorption peak, as seen in the derivative spectra, occurs at 8,986.3 eV in Sample 4 (black), and 8,986.4 eV in Sample 5 (blue). In both cases, the Cu ratios are held constant with respect to Zn relative to Sample 3, so the change in peak position is not related to any Cu-related antisite structure. Instead, the immediate area surrounding the Cu-absorber must be altered vis-à-vis changes in the ligand strength. To instigate this in Sample 4, it is likely that an area of excess Zn-S bonds are forming in close proximity due to excess Zn_{Cu}^{\bullet} pairing with V'_{Cu} . This causes $[V'_{Cu} + Zn_{Cu}^{\bullet}]^0$ antisite-vacancy pairs to form.²⁹ This pairing would act to isolate the effects of the antisites and greatly reduce their effects on the charge transfer. This would then result in the slightly decreased area under the peak in Sample 4 relative to Sample 3, but in a larger area relative to Sample 2. This is exactly what is observed in Table 4.2. Conversely, in Sample 5 (Figure 4.3), the shift to higher energy could be associated with deep-donor level $Sn_{Zn}^{\bullet\bullet}$ antisites due to the high Sn presence, or simply reduced Zn_{Cu}^{\bullet} relative to the other samples.^{3, 18, 30} Again, reduced Zn antisites would reduce the peak area relative to Sample 3, and Sn antisites would further decrease it. Instead, the actual peak area is almost identical to that of Sample 3, suggesting Cu vacancies must also be present.

In much the same way, the Zn XANES can give information regarding the local environment for that metal center. Zn spectra are presented below in Figure 4.4 and are slightly offset to provide improved visualization. The Zn XANES contain far less features relative to the Cu XANES, but just as much information. The lack of any pre-edge features prior to the edge-onset at 9,659 eV confirms the lack of any quadrupole-allowed $1s \rightarrow 3d$ mixing. This lack of pre-edge features in all spectra suggests a well conserved symmetry around the Zn, with a d^{10} structure and no ligand-metal orbital mixing. Furthermore, the Zn XANES lacks any features prior to the principle absorption peak at exactly 9,665.1 eV in every sample.

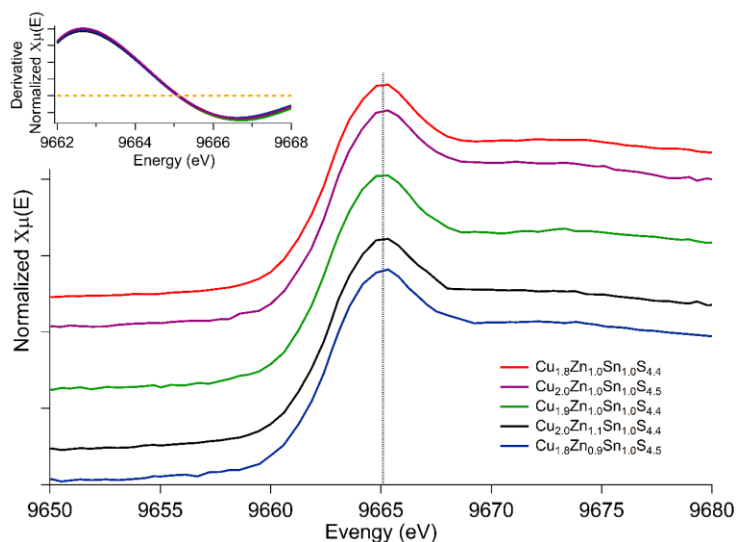


Figure 4.4 Zn K-edge XANES spectra showing changes in the Cu/(Zn+Sn) ratio (red < green < purple), and changes in the Zn/Sn ratio (blue < green < blue). A vertical line (grey) is shown to denote the main peak at 9,665.1 eV. Samples are ordered by sample number, with Sample 1 (red) being at the top, and Sample 5 being at the bottom (blue). Derivative of the XANES spectra is shown in the inset (top left).

This is especially clear when viewing the derivative spectra (Figure 4.4 inset), with all 5 samples intersecting at the zero crossing. The peak area is a bit higher for both Sample 2 (highest), and Sample 1 (Table 4.2), both of which have reduced Zn_{Cu}^{\bullet} antisites, and thus less charge transfer to the Zn sites. Samples 3, 4, and 5 all show the same peak areas. Although at first glance, this seems counterintuitive, the consistency shows that there are equivalent Zn_{Cu}^{\bullet} antisites throughout these films. We can thus conclude the high similarity is due to the shared antisite formation in all 5 films.

The lack of a rising edge feature in any of the spectra shown in Figure 4.4 means that the ligands are not contributing to the spectra through shake-down transitions. Although not indicative of anything particular to the Zn spectra, this lack of shake-down transitions is vital when comparing the Zn and Cu spectra (Figure 4.4 and Figure 4.3 respectively). The Cu spectra were subject to the subtle changes in the ligand environment, whereas the Zn centers are not. As such, the Zn spectra are far more consistent, and show next to no deviations from each other. The Zn metal center must remain highly unchanged,

regardless of the position within the crystal lattice.³¹ A corollary of this, the aforementioned Zn_{Cu}^{\bullet} must distort the lattice to create even Zn sites across the film. The Zn site must also be highly conserved, with no geometric or charge deviations, to yield a single absorption peak for all samples.³² The full d-shell ensures the absorption is directly related to the geometry, and the single absorption peak seen in all spectra of Figure 4.4 highlights the singular nature of the Zn site in all samples.³¹

The Sn XANES (Figure 4.5) are very similar to the Zn spectra (Figure 4.4) in that there are limited features to observe. The Sn spectra will naturally show less features due to the increased broadening in the absorption peak. This arises due to the core-hole lifetimes, which are much shorter in heavier elements.³³⁻³⁴ Shorter core-hole lifetimes result in spectral broadening that can blur out small features in the XANES spectra.³³ As such, only major changes in geometry or charge will be accurately detected in the XANES spectra.

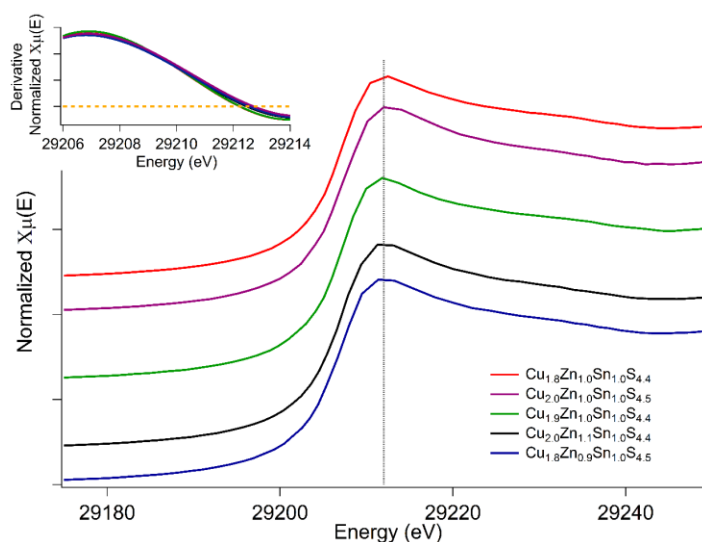


Figure 4.5 Sn K-edge XANES spectra showing changes in the Cu/(Zn+Sn) ratio (red < green < purple), and changes in the Zn/Sn ratio (blue < green < blue). A vertical line (grey) is shown to denote the main peak at 29,212.0 eV. Samples are ordered by sample number, with Sample 1 (red) being at the top, and Sample 5 being at the bottom (blue). Derivative of the XANES spectra is shown in the inset (top left).

As with the other two metal centers, Sn shows no pre-edge feature in any of the spectra seen in Figure 4.5, indicating the metal center once again shares similar symmetry across all samples, with a d^{10} structure and no ligand-metal orbital mixing. The principle peak, however, shows small deviations around 29,212 eV, the expected peak associated with Sn(IV) centers.³⁵ These deviations are most visible in the derivative of the XANES (Figure 4.5 inset). The deviations follow the same general pattern as with the Cu centers, with the Sample 1 (red) peak occurring at 29,212.3 eV, Sample 2 (purple) peak occurring at 29,212.7 eV, and Sample 3 (green) peak occurring at 29,212.3 eV. Again, these are smaller deviations than the core-hole lifetimes, but are strongly suspected to result from changes in the metals bound to the sulfur centers around Sn, for the same reasons as previously indicated in the Cu XANES discussions. Furthermore, the peak area ratios are generally opposite to those of Cu, with samples that have a higher Cu peak area tending to have a lower Sn peak area (Table 4.2). The close to stoichiometric Sample 2 shows the highest peak value, and the greatest peak area. Increases in the antisite Zn_{Cu}^{\bullet} occurrence throughout the film will lead to increased electron withdrawing on the sulfur centers, which is manifesting in the decreased absorbance peak, and thus decreased peak area. Again, Samples 3 and 1 have the same peak maximum, and similar peak area, corroborating the previously discussed presence of Cu vacancies. Any Sn related antisite formation in these samples remains highly unlikely, due to both the lack of change in the photoresponse – any $Sn_{Zn}^{\bullet\bullet}$ antisites would result in deep-level charge carrier traps and reduce the photoresponse – and lack of deviation in the Sn content. Sample 4 (black) with less Sn, and Sample 5 (blue) with more Sn, have the potential for these defects. Both samples show peaks at 29,212.5 eV, which is more than the corresponding sample with equivalent Cu ratios (Sample 3), and higher peak area ratios. In the case of additional Zn, the explanation of higher Zn_{Cu}^{\bullet} antisites remains convincing; however, in an environment of excess Sn, as in Sample 5, the presence of some $Sn_{Zn}^{\bullet\bullet}$ antisites is more likely, as this is the one instance where the Sn peak area ratio differs from the trend observed in the Cu spectra (Table 4.2). In both cases, the higher charge on the replacement atom in the antisite would have similar effects, with $Sn_{Zn}^{\bullet\bullet}$ antisites having two times as much of a charge change as Zn_{Cu}^{\bullet} . It is possible that the number of $Sn_{Zn}^{\bullet\bullet}$ is

small enough to not detract from the photoresponse, but will require additional EXAFS analysis to corroborate it.

Taken as a whole, the XANES spectra (Figure 4.3, Figure 4.4, and Figure 4.5) provide a clear breakdown of the electronic properties of each metal center in the nanocrystals. Each metal center has a distinct tetrahedral geometry, and is tetrahedrally bound to 4 sulfur atoms. At near stoichiometric values of the Cu/(Zn+Sn) ratio, there are very limited Zn_{Cu}^{\bullet} antisites present, but these increase as the Cu content decreases. These substitutions appear to effect the site significantly, as there are no apparent changes to the Zn structure despite this change. As such, the substitution site appears to adapt an identical feature as the typical Zn site, with no major changes to the Sn sites. Further decreases to the Cu/(Zn+Sn) ratio to 0.89 appear to introduce some Cu vacancies in addition to the antisites, again without affecting the Sn. Changes in the Zn/Sn ratio have less of an effect on the metal sites. The relatively small peak shifts in the Cu and Sn XANES, along with the unchanged Zn XANES, suggest that the underlying changes in composition are both subtle, and highly delocalized. To further explore these trends, full EXAFS analysis and fitting were required.

4.3.3 EXAFS

The structural information contained in the EXAFS region is even more useful. The EXAFS region is often plotted as a wave vector, known as k-space. In these spectra, the energy is converted to a photoelectron wavenumber, k , where $k = \frac{\sqrt{(2m_e)(E-E_0)}}{\hbar}$.⁴⁰ As such, k is a function of the absorption oscillations relative to the threshold energy, E_0 . This serves to create a sinusoidal wave with a distinct frequency for each absorber-scatterer relationship.^{9, 37-38} This ensures that any minor change in the local structure will manifest as a change in the k-space spectra.³⁶ Through a Fourier transform, the k-space is converted to the pseudo radial (R-space) spectrum. Each peak of the R-space spectrum corresponds with a single scattering path length.^{9, 28, 36} Through fitting the peaks to a model compound, the exact path lengths can be established.^{33, 36, 39} Fitting parameters for all three metal centers are presented in Table 4.3 and Table 4.4 on the following pages.

Based on the fitting parameters presented in both Table 4.3 and Table 4.4, it becomes very quickly apparent that the coordination changes are very small. The results of these fits, and their corresponding spectra are discussed by metal center below, with respect to the underlying structural differences identified in the XANES spectra. The full Cu EXAFS can be seen in both k-space and R-space in Figure 4.6.

Table 4.3 EXAFS fitting parameters for Samples 1-3 at metal center. Each bond length has an error of ± 0.02 Å or less, and are fairly close across all samples, as expected. Energy shifts (ϵ_0) were held constant for all scattering paths, and were less than 3.5 eV in all cases.

Edge	Neighbor	Sample 1			Sample 2			Sample 3		
		N	σ^2 (Å ²)	r (Å)	N	σ^2 (Å ²)	r (Å)	N	σ^2 (Å ²)	r (Å)
Cu	S	4.0	0.00724	2.294	4.0	0.00775	2.291	4.0	0.00802	2.296
	Cu/Zn	4.0	0.00709	3.776	4.0	0.00995	3.786	4.0	0.00914	3.838
	Sn	4.0	0.00792	3.772	4.0	0.0108	3.783	4.0	0.00735	3.817
	S2	12	0.0143	4.450	12	0.0197	4.488	12	0.0186	4.465
Zn	S	4.0	0.00676	2.322	4.0	0.00885	2.331	4.0	0.00660	2.329
	Cu/Zn	4.0	0.00417	3.819	4.0	0.00846	3.917	4.0	0.00596	3.889
	Sn	4.0	0.0166	3.828	4.0	0.0103	3.802	4.0	0.00787	3.863
	S2	12	0.0104	4.521	12	0.0120	4.512	12	0.0143	4.635
Sn	S	4.0	0.00641	2.387	4.0	0.00619	2.412	4.0	0.00648	2.385
	Cu/Zn	4.0	0.00983	3.797	4.0	0.00866	3.987	4.0	0.00878	3.741
	Sn	4.0	0.0157	3.992	4.0	0.00892	3.968	4.0	0.00962	4.061
	S2	12	0.0150	4.642	12	0.0113	4.531	12	0.0138	4.607

Table 4.4 EXAFS fitting parameters for Sample 4 and 5 at metal center. Parameters and error margins are the same as in Table 4.3.

Edge	Neighbor	Sample 4			Sample 5		
		N	σ^2 (\AA^2)	r (\AA)	N	σ^2 (\AA^2)	r (\AA)
Cu	S	4.0	0.00699	2.293	4.0	0.00834	2.293
	Cu/Zn	4.0	0.00826	3.758	4.0	0.00943	3.691
	Sn	4.0	0.00717	3.756	4.1	0.00910	3.702
	S2	12	0.0195	4.425	12	0.0191	4.384
Zn	S	4.0	0.00909	2.345	4.0	0.00602	2.321
	Cu/Zn	4.1	0.00871	3.748	4.0	0.00631	3.831
	Sn	4.0	0.00785	3.764	4.1	0.00669	3.814
	S2	12	0.0107	4.590	12	0.0169	4.499
Sn	S	4.0	0.00730	2.379	4.0	0.00713	2.386
	Cu/Zn	4.1	0.00892	3.867	4.0	0.00933	4.001
	Sn	3.9	0.00908	3.981	4.0	0.00963	3.972
	S2	12	0.0148	4.662	12	0.00935	4.600

The bond length error has been fixed at 0.02 \AA , the maximum value produced by the fitting. While some bond lengths are theoretically more precise, this value reflects the real limits of the model, given the small deviations being examined. On changing the Cu/(Zn+Sn) ratio, the Cu k-space spectra (Figure 4.6A) are comparable in the early k-space oscillations ($2\text{-}6 \text{ \AA}^{-1}$), indicating that the local Cu-S bonding structure is well conserved.^{11, 36} Only Sample 1 (red) shows some minor deviations in the peak at 7.8 \AA^{-1} , though it is hard to determine if this is simply due to the noise in the region, or due to disorder. This is consistent with the structural properties identified in the XANES

(Figure 4.3). The late k-space oscillations (7-12 \AA^{-1}) of Figure 4.6A are not as comparable in intensity, though they maintain the periodicity, as indicated by the highly congruent peak mid-points occurring at each grey divider.

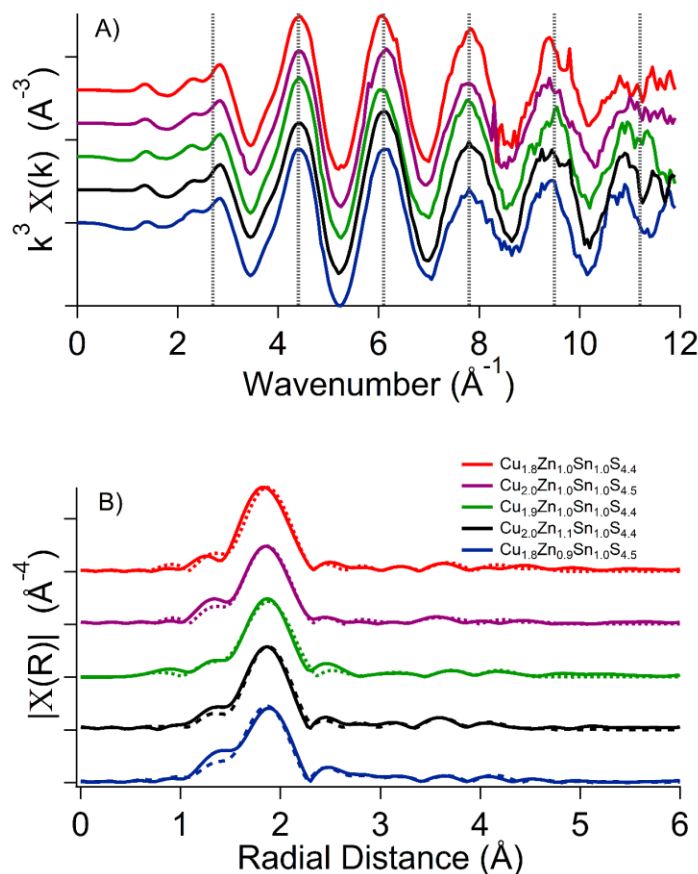


Figure 4.6 Cu EXAFS for each sample in k-space A), and R-space B). The k-space spectra are divided by periodic grey lines every 1.7\AA^{-1} beginning at 2.7\AA^{-1} for ease of comparison. Each R-space spectrum has been overlain with its corresponding fit (dashed line) using the Artemis software package. Samples are ordered by sample number, with Sample 1 (red) being at the top, and Sample 5 being at the bottom (blue), with fitting mismatch factors of 0.020, 0.021, 0.019, 0.023, and 0.021 respectively. The rest of the parameters are presented in Table 4.3 and Table 4.4.

Beyond 12\AA^{-1} , interference from the nearby Zn K-edge prevents any meaningful data. This means that the data is only complete up to the interactions of 3.5\AA (the approximate square root of the total length of the k-space spectra). This means the data for the second

shell fit, which contains the metals, is an approximation only. As such, the overall structure does not change – thus no observable changes in the periodicity – but features several small, random deviations throughout the structure that mute the signal in the late k-space spectrum of Sample 2. This is observed in the intensity of the peak at 7.8 \AA^{-1} , which is reduced in Sample 2 (purple) compared to the samples containing less Cu: Sample 1 (red) and Sample 3 (green). This indicates a less rigid ordering in the higher Cu samples.^{33,39} Given the expected lack of extensive Zn_{Cu}^{\bullet} antisites present throughout this sample, it is likely that the $[Cu'_{Zn} + Zn_{Cu}^{\bullet}]^0$ antisite pairs and V'_{Cu} occur randomly throughout the sample.^{3,29} Conversely, Sample 1 (red) has plenty of excess Zn, but due to the comparable oscillations with Sample 3 (green), the total Zn_{Cu}^{\bullet} antisite appear to be relatively the same between these two samples. This further confirms the presence of V'_{Cu} in Sample 1, to go along with the known Zn_{Cu}^{\bullet} antisite present in each of the samples. These additional antisites in Sample 1 and 2 relative to Sample 3 are likely contributing to the signal breakdown observed around the 11.2 \AA^{-1} period.

A similar event occurs on alteration of the Zn/Sn ratio. Sample 4 (black) is highly comparable with Sample 3 (green) until very late in the k-space spectra (Figure 4.6A) at 11.2 \AA^{-1} , whereas Sample 5 (blue) shows decreased intensity at the 7.8 \AA^{-1} peak. The lower Zn content of Sample 5 exhibits the same features as those observed in Sample 1 (red). With similar Zn and Cu, Sample 5 contains regions of Zn_{Cu}^{\bullet} substitutions similar to Sample 1, and excess Sn. This would lead to non-uniform distribution of the more limited Cu and Zn, likely creating small, albeit significant, regions of excess Sn-S structure.⁴⁴ This can be contrasted with Sample 4, which exhibits comparable structure with Sample 3. Here, although the excess Zn can be associated with increased pairing between Cu and Zn antisites, it has already been established above that these contribute little disorder at the given Cu/(Zn+Sn) ratio. This leaves deep-donor level $Sn_{Zn}^{\bullet\bullet}$ antisite as the primary source of these discrepancies in Sample 5, whereas Sample 4 appears to be a good balance of the metals. Overall, the data points to less rigid ordering being a function of higher Cu, Zn, and Sn contents.

The R-space spectra (Figure 4.6B) are overlain with a multishell fit incorporating Cu-S, Cu-Cu, Cu-Zn, and Cu-Sn bonds from a theoretically unblemished kesterite CZTS

crystal. As such, site-specific bond lengths were determined for each of the different scatterers. The principle interaction in the first shell, the Cu-S bond, shows a high degree of consistency, regardless of the Cu/(Zn+Sn) ratio, with each bond appearing at 2.29 Å (Figure 4.6B). This agrees with the XANES data (Figure 4.3) and the k-space spectra (Figure 4.6A), as any deviation here would manifest in the principle absorption, and in the early k-space oscillations. There are, however, some deviations observed in the surrounding metals that make up the second shell. Samples 1 (red) and 2 (purple) show Cu-Cu/Zn distances of 3.77 Å, and of 3.79 Å respectively. Their corresponding Cu-Sn bond is 3.77 Å for Sample 1, and 3.78 Å for Sample 2. Each is well within margins of error for these to be considered equivalent bonds, and given the truncated nature of the usable k-space, must be taken as such. Sample 3 (green) shows slightly elongated lengths of 3.84 Å Cu-Cu/Zn, and 3.82 Å Cu-Sn, but these must be evaluated alongside the values determined via the Zn and Sn spectra to eliminate the greater error associated with the weaker Cu data. In each case, the slightly longer distances between atoms in Sample 3 suggests a more loosely-bound structure, which is more in line with the bond lengths of the pure CZTS kesterite structure.^{6, 41} This is likely the reason for the comparable photoresponses, despite the reported changes. Although the increase in ideal substitutions would contribute favorably to the photoresponse, the above-noted changes in the bond lengths would create unfavorable size constraints, allowing less vibrational freedom in the crystal structure, and additional disorder in crystal alignment due to the smaller size. Both would contribute adversely to the photoresponse of Sample 1 and 2.

Similar results can be seen in the R-space as a result of changes in the Zn/Sn ratio (Figure 4.6B). The initial Cu-S bond remains at 2.29 Å in both Samples 4 and 5, as expected. At high Zn content, Sample 4 (black) has 3.76 Å Cu-Cu/Zn distance, and 3.76 Å for Cu-Sn distances. This is an equivalent crystal to the high Cu-content samples. The increase in Zn_{Cu}^{\bullet} antisite alone does not contribute to shorter bonds within the structure. At increased Sn content (Sample 5), the Cu-Cu/Zn distance is further reduced to 3.70 Å, and the Cu-Sn bonds reduced to 3.70 Å. This is now the source of the reduced crystal structure. Given the expanded charge associated with increased Sn(IV) content, this also makes sense. It is therefore consistent with $Sn_{Zn}^{\bullet\bullet}$ antisite formation, which would place the heavier, larger Sn atoms throughout, contributing to increased lattice distortions.^{4, 29}

The close correlation between the Cu and Zn centers previously noted would then manifest in the Zn EXAFS. These signals are in both k-space, and R-space spectra are displayed in Figure 4.7.

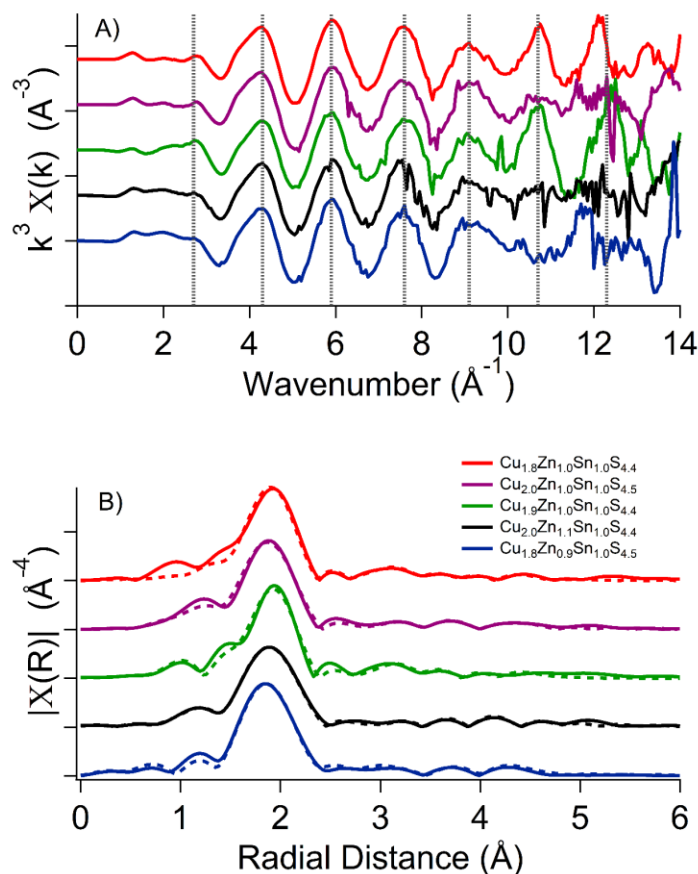


Figure 4.7 Zn EXAFS for each sample in k-space A), and R-space B). The k-space spectra are divided by periodic grey lines every 1.6 \AA^{-1} beginning at 2.7 \AA^{-1} for ease of comparison. Each R-space spectrum has been overlain with its corresponding fit (dashed line) using the Artemis software package. Samples are ordered by sample number, with Sample 1 (red) being at the top, and Sample 5 being at the bottom (blue), with fitting mismatch factors of 0.015, 0.010, 0.019, 0.005, and 0.021 respectively. The rest of the parameters are presented in Table 4.3 and Table 4.4.

As in the Cu (Figure 4.6A), the Zn k-space spectra (Figure 4.7A) show conserved periodicity throughout all samples further confirms the lack of distinct secondary phases, though Sample 1 does show some late deviations.^{36, 42} That these deviations occur more

pronounced in the Zn spectrum than those seen in the Cu spectrum indicate that this is a disorder, rather than an artifact. This further confirms the presence of both Zn_{Cu}^{\bullet} antisites, and V'_{Cu} , located randomly throughout the film. Disorder in crystal alignment can also create such patterns, though to a lesser extent.⁹ Decreases in the Cu/(Zn+Sn) ratio appear to remove this issue in periodicity, yet Sample 2 (purple) shows decreased intensity at the 10.7 Å⁻¹ and 12.3 Å⁻¹ peaks, similar to the observations made in the Cu k-space (Figure 4.6A). The same appears to be true for deviations in the Zn/Sn ratio. Sample 4 (black) and Sample 5 (blue) show decreased intensity in the late regions, at 10.7 Å⁻¹ and 12.3 Å⁻¹, again consistent with the Cu data, indicating increased disorder among the antisites. This corresponds with the previously reported Zn-S abundance due to excess Zn_{Cu}^{\bullet} antisites, and shows higher disorder in samples of low Zn/Sn.

The R-space spectra (Figure 4.7B) visually appear to have variation about the Zn centers; however, the first shell, Zn-S bond, appears at 2.32 Å in Samples 1 and 5, 2.34 Å for Sample 4, and 2.33 Å in Samples 2 and 3. All of these are within margins of error, and thus not significantly changed.^{4,9} Second shell metal-to-metal bond lengths for Zn-Cu/Zn were 3.82 Å for Sample 1, and 3.89 Å for Sample 3. This bond length extends to 3.92 Å in Sample 2. Given that the Cu was shown to be less rigidly ordered in Sample 2, it is expected that Zn sites would also show this trend. Changes to the Zn/Sn ratio were also found to contribute to the bond lengths. The high Zn content Sample 4 showed Zn-Cu/Zn bonds of 3.74 Å. The low Zn content Sample 5 showed 3.83 Å. In both cases, deviations from the 1:1 ratio of Zn:Sn contribute to bond shortening, and a contraction of the observed crystal lattice. This leaves Sample 3 with the least vibrational rigidity, but the most consistent kesterite crystal lattice.³⁻⁶

Unlike the Cu and Zn centers, Sn has been consistent throughout all of the samples, and throughout all of the analyses discussed herein. As such, the Sn EXAFS spectra should maintain a high degree of similarity, with the only expected changes to be the metal-metal bond lengths, and confirmation or repudiation of deep-donor level $Sn_{Zn}^{\bullet\bullet}$ antisites in Sample 5. The Sn k-space and R-space spectra are shown in Figure 4.8. As expected, the k-space spectra (Figure 4.8A) show only small deviation among the samples. All spectra show high periodicity, with no unexpected changes, even at high wavenumber.

Even the peaks at 9.2 \AA^{-1} , 10.8 \AA^{-1} , and 12.4 \AA^{-1} of Sample 5 show consistent oscillations with the other samples. This is easily observable despite the increased noise in the region. This strongly refutes the notion of any $\text{Sn}_{\text{Zn}}^{\bullet\bullet}$ antisites presence in Sample 5. Presence of $\text{Sn}_{\text{Zn}}^{\bullet\bullet}$ would contribute adversely to photoresponse, so a lack of these substitutions is more in-line with the consistent photoresponse among all five samples.

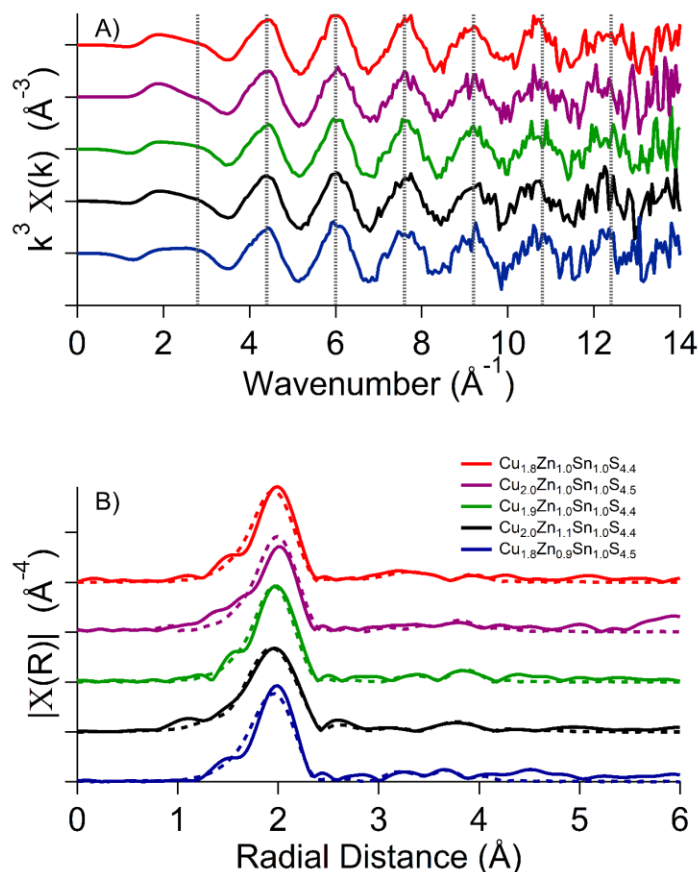


Figure 4.8 Sn EXAFS for each sample in k-space A), and R-space B). The k-space spectra are divided by periodic grey lines every 1.6 \AA^{-1} beginning at 2.8 \AA^{-1} for ease of comparison. Each R-space spectrum has been overlain with its corresponding fit (dashed line) using the Artemis software package. Samples are ordered by sample number, with Sample 1 (red) being at the top, and Sample 5 being at the bottom (blue), with fitting mismatch factors of 0.054, 0.035, 0.040, 0.079, and 0.056 respectively. The rest of the parameters are presented in Table 4.3 and Table 4.4.

The R-space spectra (Figure 4.8B) shows the expected well conserved first shell, with each sample showing a Sn-S bond distance of around 2.38 to 3.41 Å. The metal-metal bonds differentiate, however, with changes in the Cu/(Zn+Sn) ratio. Samples 1 and 2 show Sn-Cu/Zn bonds of 3.80 and 3.99 Å, and Sn-Sn bonds of 3.99 and 3.97 Å respectively. These bonds are slightly deviated in Sample 3, with the Sn-Cu/Zn bond being shorter at 3.74 Å, whereas the Sn-Sn bonds show higher at 4.06 Å. This deviation would arise due to the size difference in the crystal lattice predicted previously. Coupled with the k-space spectra (Figure 4.8A), the Sn is evenly distributed across each lattice, despite the size differences. Changes in the Zn/Sn ratio have more of an effect on this. At high Zn/Sn ratios (Sample 4), the Sn-Cu/Zn bond expands to 3.87 Å, and in low Zn environments, it expands to 4.01 Å (Sample 5). This is offset by changes in the Sn-Sn bonds, which are 3.98 Å and 3.97 Å in each respectively. This suggests additional crystal strain in both Samples 4 and 5 relative to the others, and would be the reason for the extended disorder noted in these samples.

4.4 Conclusions

The various antisites present in high photoresponse CZTS NC-based films of different compositions were explored through SR-XAFS measurements. It was found that samples with a Cu/(Zn+Sn) ratio of 0.95 and Zn/Sn ratio of 1.0 showed the most beneficial structure, with advantageous Zn_{Cu}^{\bullet} antisites spread periodically throughout the films. Increases in either ratio introduced increased disorder among the antisites. Increasing the Zn content created too many Zn_{Cu}^{\bullet} antisites, and created regions of high Zn-S like structure, whereas increased Cu content allowed for additional Cu'_{Zn} antisites, which in turn leads to $[Cu'_{Zn} + Zn_{Cu}^{\bullet}]^0$ antisite pairs. These contribute to not only increased disorder within the films, but also tighter packing of the crystal. This appears to be the trade-off that creates the equivalent photoresponse observed in all of these samples. Similarly, decreases in Zn content contribute to additional disadvantageous Cu'_{Zn} antisites, but again result in smaller bond lengths. Decreases in Cu content lead to increased disorder in the $[Cu'_{Zn} + Zn_{Cu}^{\bullet}]^0$ antisite pairs due to the decreased Cu'_{Zn} antisites. Both cases also lead to more contracted bond lengths. From this, it appears that a trade-off occurs between the creation of these advantageous substitutions, and the

increased disorder due to crystal misalignment across the film. This is the likely reason for the equivalent photoresponse despite the differing metal concentrations, and therefore differing amounts of advantageous antisites within the films. Initial decreases in the Cu content yield increased Zn_{Cu}^{\bullet} antisites, but eventually start forming increasing Cu vacancies, which eliminate any advantageous effects of the antisites. Increased Cu content, however, also leads disadvantageous $[Cu'_{Zn} + Zn_{Cu}^{\bullet}]^0$ antisite pairs. This gives the idea that each structural abnormality has some effect on the photoresponse, and that samples constructed with similar composition will experience different ratios of these antisites, but ultimately they have a relatively equal balance of advantageous and disadvantageous ones, thereby yielding equivalent photoresponse. As such, film fabrication in low-cost environments should include the above mentioned ratios to maximize the formation of advantageous antisites, without overly increasing the disorder.

4.5 References

1. Liu, F.; Yan, C.; Huang, J.; Sun, K.; Zhou, F.; Stride, J. A.; Green, M. A.; Hao, X., *Adv. Energy Mater.* **2016**, *6*, 1600706.
2. Chen, S. Y.; Gong, X. G.; Walsh, A.; Wei, S. H., *Appl. Phys. Lett.* **2010**, *96*, 021902.
3. Scragg, J. J. S.; Choubrac, L.; Lafond, A.; Ericson, T.; Platzer-Björkman, C., *Appl. Phys. Lett.* **2014**, *104*, 041911.
4. Colina-Ruiz, R. A.; Mustre de Leon, J.; Lezama-Pacheco, J. S.; Caballero-Briones, F.; Acosta-Alejandro, M.; Espinosa-Faller, F. J., *J. Alloys Compd.* **2017**, *714*, 381.
5. Schelhas, L. T.; Stone, K. H.; Harvey, S. P.; Zakhidov, D.; Salleo, A.; Teeter, G.; Repins, I. L.; Toney, M. F., *Phys. Status Solidi B* **2017**, 1700156.
6. Espinosa-Faller, F. J.; Conradson, D. R.; Riha, S. C.; Martucci, M. B.; Fredrick, S. J.; Vogel, S.; Prieto, A. L.; Conradson, S. D., *J. Phys. Chem. C* **2014**, *118*, 26292.
7. Todorov, T. K.; Tang, J.; Bag, S.; Gunawan, O.; Gokmen, T.; Zhu, Y.; Mitzi, D. B., *Adv. Energy Mater.* **2013**, *3*, 34.
8. Glazoff, M. V., *Appl. Phys. A* **2016**, *122*, 386.
9. Teo, B. K., *EXAFS: Basic Principles and Data Analysis*; Springer: Berlin, 1986.
10. Toyama, T.; Konishi, T.; Tsuji, R.; Maenishi, R.; Arata, A.; Yudate, S.; Shirakata, S., *Phys. Status Solidi C* **2015**, *12*, 721.

11. Siah, S. C.; Jaramillo, R.; Chakraborty, R.; Erslev, P. T.; Sun, C. J.; Weng, T. C.; Toney, M. F.; Teeter, G.; Buonassisi, T., *IEEE J. Photovolt.* **2015**, *5*, 372.
12. Samrath, N.; Mishra, A., *J. Phys. Conf. Ser.* **2016**, *755*, 012045.
13. Stöhr, J., *NEXAFS Spectroscopy*; Springer: Berlin, Germany, 1992.
14. Vaccarello, D.; Tapley, A.; Ding, Z., *RSC Adv.* **2013**, *3*, 3512.
15. Ravel, B.; Newville, M., *J. Synchrotron Radiat.* **2005**, *12*, 537.
16. Momma, K.; Izumi, F., *J. Appl. Crystallogr.* **2011**, *44*, 1272.
17. Ankudinov, A. L.; Ravel, B.; Rehr, J. J.; Conradson, S. D., *Phys. Rev. B* **1998**, *58*, 7565.
18. Scragg, J. J.; Dale, P. J.; Peter, L. M.; Zoppi, G.; Forbes, I., *Phys. Status Solidi C* **2008**, *245*, 1772.
19. Eberhardt, W.; Himpsel, F. J., *Phys. Rev. B* **1980**, *21*, 5572.
20. Kau, L. S.; Spira-Solomon, D. J.; Penner-Hahn, J. E.; Hodgson, K. O.; Solomon, E. I., *J. Am. Chem. Soc.* **1987**, *109*, 6433.
21. Hsiao, M. C.; Wang, H. P.; Yang, Y. W., *Environ. Sci. Technol.* **2001**, *35*, 2532.
22. Kau, L. S.; Hodgson, K. O.; Solomon, E. I., *J. Am. Chem. Soc.* **1989**, *111*, 7103.
23. Gaur, A.; Shrivastava, B. D.; Joshi, S. K., *J. Phys. Conf. Ser.* **2009**, *190*, 012084.
24. Blackburn, N. J.; Strange, R. W.; Reedijk, J.; Volbeda, A.; Farooq, A.; Karlin, K. D.; Zubieta, J., *Inorg. Chem.* **1989**, *28*, 1349.
25. Tomson, N. C.; Williams, K. D.; Dai, X.; Sproules, S.; DeBeer, S.; Warren, T. H.; Wieghardt, K., *Chem. Sci.* **2015**, *6*, 2474.
26. Sarangi, R., *Coord. Chem. Rev.* **2013**, *257*, 459.
27. Vila, F.; Rehr, J. J.; Kas, J.; Nuzzo, R. G.; Frenkel, A. I., *Phys. Rev. B* **2008**, *78*, 121404.
28. Nozik, A. J.; Memming, R., *J. Phys. Chem.* **1996**, *100*, 13061.
29. Chen, S.; Wang, L. W.; Walsh, A.; Gong, X. G.; Wei, S. H., *Appl. Phys. Lett.* **2012**, *101*, 223901.
30. Tanaka, K.; Takamatsu, Y.; Miura, S., *Phys. Status Solidi C* **2017**, *14*, 1600138.
31. Cui, P.; Wang, Y.; Chu, W.; Guo, X.; Yang, F.; Yu, M.; Zhao, H.; Dong, Y.; Xie, Y.; Gong, W.; Wu, Z., *Sci. Rep.* **2014**, *4*, 7453.
32. Akgül, F. A., *Compos. Part B Eng.* **2016**, *91*, p. 589.
33. Penner-Hahn, J. E., *Comprehensive Coordination Chemistry II: From Biology to Nanotechnology*; Elsevier: Boston, 2003; Vol. 2.
34. D'Angelo, P.; Migliorati, V.; Persson, I.; Mancini, G.; Longa, S. D., *Inorg. Chem.* **2014**, *53*, 9778.

35. Grandjean, D.; Benfield, R. E.; Nayral, C.; Maisonnat, A.; Chaudret, B., *J. Phys. Chem. B* **2004**, *108*, 8876.
36. Zhang, P., *J. Phys. Chem. C* **2014**, *118*, 25291.
37. Vlais, G.; Olivi, L., *Croat. Chem. Acta* **2004**, *77*, 427.
38. Chevrier, D. M.; Zeng, C.; Jin, R.; Chatt, A.; Zhang, P., *J. Phys. Chem. C* **2015**, *119*, 1217.
39. Chevrier, D. M.; Meng, X.; Tang, Q.; Jiang, D.; Zhu, M.; Chatt, A.; Zhang, P., *J. Phys. Chem. C* **2014**, *118*, 21730.
40. Walsh, A.; Chen, S.; Gong, X.; Wei, S.-H.; Ihm, J.; Cheong, H. In *Crystal Structure and Defect Reactions in the Kesterite Solar Cell Absorber Cu₂ZnSnS₄ (CZTS): Theoretical Insights*, AIP Conf. Proc., 2011; p 63.
41. Jewell, L.; Rocco, S.; Bridges, F.; Carter, S. A., *Phys. Rev. Applied* **2017**, *7*, 064026.
42. Huang, J. H., *Phys. Rev. B* **1998**, *58*, 12.

Chapter 5

5 Probing the CZTS/CdS Heterojunction Utilizing Photoelectrochemistry and X-ray Absorption Spectroscopy

The importance of renewable resources is becoming more and more influential on research due to the depletion of fossil fuels. Cost-effective ways of harvesting solar energy should also be at the forefront of these investigations. $\text{Cu}_2\text{ZnSnS}_4$ (CZTS) solar cells are well within the frame of these goals, and a thorough understanding of how they are made and processed synthetically is crucial. The CZTS/CdS heterojunction was examined using photoelectrochemistry and synchrotron radiation (SR) spectroscopy. These tools provided physical insights into this interface that was formed by electrophoretic deposition of CZTS nanocrystals (NCs) and chemical bath deposition (CBD) of CdS for the respective films. It was discovered that CBD induced a change in the local and long range environment of the Zn in the CZTS lattice, which was detrimental to the photoresponse. X-ray absorption near-edge structures (XANES) and extended X-ray absorption fine structures (EXAFS) of the junction showed that this change was at an atomic level and was associated with the coordination of oxygen to zinc. This was confirmed through FEFF fitting of the EXAFS, and through IR spectroscopy. It was found that this change in both photoresponse and in the Zn coordination can be reversed with the use of low temperature annealing. Investigating CZTS through SR techniques provides detailed structural information of minor changes from the zinc perspective.

5.1 Introduction

The next step is to identify the effectiveness of the CZTS/CdS hetero-junction in our layer by layer strategy. The interaction between CZTS and CdS is important since the buffer layer's sole purpose is to facilitate photogenerated electron transfer out from the absorber layer into an n-type semiconductor.¹⁻³ Methodologically, chemical bath deposition (CBD) of CdS films has been reported utilizing a time-controlled chemical

This chapter is a version of previously published work in J. Chem. Phys., 2018, 148, 134702-9.

reaction for depositing a thin layer through precipitation.⁴ CBD typically involves the use of aqueous conditions in order to heterogeneously nucleate CdS on substrates.⁵ One nucleation pathway involves the deposition of Cd(OH)₂ onto the substrate to provide a catalytic surface on which thiourea can decompose.⁶ This coupling with aqueous environment can allow for oxidation or coordination of –OH and –OH₂ to the surface of exposed CZTS. A positive effect on the photocurrent generation through photoelectrochemical measurements (PECMs) by the addition of CdS films has been seen in electrodeposited CIGS, CIS and CZTS films;⁷⁻⁹ however, in the case of nanocrystals prepared and deposited onto a substrate, they might be significantly different.

Synchrotron radiation (SR) with energy tunable X-rays is a powerful tool in examining the local environments at atomic levels via absorption spectroscopy, which can be utilized for a vast number of applications in many research fields.¹⁰⁻¹³ SR has many options for a wide range of transition metal elements as well.¹⁴⁻¹⁶ For solar energy materials, while SR is typically reserved for the detection of secondary phases and disordered atoms,^{12, 17-20} the use of X-ray absorption near-edge structures²¹⁻²² (XANES) and extended X-ray absorption fine structures²³⁻²⁴ (EXAFS) can probe the local and extended environments of a target atom, respectively. Previously, XANES was used to correlate the differences in electronic structures to local compositions in CZTS and CIS light absorbing layers with varied photocurrents, giving new details into the physical aspect of photoelectrochemistry.²⁵⁻²⁶ Through probing the CZTS thin films with the addition of new layers, an examination of the effects by these new layers has been realized in this work. Alternations in the local and extended structures can be used to determine the cause for changes in photoelectrochemical performance as a function of spectral change at an atomic site of interest.

Employing a cooperative use of both SR spectroscopies and electrochemistry, a CZTS-based solar cell should be dynamically characterized at each interface. The targeted CZTS/CdS heterojunction is an interface of particular importance as it is the interaction of this layer that facilitates electron transfer, resulting in high efficiency devices.^{7, 27-28} The balance between high efficiency and low associated cost is often precarious with respect to processing of solar devices. The necessity of high-energy steps might negate

the purpose of utilizing CZTS as a light absorbing layer in order to reduce costs. The addition of a layer can change the local environment of the CZTS, leading to enhancement or degradation of the effectiveness of the absorbing layer. These physicochemical aspects are important to uncover. Our strategy of a step-wise optimization for a photovoltaic device is the balance of effectiveness and cost, particularly for the objective of implementation into mass production.

5.2 Experimental

5.2.1 Fabrication

CZTS NCs were fabricated solvothermally as previously reported,¹³ and as described in Chapter 4.2.1. Resultant NCs were cleaned using isopropanol (Sigma-Aldrich, $\geq 99.7\%$), dispersed in isopropanol to 2 g/L, and electrophoretically deposited onto fluorine-doped tin oxide-coated glass (FTO) (Sigma-Aldrich with sheet resistance of 13 Ω /piece),²⁹ using a Keithley 2400 source meter (Tektronix, Beaverton, OR). A ~ 1 μm thick CZTS deposition was made for each film by holding a constant 0.24 mA/cm² current for 40s.

CdS was deposited on each CZTS film via chemical bath deposition (CBD), based on previously reported methods.⁷ A mixture of 1.5 mM CdSO₄ (Fischer Scientific, 98%), and 1.5 M NH₄OH (Caledon, $\geq 99\%$) were stirred for 30 minutes and heated to 65 °C. Following temperature stabilization, 7.5 mM thiourea (Sigma-Aldrich, $\geq 99\%$) was added, and the CZTS films dipped into the solution. The reaction was allowed to proceed for 10 minutes, resulting in a deposition of ~ 50 nm CdS on top of the CZTS films.

The resultant CZTS/CdS films were placed in a ThermoScientific Lindberg Blue M Tube Furnace (Asheville, NC) with a specially designed quartz tube to provide an inert Ar atmosphere for annealing. The tube was purged three times, evacuating via vacuum pump to below -200 kPa to ensure oxygen removal. The tube was refilled with Ar at 70 kPa after each purge. The temperature was raised to 250 °C at a rate of 25 °C/min, and films were annealed at 250 °C for 50 minutes. At the conclusion of the process, the furnace was opened and the tube raised above the heating bed to allow natural cooling to room temperature. The tube was purged once more prior to opening.

5.2.2 Characterization

Photoelectrochemical measurements (PECMs) were carried out to access the light absorbing film quality,^{7, 13, 30-31} as described in Chapter 1.4.1. Defects are indicated by Kröger-Vink notation, as described in Chapter 3.3.1.

EXAFS measurements of the Cu, Zn, Sn and Cd K-edges were performed at the CLS@APS 20-BM beamline at the Advanced Photon Source (APS) at the Argonne National Laboratory in Argonne, IL. CZTS and CZTS-CdS films were capped by Kapton tape, and the beam was in focus mode. A Si (111) monochromator and a 400 μm vertical slit was used over 8.78 to 9.52 keV for the Cu K-edge, 9.46 to 10.4 keV for the Zn K-edge, and 29.004 to 30.069 keV for the Sn K-edge. A vertical slit of 1,500 μm was used over 26.537 to 27.550 keV for the Cd K-edge to account for the size difference. The samples were placed at a 45° angle with respect to the incident photons, which were perpendicular to the 13-element Canberra detector. The maximum count rate for each element of the detector was set at 50,000 counts per second, and all scans were replicated to achieve a sum of two million total counts per element for each metal center in CZTS, and one million total counts for the Cd center. All spectra were normalized to the incident photon flux, I_o , and calibrated against a reference foil (EXAFS Materials Inc.). The Cu foil was 7.5 μm thick, the Zn foil was 10 μm , and the Sn foil was 50 μm . Cd was calibrated relative to the Sn foil.

Data was treated using the software packages Athena and Artemis. Fluorescence yield was plotted over a corrected energy range, defined as $\mu(E)$, in which the pre-edge is normalized to zero, and the post-edge to unity.³²⁻³³ The threshold energies, E_0 , were set to 8,979 eV for the Cu K-edge, 9,659 eV for the Zn K-edge, 29,200 eV for the Sn K-edge, and 26,711 for the Cd K-edge. The EXAFS data was transformed into the photoelectron momentum vector k space. To compensate for oscillatory decay, and due to the presence of heavier atoms contributing to this decay, a cubic k -weighting was employed.³³⁻³⁶ A Fourier transform was applied using a Hanning window over a k -range from 3 to 11 \AA^{-1} , to produce the R-space radial distance spectrum plot. This plot has been displayed without phase correction, and was aligned using the Artemis software package and fit using a FEFF modeling package, according to the standard practices

outlined in literature.³⁷⁻³⁸ These fittings were made to match measured spectra with that of the pure kesterite CZTS model, as calculated from the crystallographic information file (cif) generated from VESTA and crystallographic structure of CZTS (JCPDS 26-0575) at room temperature.³⁹ These Fourier transformed fittings allowed for quantification of the bond distances seen in the experimental EXAFS.³⁸ The additional peak seen in the Zn spectrum in R-space (see Figure 5.3 below) was fit by addition of a single scattering path (SSP) to the expected paths within the kesterite CZTS structure.^{32, 40} This SSP was initially based on a Zn-O bond, having a shorter distance than that of a Zn-S bond in the normal kesterite parameters. The E_0 and amplitude reduction factor associated with the SSP were set to be identical for all scattering pathways in the structure.^{32, 40} The bond length was determined from the fit. The origin of the Zn-O bond was then confirmed through IR study using a Perkin Elmer Spectrum Two ATR FT-IR-spectrometer.

5.3 Results and Discussion

5.3.1 Photoelectrochemical Measurements

Photoresponse is one of the key metrics used to evaluate the effectiveness of the CZTS and CZTS-CdS films. In the presence of light, rapid increases in charge-carrier flow occur within the CZTS film, which can be readily scavenged by MV^{2+} in solution and measured electrochemically.⁷ Ideal device fabrication would yield greater charge-carrier flow with the addition of each subsequent layer; however, the introduction of defects and distortions to the lattice within the films, and at the interface between films, often yield charge-carrier traps that result in recombination of charges.⁴²⁻⁴⁴ This detrimentally impacts the device performance. Within the CZTS-based device, this is most commonly seen at the CZTS-CdS heterojunction, but the effects can often be mitigated through post-processing steps.^{8, 43}

The CdS buffer layer acts to protect the CZTS from subsequent processing steps, while its lattice-matching properties facilitate the electron transfer from CZTS into an n-type semiconductor layer.^{1, 45} Figure 5.1 illustrates the PECM response change on addition of the CdS layer, and the effectiveness of annealing as a post processing treatment for our films.

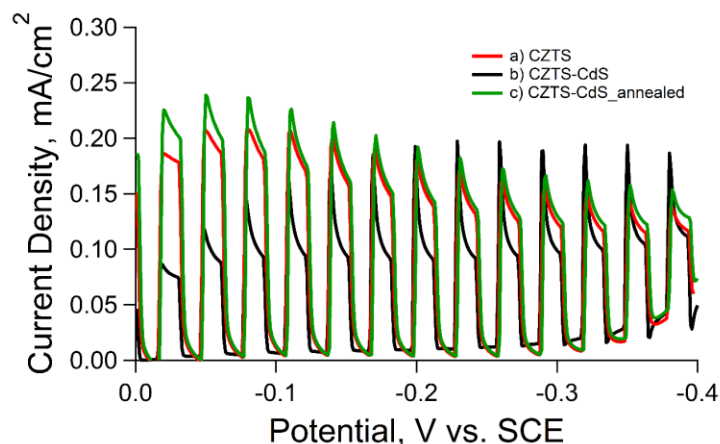


Figure 5.1 PECM result for the CZTS film, and effects of CdS addition, with and without post-processing. Left untreated, addition of CdS layer reduces current density, particularly at low negative potentials, and shows increased recombination, as seen through the sharp decrease in photoresponse following initial excitation. Post-processing via annealing restores previous current densities.

An example of PECM results from CZTS, CZTS-CdS, and low temperature annealed CZTS-CdS films has been shown in Figure 5.1. Under initial illumination, the CZTS film (trace a in Figure 5.1) shows sharp increases in current density, as a result of the transfer of electrons from the film to the MV^{2+} , reducing it to MV^+ . At this point, decay in the current density is noted as a result of recombination at the film surface. This is seen as the sloped decrease following the initial photoresponse. On removal of the light stimulus, the production of charge-carriers ceases, and the current density drops down. The effect is not instantaneous, however, as a small dark current persists for a short time after the stimulus is removed, as MV^{2+} reduction continues to be favored over recombination. It should also be noted that the current density in the dark begins to increase at -0.3 V, consistent with a shift from a rectifying (Schottky) junction to a non-rectifying (Ohmic) junction.⁴⁶⁻⁴⁸ Charges begin to flow freely through the film at this point, known as the breakdown voltage, explaining the decline observed in the photoresponse at potentials more negative than -0.3 V.

Upon addition of the CdS layer to form a CZTS-CdS heterojunction (trace b in Figure 5.1), the initial photoresponse is muted in comparison to the CZTS film. The possible

introduction of traps at the interface, and the energetic difference between the conduction band of the two materials, often described as a cliff-configuration,⁴⁹⁻⁵⁰ results in a recombination of the photoexcited electrons within the film, preventing them from interfacing with MV^{2+} and thus reducing the observed photoresponse. The presence of these traps and recombination sites at higher negative potentials are confirmed by both the increased steepness in the photocurrent decay, and by the presence of an overshoot – noted by the downwards spike at the initiation of the dark segments.⁵¹ This occurrence can be compared to the PECM of the CZTS film. At the initiation of the dark phase, the negative overshoot shows recombination is now favored over continued MV^{2+} reduction. It is this issue that necessitates post-processing steps to remove traps, and restore the desired separation of charge-carriers to yield high current densities.

Annealing the CZTS-CdS film at 250 °C (trace c in Figure 5.1) eliminates the negative overshoot and restores the photoresponse of the film to pre-CdS levels. Up to the breakdown voltage at -0.3 V, where the dark current begins increasing and the photocurrent decreasing, the photoresponse remains high at rates equivalent to that of the CZTS film. This suggests the removal of charge-carrier traps from the heterojunction in the annealing step, enabling a more fluid transition of electrons across the interface. This implies that the annealing step is necessary for the facilitation of efficient charge-carrier diffusion through the films, yet runs counter to the goal of producing CZTS photovoltaic devices at low-cost. This demands the determination of the identity of the traps, and exploration as to their removal without the need for long-duration, high temperature post-processes.

5.3.2 XANES Analysis

Synchrotron radiation is a powerful technique for probing subtle differences in the local and extended structure of the films. In particular, the various regions of XAFS allow focus on the immediate chemical environment, and the extended, more complex interactions of the metal centers within the film.^{34-35, 37, 40, 52-53} Each metal center in both the CZTS and the CZTS-CdS films are expected to be directly bound to sulfur atoms only, which would reduce a complex structure into individual, local-area interactions between the metal centers and their neighboring sulfur atoms. Based on literature, these

interactions would be expected to produce a single strong peak in the XANES near-edge region.⁵² The XANES spectra for each metal center of the three samples have been presented in Figure 5.2.

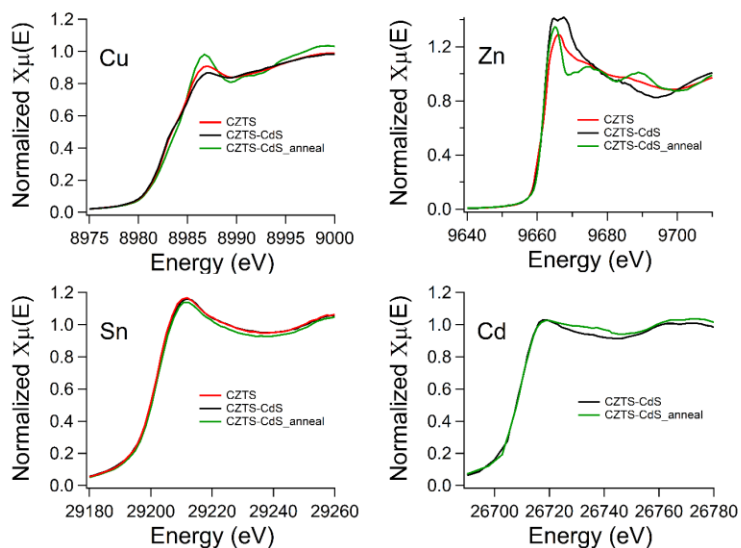


Figure 5.2 Metal K-edge XANES for each of the metal centers found in CZTS and CZTS-CdS films. Crystal structure as denoted by the change in immediate post-edge oscillations shows Zn center to be especially vulnerable to deformations caused by CdS addition. Annealing creates more distinct oscillations at the Cu and Zn centers. Note the absence of a Cd spectrum for the CZTS film.

Each of the four metal centers, Cu, Zn, Sn, and Cd, have been examined at the K-edge for each of the films, with interpretations built on past analyses of the CZTS layer.

Beginning at the Cu K-edge (Figure 5.2 Cu), there appears to be an effect of CdS addition on the Cu site. The peak at 8,986 eV is broadened and reduced in intensity following CdS deposition, and then sharpened following annealing. Following annealing, the peak is seen to be even sharper than that of just the CZTS layer, indicating the annealing process is enhancing the crystallinity in CZTS. Increasing intensity of the main peak is the direct result of stronger absorption, which arises due to increased uniformity among the atomic orbitals involved. The corresponding rising-edge structure is likely confirming the Cu atoms are bound to four S atoms in a tetrahedral manner.^{34, 38, 52, 54} This observation, couple with the lack of pre-edge features confirms the lack of Cu²⁺

within the films, which precludes major disruptions and electron trapping barriers associated with Cu^{2+} phases within the cell, and ensures the lack of excessive distortion from the expected tetrahedral geometry.^{52,55} The main peak can then be interpreted independent of orbital mixing, or the effects of oxidation change about the metal center.⁵⁵⁻⁵⁶ The edge structure suggests strong Cu^+ presence in the Cu centers of the film in both the CZTS and CZTS-CdS films, despite the likely increase to the overall disorder in the CZTS symmetry following CBD of CdS, seen as a decrease in the Cu main peak intensity following CdS deposition in Figure 5.2. Antisites between the Cu and Zn atoms in the lattice, at non-regular intervals, easily account for some of these observation, though they should appear to be conserved through CBD.^{52,57} The increased disorder would thus have to be attributed to some other structural alteration. After annealing, the rising-edge structure mostly disappears, with a much less visible remnant of the peak. The annealing step is therefore likely creating an association between the CdS layer and the CZTS layer through the shared sulfur atoms, weakening the measured ligand strength. This could be the result of electron back-donation from the S atoms into the CdS layer, creating partially depleted strength in the Cu-S bonds, or it could be simply creating a less tightly bound 4p level due to the added electron density around Cd. We still do not see any of the characteristic pre-edge structure at 8,979 eV, that would be associated with a Cu^{2+} site.¹⁸ The spectrum of the CZTS-CdS film after annealing suggests the Cu^+ site remains, but with a much more intense absorption, and thus more uniform film. This is consistent with the post-edge region, where we see more clearly defined states at the Cu site following annealing. The increased uniformity would result in less contribution of local effects to the measured PECMs. In addition, a small shift to lower energy in the principle peak in the post-edge can be seen in the annealed sample, which indicates that some electron density is being lost from the site. The lack of change from CZTS to CZTS-CdS implies that CdS deposition does not alter the Cu sites, which in turn are not likely contributing to the drastic decrease in photoresponse seen in Figure 5.1. To the contrary, Cu data would suggest the annealed sample should show increased photoresponse relative to the CZTS, and CZTS-CdS films due to uniformity, though a slight decrease in the p-type nature of the CZTS near and at the interface.

At the Zn K-edge, the changes in the spectra become far more distinct (Figure 5.2 Zn). In all three cases, the edge is devoid of any changes. This observation is in contrast to what was observed in the Cu spectra, where we see the small shoulder peak in the edge structure decrease in prominence after annealing. We also observe a change in the near-edge peak as a result of CdS addition. In the as-deposited films, there is a single peak at the edge. The Zn XANES has clearly changed with the addition of CdS, where there are now 2 peaks, and is no longer consistent with literature for CZTS.¹² Such a change could be the result of changes in the Zn-S bonding, and thus changes in the associated unoccupied p-states; however, such a case would not manifest as different neighbors in the EXAFS, as is the case with these samples.^{34, 58-60} The addition of the CdS layer should not change the Zn interactions in the XANES region, given that the only nucleophilic component in either layer is sulfur. This means that these observed changes in the XANES are most likely the result of changes in the local environment. As such, the double peak in the sample with CdS is indicative of non-consistent local Zn environments throughout the film, and a deviation from the normal Zn K-edge spectra reported in literature for CZTS.^{37-38, 61} The additional peak in the CZTS-CdS film is therefore most likely a source of charge-carrier trap development predicted in Figure 5.1. After annealing the film, the XANES spectrum returns to the expected single peak at the edge. Both the as-deposited CZTS, and the annealed sample, are consistent with literature.⁵² Furthermore, the annealing process leads to a higher number of oscillations in the post-edge. This means that the effects from more distant neighbors are more visible in the annealed films, which is consistent with a loss of disorder in that film, and matches well with the observations made in the Cu XANES.

The Sn XANES (Figure 5.2 Sn) shows almost no deviation among the three samples, lacking any pre-edge structure, and maintaining oscillatory congruency from CZTS through CdS addition, and annealing. The annealed sample does potentially show a small shift to lower energy, remaining consistent with the previously mentioned possible sulfur loss; however, the shift is extremely small, and could be nothing. This is the only center that does not show additional oscillations on annealing, suggesting that the Sn site is highly conserved throughout the fabrication process, and likely is not contributing to the observed changes in photocurrent; however, the core-hole broadening at this high energy

would obscure any minor changes.^{33, 37-38} Thus, we can conclude that the Sn sites are conserved beyond the minor deviations noted at the Cu and Zn edges.

The Cd XANES (Figure 5.2 Cd) has some additional noise in the spectra, due to the small thickness of the CdS film (50 nm) relative to the micron-thick CZTS, but is clearly well conserved within the pre-edge and edge regions. The annealing of the film appears to have a similar effect as on the CZTS-based metal centers, with an increase in order manifesting in the dampening of the post-edge oscillations due to multiscattering resonances. The cause of this could be attributed to the removal of surface states in the film, or improved overlap between films at the CZTS-CdS interface.^{1, 27, 62} This may contribute to the photocurrent changes via the removal surface-state trapping, and could be contributing to the observed photoresponse increase post-annealing.

5.3.3 EXAFS Analysis

Based on the observations within the XANES regions, it is clear that during the addition of CdS, the deposition procedure fundamentally changes the local environment for the metals within CZTS film, especially at the Zn sites. Through annealing, some of the effects can be removed, but the process has been shown to not simply return the CZTS electron structure to that of the pre-CdS film. The local deviations in electron density and subsequent changes in site-specific electron structure will therefore likely manifest in long-range structure and bond length changes that would primarily affect the photoresponse, manifesting in the PECMs. Through EXAFS, this can be explored in detail to identify the effects of the previously noted interactions on the overall film structure. The R-space profile, which corresponds to the magnitude of the Fourier Transform (FT) of the EXAFS data for each film at each metal center has been shown in Figure 5.3.

Examination of the Cu EXAFS data (Figure 5.3 Cu) shows a highly conserved first radial distance. This is seen as a single high peak in all spectra within Figure 5.3, and corresponds with the principle Cu-S bond expected for CZTS. Given the Cu-S bond is maintained throughout the film manufacturing process, which is the confirmation that the CZTS films are consistent, and that the CZTS is devoid of secondary phases in each step.

These agree well with previously determined ideal situations presented in literature.^{52, 60, 63-64} In both a) and b), the peak is relatively broad, showing a long leading edge. This is not present in the annealed film c). From the XANES (Figure 5.2 Cu), we know that annealing confers an added level of order to the film. This would then increase long-range order and manifest itself in narrower, more defined peaks within the XANES spectra. Within the context of the Cu XANES (Figure 5.2 Cu), we can conclude that the source of the deviation is long-range order contributing to a more congruent film and increased electron sharing throughout the film as opposed to short-range defects, and thus not likely contributing to the trapping of charge-carriers.

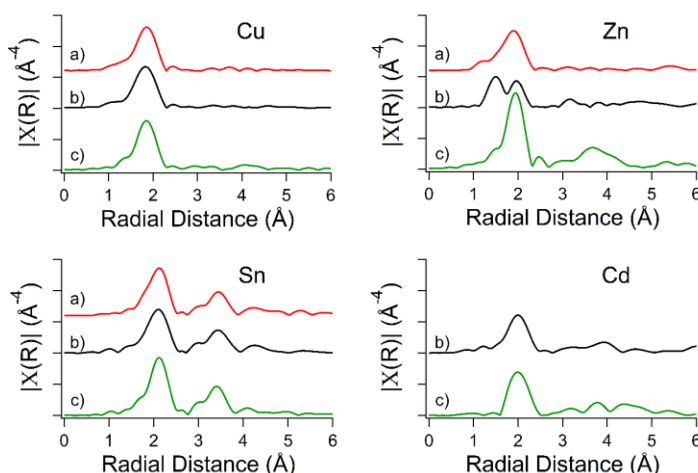


Figure 5.3 The magnitude of the EXAFS data FT for the Cu, Zn, Sn, and Cd metal sites in a CZTS film (trace a), a CZTS-CdS film (trace b), and an annealed CZTS-CdS film (trace c).

The Zn EXAFS data (Figure 5.3 Zn) has a much greater significance. As was the case in the XANES spectrum, (Figure 5.2 Zn), the introduction of the CdS layer yields the formation of a secondary bond to the Zn atoms. The second peak is consistent with the Zn-S peak seen in both the CZTS (trace a in Figure 5.3 Zn) and annealed (trace b in Figure 5.33 Zn) films at around 2 Å. Given that the other Zn-nearest neighbor is shorter (~ 1.5 Å), it is almost certainly due to the presence of a low Z atom, most likely oxygen, coordinating to the Zn center at some point during the CdS deposition. This neighboring atom is removed during the annealing step, which confirms what was seen via XANES

and PECMs, and is the mostly likely candidate to be contributing to the decreased charge carrier flow identified in the CZTS-CdS film (trace b in Figure 5.1). It should be noted that the peak heights, though both significant contributors to the overall structure, should not be directly compared in the radial distance plots. These are caused by scattering centers with different Z , which tells the attenuation and effect of k -weighting in combination with thermal and defect effects in their contribution to the peak height. Removal of the low Z atom during the annealing process is also confirmed, with the spectrum (trace c Figure 5.3 Zn) showing the complete removal of the peak at 1.5 Å. The annealing also confers improved local order at the Zn site. This is seen in both the narrower peak at 2 Å, and the emergence of peaks at higher distances, an indicative of complex scattering via second and third nearest neighbors.¹² As was the case with XANES, the increased homogeneity as a result of thermal annealing appears to be primarily about the Cu and Zn centers.

The Sn EXAFS (Figure 5.3 Sn) shows the effects of improved order in the 2 – 4 Å region subtler than the Cu and Zn centers. The peak corresponding to the first nearest neighbor appears to be narrower, and better defined, suggesting less disorder is present at the Sn sites. This phenomenon is also observed in the peaks corresponding to the second nearest neighbors. The narrower peaks in both first and second nearest neighbors further confirm the presence of reduced disorder within the annealed (trace c in Figure 5.3) samples. The fact that these peaks in the second neighbor position can be compared from CZTS through CdS deposition and annealing further confirms the previous assertion that Sn sites remain consistent throughout the process.

The FT peaks in the Cd EXAFS also appear larger post-annealing (Figure 5.3 Cd), suggesting the observed broadening of the XANES signal correctly analyzed, and there is increased order within the post-annealed film. This would result in fewer charge-carrier traps in bulk CdS, and reduce surface states. This would likely contribute to a more ideal overlap and improved charge-carrier passage due to the improved interaction between the Cd metal center and the CZTS layer.

5.3.4 Identification of the Short Zn-Nearest Neighbor Bond

From the XANES and EXAFS data, it is clear that the addition of the CdS layer has the potential to introduce structure to the heterojunction at the Zn sites within the CZTS film. Fittings of the Cu, Sn, and Cd spectra show no statistically significant deviation in the first nearest neighbor – that is, the first metal-sulfur bond – as predicted in past XANES and EXAFS analyses.⁶⁵ There was significant change in the Zn spectra. By fitting the Zn spectrum of the CZTS-CdS sample (trace b in Figure 5.3 Zn), the peak identities can be determined, as seen in Figure 5.4.

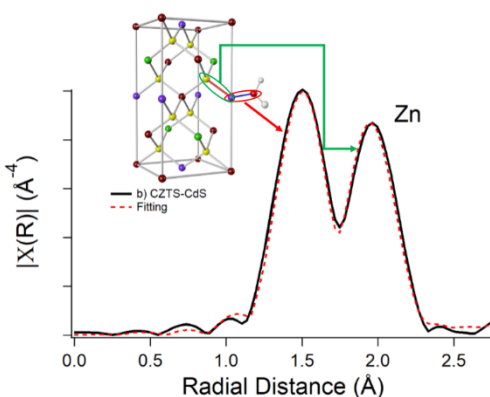


Figure 5.4 Fitting of the first shell Zn EXAFS. The curve was based on the FEFF fit of the CZTS kesterite crystal. The extra scattering pathway was added to account for the first major peak which is of a low Z atom origin.

The fitting parameters for Figure 5.4 for the Zn-S peak were: $e_0 = 1.8 \pm 1.6$ eV, $r = 2.333 \pm 0.016$ Å, $S_0^2 = 0.90 \pm 0.07$, and $\sigma^2 = 0.013 \pm 0.004$ Å², and CN = 3.9 ± 0.3 . For the Zn-low Z atom bond, $e_0 = 1.8 \pm 1.6$ eV, $r = 2.012 \pm 0.030$ Å, $S_0^2 = 0.90 \pm 0.07$, and $\sigma^2 = 0.009 \pm 0.002$ Å², and CN = 1.9 ± 0.5 . The proposed structure is shown, with the corresponding bonds identified.

The fitting of the first shell of the Zn EXAFS from the CZTS-CdS film (trace b Figure 5.3 Zn) shows very reasonable with two separate scattering pathways. The first peak, Zn coordinating with an interstitial, is the peak introduced during the CdS deposition, while the second peak is the expected Zn-S bond found in CZTS. In each case, the e_0 values represent the deviation between the energy grids of the data and the fits. Large values of

e_0 would represent a poorly chosen edge step energy or model. In both bonds, these were small, confirming the edge-step energy from the XANES spectrum (trace b Figure 5.2 Zn). The Δr values represent the adjustments to the interatomic distance required to make the fit work, and are relative to the theoretically perfect CZTS model. The small uncertainty values for the r values are an indication that the bond distances are consistent with the model. The σ^2 is consistent and reasonably small, at around 0.01 for each peak. The σ^2 variable contains the static and thermal disorder parameters, so a larger value would indicate a major deviation from the experimental work. The S_0^2 value represents the amplitude reduction parameter due to the many-electron effect. It is acceptable at values near 1.0, and is maintained for each species via chemical transferability. It should be noted though that the fitting requires a single amplitude reduction factor for each of the two peaks, making them congruent forms of each other. Thus, coordination number, CN, can be determined from the refined amplitude parameter, $CN \cdot S_0^2$. Peak heights should thus not be taken as being of equal contribution to the overall structure. From this, the bond lengths can be compared, to provide a reasonable estimate as to the identity of the introduced species. The Zn-S bond is calculated to be 2.333 Å, consistent with literature values of 2.334 Å, and shows a coordination number of about 4.^{64,66} The smaller Zn bond is measured relative to this, and is 2.012 Å, with a coordination number of about 2. This radial distance is typical of Zn-O and Zn-OH₂ bond lengths, which are 1.95 Å and 2.08 Å respectively.⁶⁷⁻⁶⁹ These bonds are very possible to form since the CdS is grown on the CZTS film in an aqueous medium.⁴⁻⁵ In fact, during CBD, CdSO₄ becomes adsorbed to the CZTS via sulfur on the Zn center, followed by ligand substitution of SO₄²⁻ with 2OH⁻ on Cd. It is then probably to form a metastable dihydroxothiurea-cadmium complex, before rearrangement to CdS. It is easily conceived that the OH⁻ or H₂O presence could be coordinating to the Zn center during the formation of the metastable complex, whereby it becomes trapped as the CdS layer forms.

5.3.5 IR-Spectroscopy

To confirm the presence of water, IR analysis was carried out on each of the three films, shown in Figure 5.5.

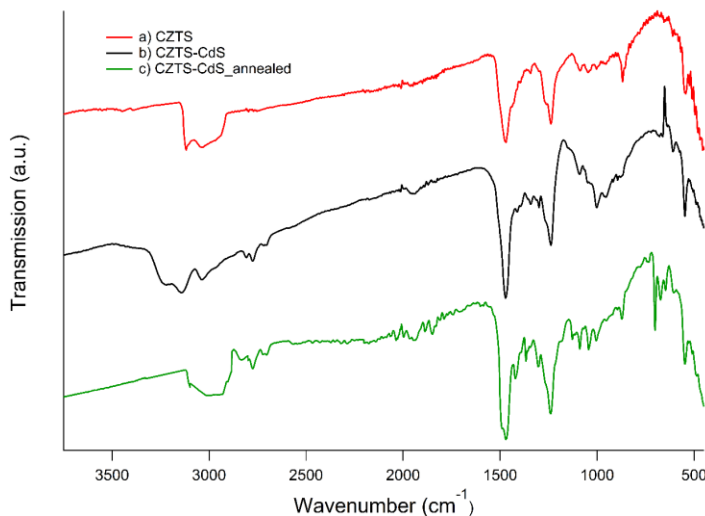


Figure 5.5 IR spectra for as-deposited CZTS (red), CZTS-CdS (black), and annealed CZTS-CdS (green).

The CZTS-CdS film shows a broad stretch above $3,000\text{ cm}^{-1}$, consistent with the presence of $\text{OH}^- / \text{H}_2\text{O}$. This broad stretch is lacking in both the CZTS and the annealed CZTS sample, indicating that there is only a water presence in the unannealed CZTS-CdS film. When taken in conjunction with the EXAFS fit (Figure 5.4), the presence of $\text{OH}^- / \text{H}_2\text{O}$ within the heterojunction can be confirmed. With regards to the observed PECMs, it is likely that the $\text{OH}^- / \text{H}_2\text{O}$ presence is functioning as a local charge-carrier trap within the heterojunction following CdS deposition, and hindering the photoresponse. We also note a broadening around the $1,000\text{ cm}^{-1}$ region, which often corresponds with oxygen bonds to other atoms. This peak is also reduced following annealing, bringing it back in similar line with the peak seen previously in CZTS pre-CBD of CdS. This further corroborates the notion that water has been integrated into the structure before annealing.

5.4 Conclusion

The CZTS/CdS heterojunction was explored through the use of photoelectrochemistry and X-ray absorption spectroscopy. It was determined that the addition of CdS through CBD reduced the photocurrent produced through the cathodic reduction of methyl viologen upon illumination. The Zn K-edge reveals a change in local environment and indicates a shortened bond formation with the Zn, from which the coordination atom is

judged to have lower atomic number (lower-Z) than S in CZTS. The decomposition of a cadmium metastable complex in the growth mechanism for CdS is most likely a cause for the coordination of water to zinc in CZTS. The PECMs indicate the localized effect, as the photoresponse is diminished, but is nowhere near eliminated. Furthermore, it was discovered that the intensity of the Zn-O bond is nearly identical to that of Zn-S. Equivalent intensities suggest a great depth of the Zn-O bond formation in the CZTS bulk. This fact is due to loose packing among the NCs, allowing for deep penetration of the water into the film. The less than perfect overlap of the NCs affords a deeper water penetration depth than surface-based only reactions. The use of annealing after the addition of CdS recovers the photoresponse and optimizes the local and extended structures of the CZTS at temperatures as low as 250 °C. Annealing allows for the elimination of negative effects with the addition of the CdS layer at a photoelectrochemical and physical level with the return of the local ordered structure as well as photocurrent. This is particularly visible in the narrowing of the Cu and Zn first nearest neighbor peaks in the EXAFS spectra. Annealing after the addition of CdS reduces the number of surface states and traps, increases the long range order, and allows for effective electron transfer across interfaces. This could ultimately allow for a potential photovoltaic device more efficient and long-lasting.

5.5 References

1. Courel, M.; Andrade-Arvizu, J. A.; Vigil-Galan, O., *Solid State Electron.* **2015**, *111*, 243.
2. Sim, H.; Lee, J.; Cho, S.; Cho, E. S.; Kwon, S. J., *J. Semicond. Tech. Sci.* **2015**, *15*, 267.
3. Morkel, M.; Weinhardt, L.; Lohmüller, B.; Heske, C.; Umbach, E.; Riedl, W.; Zweigart, S.; Karg, F., *Appl. Phys. Lett.* **2001**, *79*, 4482.
4. O'Brien, P.; McAleese, J., *J. Mater. Chem.* **1998**, *8*, 2309.
5. Mugdur, P. H.; Chang, Y. J.; Han, S. Y.; Su, Y. W.; Morrone, A. A.; Ryu, S. O.; Lee, T. J.; Chang, C. H., *J. Electrochem. Soc.* **2007**, *154*, D482.
6. Voss, C.; Chang, Y. J.; Subramanian, S.; Ryu, S. O.; Lee, T. J.; Chang, C. H., *J. Electrochem. Soc.* **2004**, *151*, C655.
7. Ye, H.; Park, H. S.; Ajhavan, V. A.; Goodfellow, B. W.; Panthani, M. G.; Korgel, B. A.; Bard, A. J., *J. Phys. Chem. C* **2011**, *115*, 234.

8. Tapley, A.; Hart, C.; Vaccarello, D.; Love, D. A.; Ding, Z., *J. Electrochem. Soc.* **2014**, *161*, H725.
9. Bär, M.; Schubert, B. A.; Marsen, B.; Wilks, R. G.; Pookpanratana, S.; Blum, M.; Krause, S.; Unold, T.; Yang, W.; Weinhardt, L.; Heske, C.; Schock, H. W., *Appl. Phys. Lett.* **2011**, *99*, 222105.
10. Ji, S.; Shi, T.; Qiu, X.; Zhang, J.; Xu, G.; Chen, C.; Jiang, Z.; Ye, C., *Sci. Rep.* **2013**, *3*, 2733.
11. Toyama, T.; Konishi, T.; Tsuji, R.; Maenishi, R.; Arata, A.; Yodate, S.; Shirakata, S., *Phys. Status Solidi C* **2015**, *12*, 721.
12. Hartman, K.; Newman, B. K.; Johnson, J. L.; Du, H.; Fernandes, P. A.; Chawla, V.; Bolin, T.; Clemens, B. M.; Cunha, A. F.; Teeter, G.; Scarpulla, M. A.; Buonassisi, T. In *Detection of ZnS Phases in CZTS Thin Films by EXAFS*, Photovoltaic Specialists Conference (PVSC), Seattle, WA, IEEE, Ed. IEEE: Seattle, WA, 2011.
13. Vaccarello, D.; Tapley, A.; Ding, Z., *RSC Adv.* **2013**, *3*, 3512.
14. Vayssieres, L.; Sathe, C.; Butorin, S. M.; Shuh, D. K.; Nordgren, J.; Guo, J., *Adv. Mater.* **2005**, *17*, 2320.
15. Petty, J. T.; Sergeev, O. O.; Ganguly, M.; Rankine, I. J.; Chevrier, D. M.; Zhang, P., *J. Am. Chem. Soc.* **2016**, *138*, 3469.
16. Saravanan, K.; Kao, C. H.; Shao, Y. C.; Wang, Y. F.; Wang, B. Y.; Wang, H. T.; Tsai, C. J.; Lin, W. C.; Pao, C. W.; Tsai, H. M.; Jang, L. Y.; Lin, H. J.; Lee, J. F.; Pong, W. F., *RSC Adv.* **2015**, *5*, 19014.
17. Just, J.; Lützenkirchen-Hecht, D.; Frahm, R.; Schorr, S.; Unold, T., *Appl. Phys. Lett.* **2011**, *99*, 262105.
18. Di Benedetto, F.; d'Acapito, F.; Bencistà, I.; Luca, A. D.; Fornaciai, G.; Frizzera, S.; Innocenti, M.; Montegrossi, G.; Pardi, L. A.; Romanelli, M., *Phys. Status Solidi C* **2013**, *10*, 1055.
19. Di Benedetto, F.; Cinotti, S.; Guerri, A.; De Luca, A.; Lavacchi, A.; Montegrossi, G.; Carla, F.; Felici, R.; Innocenti, M., *ECS Trans.* **2013**, *58*, 59.
20. Mendis, B. G.; Shannon, M. D.; Goodman, M. C. J.; Major, J. D.; Claridge, R.; Halliday, D. P.; Durose, K., *Prog. Photovoltaics* **2014**, *22*, 24.
21. Lee, K. E.; Shivhare, A.; Hu, Y.; Scott, R. W. J., *Catal. Today* **2017**, *280*, 259.
22. Nassiri, H.; Lee, K. E.; Hu, Y.; Hayes, R. E.; Scott, R. W.; Semagina, N., *ChemPhysChem* **2017**, *18*, 238.
23. Chambers, S. A.; Droubay, T. C.; Kaspar, T. C.; Nayyar, I. H.; McBriarty, M. E.; Heald, S. M.; Keavney, D. J.; Bowden, M. E.; Sushko, P. V., *Adv. Funct. Mater.* **2017**, *27*, 1605040.
24. Kaspar, T. C.; Sushko, P. V.; Bowden, M. E.; Heald, S. M.; Papadogianni, A.; Tschammer, C.; Bierwagen, O.; Chambers, S. A., *Phys. Rev. B* **2016**, *94*, 155409.

25. Vaccarello, D.; Liu, L. J.; Zhou, J. G.; Sham, T. K.; Ding, Z. F., *J. Phys. Chem. C* **2015**, *119*, 11922.
26. Tapley, A.; Liu, L.; Cui, X.; Zuin, L.; Love, D. A.; Zhou, J.; Sham, T.-K.; Ding, Z., *J. Phys. Chem. C* **2015**, *119*, 20967.
27. Schwartz, C.; Nordlund, D.; Weng, T.-C.; Sokaras, D.; Mansfield, L.; Krishnapriyan, A. S.; Ramanathan, K.; Hurst, K. E.; Prendergast, D.; Christensen, S. T., *Sol. Energ. Mat. Sol. Cells* **2016**, *149*, 275.
28. Murali, K. R.; Thilagavathy, K.; Vasantha, S.; Gopalakrishnan, P.; Rachel Oommen, P., *Sol. Energy* **2010**, *84*, 722.
29. Perini, L.; Vaccarello, D.; Martin, S.; Jeffs, K.; Ding, Z., *J. Electrochem. Soc.* **2016**, *163*, H3110.
30. Turnbull, M. J.; Khoshmashrab, S.; Wang, Z.; Harbottle, R.; Sham, T.-K.; Ding, Z., *Catal. Today* **2016**, *260*, 119.
31. Khoshmashrab, S.; Turnbull, M. J.; Vaccarello, D.; Nie, Y.; Martin, S.; Love, D. A.; Lau, P. K.; Sun, X.; Ding, Z., *Electrochim. Acta* **2015**, *162*, 176.
32. Ravel, B.; Newville, M., *J. Synchrotron Radiat.* **2005**, *12*, 537.
33. Newville, M., *Rev. Mineral. Geochem.* **2014**, *78*, 33.
34. Teo, B. K., *EXAFS: Basic Principles and Data Analysis*; Springer: Berlin, 1986; Vol. 9.
35. Teo, B. K.; Joy, D. C., *EXAFS Spectroscopy: Techniques and Applications*; Plenum Press: New York, 1981.
36. Koningsberger, D. C.; Prins, R., *X-Ray Absorption: Principles, Applications, Techniques of EXAFS, SEXAFS, and XANES*; Blackwell: Eindhoven, The Netherlands, 1988.
37. Zhang, P., *J. Phys. Chem. C* **2014**, *118*, 25291.
38. Chevrier, D. M.; Yang, R.; Chatt, A.; Zhang, P., *Nanotechnology Reviews* **2015**, *4*, 193.
39. Momma, K.; Izumi, F., *J. Appl. Crystallogr.* **2011**, *44*, 1272.
40. Ravel, B., *J. Synchrotron Radiat.* **2015**, *22*, 1258.
41. Scragg, J. J.; Dale, P. J.; Peter, L. M.; Zoppi, G.; Forbes, I., *Phys. Status Solidi C.* **2008**, *245*, 1772.
42. Mitzi, D. B.; Gunawan, O.; Todorov, T. K.; Wang, K.; Guha, S., *Sol. Energ. Mat. Sol. Cells* **2011**, *95*, 1421.
43. Katagiri, H.; Jimbo, K.; Maw, W. S.; Oishi, K.; Yamazaki, M.; Araki, H.; Takeuchi, A., *Thin Solid Films* **2009**, *517*, 2455.
44. Muhunthan, N.; Singh, O. P.; Thakur, M. K.; Karthikeyan, P.; Singh, D.; Saravanan, M.; Singh, V. N., *J. Sol. Energy* **2014**, *2014*, 1.

45. Liang, S.; Sheng, H.; Liu, Y.; Huo, Z.; Lu, Y.; Shen, H., *J. Cryst. Growth* **2001**, *225*, 110.
46. Saha, S. K.; Guchhait, A.; Pal, A. J., *Phys. Chem. Chem. Phys.* **2012**, *14*, 8090.
47. McDonnell, S.; Addou, R.; Buie, C.; Wallace, R. M.; Hinkle, C. L., *ACS Nano* **2014**, *8*, 2880.
48. Polizzotti, A.; Repins, I. L.; Noufi, R.; Wei, S.-H.; Mitzi, D. B., *Energy Environ. Sci.* **2013**, *6*, 3171.
49. Siebentritt, S., *Thin Solid Films* **2013**, *535*, 1.
50. Fermin, D. J.; Duong, H. D.; Ding, Z.; Brevet, P. F.; Girault, H. H., *Phys. Chem. Chem. Phys.* **1999**, *1*, 1461.
51. Colina-Ruiz, R. A.; Mustre de Leon, J.; Lezama-Pacheco, J. S.; Caballero-Briones, F.; Acosta-Alejandro, M.; Espinosa-Faller, F. J., *J. Alloys Compd.* **2017**, *714*, 381.
52. Winick, H.; Doniach, S., *Synchrotron Radiation Research*; Plenum Press: New York, 1980, p 743.
53. Gaur, A.; Shrivastava, B. D.; Joshi, S. K., *J. Phys. Conf. Ser.* **2009**, *190*, 012084.
54. DeBeer George, S.; Basumallick, L.; Szilagy, R. K.; Randall, D. W.; Hill, M. G.; Nersissian, A. M.; Valentine, J. S.; Hedman, B.; Hodgson, K. O.; Solomon, E. I., *J. Am. Chem. Soc.* **2003**, *125*, 11314.
55. Getty, K.; Delgado-Jaime, M. U.; Kennepohl, P., *Inorg. Chim. Acta* **2008**, *361*, 1059.
56. Chen, S.; Tao, H.; Shen, Y.; Zhu, L.; Zeng, X.; Tao, J.; Wang, T., *RSC Adv.* **2015**, *5*, 6682.
57. Garino, C.; Borfecchia, E.; Gobetto, R.; van Bokhoven, J. A.; Lamberti, C., *Coord. Chem. Rev.* **2014**, *277-278*, 130.
58. Erslev, P. T.; Young, M. R.; Li, J. V.; Siah, S. C.; Chakraborty, R.; Du, H.; Lad, R. J.; Buonassisi, T.; Teeter, G., *Sol. Energy Mater. Sol. Cells* **2014**, *129*, 124.
59. Siah, S. C.; Jaramillo, R.; Chakraborty, R.; Erslev, P. T.; Sun, C. J.; Weng, T. C.; Toney, M. F.; Teeter, G.; Buonassisi, T., *IEEE J. Photovolt.* **2015**, *5*, 372.
60. Toyama, T.; Konishi, T.; Seo, Y.; Tsuji, R.; Terai, K.; Nakashima, Y.; Maenishi, R.; Arata, A.; Yudate, S.; Tsutsumi, Y.; Shirakata, S., *Jpn. J. Appl. Phys.* **2015**, *54*, 15503.
61. Furlong, M. J.; Froment, M.; Bernard, M. C.; Cortes, R.; Tiwari, A. N.; Krejci, M.; Zogg, H.; Lincot, D., *J. Cryst. Growth* **1998**, *193*, 114.
62. Tsai, H. W.; Chen, C. W.; Thomas, S. R.; Hsu, C. H.; Tsai, W. C.; Chen, Y. Z.; Wang, Y. C.; Wang, Z. M.; Hong, H. F.; Chueh, Y. L., *Sci. Rep.* **2016**, *6*, 19102.
63. Espinosa-Faller, F. J.; Conradson, D. R.; Riha, S. C.; Martucci, M. B.; Fredrick, S. J.; Vogel, S.; Prieto, A. L.; Conradson, S. D., *J. Phys. Chem. C* **2014**, *118*, 26292.

64. Turnbull, M. J.; Vaccarello, D.; Yiu, Y. M.; Sham, T. K.; Ding, Z., *J. Chem. Phys.* **2016**, *145*, 204702.
65. Wei, S. H.; Zunger, A., *J. Appl. Phys.* **1995**, *78*, 3846.
66. Ohtaki, H.; Yamaguchi, T.; Maeda, M., *Bull. Chem. Soc. Jpn.* **1976**, *49*, 701.
67. Ohtaki, H.; Radnai, T., *Chem. Rev.* **1993**, *93*, 1157.
68. Fatmi, M. Q.; Hofer, T. S.; Randolph, B. R.; Rode, B. M., *J. Chem. Phys.* **2005**, *123*, 054514.

Chapter 6

6 Favorable Bond and Band Structures of $\text{Cu}_2\text{ZnSnS}_4$ and CdS Films and Their Photovoltaic Junctions

Finely tuned 1 μm thick $\text{Cu}_2\text{ZnSnS}_4$ (CZTS, p-type) films, 50 nm thick CdS layers (n-type) and their 1 $\mu\text{m}/2$ nm p-n junction were fabricated inexpensively. Synthesized bulk CZTS and CdS was analyzed for structural deviations and crystal defects using synchrotron-based (SR) X-ray absorption fine structure (XAFS) techniques along with simulated XAFS patterns. The structural properties of the two materials were discovered to favor photovoltaic activity. Interface valence band (VB) structures of the CZTS/CdS p-n junction were measured through SR X-ray Photoelectron Spectroscopy (SR-XPS) and compared with the ones simulated using Density Functional Theory. A full band diagram was constructed from the bulk measurements, and SR-XPS of the interface, providing guidelines in optimizing charge-carrier extraction from the CZTS absorber to CdS buffer layer. It turns out that a small spike-like interface in the conduction band overlap was formed, maintaining a strong internal bias, while favoring a small energy barrier to prevent large-scale recombination from occurring. A large open circuit voltage is anticipated from a solar cell device to be built on this p-n junction.

6.1 Introduction

Structural components of the CZTS layer contribute to the p-type character.¹⁻² As such, the charge-carrier flow will depend on the degree to which the sub-structures such as vacancies, antisites, and secondary phases, permeate the film, and the surface has been oxidized.³⁻⁵ Removal of oxides and secondary phases create favorable conditions for charge-carrier flow, while vacancies and antisites will contribute positively to the tuning of band structures of the material.⁵⁻⁶ By adjusting the band structure to promote desirable sub-structure within the crystal, the extraction of charge-carriers can be maximized.

CdS films can also be tuned to select for specific n-type properties, and contribute heavily in the creation of an ideal p-n junction. Fabrication temperature, reagents, and all contribute to the band characteristics of the film.⁷⁻⁹ As such, deposition conditions are

selected to create an ideal overlap between the conduction band (CB) of the CdS, and CZTS layers. This requires a situation in which the CB of the CdS lies slightly above that of the CZTS in the space-charge region (SCR), creating a small energy barrier for the electrons to overcome. This is known as a spike-like junction, and aids in maintaining a high open-circuit potential (V_{oc}).¹⁰⁻¹¹ The valance band (VB) of the CdS must not be close to that of the CZTS, however, so as to maintain a high internal potential, and prevent recombination due to a SCR.¹²⁻¹³ This has been discussed in Chapter 1.3.2.

The accuracy of the measurements in both the bulk materials, and in the band structure is paramount to designing the interface. Maximal accuracy can be achieved through the use of the energy tunable X-rays of a synchrotron radiation (SR) source. This allows for examination of the local environments at atomic levels via X-ray absorption fine structure (XAFS) and extended X-ray absorption fine structure (EXAFS), and for precision surface measurements of the VB at the film surface through X-ray photoelectron spectroscopy.^{11, 14-15} The combination of XAFS and EXAFS can be used to identify different states of individual atoms within a crystal structure, and then quantify the various structural components that make up those states.¹⁶⁻¹⁷ These can then be linked to the known atomic ratios to ascertain the extent to which different sub-structures exist within the film. A deeper examination of the VB can be carried out through SR-XPS.

In this Chapter, finely tuned 1 μm thick CZTS films were fabricated using electrochemical deposition of Cu, Sn, and Zn films on molybdenum coated glass substrates and sulfurization, and 50 nm thick CdS layers were prepared via an optimized chemical bath deposition (CBD). Employing a cooperative use of experimental and theoretical measures of both benchtop and SR spectroscopies, the band and band structures of the CZTS light-absorbing layer were determined. Structural features within the CZTS and CdS films were used to explain observations within the band structures, and outline a full band schematic for each of them. An optimally designed p-n junction was then formed. The two-layer interface was then probed, and compared against the theoretical structure determined through the bulk measurements and theoretical calculations, thus ensuring self-consistency throughout the process. From these, a full band schematic of the junction was constructed, and the charge-carrier flow through the

SCR identified with relation to the structural components of the films. It was discovered that a small spike-like interface in the conduction band overlap in SCR was formed, which maintains a strong internal bias, while favoring a small energy barrier to prevent large-scale recombination from occurring.

6.2 Experimental

6.2.1 Fabrication

CZTS films were fabricated using galvanostatic electrodeposition of metal precursors with an EG&G PAR 363 potentiostat (EG&G Princeton Applied Research, Oak Ridge, TN), followed by high-temperature sulfurization. The electrodeposition and sulfurization procedures were optimized. A three-electrode system with the Mo-coated glass (University Wafer Inc., Boston, Massachusetts) as the working electrode, was employed to deposit the metal precursors. Copper was deposited on top of the molybdenum using a constant current density of 2.5 mA/cm² applied on the working electrode immersed in a solution containing 25 g/L CuSO₄•5H₂O (Sigma-Aldrich, 99.995%), 120 g/L NaOH (Sigma-Aldrich, 97% pellets), and 37.5 g/L D-sorbitol (Sigma-Aldrich, ≥98%). Tin was deposited on top of the copper layer with a current density of 6.0 mA/cm², and a tin sulfate 89-TI RTU solution (Technic Inc., Cranston, RI). Finally, a current density of 3.0 mA/cm² was applied to the working electrode with the copper and tin layers to deposit zinc and the electrochemical bath was comprised of 8 g/L ZnCl₂ (Sigma-Aldrich, 99.999%), 150 g/L KCl (Sigma-Aldrich, ≥99.0%), and 8 g/L poly[bis(2-chloroethyl) ether-alt-1,3-bis[3-(dimethylamino)propyl]urea] (Sigma-Aldrich, 62% wt% in H₂O). Each of the resulting stacked metal films was washed in Type 1 water (Milli-Q Ultrapure Water Systems, Millipore Corp., Germany), and dried with argon gas flow. The stacked metal film samples were then placed in a Thermoscientific Lindberg Blue M Tube Furnace (Ashvill, NC) with a specially designed quartz tube for desired argon and vacuum purges. An optimized ratio of 10 mg/cm² was used for sulfur powder mass-to-sample surface area. The quartz tube was purged three times via vacuum pump to <200 kPa, and then filled with argon to a pressure of 0.75 bar. The furnace was then held at 250 °C for 20 minutes, followed by 30 minutes at 550 °C, with a ramp rate of 50 °C/min to reach each set-point. These were carried out to vaporize the sulfur powder, and have it permeate the

metallic stacks to form CZTS, in a similar way as Ye *et al.* infused selenium into their electrodeposited CIGS cells.¹⁸ Following CZTS formation, the furnace was shut off and the system purged to remove excess sulfur vapor. The quartz tube was finally re-filled with argon to 0.75 bar, and raised above the heating bed to cool down. The fabricated CZTS films were etched with 0.5 M acetic acid to remove copper oxides¹⁹ and residuals on the CZTS surface, and increase p-type character, as has been accomplished in other p-type materials.²⁰ This will have the added benefit of passivating any charged point-defects, and act as a milder etchant than the commonly used KCN reported by Shoushuai *et al.*,⁵ or the HCl treatment used by Chen *et al.*²¹

CdS was deposited on the CZTS films via chemical bath deposition (CBD). The methods were modified from Ye *et al.* based the trends reported by Liu *et al.* and Moualkia *et al.*.^{8-9,18} Briefly, a mixture of 103.5 mg Cadmium acetate (Sigma-Aldrich, 99.99%), ammonium acetate (Sigma-Alrich $\geq 99.99\%$), and 4.5 M NH₄OH (Caledon, $\geq 99\%$) in Type 1 water were heated to 65 °C and stirred for 30 minutes. 1.5 mL of 0.5 M thiourea (Sigma-Aldrich, $\geq 99\%$) was added, and heated for 30 additional minutes, followed by submersion of the samples for the CdS formation. The reaction was allowed to proceed for 10 minutes, yielding a 50 nm CdS film as we detailed elsewhere.²² For the interface, a series of samples were made, with submersion times ranging from 20 – 60 s. The resultant films were placed under vacuum at 200 degrees for 20 minutes in an Ultratech / Cambridge NanoTech Savannah S200 Atomic Layer Deposition (ALD) instrument (Waltham, MA) reaction chamber to remove any water intercalation that occurred during CBD, as we reported previously.²³ Defects are indicated by Kröger-Vink notation, as described in Chapter 3.3.1.

6.2.2 Characterization

XAFS measurements of the Cu, Zn, and Sn K-edges were performed at the CLS@APS 20-BM beamline at the Advanced Photon Source (APS) at Argonne National Laboratory in Argonne, IL. The beam was used in focus mode. A Si (111) monochromator and a 400 μm vertical slit was used over 8.78 to 9.52 keV for the Cu K-edge, 9.46 to 10.4 keV for the Zn K-edge, and 29.004 to 30.069 keV for the Sn K-edge. Samples were placed 45° to the incident photons, and the 13-element Canberra detector was placed perpendicular

to the beam. Detector saturation was set to 50,000 cps, and replicates were taken to a sum of 2 million total counts per element. Spectra were normalized to the incident photon flux, I_o , and calibrated against a standard reference foil (EXAFS Materials Inc.). The standards used for energy calibration included a 7.5 μm thick copper foil, 10 μm zinc foil, and 50 μm tin foil.

XAFS were compared against each other and to the theoretical ones of the CZTS kesterite structure predicted by means of the software package WIEN2k (Institute of Materials Chemistry, Vienna, Austria), that uses density functional theory (DFT).²⁴⁻²⁵ This software uses a full-potential augmented plane-wave, and local orbitals methods, to simulate the expected XAS spectrum, assuming a perfect crystal lattice. The generalized gradient approximation (GGA) was used to account for density changes across the films.²⁶⁻²⁸ EXAFS fittings were performed using the Artemis software package, and the FEFF8 multiscattering code.^{16,29} A tetragonal kesterite unit cell, space group $I\bar{4}$, of 5.4 Å by 10.7 Å was extended to a cluster of 500 total atoms, with a maximum path expansion of 8.0 Å.

Band gap measurements were taken using a Varian Cary 50 spectrometer (Agilent, Santa Clara, California) to measure UV-vis absorption of each of the CZTS and CdS. Formed CZTS were removed from the back contact through physical abrasion, and dispersed in isopropanol to 0.5 g/L. The mixture was then sonicated for 30 minutes to achieve a very fine dispersion, and placed in a 1 cm x 1 cm quartz cuvette. CZTS and CdS films were also measured at a grazing angle of $\sim 3^\circ$ to the incident beam, to ensure no peak shifts resulted from the dispersion. These were converted to Tauc plots, relating the absorption coefficient to the wavelength energy. A Hitachi S-4500 field emission microscope with a 100 kV EDX system was used to determine sample composition.

The XPS analyses were carried out with a Kratos Axis Ultra spectrometer (Kratos Analytical, Chestnut Ridge, New York) using a monochromatic Al K(alpha) source (15mA, 14kV). XPS probes the surface of the sample to a maximum depth of 5-7 nanometres, and has detection limits ranging from 0.1 to 0.5 atomic percent depending on the element.³⁰ The instrument work function was calibrated to give a binding energy

(BE) of 83.96 eV for the Au 4f_{7/2} line for metallic gold and the spectrometer dispersion was adjusted to give a BE of 932.62 eV for the Cu 2p_{3/2} line of metallic copper. The Kratos charge neutralizer system was used on all specimens. Survey scan analyses were carried out with an analysis area of 300 x 700 microns and a pass energy of 160 eV. High resolution analyses were carried out with an analysis area of 300 x 700 microns and a pass energy of 20 eV. Spectra have been charge corrected to the main line of the carbon 1s spectrum (adventitious carbon) set to 284.8 eV. Spectra were analyzed using CasaXPS software (version 2.3.14).

Synchrotron XPS (SR-XPS) was carried out at the Canadian Light Source on the Variable Line Spacing Plane Grating Monochromater (VLS-PGM, 11ID-2) beamline. Measurements were taken at a flux $> 1 \times 10^{11}$ on a $500 \times 500 \mu\text{m}$ spot size. Incoming photons were set at 225 eV. The beam energy was calibrated using gold foil at the Au fermi level emission. The valence band binding energy has been measured relative to the Fermi level of a clean Mo film in good electrical contact with the sample.

6.3 Results and Discussion

6.3.1 Insight into CZTS Structure

The K-edge XAFS spectra (black) for the Cu, Zn, and Sn metal centers in the formed CZTS are seen in Figure 6.1, alongside the theoretical spectra (blue) predicted based on a pure CZTS kesterite lattice, which yields penetrative information of the bulk states. As such, any deviations should be consistent in all three edges in a perfectly crystalline film, and localized to edge pairs in the event of antisite formations.¹⁵

Figure 6.1A indicates the extent to which the Cu centers in the experimental films deviate from those in a perfect lattice, and offers insight into the overall disorder.³¹ The first peak corresponds to the dipole-allowed 1s \rightarrow 4p transition occurring at 8,986.1 eV. This is consistent with the expected Cu⁺ center in kesterite CZTS,³² and aligns well with the model, whose peak occurs at 8,986.2 eV. The rest of the Cu K-edge spectrum shows only small deviations from the theoretical model, with the most notable ones occurring in the peaks directly following the edge. Whereas the model predicts decreasing intensity

relative to the first peak, we observed either a weaker peak at the edge, seen at 8,986.2 eV, or a stronger second and third peak at 8,998.6 eV and 9,009.7 eV respectively.

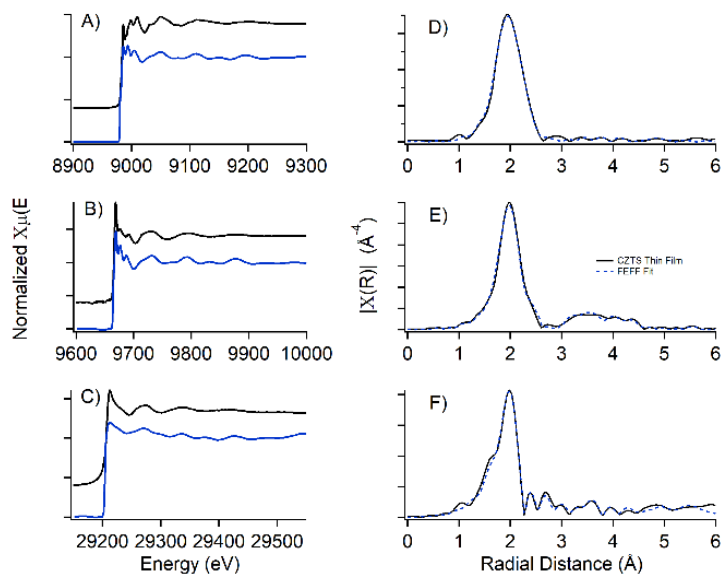


Figure 6.1 Metal K-edge XAFS spectra for the (A) Cu, (B) Zn, and (C) Sn metal centers in the CZTS film (black), alongside the corresponding theoretical spectra for a pure CZTS kesterite (Chapter 1.3.4). The experimental spectra have been offset for better visual comparison. Fitting of the radial distance space (R-space), Fourier Transform (FT) of the EXAFS signals, is shown for (D) Cu, (E) Zn, and (F) Sn metal centers, respectively. All fittings used a k^3 weighting to maximize signal in the high k -ranges. Full fitting parameters are provided in Supporting Information.

Since the intensity and position of these peaks are a function of the ligand field strength and geometry around the absorbing atom respectively,^{15, 32-33} the deviations are the result of localized changes in the crystal structure. Structural deviations in the CZTS film have a profound impact on the formed p-n junction.³⁴ As such, accurate modeling of the film relies on precise knowledge of the underlying structure. These can then be broken down into bulk film, and surface film contributions. Changes in the bulk determine the overall crystallinity of the film, while surface contributions alter the electronic structure of the p-n junction, thus affecting the ease with which charge-carriers can flow between the films. To this end, these are likely the result of antisites and vacancies, and will be confirmed

through FEFF fitting of the EXAFS in subsequent discussion. The signal in the experimental spectrum also appears to degrade more rapidly than in the model. Since the density of states are calculated using an energy minimum, and involve a lot of parameters, this should not be taken as relevant.³⁵⁻³⁶ The thermal effects of conducting the experimental measurements at room temperature, and lifetime broadening in the signal, would also contribute to the more rapid signal degradation observed.

The experimental and theoretical Zn spectra (Figure 6.1B) are remarkably similar in their features. The first peak at the edge, corresponding to the Zn 1s \rightarrow 4p transitions, occurs at 9,665.0 eV both experimentally, and theoretically, and are consistent with literature.³⁷ The first two peaks after the edge show small energy shifts, and increases in broadness, relative to the theoretical spectrum. The experimental peaks are also less prominent. Antisite formation within the crystal structure again accounts for these changes. Taken together with the observations on the Cu spectrum, the presence of antisite markers in both the Cu and Zn spectra is indicative of a possible Cu'_{Zn} single acceptor, or a Zn^{\bullet}_{Cu} single donor site, as discussed previously on CZTS nanocrystal films.³⁸⁻⁴¹ Single acceptor Cu vacancies, V'_{Cu} , and double acceptor Zn-vacancies, V''_{Zn} , are also possible explanations. These defects are theoretically calculated disorder formations arising during CZTS fabrication, and have been shown in sputtered CZTS films.^{6, 42-43} The deeper acceptor sites contribute favorably to charge-carrier physics at the barrier, while shallow acceptors, and donor sites, are less favorable and often affect performance adversely.^{6, 44-45} V'_{Cu} would also contribute favorably to performance.⁴⁶ Each of these structures in the film would result in observable shifts in the valance band and the band gap. It should also be noted that like the Cu spectrum, the thermal effects of measuring at room temperature result in less defined oscillations of the Zn spectra relative to the theoretical model.

The experimental Sn spectrum in Figure 6.1C differs from those discussed above in that it is the first peak, representing the 1s \rightarrow 5p transitions, that shows the deviation from the simulation curve, rather than the subsequent peaks. A stronger first peak at the edge (29,212.4 eV) indicates a more accessible transition to the 5p states, and thus coordination changes, oxidation changes, or ligand effects on the site.¹⁴⁻¹⁵ Any large

deviations from the expected coordination would result in major secondary phase formation, and result in large structural deviations that were not seen in the films. Furthermore, changes of this nature would have been even more apparent in the Cu and Zn spectra, which have much longer core-hole lifetimes than Sn.¹⁴⁻¹⁵ Changes in oxidation state would be expected to yield larger shifts in the peak positioning, allowing those to be discounted.¹⁴ Ligand effects, however, would arise from the suggested antisite and vacancy formation predicted from the Cu and Zn spectra, and are the likely source. It is plausible to eliminate antisites and vacancies involving Sn, as both of these would likely cause greater deviation from the model in subsequent peaks. The Sn spectrum also shows the same thermal degradation relative those noted in the Cu and Zn spectra.

As the photoelectron wave function interacts with nearby atoms, the corresponding X-ray absorption is slightly altered. These alterations are thus directly linked to structural information in the EXAFS region, and lead to quantifiable results.⁴⁷ The refined experimental EXAFS signals could then be quantitatively used to elucidate CZTS structures, with deviations described above. Figure 6.1D-1F depicts the radial distribution of the first shell of each metal of interest, fit in radial distance space using the techniques reported by Rehr *et al.*²⁹ The kesterite CZTS model provides a very strong basis on which an excellent fit was obtained for all three metal centers in Figure 6.1; however, all three metal centers showed distinct features that deviate from the ideal structure. Full fitting parameters can be viewed in Table 6.1. The Cu nearest neighbor peak (Figure 6.1D) is relatively broad, and the fitting showed two distinct bond lengths for the metal-to-sulfur bond, listed as S(1) in Table 6.1. It should be noted that when the bonds are less than 0.1 Å, it cannot be fully resolved with FT. The theoretical Cu-S bond in kesterite CZTS is 2.332 Å. Experimentally, the smaller of the bonds is 0.02 Å shorter than the theoretical, and accounts for 37.5% of the first shell bonds. The longer bond is 2.399 Å, which while more than the 0.05 Å practical limit of detection using EXAFS, is less than the 0.1 Å limit to achieve full resolution. This means that while two bond lengths do contribute, resolving one from the other is difficult, and should be consistent with other measurements to ensure authenticity.

Table 6.1 Fitting parameters using FEFF8 code and Artemis software for each of (A) Cu, (B) Zn, and (C) Sn metal centers. The first neighboring S atom has been split to show the two different bond lengths separately in each of the parameter sets.

Neighbor	Cu Fit Parameters				
	N	S ₀ ²	e ₀ (eV)	σ ² (Å ²)	r (Å)
S (1)	1.5 ± 0.2	0.93 ± 0.01	1.4 ± 0.4	0.0118 ± 0.0001	2.312 ± 0.005
	2.5 ± 0.2	0.93 ± 0.01	1.4 ± 0.4	0.0118 ± 0.0001	2.399 ± 0.005
Cu/Zn (1)	3.6 ± 0.2	0.93 ± 0.01	1.4 ± 0.4	0.0117 ± 0.0001	3.808 ± 0.004
Cu/Zn (2)	4.4 ± 0.2	0.93 ± 0.01	1.4 ± 0.4	0.0117 ± 0.0001	3.818 ± 0.004
Sn	4.0 ± 0.2	0.93 ± 0.01	1.4 ± 0.4	0.0120 ± 0.0002	3.829 ± 0.005
S (2)	3.8 ± 0.3	0.93 ± 0.01	1.4 ± 0.4	0.0144 ± 0.0004	4.446 ± 0.003
S (3)	8.2 ± 0.3	0.93 ± 0.01	1.4 ± 0.4	0.0147 ± 0.0006	4.532 ± 0.004
Neighbor	Zn Fit Parameters				
S (1)	1.5 ± 0.2	0.93 ± 0.01	3.0 ± 0.5	0.0083 ± 0.0001	2.241 ± 0.004
	2.5 ± 0.2	0.93 ± 0.01	3.0 ± 0.5	0.0083 ± 0.0001	2.356 ± 0.004
Cu/Zn (1)	2.8 ± 0.3	0.93 ± 0.01	3.0 ± 0.5	0.0146 ± 0.0008	3.850 ± 0.010
Cu/Zn (2)	5.2 ± 0.3	0.93 ± 0.01	3.0 ± 0.5	0.0146 ± 0.0008	3.925 ± 0.010
Sn	4.0 ± 0.3	0.93 ± 0.01	3.0 ± 0.5	0.0166 ± 0.0004	3.829 ± 0.006
S (2)	3.8 ± 0.4	0.93 ± 0.01	3.0 ± 0.5	0.0186 ± 0.0007	4.474 ± 0.004
S (3)	8.2 ± 0.4	0.93 ± 0.01	3.0 ± 0.5	0.0198 ± 0.0008	4.601 ± 0.006

Neighbor	Sn Fit Parameters				
S (1)	0.2 ± 0.1	0.93 ± 0.01	2.7 ± 0.9	0.0071 ± 0.0002	2.361 ± 0.003
	3.8 ± 0.1	0.93 ± 0.01	2.7 ± 0.9	0.0071 ± 0.0002	2.396 ± 0.003
Cu/Zn (1)	0.4 ± 0.3	0.93 ± 0.01	2.7 ± 0.9	0.0088 ± 0.0004	3.882 ± 0.007
Cu/Zn (2)	7.6 ± 0.3	0.93 ± 0.01	2.7 ± 0.9	0.0088 ± 0.0004	3.974 ± 0.007
Sn	4.0 ± 0.4	0.93 ± 0.01	2.7 ± 0.9	0.0113 ± 0.0002	4.036 ± 0.005
S (2)	0.8 ± 0.4	0.93 ± 0.01	2.7 ± 0.9	0.0127 ± 0.0005	4.370 ± 0.006
S (3)	11.2 ± 0.4	0.93 ± 0.01	2.7 ± 0.9	0.0131 ± 0.0007	4.612 ± 0.006

This approach has been used in the past with similarly separated bonds, on complex systems.⁴⁸ While not drastically different, the two bond lengths indicate the presence of two separate Cu environments. This is consistent with the structural deviations seen in the XAFS (Figure 6.1A). A V'_{Cu} or V''_{Zn} would result in the shared charge distribution of the sulfur atom being repelled by the like-charged neighboring sulfurs, and reduce the metal-sulfur bonds.⁴⁹⁻⁵⁰ The antisite defects would tend towards lengthening with increased atomic radius.⁵¹⁻⁵² Therefore, Cu'_{Zn} antisites would have the opposite effect of a V'_{Cu} , and relax the Cu-S bond length.⁵¹⁻⁵² Given the high ratio of elongated Cu-S bonds revealed by the fit, there appear to be significant Cu'_{Zn} antisites within the crystal. V'_{Cu} are also possible, given that the effect of the vacancies on the bond lengths would be less pronounced,^{2, 52-53} but are less prevalent than the antisites. A similar situation is seen in the lengthier Cu-Cu, and Cu-Zn distances. With these, the difference between the two distances is much smaller, and so more challenging to interpret. It is further complicated by the Z+1 uncertainty in the FEFF calculations, making it difficult to differentiate Cu from Zn neighbors in the second shell. The clearest indication comes from the change in the ratio of the bond distances. Whereas the first shell had 37.5% shorter bonds, the second shell Cu-Cu and Cu-Zn bonds are 45% of the shorter variety. For the ratio to

change like this, there must be a significant increase in tighter bonding in the second shell, despite a relative relaxation of the first shell. This is further indication of V'_{Cu} present in the film, in addition to the Cu'_{Zn} antisites, as these would tighten the overall lattice and result in reduced distances to the second shell in more than just the immediate atomic distance. It could also be indicative of the Zn^{\bullet}_{Cu} antisite, as Zn^{2+} has a much smaller radius than Cu^+ , and thus would increase the bonding. Compositionally, the films have a Cu/Zn/Sn ratio of 1.73/1.10/1.00 with a Cu/(Zn+Sn) ratio of 0.83 ± 0.02 , a Cu/Sn ratio of 1.73 ± 0.03 , and a Zn/Sn ratio of 1.10 ± 0.01 , as measured by EDX, increasing the likelihood of V'_{Cu} . These ratios also have the effect of reducing the chances of localized defect-clusters.⁵⁴ The Cu-Sn does not show any deviation, a phenomenon that is discussed further along with the Sn EXAFS; however, when combined with the extended bond lengths of the third shell – S(2) and S(3) in the SI – sulfurs, it appears that the Sn forms a fairly unchanging sub-lattice, and does not participate much in antisite or vacancy formation within the films.

The Zn EXAFS (Figure 6.1E) shows the same first shell features as the Cu EXAFS (Figure 6.1D), with 37.5% of the Zn-S bonds forming a smaller than expected bond length, and 62.5% forming a longer bond. This does not indicate a V''_{Zn} though, since it is known from EDX measurements that Zn is in stoichiometric excess. While this could also be indicative of Zn^{\bullet}_{Cu} antisites, the ratio being identical to the Cu EXAFS would suggest that these two features are highly correlated. As such, V'_{Cu} , as well as Cu'_{Zn} , and Zn^{\bullet}_{Cu} antisites, must be contributing to the observations in both spectra (Figure 6.1D and Figure 6.1E). Unlike in the Cu spectra though, the relative ratio of small Zn-Cu and Zn-Zn bonds remains around the same at 35%, rather than increase to 45% as the Cu did. The Sn sites also remain constant in the Zn spectra as well. This further emphasizes the high presence of V'_{Cu} , and higher prevalence of Zn^{\bullet}_{Cu} sites relative to Cu'_{Zn} sites. The ratio of the third shell Zn-S distances is the same as in the Cu EXAFS as well, as would be expected with such a high correlation between the features seen in both element centers. These stoichiometric compositions are very similar to those of our CZTS nanocrystals published elsewhere.^{39-41, 55}

The Sn neighboring atom radial distribution (Figure 6.1F) is the only fit that deviates from the ratios previously noted. Instead, only about 5% of the Sn-S first shell bonds are short. While the spectrum was not able to be fit with a single bond distance, there is significantly less deviation about the Sn site than those of the other two metal centers. This concurs with the previously noted trend that the Sn center appears mostly unperturbed by the antisite formations between Cu and Zn. It also implies that any contributions from Sn to antisite formation is highly limited. The presence of the much large Sn atom forming a $Sn_{Cu}^{\bullet\bullet}$ or $Sn_{Zn}^{\bullet\bullet}$ antisite would drastically change the bond lengths; therefore, this antisite is not likely present in any significant quantity within the film. This is ideal, and likely the result of good metal ratio control in the films.⁵⁴ The short distance to the second shell neighbors also makes up only 5% of the cases. This high correlation between the first and second shell neighbor distances also corresponds to a self-consistent structure among the Cu and Zn centers. This means that the V'_{Cu} and the Cu and Zn antisites are consistent throughout the film, and relatively ordered in their formation. These observations are shown to be consistent with the data presented in the subsequent sections.

6.3.2 CZTS Band Structure

Having examined the structural components of the CZTS films, their contributions to the electronic structure can then be examined via XPS, and their band structures be determined. The resultant spectra are given in Figure 6.2. The Zn^{2+} 2p_{3/2} peak (Figure 6.2A) shows the typical binding energy of a Zn^{2+} metal center, at 1,021.7 eV, with a small shoulder at higher energy.^{54,56} This is consistent with monodisperse Zn sites throughout the CZTS film as shown from the above synchrotron spectroscopy,⁵⁷ and a lack of secondary phase formation as seen in our previous report.⁵⁸ A zinc sulfide fitting shows strong correlation with the experimentally obtained spectra. As such, the vacancies or antisites within the structure are spread throughout the film, and are not clustered together. This further agrees with the EXAFS analysis (Figure 6.1), and supports the phenomenon of copper-deficient stoichiometry, with local antisite and vacancy formation.

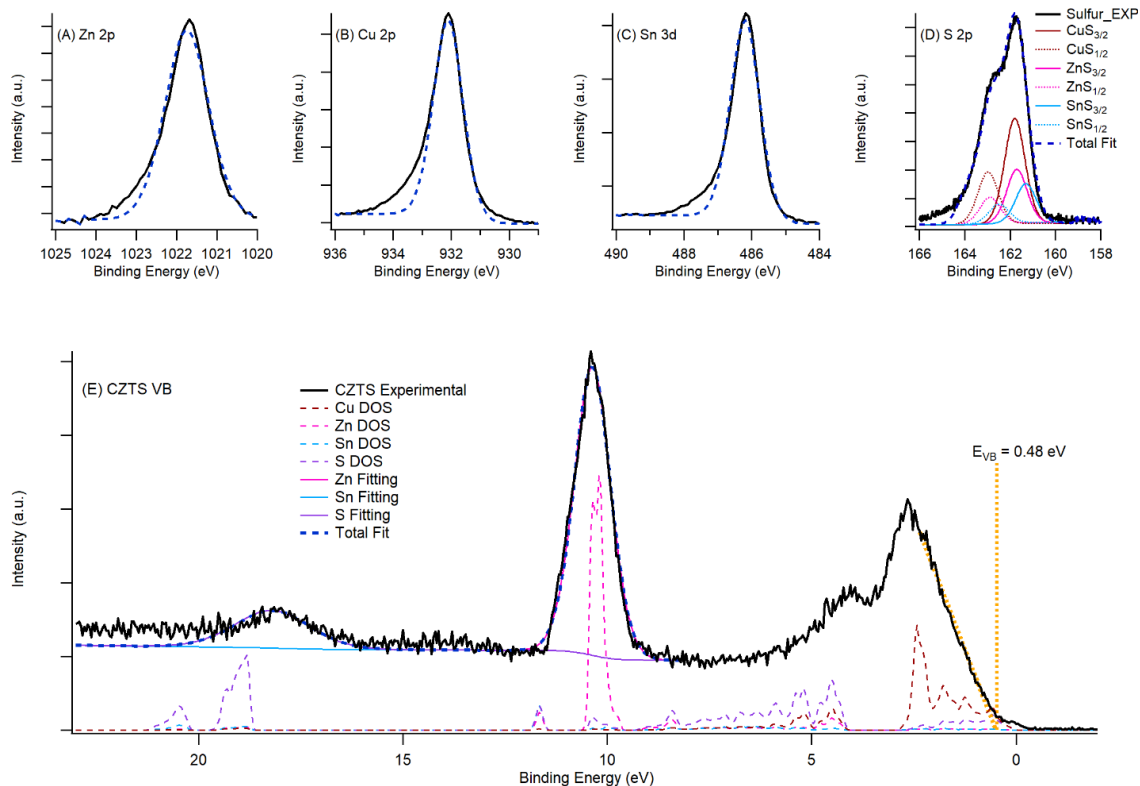


Figure 6.2 High resolution core level XPS for each of the (A) $\text{Zn}^{2+} 2p_{3/2}$, (B) $\text{Cu}^+ 2p_{3/2}$, (C) $\text{Sn}^{4+} 3d_{5/2}$, and (D) $\text{S}^{2-} 2p_{3/2}$ & $2p_{1/2}$ in the CZTS film, and their corresponding best fit (blue dashed line). The sulfur spectrum has been further curve-fit into its known components (Brown: Cu_2S , Pink: ZnS , Blue: SnS_2), confirming the known metal ratios with which the sulfur atoms combine. The SR-XPS (E) for the CZTS valence band overlays the CZTS density of states as determined using GGA. Linear extrapolation of the leading edge marks the valence band energy (E_{VB}).

There is some small additional electron intensity at higher energy that cannot be fit using the single sulfide and is likely a product of the two different Zn-S bond lengths observed from the EXAFS analysis. This is consistent with the Cu $2p_{3/2}$ peak (Figure 6.2B), which is also a single peak, occurring at 932.1 eV. This Cu $2p_{3/2}$ peak is consistent with literature values for Cu_2S sites for CZTS, and confirmed using the modified Auger parameter (Figure 6.3) reported by our group and others.^{54, 58}

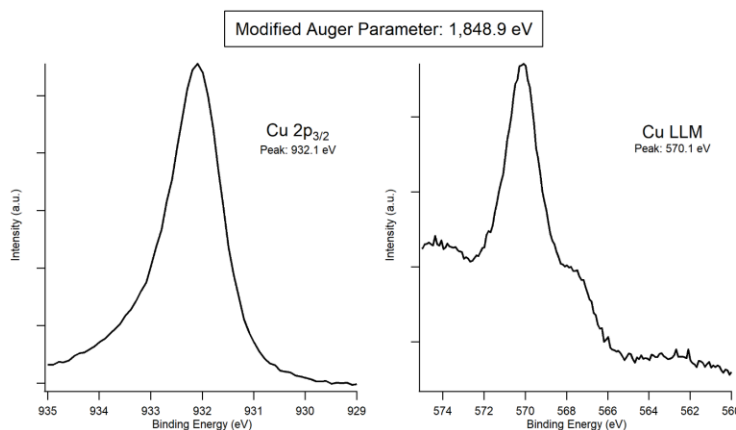


Figure 6.3 The Cu 2p_{3/2} and Cu LLM peaks for the CZTS sample. The binding energy for the Cu 2p_{3/2} is for similar for the different Cu oxidation states, but can be distinguished by the Modified Auger Parameter (MAP). Cu²⁺ has a MAP of 1,851.2 eV, and Cu⁺ has a MAP of 1,849.2 eV. In this way, it was determined that only Cu⁺ was present in the CZTS samples.

The fitting again shows a single copper sulfide presence, with the only deviation being a small tailing towards higher binding energies. Of note, this tail is a lot more prominent in the Cu 2p_{3/2} peaks than in the Zn. Its presence in both spectra is significant because it also suggests a tighter electron bonding is present in some of the Cu and Zn sites relative to the majority of the film. These tighter bonding regions can be observed for both in the EXAFS and the XPS confirms their presence, and can be attributed to redistribution of the sulfide bonds on atoms near V'_{Cu} sites. Much like in the XAFS and EXAFS spectra, the Zn sites appear to be more highly conserved regardless of the changes in the local environments around them, leading to the reduced definition in the shoulder. The Cu-sites therefore contribute more towards the non-uniformity in the films, through antisites and vacancies, which is consistent with high efficiency CZTS formation presented in literature.⁵⁹⁻⁶⁰ The Sn 3d_{5/2} (Figure 6.2C) is much the same, with a single peak at 486.2 eV. This is consistent with literature values for Sn⁴⁺ sites in CZTS.^{54, 61-62} The fitting once more yields the edge deviation at higher energy, and appears to be highly similar to the edge seen in the Cu fitting. The effect was understated in the EXAFS fit compared to the XPS, which suggests a possible change in the ratio obtained from EXAFS (Figure 6.1F).¹⁴⁻¹⁵ Given the high consistency between the EXAFS and XPS results in all other

cases, it is probable that the values are simply understated in the EXAFS due to the limits previously stated.

The S $2p_{3/2}$ and $2p_{1/2}$ peaks (Figure 6.2D) overlap, and were subsequently fit based on a combination of all metal sulfides, and their corresponding EDX-determined ratios, and the 37.5 : 62.5 short-to-long bond ratio predicted by the EXAFS. The individual peaks that make up the long bonding were shown, while the short bond peaks were omitted for clarity. These known metal ratios (1.73/1.10/1.00 for Cu/Zn/Sn) produced a very good fit that overlaps completely with the experimental spectrum. Such a fit was attempted to prove the validity of the data extracted from the crystal structure, and was only used due to the nature of having previously determined all parameters involved. Given the high degree of fit, all theoretical data is very consistent with the CZTS measurements.

Through analysis of the positioning of the binding energy of each atomic cite in the CZTS layer, especially that of the valence band, the effect of the identified substructures to the overall flow of electrons can be determined. Using SR-XPS, the CZTS valence band (VB) spectrum (Figure 6.2E) was plotted against the density of states (DOS) computed from an antisite and vacancy-free CZTS model. The VB peaks were also fit similarly to the rest of the XPS, excluding the region from 0 – 5 eV. This exclusion was made due to the partial DOS of all elements that make up the region, and hybridization of the Cu d-orbitals with S p-orbitals, rendering Gaussian fitting ineffective.⁶³ The fittings of all metal DOS are excellent, with relative heights and peak positions matching well. This is in agreement with the previously presented data. As expected, notable shifts were observed in relation to the sulfur DOS. The DOS at 18.8 eV appears at 18.1 eV experimentally, and the DOS at 11.6 eV is not visible in the experimental spectrum. Given a similar shift to lower energy, this state would be obscured within the much stronger Zn DOS. Furthermore, the experimental sulfur peaks are significantly broader than their metal counterparts, and all experimental peaks are broad relative to the Gaussian broadening of 0.04 eV set for the theoretical DOS peaks. These broadenings arise from the antisite and vacancy presence within the experimental film, which further confirm the model presented. The valance band energy (E_{VB}) is observed at 0.48 eV, and the V'_{Cu} produce the literature described additional small states observed in the region

between the E_{VB} and 0 eV as described in an theoretically optimized crystal structure.⁴ These additional states would contribute favourably to the charge-transfer process.^{6, 43, 54,}
⁶⁴ In order to assess the impact of these structural properties on charge-carrier physics, particularly at the CZTS-CdS interface, their effects on the valence band are most important, and are discussed in a later section.

6.3.3 CdS Band Structure

CdS XPS was also measured, and fit for the Cd 3d, and S 2p, and SR-XPS of the valence band was plotted against the DOS from the DFT calculations. These data are presented in Figure 6.4.

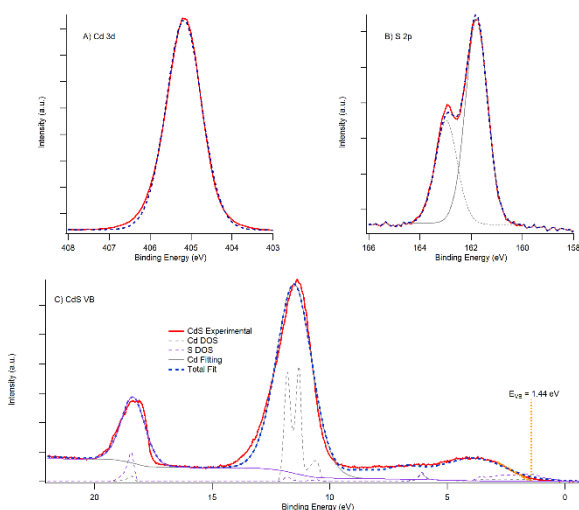


Figure 6.4 High resolution core level XPS for each of the (A) $\text{Cd}^{2+} 3d_{5/2}$, (B) $\text{S}^{2-} 2p_{3/2}$ and $2p_{1/2}$ in the CdS film, and their corresponding best fit (blue dashed line). The SR-XPS for (C) the CdS valence band overlays the CdS density of states as calculated using GGA. Linear extrapolation of the leading edge marks the E_{VB} .

The Cd $3d_{5/2}$ spectrum (Figure 6.4A) shows a single peak at 405.2 eV, consistent with literature reported value of sputtered CdS.⁶² Likewise, the S 2p CL spectrum (Figure 6.4B) is fit with a single sulfide, showing both the $2p_{3/2}$ and the $2p_{1/2}$ peaks. In both cases, the experimental and theoretical curves are well matched, and together constitute a highly conserved and consistent CdS structure. This is expected for a simple zinc-blende CdS structure.⁶¹⁻⁶² The CdS valence band (Figure 6.4C), is much the same, with the

sulfur states at 18.3 eV, and the Cd states at 11.5 eV, lining up well with the theoretical DOS. Some of the resolution seen in the DOS is not present in the experimental peak due to peak broadening caused by thermal variation. The sulfur DOS at low energy also appear to have been obscured in the experimental spectrum. Nonetheless, a clear E_{VB} was determined to be at 1.44 eV. This is in very good agreement with reported value of sputtered CdS in literature,⁶² and appears slightly higher than the DOS predict. Effective charge-carrier transfer is not limited to the properties of the bulk CZTS absorber material, but is mostly affected by the interface between the absorber and buffer layers in the device.⁶⁵ In this case, that is the CZTS-CdS interface. To accurately interpret the interface, bulk properties depicted above for the CdS buffer layer are required.

6.3.4 CZTS/CdS Interface

At the CZTS and CdS interface, these two layers connect through S atoms as both share metal-sulfide bonds. This will cause a shift in each of the metal-sulfide XPS peaks, and a blending of the features observed in the valence bands.^{5, 61, 66} The degree to which these CL peaks shift is indicative of non-equivalent environments within the film. These measurements do not change by more than 0.04 eV from film to film, even when doing minor compositional changes; however, the shifts are much higher in the SCR due to the drastic changes in electron density. In a solar device, this constitutes the interfacial region. The degree to which these peaks shift determines the band bending, and thus the ease by which charge-carriers can cross this boundary. Figure 6.6 illustrates the interfacial XPS measurements. As expected, the interface contains all four metal atoms, and sulfur, in the same general state they were observed in the bulk materials. A series of samples was constructed with various CdS thicknesses, and the VB spectra taken for each. When the CdS was too thin, the X-rays penetrated into the bulk CZTS, and the measured E_{VB} mated with the 0.48 eV seen in Figure 6.2. When the CdS was too thick, the beam did not penetrate deep enough to measure the interface, and the typical CdS VB (Figure 6.4) was measured. These can be viewed in Figure 6.5. It was found that CdS thickness of about 2 nm can ensure the measurement occurs only within the depletion region that forms the SCR.

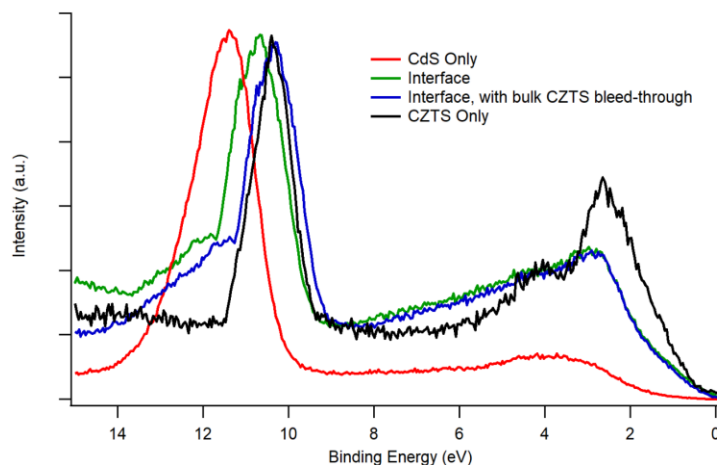


Figure 6.5 Comparison of the SR-XPS VB spectra of the interface at different CdS layer depths, to bulk CZTS and CdS. The measured E_{VB} of the interface is distinct, and the partial DOS of both bulk CZTS and CdS blend together to create a very broad band from 0 – 8 eV.

Due to the narrow penetration depth of the X-rays, the material probed will all be at the most effected regions of charge-depletion, and thus expand the effective region at which we can measure the interface. The interfacial Zn CL peak (Figure 6.6A) has shifted up to 1,022.1 eV, which is 0.4 eV higher than in the bulk (Figure 6.2A). Unlike in the bulk CZTS, a single sulfide fit is sufficient, with no extending shoulder at higher energies. As such, the interfacial Zn-S bond length is more consistent than was observed in the CZTS only, and was therefore indicative of a highly conserved interfacial boundary. The same holds true for the other three metal atoms. The interfacial Cu CL peak (Figure 6.6B) occurs at 932.3 eV, which is also higher than in the bulk (Figure 6.2B) by 0.2 eV. The higher energy shoulder is also missing from this interfacial peak. The interfacial Sn CL peak (Figure 6.6C) shifts up from the bulk (Figure 6.2C) by 0.6 eV to 436.8 eV, and is again best fit by a single sulfide. Similarly, the interfacial Cd CL (Figure 6.6D) shows a single peak at 405.4 eV, shifted up by 0.2 eV from the bulk peak (Figure 6.4A). In each case, the slightly higher binding energy constitutes a tighter bond between the metal center and the sulfurs bound to it, which comes about as the electrons are shared across the interface due to charge depletion. The V'_{Cu} are again noticeable through the shift value. Where additional electron distribution has moved onto the Zn centers at V'_{Cu} , the

shared distribution with the Cd centers becomes more prominent, which leads to the greatest CL shift occurring in the Zn center.

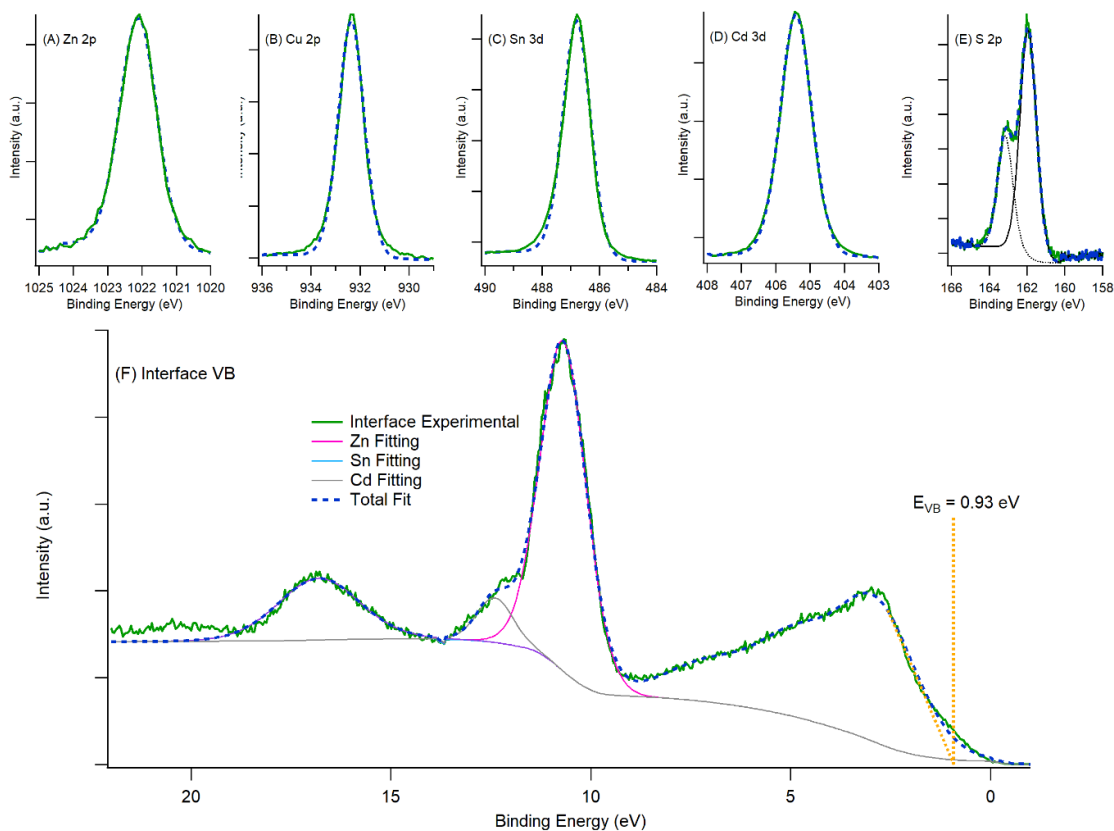


Figure 6.6 High resolution core level XPS of the CZTS-CdS interface for each of the (A) Zn^{2+} $2p_{3/2}$, (B) Cu^+ $2p_{3/2}$, (C) Sn^{4+} $3d_{5/2}$, (D) Cd^{2+} $3d_{5/2}$, and (E) S^{2-} $2p_{3/2}$ and $2p_{1/2}$ in the CZTS-CdS interface, and the SR-XPS for the valence band (F). The corresponding best fit is overlaid in blue. Linear extrapolation of the leading edge marks the E_{VB} .

This also has the effect on the shift in the Cd center relative to that reported in literature.⁶² The S CL peaks (Figure 6.6E) also shift to higher energy than in either the CZTS (Figure 6.2D) or CdS (Figure 6.4B) bulk layers. The S $2p_{3/2}$ peak at the interface occurs at 162.0 eV, which is 0.3 eV above the S $2p_{3/2}$ peak in CZTS, and 0.2 eV above that in the CdS. In each case, the binding at the interface is slightly higher, due to the depletion region forming between the p-type CZTS, and the n-type CdS layers; however, the shifts are relatively even across the atoms that do not participate in antisite and vacancy formation.

As such, the efficiency of charge-carrier transfer through the depletion region is most dependent on the Cu and Zn metal centers, and how their antisite and vacancy sites form throughout the film.

The interfacial VB spectrum (Figure 6.6F) shows many of the same properties as the CL spectra. Each of the Zn and Cd peaks are seen to be shifted by 0.3 eV, and the area between the E_{VB} and 7 eV appears to be several peaks combined into one broad peak. The individual peaks were fit based on the expected ones from the CZTS VB spectrum (Figure 6.2E), and those from the CdS VB spectrum (Figure 6.4C). The S state that showed up at 18.1 eV in the CZTS is now shifted to 17.0 eV, which indicates that this is now found in the depletion region, and additional negative charges will now be associated with the sulfur centers in the CZTS portion of the interface. There is also potentially a separate interfacial state at 20.4 eV, which we postulate to be the electron depleted S state previously associated with the CdS; however, this state is not very well defined, and is not resolved enough to assign with any certainty, so was left out of the fit. The E_{VB} of the interface lies between those of the two layers, at 0.93 eV.

6.3.5 Constructing the Band Diagram

In order to determine the conduction band offset (CBO) of the interface, the optical band gap was measured using a Tauc Plot conversion of the UV-vis absorbance spectrum for each of the materials, as seen in Figure 6.7. Linear extrapolation of the linear portion of the Tauc Plot yields the optical band gap of the material in question. The CZTS (Figure 6.7A) has a band gap of 1.41 eV, which corresponds with excitation energies just slightly smaller than the most intense region of the solar spectrum.⁶⁷ As such, the material is ideally suited to maximize solar absorbance and promote large quantities of electrons into the CZTS conduction band. These electrons will then ideally flow to a well matched CdS conduction band at an energy level slightly below that of the CZTS conduction band.^{11, 68-}
⁶⁹ The CdS (Figure 6.7B) has a much wider band gap than CZTS, at 2.21 eV, and will therefore allow photons to reach the CZTS for absorption, and also prevent electron back-flow by creating a wide gap between the CZTS VB and CdS VB.

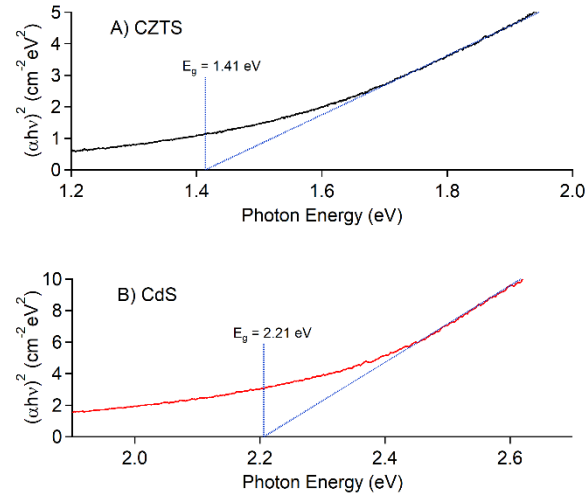


Figure 6.7 Optical band gap as measured via Tauc Plot conversion of the UV-vis absorbance spectrum of (A) CZTS, and (B) CdS.

From these measurements, the E_{VB} and E_{CB} can be utilized to determine the band banding, and energy offsets between the core levels and the E_{VB} for each of the bulk materials.^{11, 62, 65, 70} The energy barrier for the valance bands at the interface, EB_{VB} , was calculated via (6.1), and is a measure of the energy difference between the E_{VB} values (relative to E_F) of the two materials (Figure 6.2E and Figure 6.4C) accounting for the band bending that arises from the unequal charge distribution created in the SCR relative to the bulk materials, when the CZTS and CdS are in contact.¹²

$$EB_{VB} = E_{VB}^{CdS} - E_{VB}^{CZTS} + E_{band\ bending} \quad (6.1)$$

The band bending is a measure of the energy difference between the CL of an atom in the bulk, and at the interface, and is defined by (6.2).

$$E_{band\ bending} = \left(E_{Sn_{3d}}^{CZTS} - E_{Sn_{3d}}^{Interface} \right) + \left(E_{Cd_{3d}}^{Interface} - E_{Cd_{3d}}^{CdS} \right) \quad (6.2)$$

In this way, using the values measured above, a band bending of -0.4 eV is obtained. In this case, the negative sign indicates a bend to a larger E_{VB} at the interface. This then gives an EB_{VB} of 0.56 eV, in a cliff-like setup. The EB_{CB} can then be calculated using the band gaps of the two materials, according to (6.3).³

$$EB_{CB} = E_g^{CZTS} - E_g^{CdS} + EB_{VB} \quad (6.3)$$

Based on the E_g measurements (Figure 6.8), the EB_{CB} is 0.24 eV in a spike-like setup.

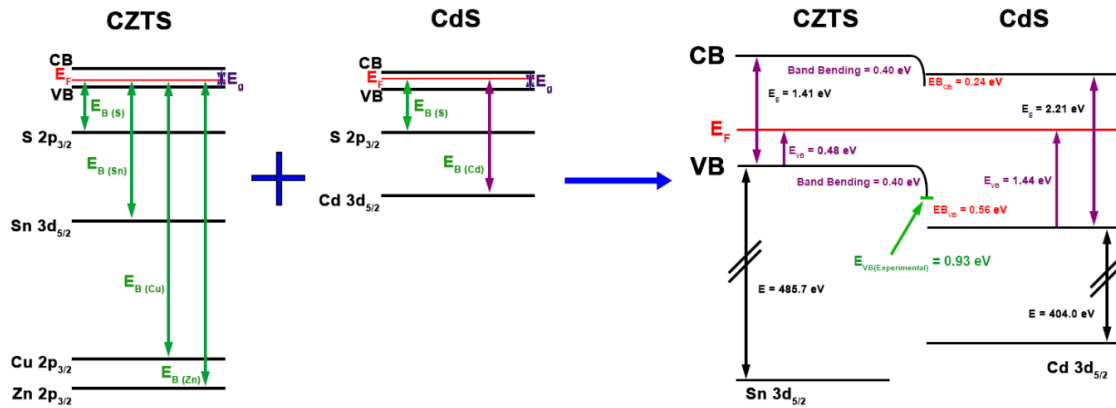


Figure 6.8 Band diagram schematic of the CZTS layer, CdS layer, and CZTS-CdS interface, with energy values included for each. The band gap region of the interface has been expanded for enhanced viewing, and thus the energy scale for the CL beneath it has been truncated, as indicated by the double hashed lines.

Using these values, the band diagram for the interface was constructed, as shown in Figure 6.8. From the determined interfacial band diagram, it is clear that the bulk CdS has a much lower CB than CZTS, as is often the case reported in literature. Yan *et al.* gave a good explanation for this band structure, and why it forms a cliff-like CBO, where the CdS CB is lower in energy than that of CZTS, and reported cliff-like EB_{CB} of 0.24 eV.⁶⁵ Santoni *et al.* report a cliff-like EB_{CB} of 0.34 eV, which is significantly larger, and Bär *et al.* report a similar cliff-like EB_{CB} of 0.30 eV.^{11, 71} This type of interface results in reduced open-circuit potentials, and thus lower device efficiencies with an increased charge recombination via defects at the interface.^{3, 65} The authors correctly assert this as a flaw in the fabrication, with Yan *et al.* reporting alternative buffer layers to obtain better overlap, and create a spike-like interface instead. This can be contrasted with Haight *et al.*, who report a spike-like EB_{CB} of 0.41 eV.⁷² Spike-like barriers do not have the effect of reducing the open-circuit potential, and can be easily overcome without increased geminate recombination if the spike is not too large. This wide variation in

reported EB_{CB} is the result of differences in the structural properties of both the CZTS and CdS materials, and their surfaces at the interface. The materials presented herein were specifically engineered to form desirable structures, based on previous studies with nanocrystalline CZTS,³⁸⁻⁴⁰ and using the knowledge presented by Yan *et al.*, Santoni *et al.*, or Haight *et al.*, to orchestrate the formation of an ideal band alignment. The band gap of the CZTS was designed to be smaller than reported by these three groups, to lower the conduction band relative to the Fermi level, by introducing the V'_{Cu} . The CdS was then engineered to have a smaller E_{VB} than the values reported above. By reducing the E_{VB} , the material is not as strong an n-type semiconductor, but will have a more favorable alignment at the CB level. As Figure 6.8 clearly shows, the CZTS band bending results in a small spike-like barrier between the lowest level of CZTS CB, and the onset of the CdS CB. A spike-like EB_{CB} of 0.24 eV was calculated at the interface (Figure 6.8), which is within the desired range to obtain high efficiency CZTS.^{3,5} Coupled with the V'_{Cu} rich CZTS, the potential for recombination sites within the band gap is limited to the Zn^{\bullet}_{Cu} antisites. As specified earlier, these antisites are less common than V'_{Cu} in the film (Figure 6.1), which should limit the potential for recombination through interfacial defects. Furthermore, the calculated band bending would yield an interfacial EB_{VB} of 0.88 eV, which matches well with the measured interfacial EB_{VB} of 0.93 eV. From the measured E_{VB} at the interface, the band bending can be measured directly, using (6.4).

$$EB_{VB} = E_{VB}^{CZTS} + E_{band\ bending} \quad (6.4)$$

The measured $E_{VB(interface)}$ and $E_{VB(CZTS)}$ then yield a 0.45 eV band bending away from E_F . This matches well with the 0.40 eV bending calculated from the bulk measurements, and further confirms that the interfacial VB does indeed capture the true interfacial states. Using this value, the EB_{CB} is found to be 0.19 eV. Both values for EB_{CB} create the same ideal spike-like barrier to prevent recombination at the interface, and support high V_{oc} in a device fabricated with this structure. The high degree of similarity between both calculated and measured band bending, and subsequent EB_{VB} , is also strong evidence that the measured V'_{Cu} at the interfacial surface are not ubiquitous, but as expected, are scattered periodically throughout the film. This would also indicate that the antisites are

even less common. These films are therefore anticipated to provide ideal charge-carrier flow through the interface, and limit recombination sites at the CZTS surface.

6.4 Conclusions

Inexpensive 1 μm thick CZTS films were fabricated using sequentially galvanostatic deposition of Cu, Sn, and Zn films on molybdenum coated glass and sulfurization based on our knowledge for forming efficient CZTS nanocrystals (Cu poor for V'_{Cu} and $Zn\bullet_{\text{Cu}}$ antisites). The desired compositions and bonding were ascertained by synchrotron spectroscopy. These stoichiometric compositions are very similar to those of our CZTS nanocrystals published elsewhere. The CZTS crystal structure and valence band matched very well with the theoretical DOS for the kesterite CZTS model, derived through DFT using GGA. These structural features were then examined for their effects on the valence band structure, confirming that Cu plays a major role in determining the E_{VB} . It was discovered by XPS and UV-vis spectroscopy that the prepared CZTS crystalline layer has a band gap of 1.41 eV with a E_{VB} of 0.48 eV below E_{F} and E_{CB} of 0.93 eV above E_{F} , demonstrating a more p-type character in the film, which will result in a greater decrease in the CBO relative to the Fermi level in the SCR.

50 nm thick CdS layers were prepared via an optimized CBD. The bandgap of the CdS buffer layer was 2.21 eV, and the E_{VB} and E_{CB} were determined as 1.44 eV below, and 0.77 eV above, the Fermi level, respectively. The CdS bonding and band structures demonstrate a less n-type character.

These two above materials, once in contact, create a potential for a stronger SCR, and thus a great charge-carrier flow across the interface, due to the spike-like setup. These were determined from the band structures of both materials and their junction. A calculated EB_{CB} of 0.24 eV was achieved, which shows a small spike-like interface in the conduction band overlap, and helps to maintain a strong internal bias, while keeping the energy barrier small enough to prevent large-scale recombination from occurring. The same is true for the 0.19 eV EB_{CB} determined using the directly measured E_{VB} . This creates an ideal environment for charge carrier separations, while the structural

components enhance the photo-excitation of electrons. The presented materials junction is anticipated to have a great V_{oc} in a solar cell device.

6.5 References

1. Ansari, M. Z.; Khare, N., *J. Phys. D* **2014**, *47*, 185101.
2. Chen, S.; Walsh, A.; Gong, X. G.; Wei, S. H., *Adv. Mater.* **2013**, *25*, 1522.
3. Sun, K.; Yan, C.; Liu, F.; Huang, J.; Zhou, F.; Stride, J. A.; Green, M.; Hao, X., *Adv. Energy Mater.* **2016**, *6*, 1600046.
4. Zhang, X.; Han, M.; Zeng, Z.; Lin, H. Q., *RSC Adv.* **2016**, *6*, 15424.
5. Gao, S. S.; Jiang, Z. W.; Wu, L.; Ao, J. P.; Zeng, Y.; Sun, Y.; Zhang, Y., *Chin. Phys. B* **2018**, *27*, 018803.
6. Kumar, M.; Dubey, A.; Adhikari, N.; Venkatesan, S.; Qiao, Q., *Energy Environ. Sci.* **2015**, *8*, 3134.
7. Khallaf, H.; Oladeji, I. O.; Chai, G.; Chow, L., *Thin Solid Films* **2008**, *516*, 7306.
8. Moualkia, H.; Hariech, S.; Aida, M. S., *Thin Solid Films* **2009**, *518*, 1259.
9. Liu, F.; Lai, Y.; Liu, J.; Wang, B.; Kuang, S.; Zhang, Z.; Li, J.; Liu, Y., *J. Alloys Compd.* **2010**, *493*, 305.
10. Sun, K.; Huang, J.; Yan, C.; Pu, A.; Liu, F.; Sun, H.; Liu, X.; Fang, Z.; Stride, J. A.; Green, M.; Hao, X., *Chem. Mater.* **2018**, *30*, 4008.
11. Santoni, A.; Biccari, F.; Malerba, C.; Valentini, M.; Chierchia, R.; Mittiga, A., *J. Phys. D* **2013**, *46*, 175101.
12. Bard, A. J.; Faulkner, L. R., *Electrochemical Methods: Fundamentals and Applications, 2nd Edition*; John Wiley & Sons, 2000.
13. Wang, W.; Winkler, M. T.; Gunawan, O.; Gokmen, T.; Todorov, T. K.; Zhu, Y.; Mitzi, D. B., *Adv. Energy Mater.* **2014**, *4*, 1301465.
14. Stöhr, J., *NEXAFS Spectroscopy*; Springer: Berlin, Germany, 1992.
15. Teo, B. K., *EXAFS: Basic Principles and Data Analysis*; Springer: Berlin, 1986.
16. Ravel, B.; Newville, M., *J. Synchrotron Radiat.* **2005**, *12*, 537.
17. Bosson, C. J.; Birch, M. T.; Halliday, D. P.; Tang, C. C.; Kleppe, A. K.; Hatton, P. D., *Chem. Mater.* **2017**, *29*, 9829.
18. Ye, H.; Park, H. S.; Ajhavan, V. A.; Goodfellow, B. W.; Panthani, M. G.; Korgel, B. A.; Bard, A. J., *J. Phys. Chem. C* **2011**, *115*, 234.
19. Chavez, K. L.; Hess, D. W., *J. Electrochem. Soc.* **2001**, *148*, G640.
20. Zarghami, M. H.; Liu, Y.; Gibbs, M.; Gebremichael, E.; Webster, C.; Law, M., *ACS Nano* **2010**, *4*, 2475.

21. Chen, R. R.; Fan, J. D.; Li, H. L.; Liu, C.; Mai, Y. H., *Royal Soc. Open Sci.* **2018**, *5*, 171163.
22. Perini, L.; Vaccarello, D.; Martin, S.; Jeffs, K.; Ding, Z., *J. Electrochem. Soc.* **2016**, *163*, H3110.
23. Turnbull, M. J.; Vaccarello, D.; Wong, J.; Yiu, Y. M.; Sham, T. K.; Ding, Z., *J. Chem. Phys.* **2018**, *148*, 134702.
24. Blaha, P.; Schwarz, K.; Sorantin, P.; Trickey, S. B., *Comput. Phys. Commun.* **1990**, *59*, 399.
25. Kohn, W.; Sham, L. J., *Phys. Rev.* **1965**, *140*, A1133.
26. Langreth, D. C.; Mehl, M. J., *Phys. Rev. B* **1983**, *28*, 1809.
27. Brandenburg, J. G.; Maas, T.; Grimme, S., *J. Chem. Phys.* **2015**, *142*, 124104.
28. Perdew, J. P.; Wang, Y., *Phys. Rev. B* **1992**, *45*, 13244.
29. Rehr, J. J.; Albers, R. C., *Rev. Mod. Phys.* **2000**, *72*, 621.
30. Werner, W. S. M., *Surf. Interface Anal.* **1992**, *18*, 217.
31. Mazalova, V. L.; Soldatov, A. V., *J. Struct. Chem.* **2008**, *49*, 107.
32. Kau, L. S.; Spira-Solomon, D. J.; Penner-Hahn, J. E.; Hodgson, K. O.; Solomon, E. I., *J. Am. Chem. Soc.* **1987**, *109*, 6433.
33. Sarangi, R., *Coord. Chem. Rev.* **2013**, *257*, 459.
34. Sung, N. E.; Kang, S. W.; Shin, H. J.; Lee, H. K.; Lee, I. J., *Thin Solid Films* **2013**, *547*, 285.
35. Janak, J. F., *Phys. Rev. B* **1978**, *18*, 7165.
36. Lejaeghere, K.; Bihlmayer, G.; Bjorkman, T.; Blaha, P.; Blugel, S.; Blum, V.; Caliste, D.; Castelli, I. E.; Clark, S. J.; Dal Corso, A.; de Gironcoli, S.; Deutsch, T.; Dewhurst, J. K.; Di Marco, I.; Draxl, C.; Dulak, M.; Eriksson, O.; Flores-Livas, J. A.; Garrity, K. F.; Genovese, L.; Giannozzi, P.; Giantomassi, M.; Goedecker, S.; Gonze, X.; Granas, O.; Gross, E. K.; Gulans, A.; Gygi, F.; Hamann, D. R.; Hasnip, P. J.; Holzwarth, N. A.; Iusan, D.; Jochym, D. B.; Jollet, F.; Jones, D.; Kresse, G.; Koepf, K.; Kucukbenli, E.; Kvashnin, Y. O.; Loch, I. L.; Lubeck, S.; Marsman, M.; Marzari, N.; Nitzsche, U.; Nordstrom, L.; Ozaki, T.; Paulatto, L.; Pickard, C. J.; Poelmans, W.; Probert, M. I.; Refson, K.; Richter, M.; Rignanese, G. M.; Saha, S.; Scheffler, M.; Schlipf, M.; Schwarz, K.; Sharma, S.; Tavazza, F.; Thunstrom, P.; Tkatchenko, A.; Torrent, M.; Vanderbilt, D.; van Setten, M. J.; Van Speybroeck, V.; Wills, J. M.; Yates, J. R.; Zhang, G. X.; Cottenier, S., *Science* **2016**, *351*, aad3000.
37. Al-Ebraheem, A.; Goettlicher, J.; Geraki, K.; Ralph, S.; Farquharson, M. J., *X-Ray Spectrom.* **2010**, *39*, 332.
38. Turnbull, M. J.; Khoshmashrab, S.; Wang, Z.; Harbottle, R.; Sham, T. K.; Ding, Z., *Catal. Today* **2016**, *260*, 119.

39. Khoshmashrab, S.; Turnbull, M. J.; Vaccarello, D.; Nie, Y.; Martin, S.; Love, D. A.; Lau, P. K.; Sun, X.; Ding, Z., *Electrochim. Acta* **2015**, *162*, 176.
40. Turnbull, M. J.; Vaccarello, D.; Yiu, Y. M.; Sham, T. K.; Ding, Z., *J. Chem. Phys.* **2016**, *145*, 204702.
41. Turnbull, M. J.; Khoshmashrab, S.; Yiu, Y. M.; Ding, Z., *Can. J. Chem.* **2018**, *1*.
42. Nagoya, A.; Asahi, R.; Wahl, R.; Kresse, G., *Phys. Rev. B* **2010**, *81*, 113202.
43. Scragg, J. J. S.; Larsen, J. K.; Kumar, M.; Persson, C.; Sendler, J.; Siebentritt, S.; Björkman, C. P., *Phys. Status Solidi B* **2016**, *253*, 247.
44. Chen, S. Y.; Yang, J. H.; Gong, X. G.; Walsh, A.; Wei, S. H., *Phys. Rev. B* **2010**, *81*, 245204.
45. Scragg, J. J.; Dale, P. J.; Peter, L. M., *Thin Solid Films* **2009**, *517*, 2481.
46. Sai Gautam, G.; Senftle, T. P.; Carter, E. A., *Chem. Mater.* **2018**, *30*, 4543.
47. Bareño, J.; Balasubramanian, M.; Kang, S. H.; Wen, J. G.; Lei, C. H.; Pol, S. V.; Petrov, I.; Abraham, D. P., *Chem. Mater.* **2011**, *23*, 2039.
48. Stillman, M. J.; Presta, A.; Gui, Z.; Jiang, D. T., *Met. Based Drugs* **1994**, *1*, 375.
49. Ji, Y.; Du, Y.; Wang, M., *Sci. World J.* **2014**, *2014*, 490853.
50. Zhang, S. B.; Wei, S. H.; Zunger, A.; Katayama-Yoshida, H., *Phys. Rev. B* **1998**, *57*, 9642.
51. Gorczyca, I.; Svane, A.; Christensen, N. E., *Phys. Rev. B* **1999**, *60*, 8147.
52. Zhong, G.; Tse, K.; Zhang, Y.; Li, X.; Huang, L.; Yang, C.; Zhu, J.; Zeng, Z.; Zhang, Z.; Xiao, X., *Thin Solid Films* **2016**, *603*, 224.
53. Reshak, A. H.; Nouneh, K.; Kityk, I. V.; Bila, J.; Auluck, S.; Kamarudin, H.; Sekkat, Z., *Int. J. Electrochem. Sci* **2014**, *9*, 955.
54. Kaur, K.; Sood, M.; Kumar, N.; Nazari, H. H.; Gudavalli, G. S.; Dhakal, T. P.; Kumar, M., *Sol. Energy Mater. Sol. Cells* **2018**, *179*, 22.
55. Vaccarello, D.; Liu, L.; Zhou, J.; Sham, T. K.; Ding, Z., *J. Phys. Chem. C* **2015**, *119*, 11922.
56. Yu, J.; Zheng, Z.; Dong, L.; Cheng, S.; Lai, Y.; Zheng, Q.; Zhou, H.; Jia, H.; Zhang, H., *Chin. Phys. B* **2017**, *26*, 046802.
57. Shin, S. W.; Pawar, S. M.; Park, C. Y.; Yun, J. H.; Moon, J. H.; Kim, J. H.; Lee, J. Y., *Sol. Energy Mater. Sol. Cells* **2011**, *95*, 3202.
58. Vaccarello, D.; Tapley, A.; Ding, Z., *RSC Adv.* **2013**, *3*, 3512.
59. Sarker, P.; Al-Jassim, M. M.; Huda, M. N., *J. Appl. Phys.* **2015**, *117*, 035702.
60. Jiang, H.; Dai, P.; Feng, Z.; Fan, W.; Zhan, J., *J. Mater. Chem.* **2012**, *22*, 7502.
61. Chen, H. J.; Fu, S. W.; Wu, S. H.; Tsai, T. C.; Wu, H. T.; Shih, C. F., *J. Phys. D* **2016**, *49*, 335102.

62. Dong, Z. Y.; Li, Y. F.; Yao, B.; Ding, Z. H.; Yang, G.; Deng, R.; Fang, X.; Wei, Z. P.; Liu, L., *J. Phys. D* **2014**, *47*, 075304.
63. Andrews, J. L.; De Jesus, L. R.; Tolhurst, T. M.; Marley, P. M.; Moewes, A.; Banerjee, S., *Chem. Mater.* **2017**, *29*, 3285.
64. Mitzi, D. B.; Gunawan, O.; Todorov, T. K.; Wang, K.; Guha, S., *Sol. Energy Mater. Sol. Cells* **2011**, *95*, 1421.
65. Yan, C.; Liu, F.; Song, N.; K. Ng, B.; Stride, J.; Tadich, A.; Hao, X., *Appl. Phys. Lett.* **2014**, *104*, 173901.
66. Kaur, K.; Kumar, N.; Kumar, M., *J. Mater. Chem. A* **2017**, *5*, 3069.
67. Guo, Q.; Ford, G. M.; Yang, W. C.; Walker, B. C.; Stach, E. A.; Hillhouse, H. W.; Agrawal, R., *J. Am. Chem. Soc.* **2010**, *132*, 17384.
68. Tetiana, O.; Archana, M.; Claudia, D.; Wolfram, C.; Bünyamin, Ü.; Vladimir, P.; Binoy, C.; Haibing, X.; Edgardo, S.; Laura Elisa, V.-R.; Kai, N.; Susan, S.; Martha Ch, L.-S.; Iver, L., *Semicond. Sci. Technol.* **2017**, *32*, 104010.
69. Tc, S. K.; Gupta, G., *RSC Adv.* **2014**, *4*, 27308.
70. Yang, G.; Li, Y. F.; Yao, B.; Ding, Z. H.; Deng, R.; Qin, J. M.; Fang, F.; Fang, X.; Wei, Z. P.; Liu, L., *J. Alloys Compd.* **2015**, *628*, 293.
71. Bär, M.; Schubert, B. A.; Marsen, B.; Wilks, R. G.; Pookpanratana, S.; Blum, M.; Krause, S.; Unold, T.; Yang, W.; Weinhardt, L.; Heske, C.; Schock, H. W., *Appl. Phys. Lett.* **2011**, *99*, 222105.
72. Haight, R.; Barkhouse, A.; Gunawan, O.; Shin, B.; Copel, M.; Hopstaken, M.; Mitzi, D. B., *Appl. Phys. Lett.* **2011**, *98*, 253502.

Chapter 7

7 Constructing the Efficient CZTS Solar Cell

Assembling specifically designed $\text{Cu}_2\text{ZnSnS}_4$ (CZTS) and CdS films to form either spike-like or cliff-like barriers at their interface can be controlled by means of a novel, inexpensive, and environmentally friendly etching process. The photoresponse was analyzed for the CZTS, and the CZTS/CdS films of the two barrier types using solution-phase photoelectrochemical measurements (PECMs). The valence band (VB) structure was evaluated before and after etching to correlate the photoresponse to structural properties in the films, using synchrotron-based (SR) X-ray Photoelectron Spectroscopy (SR-XPS). The band structures of the CZTS, CdS, ZnO, and Al-doped ZnO (AZO) were assessed by SR-XPS and UV-vis absorbance spectra, and a full band diagram was constructed in each situation. Thin-film solar cell devices based on both the spike-like and cliff-like configurations of the CZTS/CdS heterojunction were fabricated, and the device efficiency evaluated against the PECM and structural components to optimize device performance. It turns out that this layer-by-layer construction, and interfacial optimization produced an open-circuit potential (V_{oc}) of 0.85 V, the highest reported to date for pure sulfide kesterite CZTS, and a high efficiency of 8.48%.

7.1 Introduction

Previous Chapters have focused extensively on the control of the CZTS layer, and of the various defects that form as a result of the methods used, and tuning this to obtain an ideal p-n junction.¹⁻² An effective p-n junction will ensure maximal charge-carrier flux out of the CZTS, provided the interface lacks in charge-carrier trap sites.³ To do this, the junction should also have a small spike-like barrier at the CZTS/CdS interface.⁴⁻⁵ When small enough, this still allows for photoexcited electrons to move across the films, but avoids the recombination commonly associated with cliff-like barriers.⁶⁻⁷ Spike-like barriers will therefore help maintain high V_{oc} , and result in enhanced efficiencies in CZTS-based devices. This is still only half of the problem though. The fabrication of these devices, and subsequent control of both the interface and structural design, must employ low-cost, uncomplicated methods and environments to remain within the

expectations of the long-term goal of cost reduction. To this end, the use of dangerous, harsh, or costly treatments, such as KCN etching,⁸ or H₂S usage,⁹ must be avoided.

In this Chapter, CZTS films were fabricated using electrochemical deposition of Cu, Sn, and Zn films on Mo-coated glass, to a highly specific elemental composition, and a thickness of 1 μm . The surface of the film was etched with glacial acetic acid, and a 50 nm coating of CdS was applied on the etched surface through chemical bath deposition (CBD). To this was added 50 nm of ZnO, and then 250 nm of Al-doped ZnO (AZO). These films were contrasted against those that did not undergo chemical etching. Through cooperative usage of SR and benchtop X-ray Photoelectron Spectroscopy (SR-XPS and XPS), and UV-vis absorption, a total scheme of the device band structure for each was constructed finely, and used to understand the electron flow through the CZTS layer, and other three layers of the full fabricated device. It was discovered that the acetic acid etching greatly augments the photoresponse in the CZTS, and produces an enhancement in both the V_{oc} and device efficiency, through alterations in the band alignment that are crucial to the formation of the desired spike-like band structure in space-charge region (SRC).

7.2 Experimental

7.2.1 Solar Cell Fabrication

CZTS and CdS films were fabricated using the methods presented in Chapter 6.2.1. Glacial acetic acid was used to etch the surface in place of the 0.5 mol/L.

An Ultratech/CambridgeNanotech Savannah S200 atomic layer deposition instrument (ALD) (Waltham, MA) was used for deposition of both ZnO and AZO. Initially, the samples were placed in the chamber, pumped down to 0.04 torr, heated to 200 °C, and held for 1 hour to remove the H₂O intercalation caused by CBD as we reported elsewhere.² For deposition, a 5 sccm flow of high purity nitrogen gas (Praxair, 99.999%), and the reactor temperature of 300 °C, was held throughout the process. Alternating 0.15 s pulses of diethylzinc (Strem Chemicals, min. 95%) and Type 1 water (Milli-Q Ultrapure Water Systems, Millipore Corp. Germany), with a 10 s wait between pulses, were used to produce the ZnO film at a 1.6 Å/cycle growth rate. This was

deposited on top of the CdS layer, to a thickness of 50 nm. The AZO layer was deposited on the ZnO, to a thickness of 250 nm. 4.7% Al-doping was achieved through the addition of an extra pulse cycle added between two sets of 10 cycles of ZnO. This extra pulse consisted of a 0.15 s pulse of trimethylaluminum (Strem Chemicals, min. 98%), a 10 s wait between pulses, and a 0.15 s pulse of Type 1 water. The total 20 pulse cycles of ZnO, and 1 pulse cycle of Al-doping, produces AZO at a 33.1 Å/cycle growth rate. Completed films were cooled to 200 °C, and left under vacuum at 0.04 torr for one hour.

7.2.2 Characterization

Photoelectrochemical measurements (PECMs) were carried out to assess the film quality of the CZTS, and of the half-device following CdS deposition,¹⁰ using the method described in Chapter 1.4.1.

XPS was carried out using a Kratos AXIS Ultra Spectrometer, with an Al K α monochromatic source, and using the same parameters described in Chapter 6.2.2. SR-XPS was carried out at the Canadian Light Source on the Variable Line Spacing Plane Grating Monochromator (VLS-PGM, 11ID-2) beamline. Measurements were taken at a flux $> 1 \times 10^{11}$ on a $500 \times 500 \mu\text{m}$ spot size. Incoming photons were set at 225 eV. The beam energy was calibrated using gold foil at the Au Fermi level (E_F) emission. The valence band binding energy has been measured relative to the E_F of a clean Mo film in good electrical contact with the sample. Band gap measurements were taken using a Varian Cary 50 UV-vis absorption spectrometer. Absorption spectra were converted to Tauc plots, relating the absorption coefficient to the wavelength energy.

Full cell conversion efficiency of the final device was carried out again using the 150 W Newport lamp with 1.5 D filter and 100 mW/cm^2 . J-V measurements were taken using an IVIUM CompactStat (Netherlands).

7.3 Results and Discussion

7.3.1 CZTS/CdS Interface

Fabrication of an efficient device requires maximum photoexcitation and extraction of electrons from the CZTS. Figure 7.1 shows the photoresponse for both etched and non-etched CZTS films, both with and without CdS.

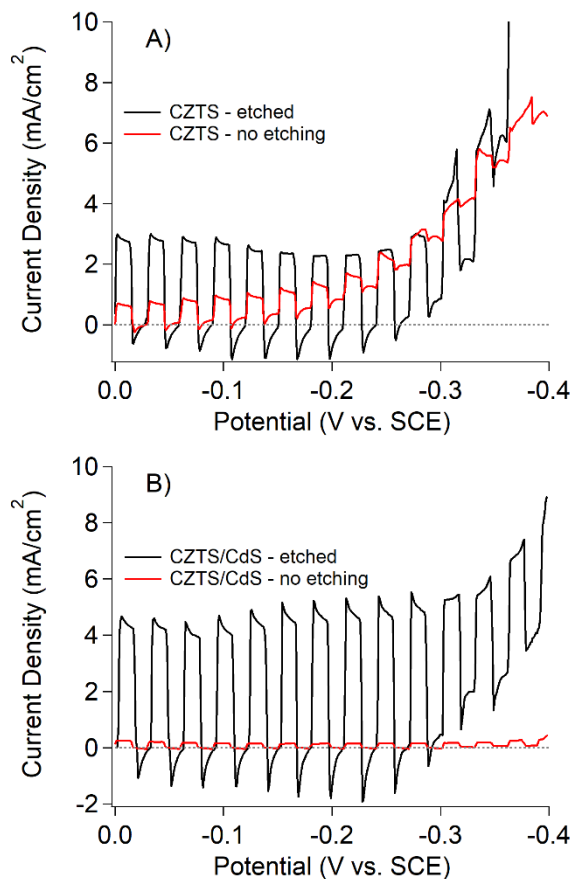


Figure 7.1 PECMs of A) CZTS only, and B) CZTS with CdS on top. Cleaning the CZTS surface (black) using a glacial acetic acid etch leads to increased current density relative to analogous films of uncleaned CZTS (red).

In each case, the current density increases rapidly when the light was turned on, and dropped back down to near zero when the light was turned off. This constitutes the current density change upon illumination, as electrons are transferred from the film into the MV^{2+} in the solution, reducing it to MV^+ .¹¹ Under illumination, the current density of

the non-etched film is 0.85 mA/cm^2 , whereas the etched film shows 2.75 mA/cm^2 . Both the etched (Figure 7.1A red) and non-etched (Figure 7.1A black) films show slow increases in the dark current at higher potentials. This occurs as the applied potential causes a shift in the p-type CZTS film from a Schottky junction to an Ohmic junction with the solution.¹² Charges are contained by the capacitance of the Schottky junction, and they begin to flow freely through the film in the Ohmic.¹²⁻¹³ This loss of capacitance occurs much quicker in the non-etched film, which would contribute to reduced open-circuit potentials (V_{oc}) in the final device. The etched surface does not have this problem. With the increased photoresponse and greater capacitance, the etching process appears to be removing many of the traps and barriers to electron flow. Thus the increased photoresponse is based on the increased conversion of photons to electrons, through a large reduction in geminate recombination and trap-induced obstruction of charge-carrier flow. This can be further explored through the transients following each change in light stimulus. There is an overshoot present in both of the transients of the two films, denoted as a decay in the current density following an initial spike when the light was turned on or off. This overshoot is indicative of a partial recombination of charge carriers, where the relative rate of recombination to the rate of charge-carrier separation is indicated by the steepness of the decay.^{10, 14} Under illumination, both films show limited current decay from the onset of the light stimulus. As such, the rates of separation are higher than those of recombination, though both processes are still occurring. Under dark conditions, the depletion of charges in the conduction band appears to result in the recombination rate overtaking that of product separation, and leads to a complete decay back to zero, while the film remains a Schottky junction. This is more pronounced in the etched CZTS. The implication is then the barriers inhibiting charge-carrier flow are more limited in the etched film, and the total geminate recombination is lower. This provides a stronger basis on which to construct the device.

The addition of the n-type CdS layer then created a p-n junction, and should enhance the photoresponse due to the creation of a depletion region at the interface, as majority-charges in both films diffuse across into the neighboring film.^{10, 15-17} This established an internal potential that would aid in charge-carrier separation.^{14, 17} In the presence of charge-carrier traps at the interface, however, the initial diffusion of charges would be

limited, creating a weaker internal potential, and lead to decreased photoresponse.^{14, 18} The etched sample (Figure 7.1B black) shows the expected enhancement, with a photoresponse of 4.67 mA/cm^2 . The transients show a steeper decay following photoresponse onset, indicating a higher rate of recombination relative to product separation in contrast to the film without CdS; however, the decay is still far more pronounced in the dark. Product separation must still be outcompeting recombination under illumination, as described by Peter *et al.*, and by Bard and Faulkner.^{11, 19-20} As such, this film provides strong photoresponse, and high product separation. The addition of CdS to the non-etched sample reduces the photoresponse to 0.18 mA/cm^2 . Though it eliminates much of the recombinatory decay seen in the other samples, the overall internal bias is greatly diminished relative to the etched CZTS, and thus the total barriers inhibiting charge-carrier flow are much higher. Electrons are not making out of the film due to these barriers, so it is likely that there are physical barriers, either through poor crystal overlaps or reduced film adhesion, present. The etching process clears up these barriers, and creates a much smoother transition from the CZTS to the CdS films.

The full device efficiency is highly dependent on the creation of a barrier free p-n junction.^{4, 21} The CZTS layer absorbs the photons, promoting electrons into the conduction band, and leaving behind an electron-depleted positively-charged 'hole'. These electron-hole pairs can then either recombine in the valence band, or separate to yield a current. On addition of the CdS layer, a p-n junction is created, which should enhance the current by creating a depletion region at the interface, setting up an internal bias that aids in driving separation of the charges.^{10, 22} These processes are mitigated by barriers, both physical and electrical, that either impede the flow of electrons at the interface, or provide alternative energy pathways that promote charge-carrier recombination. In both cases, solution-phase PECMs can be used to measure the separation and recombination processes, and evaluate the effectiveness of the junction.

Based on the enhanced photoresponse, the etching must be altering the structure of the surface. This should then be visible in the valence band of each film. Changes in the band structures in the CZTS film were probed using SR-XPS as shown in Figure 7.2.

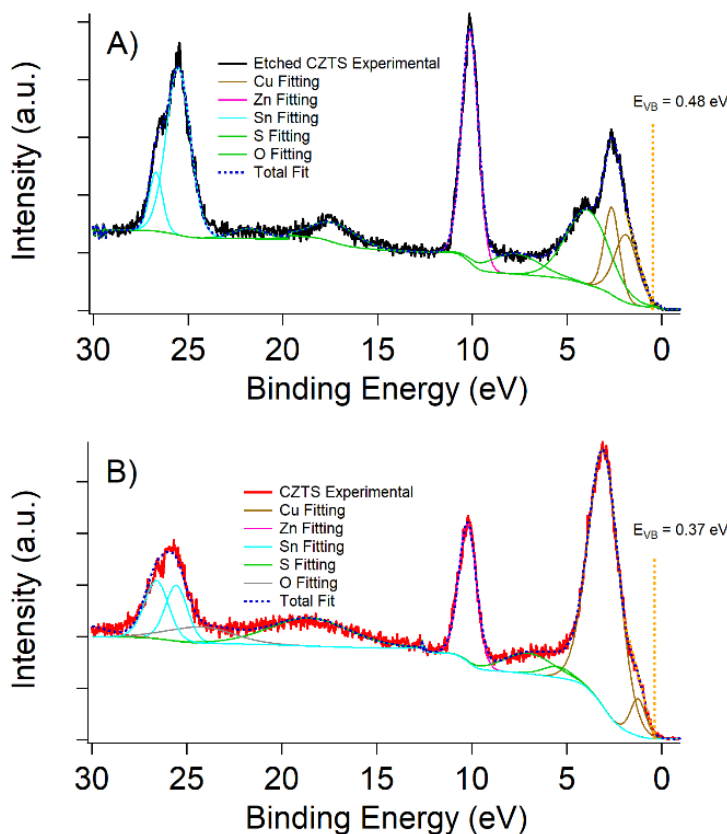


Figure 7.2 Valence band spectra of the A) etched, and B) non-etched CZTS film via SR-XPS. Linear extrapolation of the leading edge marks the valence band energy (E_{vB}).

In general, the CZTS VB is populated by the Cu and Zn 3d, and Sn 4d orbitals. The Cu states form the valence band onset, and so contribute most to the band kinetics observed in the PECM. The region from 0 – 5 eV is composed of many partial densities of state (DOS) that make up the band, and so cannot be fit by a simple Gaussian curves. The area has therefore been fit to show the three clusters within the band, and how they change relative to each other. None of these have been used for any sort of quantitative stoichiometry analysis.

Figure 7.2A shows an ordered valence band of the etched films. Here, the partial DOS again comprise the band region from 0 – 5 eV, with the two lowest clusters being dominated by Cu states. These no longer comprise the most intense peak, and show a

clear delineation between the Cu-dominated cluster, and the S-dominated cluster states, with the low-energy cluster peaks at 1.91 eV and 2.67 eV, and the S-dominated cluster peak at 4.07 eV. The peak at 1.91 eV is shifted to a higher binding energy relative to the non-etched sample, while the other two peaks drop to significantly lower binding energy. This puts the VB region into a more compact, more ordered band structure. The broad contribution from predominantly sulfur states about 7.51 eV are slightly higher as well, indicating that the etched surface has a greater p-type character, holding the sulfur atoms more tightly in the lattice. The Zn 3d peak at 10.15 eV is barely altered from the non-etched version, and shows only a small reduction in binding energy. These are the effects of the greater p-type character in the film.^{14, 18} The Sn 4d peaks also shift relatively slightly, with peaks at 25.47 eV and 26.69 eV. The peak at higher binding energy is also reduced drastically. In this case, where there are still two distinct Sn environments, with significantly less contribution from the higher binding energy region, there is more electron density shifted to the Sn sites, which mostly occurs through V'_{Cu} .^{17, 23-24}

Overall, the etched sample has a more ordered structure. This increased order would contribute favorably to the flow of charge-carriers across the interface, and is likely the main reason for the drastic enhancement of the CZTS photocurrent described in Figure 7.1A. The improved kinetics of the etched CZTS would then improve the CZTS/CdS interface charge-carrier transfer. This would constitute a more ideal interfacial region within the SCR, and should therefore yield superior device performance over the non-etched CZTS/CdS interface. In the non-etched sample (Figure 7.2B), the most intense cluster of states occurs at 3.12 eV. There is only a small shoulder at 1.25 eV. These present the case for a highly variable band, likely the result of a high concentration of detrimental Zn_{Cu}^{\bullet} and Cu_{Zn}' antisite pairs, given that the primary contributor to these clusters is the Cu partial DOS. The cluster primarily comprised of S states has become obscured within the broad cluster, with a peak at 5.51 eV, and therefore only contribute a small tailing to the main peak. There are also some partial sulfur states, as indicated by the peak at about 7.11 eV; however, this is far enough from the Cu-dominated cluster that it doesn't contribute to the broadness. The apparent non-equivalence in the Cu states would be the primary contributing factor to the peak broadness, and would also form a basis for the photocurrent decrease observed on CdS addition (Figure 7.1B red). The

effects of multiple Cu states have been studied extensively in literature,²³⁻²⁴ and have been shown to be detrimental to charge-carrier transfer, and limit the V_{oc} .²⁴⁻²⁵ The Zn peak is highly conserved at 10.21 eV, whereas the Sn-peak shows two distinct binding energies, at 26.57 eV and 26.73 eV. This occurs despite the relative stability of the Sn site. In order for the Sn 4d peaks to yield two peaks, the Sn centers must be in two distinct environments. Combined with the broadness in the Cu-dominated cluster, it is likely that the Cu'_{Zn} and V'_{Cu} on the surface are contributing to a highly non-uniform stoichiometry at the surface, and thus contributing to unequal paths for charge-carriers to travel. Furthermore, the intensity of the cluster relative to the rest of the spectrum is notably higher than expected.²⁶ This would suggest a Cu rich surface to these samples.

7.3.2 Solar Cell Band Structure

Charge-transfer through the film was examined via UV-vis absorption, and SR-XPS of the VB in each of the upper layers, which are presented in Figure 7.3. As seen in Figure 7.3A, the band gaps can be extracted by extrapolating to zero for the linear portion of the resulting spectra²⁷⁻²⁸ in Tauc plots. Increasing band gaps for each additional layer placed on top of the CZTS were determined. The CZTS had the smallest band gap, at 1.43 eV, and thus absorbs strongly in the most intense region of the solar spectra, followed by CdS at 2.20 eV, ZnO at 3.37 eV, and AZO at 3.41 eV. This increasing order confirms that the lower energy photons are indeed reaching the CZTS layer, and will induce photoexcitation much the same as was observed in the PECMs (Figure 7.1). It is important to note that the E_g is highly tunable, and that the displayed plot is of a highly controlled CZTS film, designed to contain such a gap, using the knowledge based on CZTS nanocrystals.²⁹⁻³² Likewise, the CdS band was engineered to yield a slightly lower E_g to better align with the CZTS bands.

A similar trend can be observed for the valance band energy values, E_{VB} , of the films (Figure 7.3B). The CdS E_{VB} was determined to be at 1.44 eV, more than 1 eV further from the E_F than was seen for the non-etched CZTS (Figure 7.2B), and 0.96 eV back from the etched CZTS (Figure 7.2A). The CdS E_{VB} is, by design, shallower than many others in literature so as to better align the bands with the CZTS, and intelligently form the optimal interface. This ensures that there is a large gap between the VB of the bulk

CZTS, and bulk CdS, which will inhibit the back-flow of charges after a depletion region has been established, and increase the capacitance of the film.^{14, 33-34} Furthermore, it will create a good internal bias, and thus increased band bending at the interface. The ZnO and AZO (Figure 7.3B) show the same trend, with a much further E_{VB} values relative to the CdS, and thus should result in unimpeded electron flow into the ZnO layer, and then through the AZO and out of the device for extraction. A VB offset is not observed in the ZnO/AZO interface; however, thermal and electrical stability of ZnO are not achieved without the addition of a dopant.^{28, 35} Thus, these two layers are coupled to allow for sustained electron extraction from the conduction bands, which provides durability to the devices.

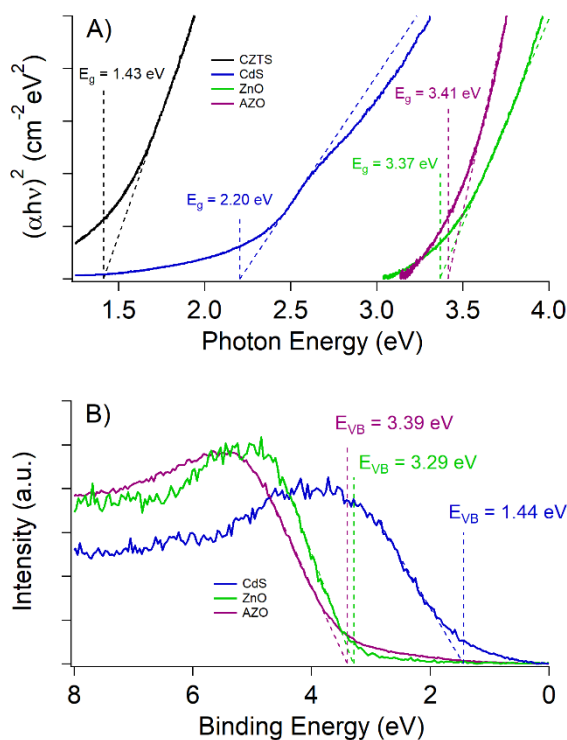


Figure 7.3 The A) Tauc plots of the UV-vis absorbance showing the optical band gap for all films in the full device, and B) the VB energy (E_{VB}) for each of the films placed above the CZTS layer.

The final device efficiency is affected mainly by the CZTS-CdS interface. The charge-carrier (electron) flow through the conduction band of each subsequent layer is crucial to

the final device performance, and therefore an ideal band alignment is required to prevent large energy barriers from detracting from the final device.³⁶⁻³⁷ In fact, the full device consists of a CZTS/CdS/ZnO/Al-doped ZnO (AZO) thin film stack. In order to be effective, photons must be able to pass through each of the upper layers so as to reach the CZTS layer and induce photoexcitation, after which charge separation can occur as previously described.^{18, 36-37} The photoexcited electron must then travel through the upper films to generate current. As such, both resistivity and charge-carrier traps in the upper layers will cause loss of conversion efficiency.³⁸

These band features were then coupled together to produce the extended band diagram (Figure 7.4), and thereby the final charge-carrier pathway through the device can be examined. As shown in Figure 7.4, the CZTS films are a p-type semiconductor in both the etched and non-etched form, having a VB closer to E_F . All three other layers are n-type, having a conduction band (CB) closer to E_F . At both the CZTS/CdS, and CdS/ZnO interfaces, the wide VB energy barrier (EB_{VB}) ensures the diode-like nature of the device, and keeps charge carriers moving from the AZO towards CZTS layer. In the etched CZTS (Figure 7.4A), the CZTS/CdS interface features a small spike-like CB energy barrier (EB_{CB}), whereas the non-etched CZTS (Figure 7.4B) yields a cliff-like EB_{CB} . Both types of interfaces have been reported for the CZTS/CdS interface, spike-like by Haight *et al.*,³⁹ and cliff-like by Sun *et al.* and Dong *et al.*,⁴⁰⁻⁴¹ and appear highly connected to the structure at the interface.

The contrast between the two films are therefore highly predictive of the eventual device output. The drop in energy in a cliff-like interface, though a small one, from the CZTS to the CdS (Figure 7.4B), promotes defect-induced charge-carrier recombination at the interface.⁴⁰ This has the effect of reducing the effective charge redistribution across the SCR, and lowering the V_{oc} . Due to the relatively close proximity of the two bands at the interface, etching the CZTS moves the band structure from a small cliff-like interface, to a spike-like interface, and is therefore the reason for the enhanced photocurrent (Figure 7.1 black) observed in these samples. It also explains why the CdS layer applied to the non-etched sample causes a reduction in photocurrent (Figure 7.1B red).

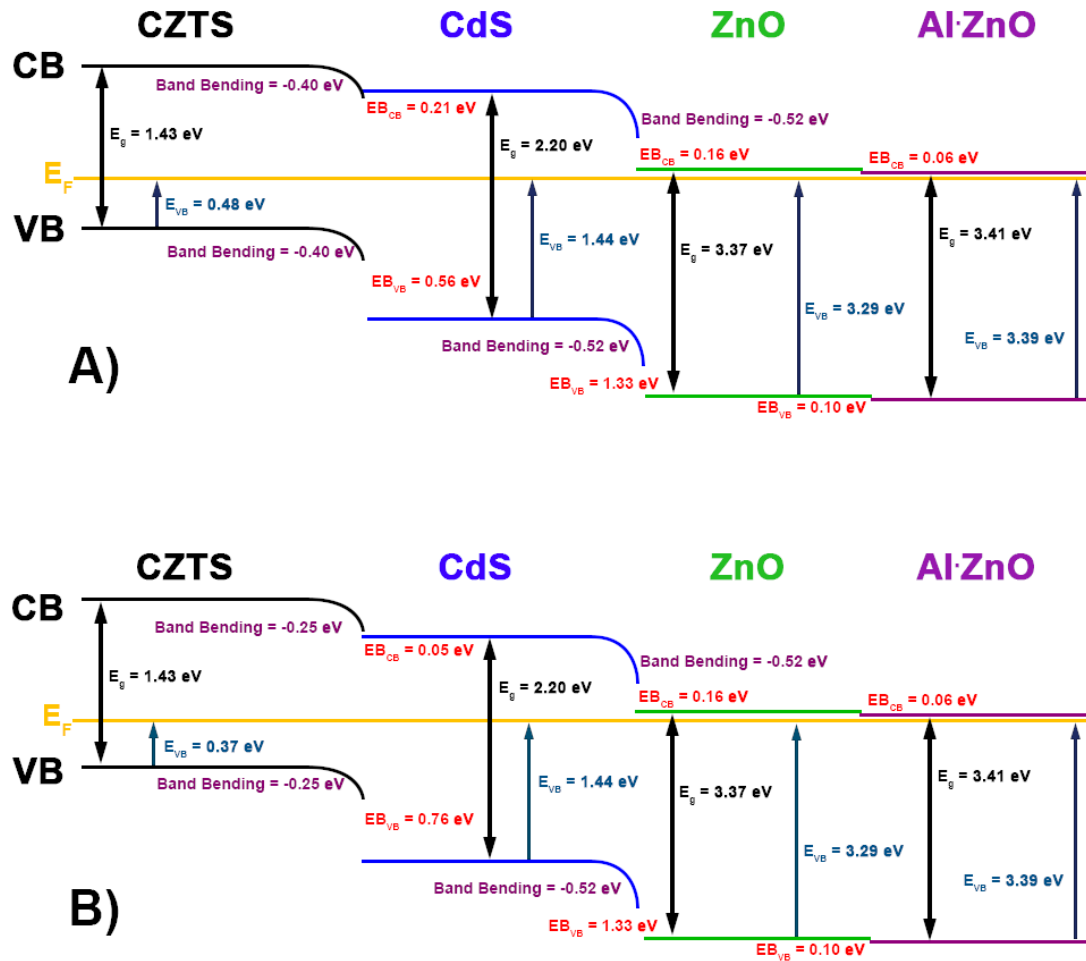


Figure 7.4 Energy band diagram for the full solar cell device A) using the etched CZTS film, and B) using the non-etched CZTS film. The relative Fermi level location has been marked as E_F .

Using the surface structures noted in Figure 7.2, the etching process is thought to be preferentially removing copper oxides, as per Chavez,⁴² creating some additional V'_{Cu} at the film surface. The increase in the CZTS EB_{VB} after etching also indicates a small increase in electron density at the surface, consistent with metal ion loss. The CdS/ZnO interface was maintained in both samples, and itself has a small cliff-like interface. Unlike the CZTS, both the CdS and ZnO are less prone to large degrees of disorder, and so the effects are much less severe.⁴³ It is expected that this would then have mildly detrimental effects on the V_{oc} , however, this is not the case in literature.⁴⁴ The reasons

behind the lack of effect of the cliff-like barrier at this interface are not completely understood. Regardless, the effects of the CdS/ZnO interface should remain constant through all films, so deviations in device performance should be solely dependent on the CZTS/CdS kinetics.

7.3.3 Full Device Performance

The etched and non-etched device performance was measured via J-V curve on 0.25 cm^2 devices, with the champions shown in Figure 7.5.

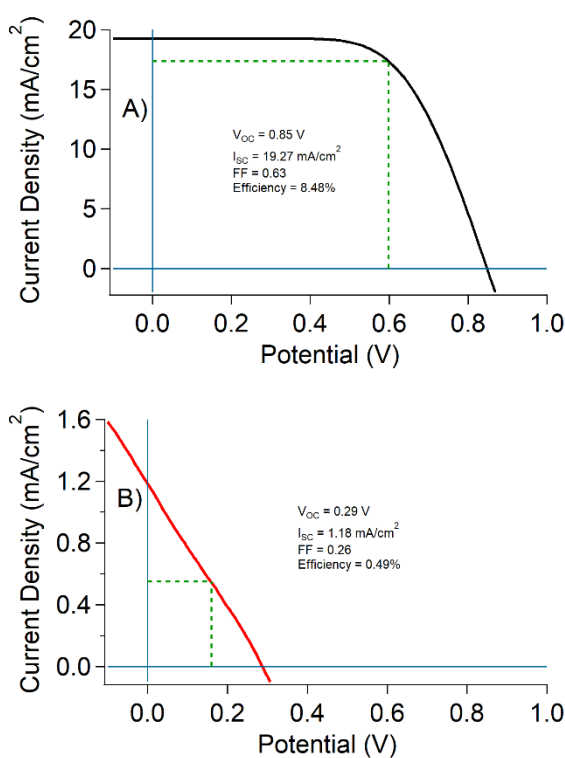


Figure 7.5 J-V curve for a champion device using (A) an etched CZTS film, and (B) a non-etched CZTS film. The current (I_{mp}) and potential (V_{mp}) at maximum power are indicated by dashed green lines, and used to calculate the Fill Factor (FF).

The device shown in Figure 7.5A had a V_{oc} of 0.85 V, which is higher than any V_{oc} reported to date for pure sulfide kesterite CZTS.^{3, 45-46} This is the result of the surface etching, and is confirmation of the band diagram given in Figure 7.4A. The can be contrasted against the 0.29 V of the non-etched CZTS device, shown in Figure 7.5B. The

difference between these Champion devices highlights the effects of the changes electron behavior at the interface, as predicted by the band structure. As the band structure suggests, a good V_{oc} should be obtained in the etched sample, while the recombination in the non-etched sample will lead to drastic V_{oc} reductions. The higher PECMs should also yield higher I_{sc} .^{10, 14} The relative efficiency of the devices should then match the internal efficiency as measured through PECMs, barring any physical defect during fabrication. The high working I_{sc} of 19.27 mA/cm² of the etched samples, and low I_{sc} of 1.18 mA/cm² is in direct agreement with the results predicted by the PECM (Figure 7.1) and the broad Cu peak observed in Figure 7.2B, whereby oxides in the interface form charge-carrier traps. The slope of the line leading from both the V_{oc} and the I_{sc} are indicative of the series and shunt resistance, respectively, which contribute to the FF.^{18, 47} Series resistance, caused by resistance in the metal contacts to the film, tends to increase when the back contact is altered from its conductive state during the fabrication process. This would cause a decrease in the slope from the V_{oc} . Shunt resistance is the resistance against charge-carrier flow through alternative pathways within the film layers.^{14, 47} While shunt resistance is high, electrons will flow according to the band diagram. When shunt resistance is low, electrons find other pathways through the device, bleeding current rapidly and causing an increase in the slope of the curve coming from the I_{sc} .^{17, 47} Both films show the presence of damage to the back contact in the form of increased series resistance, likely caused during the high temperature sulfurization step; however the etched film shows significantly increased shunt resistance, which lead to the drastically increased FF of 0.63 against 0.26. Solar cell performance relies on a high V_{oc} , high short-circuit current (I_{sc}), and a highly capacitive, low resistance film. The above values led to significantly increased efficiency of the working device based on the etched CZTS, at 8.48%, relative to the non-etched 0.49%. It can be concluded from the efficiency difference that the non-etched surface of the CZTS film is prone to unpredictable surface states that not only reduce the photoresponse of the film, but also allows for shunting of the charge-carriers away from the pathways outlined in the band structure diagram.

These devices were then scaled up to 6x the size, at 1.5 cm², and the devices performance measured (Figure 7.6).

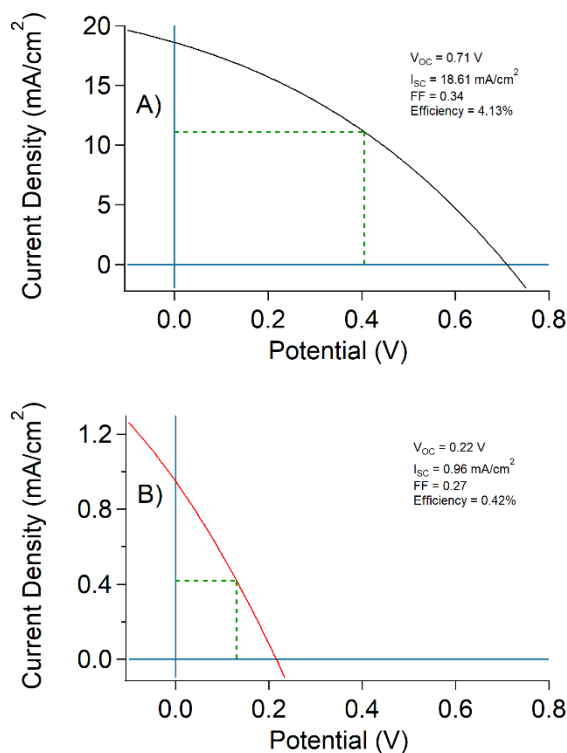


Figure 7.6 J-V curve of the large-sized CZTS device fabricated with the A) etched, and B) non-etched, CZTS. The current (I_{mp}) and potential (V_{mp}) at maximum power are indicated by dashed green lines, and used to calculate the Fill Factor (FF).

As expected, the etched CZTS device still shows drastically higher device efficiency, at 4.13%, than the 0.42% non-etched CZTS device. Compared to the smaller devices though, the I_{sc} and V_{oc} of the non-etched CZTS device do not change that drastically on scaling; however, the etched CZTS device shows significant decreases in V_{oc} . The other major difference is the slope of the shunt resistance. Whereas the small etched CZTS device (Figure 7.5A) showed high shunt resistance – manifested as a highly consistent current density over a large potential region, scaling up device (Figure 7.6A) led to drastic decreases in shunt resistance, and a steeper decrease in the current density, and thus decreased FF. This is indicative of non-equivalent regions within the etched CZTS films, and speaks to the homogeneity of the CZTS layer. As such, while the band structure and chemical barriers at the interface dictate the I_{sc} and V_{oc} , the I_{mp} and V_{mp} are more closely linked to the uniformity of the underlying bulk CZTS layer, which lacks

consistency on a large scale. Even so, the etching process solves the problem associated with features on the surface, and aligns the bands to produce ideal charge-carrier transfer. Films can then be enhanced further through increased homogeneity in the CZTS bulk, and through protection of the Mo back contact during CZTS formation so as to reduce series resistance seen in all presented samples.

7.4 Conclusion

CZTS films were fabricated using inexpensive electrochemical deposition of Cu, Sn, and Zn films on Mo-coated glass, to a highly specific elemental composition, and a thickness of 1 μm . The surface was etched with glacial acetic acid to enhance charge-carrier flux at the surface, and resulted in a significantly higher photoresponse in the etched samples. On addition of a 50 nm CdS layer, etched CZTS/CdS junction yielded an increased in photoresponse, while non-etched CZTS/CdS interfaces displayed a reduction in photocurrent. This was shown to be the result of changes in the VB at the surface of the CZTS film, and resulted in changes in the copper states that make up the lowest binding energies in the VB. These changes created an increased surface EB_{VB} in the etched sample, while maintaining the band gap of the material. The CB is therefore lowered relative to E_F , and thus relative to the CB of the CdS layer. The etched CZTS/CdS junction created a small spike-like barrier at the interface, while the non-etched CZTS/CdS one formed a small cliff-like barrier.

ZnO and AZO layers of 50 nm, and 250 nm respectively were added sequentially on top of the CdS layer to complete the device. The CdS/ZnO interface forms a cliff-like barrier in both samples, and does not result in V_{oc} losses. The etched CZTS had high V_{oc} of 0.85 V and I_{sc} of 19.27 mA/cm^2 , whereas the non-etched CZTS solar cells were greatly diminished their V_{oc} to 0.29 V. The I_{sc} was also much lower, at 1.18 mA/cm^2 . Etching the surface not only results in a 10-fold enhancement of these films, but also maximizes charge-carrier flux across the interface.

The photo conversion efficiency of the solar devices scaled up to the size of 1.5 cm^2 was determined to be 4.13%. Further enhancements to the device efficiency appear tied to the

bulk CZTS homogeneity and by limiting adverse reactions at the Mo/CZTS interface so as to reduce the series resistance, and thereby increase the fill factor.

7.5 References

1. Perini, L.; Vaccarello, D.; Martin, S.; Jeffs, K.; Ding, Z., *J. Electrochem. Soc.* **2016**, *163*, H3110.
2. Turnbull, M. J.; Vaccarello, D.; Wong, J.; Yiu, Y. M.; Sham, T. K.; Ding, Z., *J. Chem. Phys.* **2018**, *148*, 134702.
3. Zhou, H.; Song, T. B.; Hsu, W. C.; Luo, S.; Ye, S.; Duan, H. S.; Hsu, C. J.; Yang, W.; Yang, Y., *J. Am. Chem. Soc.* **2013**, *135*, 15998.
4. Deyasi, A.; Chakraborty, T.; Datta, S. In *Effect of Quasi-Fermi Level on Computing Quantum Efficiency in p-n Junction Solar Cell*, 2017 Devices for Integrated Circuit (DevIC), 23-24 March 2017; 2017; pp 76.
5. Yang, M.; Ma, X.; Jiang, Z.; Li, Z.; Liu, S.; Lu, Y.; Wang, S., *Physica B* **2017**, *509*, 50.
6. Bar, M.; Schubert, B. A.; Marsen, B.; Wilks, R. G.; Pookpanratana, S.; Blum, M.; Krause, S.; Unold, T.; Yang, W.; Weinhardt, L.; Heske, C.; Schock, H. W., *Appl. Phys. Lett.* **2011**, *99*, 222105.
7. Sun, K. W.; Huang, J. L.; Yan, C.; Pu, A. B.; Liu, F. Y.; Sun, H.; Liu, X.; Fang, Z.; Stride, J. A.; Green, M.; Hao, X. J., *Chem. Mater.* **2018**, *30*, 4008.
8. Shoushuai, G.; Zhenwu, J.; Li, W.; Jianping, A.; Yu, Z.; Yun, S.; Yi, Z., *Chin. Phys. B* **2018**, *27*, 018803.
9. Gu, Y. C.; Shen, H. P.; Ye, C.; Dai, X. Z.; Cui, Q.; Li, J. B.; Hao, F.; Hao, X. J.; Lin, H., *Adv. Funct. Mater.* **2018**, *28*, 1703369.
10. Ye, H.; Park, H. S.; Ajhavan, V. A.; Goodfellow, B. W.; Panthani, M. G.; Korgel, B. A.; Bard, A. J., *J. Phys. Chem. C* **2011**, *115*, 234.
11. Peter, L. M.; Wijayantha, K. G. U.; Tahir, A. A., *Faraday Discuss.* **2012**, *155*, 309.
12. Liang, S.; Sheng, H.; Liu, Y.; Huo, Z.; Lu, Y.; Shen, H., *J. Cryst. Growth* **2001**, *225*, 110.
13. Saha, S. K.; Guchhait, A.; Pal, A. J., *Phys. Chem. Chem. Phys.* **2012**, *14*, 8090.
14. Mitzi, D. B.; Gunawan, O.; Todorov, T. K.; Wang, K.; Guha, S., *Sol. Energ. Mat. Sol. Cells* **2011**, *95*, 1421.
15. Zhuk, S.; Kushwaha, A.; Wong, T. K. S.; Masudy-Panah, S.; Smirnov, A.; Dalapati, G. K., *Sol. Energy Mater. Sol. Cells* **2017**, *171*, 239.
16. Sah, C. T.; Noyce, R. N.; Shockley, W., *Proc. IRE* **1957**, *45*, 1228.
17. Lie, S.; Sandi, M. I.; Tay, Y. F.; Li, W.; Tan, J. M. R.; Bishop, D. M.; Gunawan, O.; Wong, L. H., *Sol. Energy Mater. Sol. Cells* **2018**, *185*, 351.

18. Wei, Y.; Zhuang, D.; Zhao, M.; Zhang, W.; Ren, G.; Wu, Y.; Sun, R.; Gong, Q.; Zhang, L.; Zhan, S.; Peng, X.; Lyu, X., *Sol. Energy Mater. Sol. Cells* **2018**, *180*, 19.
19. Peter, L. M.; Ponomarev, E. A.; Fermín, D. J., *J. Electroanal. Chem.* **1997**, *427*, 79.
20. Bard, A. J.; Faulkner, L. R., *Electrochemical Methods: Fundamentals and Applications, 2nd Edition*; John Wiley & Sons, 2000.
21. Shockley, W.; Queisser, H. J., *J. Appl. Phys.* **1961**, *32*, 510.
22. Kameyama, T.; Osaki, T.; Okazaki, K.; Shibayama, T.; Kudo, A.; Kuwabata, S.; Torimoto, T., *J. Mater. Chem.* **2010**, *20*, 5319.
23. Kaur, K.; Sood, M.; Kumar, N.; Nazari, H. H.; Gudavalli, G. S.; Dhakal, T. P.; Kumar, M., *Sol. Energy Mater. Sol. Cells* **2018**, *179*, 22.
24. Scragg, J. J. S.; Larsen, J. K.; Kumar, M.; Persson, C.; Sandler, J.; Siebentritt, S.; Platzer Björkman, C., *Phys. Status Solidi B* **2016**, *253*, 247.
25. Chen, S.; Walsh, A.; Gong, X. G.; Wei, S. H., *Adv. Mater.* **2013**, *25*, 1522.
26. Chen, H. J.; Fu, S. W.; Wu, S. H.; Tsai, T. C.; Wu, H. T.; Shih, C. F., *J. Phys. D* **2016**, *49*, 335102.
27. Murphy, A. B., *Sol. Energy Mater. Sol. Cells* **2007**, *91*, 1326.
28. Lai, H. H. C.; Basheer, T.; Kuznetsov, V. L.; Egdell, R. G.; Jacobs, R. M. J.; Pepper, M.; Edwards, P. P., *J. Appl. Phys.* **2012**, *112*, 083708.
29. Khoshmashrab, S.; Turnbull, M. J.; Vaccarello, D.; Nie, Y.; Martin, S.; Love, D. A.; Lau, P. K.; Sun, X.; Ding, Z., *Electrochim. Acta* **2015**, *162*, 176.
30. Turnbull, M. J.; Khoshmashrab, S.; Wang, Z.; Harbottle, R.; Sham, T.-K.; Ding, Z., *Catal. Today* **2016**, *260*, 119.
31. Turnbull, M. J.; Vaccarello, D.; Yiu, Y. M.; Sham, T. K.; Ding, Z., *J. Chem. Phys.* **2016**, *145*, 204702.
32. Vaccarello, D.; Tapley, A.; Ding, Z., *RSC Adv.* **2013**, *3*, 3512.
33. Yan, C.; Liu, F.; Song, N.; K. Ng, B.; Stride, J.; Tadich, A.; Hao, X., *Appl. Phys. Lett.* **2014**, *104*, 173901.
34. Santoni, A.; Biccari, F.; Malerba, C.; Valentini, M.; Chierchia, R.; Mittiga, A., *J. Phys. D* **2013**, *46*, 175101.
35. Caglar, Y.; Ilican, S.; Caglar, M.; Yakuphanoglu, F., *Spectrochim. Acta A* **2007**, *67*, 1113.
36. Saha, U.; Alam, M. K., *RSC Adv.* **2018**, *8*, 4905.
37. Yu, J. L.; Zheng, Z. M.; Dong, L. M.; Cheng, S. Y.; Lai, Y. F.; Zheng, Q.; Zhou, H. F.; Jia, H. J.; Zhang, H., *Chin. Phys. B* **2017**, *26*, 046802.
38. Lindahl, J.; Keller, J.; Donzel-Gargand, O.; Szaniawski, P.; Edoff, M.; Törndahl, T., *Sol. Energy Mater. Sol. Cells* **2016**, *144*, 684.

39. Haight, R.; Barkhouse, A.; Gunawan, O.; Shin, B.; Copel, M.; Hopstaken, M.; Mitzi, D. B., *Appl. Phys. Lett.* **2011**, *98*, 253502.
40. Sun, K.; Yan, C.; Liu, F.; Huang, J.; Zhou, F.; Stride, J. A.; Green, M.; Hao, X., *Adv. Energy Mater.* **2016**, *6*, 1600046.
41. Dong, Z. Y.; Li, Y. F.; Yao, B.; Ding, Z. H.; Yang, G.; Deng, R.; Fang, X.; Wei, Z. P.; Liu, L., *J. Phys. D* **2014**, *47*, 075304.
42. Chavez, K. L.; Hess, D. W., *J. Electrochem. Soc.* **2001**, *148*, G640.
43. Hana, S.; Jeongmin, L.; Seongjae, C.; Eou-Sik, C.; Sang Jik, K., *J. Semicond. Tech. Sci.* **2015**, *15*, 267.
44. Kaur, K.; Kumar, N.; Kumar, M., *J. Mater. Chem. A* **2017**, *5*, 3069.
45. Sun, K.; Yan, C.; Huang, J.; Sun, K.; Sun, H.; Jiang, L.; Deng, X.; Stride, J.; Hao, X.; Liu, F., *J. Alloys Compd.* **2018**, *750*, 328.
46. Zhou, H. P.; Hsu, W. C.; Duan, H. S.; Bob, B.; Yang, W. B.; Song, T. B.; Hsu, C. J.; Yang, Y., *Energy Environ. Sci.* **2013**, *6*, 2822.
47. Dalapati, G. K.; Zhuk, S.; Masudy-Panah, S.; Kushwaha, A.; Seng, H. L.; Chellappan, V.; Suresh, V.; Su, Z.; Batabyal, S. K.; Tan, C. C.; Guchhait, A.; Wong, L. H.; Wong, T. K. S.; Tripathy, S., *Sci. Rep.* **2017**, *7*, 1350.

Chapter 8

8 Concluding Remarks and Outlook

Throughout this thesis, a systematic, layer-by-layer approach is taken to fabricate $\text{Cu}_2\text{ZnSnS}_4$ -based (CZTS) solar cells. Each layer was examined, and the structural, optical, and charge-carrier properties were utilized to tune the bulk and interfacial material for maximal photovoltaic effects. Additional attention was paid to the CZTS light-absorbing layer. Two different methods for fabricating the CZTS were developed in tandem, one yielding nanocrystals (NCs), and the other yielding crystalline thin-films. In maintaining the long-term goals of the industry, preference was given to low-cost, environmentally friendly materials and procedures.¹⁻³ The final goal was achieved, with a low-cost device fabricated with an efficiency of 8.5%.

8.1 Conclusions

In the layer-by-layer approach, methods were employed to test the charge-carrier properties of the layers without requiring full device fabrication. In this way, observations could be directly tied to structural and photoelectrochemical features. Photoelectrochemical measurements (PECM) were employed, creating a Schottky barrier at the solid-liquid interface between the CZTS and methyl viologen solution, providing a quick and accurate measure of charge-carrier flux on illumination, or photoresponse.⁴⁻⁵ The best nanocrystal (NC) films produced 0.045 mA/cm^2 (Chapter 2), and form the starting point for tracking progress throughout the thesis. These were then directly compared to structural properties of the film, including localized structure, through synchrotron-based (SR) X-ray techniques, especially X-ray Absorption Fine Structure (SR-XAFS). CZTS NCs were fabricated via a low-temperature, one-pot solvothermal synthesis in an open-air ambient pressure environment. These were electrophoretically deposited to form a complete absorber layer, and then tested for charge-carrier flux on illumination. The simplest form or structure, the compositional ratios, were examined, and a method for controlling this ratio was developed through the combination of metal precursor availability, and sulfur availability within the reaction vessel. This process is

well described in Chapter 2, and indicated a Cu-poor, Zn-rich stoichiometry produced the best results.

With this compositional control, the photoresponse was linked to different metal ratios, and films with high photoresponse were examined in more detail, measuring the charge-carrier kinetics, and linking them to the qualitative and quantitative features determined through SR-XAFS (Chapter 3). NCs with high Cu / (Zn+Sn) ratios were linked to lattice distortions caused by non-uniform Cu'_{Zn} antisites, which lead to reduced photoresponse. Setting this ratio to about 0.87, and this problem goes away. The Zn / Sn ratio has similar effects, with high Zn causing lattice compressions that result from Zn^{\bullet}_{Cu} antisites and V'_{Cu} that limit charge-carrier flow in the bulk. High Sn, on the other hand, causes deep-trap $Sn^{\bullet\bullet}_{Zn}$ formation, and kills photoresponse. This ratio must therefore be kept around 1.15 to maximize photoresponse; however, this means the ideal film will have a Zn^{\bullet}_{Cu} antisites and V'_{Cu} presence. These have to be controlled, especially the Zn^{\bullet}_{Cu} antisites at the interface, to prevent excessive recombination when moving to a solid-solid interface in the full cell. This stoichiometric refinement allowed for a 3x enhancement in photoresponse, to 0.15 mA/cm² (Chapter 3).

Control of the antisites was sought through intense XAFS examinations of films within a very narrow compositional range (Chapter 4). By keeping the Cu / (Zn+Sn) ratio below 0.95, the Zn^{\bullet}_{Cu} antisite distribution is most uniform, especially when paired with a 1:1 Zn / Sn ratio. Unfortunately, this conflicts with the methods for limiting deep-trap $Sn^{\bullet\bullet}_{Zn}$ formation and maximizing photoresponse. The Cu content must be reduced, and the Zn content increased, to minimize the defects that inhibit photoresponse. A trade-off must then be made between the creation of those advantageous defects, the Zn^{\bullet}_{Cu} antisites and V'_{Cu} , and the increased disorder due to crystal mis-alignment across the film. How different CZTS compositions behave thus depends particularly on how these structures affect charge-carrier distribution across the CZTS/CdS barrier. These refinements enhanced the photoresponse further to 0.20 mA/cm², and established a good knowledge based on which to begin fabricating the device through deposition of subsequent layers.

CdS was added to the films through chemical bath deposition (CBD), and the CZTS film structure again examined (Chapter 5). Unlike previous measurements, the CBD introduced an additional Zn-O bond throughout the film, in appreciable quantities. This was identified as a major reason for the continued reduction in photocurrent following CdS addition, and determined to be water intercalation resulting from submersion in the CBD medium. Post-processing annealing treatments were used to remove this charge-carrier barrier, and achieve similar photoresponse in treated CZTS/CdS films as in pure CZTS, as high as 0.23 mA/cm^2 . While a successful treatment, this failed to result in the expected enhancement, leading to the conclusion that something else was limiting charge-carrier flow across the interface. The most probable cause being some of the defects being specifically selected for in the CZTS, or some of the photoresponse was being lost to poor alignment of the band structure of the two materials.

Prior to continuing with the structural engineering, the band structure was tuned to produce optimal spike-like barriers to minimize recombination at the CZTS/CdS interface, and ultimately produce high open-circuit potentials (V_{oc}) of 0.71 V or better. (Chapter 6). This tuning was successfully accomplished on electrodeposited CZTS films, by probing the surface states with SR X-ray Photoelectron Spectroscopy (SR-XPS), and tuning the EB_{VB} (VB energy barrier) to create a well-tuned band structure. During the band structure tuning, the compositional changes appeared to be less consistent at controlling the surface structure, and thus were ineffective at maintaining a barrier-free interface. This necessitated the application of surface treatments to reproduce the consistency previously noted. This was accomplished via acetic acid etching. Application of the etchant not only generated the ideal band structure, but also allowed for the formation of the ideal spike-like CB overlap.

In Chapter 7, films showed massive increases to the PECM, by a factor of 10 to 2.75 mA/cm^2 for the CZTS layer, which is 55x the originally measured photoresponse. To avoid complications in the full device, very uniform window layer films were deposited using an atomic layer deposition instrument (ALD). These ensured that everything observed was a function of the CZTS and CdS interface, and built upon the correlations established through the structural studies. Using the etched surface, and ideal band

structure, the highest V_{oc} reported to date – 0.85 V - was achieved, and devices reached efficiencies as high as 8.48%. Photoresponse was further enhanced to 4.67 mA/cm² or 93x initial values. Scaling-up the full device indicated the CZTS film was still not uniform, as the large device efficiency averaged only slightly above 4.13%, though it was fairly effective at maintaining a very high V_{oc} above 0.71 V.

8.2 Outlook and Project Future

The data presented within this thesis provides a solid foundation for the continued enhancement of CZTS solar cells. Despite the 8.48% efficiency, the series resistance can be improved upon, and the films are not homogenous enough to fully scale up. Gaps and pinholes within the device, as well as the predicted heterogeneity of defects within the CZTS layer, all contribute to reducing the shunt resistance of the scaled-up device, and thus reduce the efficiency. The first step to improving the viability of these devices will be introducing better control of these regions through continued compositional engineering using the methods discussed. As shown in Figure 8.1, these problems are actually quite prevalent on the microscale, despite the progress that has been made.

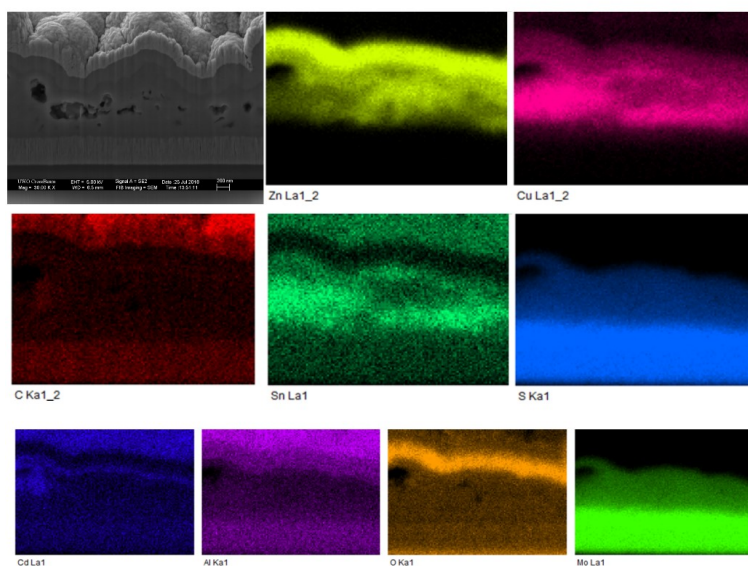


Figure 8.1 CZTS full device structure, with heterogeneous distribution of metals within the CZTS layer. Gaps and pinholes are also readily visible within the same layer.

That devices with these features can still yield 4.13% or better, and even 8.48% in more uniform regions, suggests that further enhancements are achievable through continued tuning the CZTS.¹ As shown, the Cu and Sn elements appear fairly uniformly distributed relative to each other, but have a small region just below the surface where they are less dense. This is directly related to an increase in Zn in the area. Fortunately, this appears to not affect the surface in most regions, and thus the cell is able to maintain high charge-carrier flux across the CZTS/CdS interface. Whether the distribution at the surface is affected by the etching procedure remains unclear at this point. Removing these type of features has to be the first step.

Further development of the process to reproduce the device efficiencies in NC films are required. At present, the surface of the NC-based film is far more complex, and etching treatments have not yet been optimized. By first understanding the effects of the etching procedure on the surface of the electrodeposited films, the effects on the NCs can be better predicted, and the process optimized. Optimized etching processes could then be tuned to produce p-n junctions similar to those presented in Chapter 6 and 7. Ultimately, the NC films are better suited to low-cost fabrication, as they do not require the sulfur atmosphere annealing step at 525 °C, and so are the preferred candidate for ultimately being integrated as a commercially viable device. Efforts to replicate the results seen in the electrochemically deposited films in CZTS NCs are expected to succeed with additional insight into the etching process.

Furthermore, the current results focus primarily on the CZTS layer, and maintain consistent CdS, ZnO, and Al-doped ZnO (AZO) layers. Environmentally, the CdS layer is less than desirable, due to the toxicity associated with Cd metal. As Cd usage is already restricted in some parts of the world, Cd-free buffer layer solutions will need to be developed, and the subsequent p-n junction refined to refit the bands. Once the CZTS layer has been fully optimized, the CdS layer will be replaced with more environmentally friendly alternatives, such as $Zn(O_xS_{1-x})$, and tuned to generate the optimal band structure. This has not been attempted while trying to optimize the CZTS, as it would further complicate the process of understanding CZTS formation and obscure possible structural controls. CdS is well studied in literature,⁶⁻⁷ and provides consistent,

predictable features against which to base CZTS improvement. ALD-built films will also likely require replacement, as this technique is rather costly. Finding alternative processes for fabricating and depositing these window layers will come after CdS replacement. In the NC-based devices, however, this is the only real costly procedure, and thus not something to be replaced in the short-term.

The current global aim of achieving \$0.05 / kWh by 2030 depend on the continued improvement to solar cell design, and reduction in fabrication costs. Thin film devices such as CZTS remain an attractive candidate to fill this requirement. Future work in tuning the CZTS and subsequent device layers can be built on the foundations discussed herein, and will prove critical to the eventual implementation, and realization of this long-term goal.

8.3 References

1. Cook, J. J.; Ardani, K. B.; Margolis, R. M.; Fu, R. *Cost-Reduction Roadmap for Residential Solar Photovoltaics (PV), 2017-2030*; United States, 2018.
2. Dresselhaus, M. S.; Thomas, I. L., *Nature* **2001**, *414*, 332.
3. Kabir, E.; Kumar, P.; Kumar, S.; Adelodun, A. A.; Kim, K. H., *Renew. Sust. Energ. Rev.* **2018**, *82*, 894.
4. Ye, H.; Park, H. S.; Akhavan, V. A.; Goodfellow, B. W.; Panthani, M. G.; Korgel, B. A.; Bard, A. J., *J. Phys. Chem. C* **2010**, *115*, 234.
5. Bard, A. J.; Faulkner, L. R., *Electrochemical Methods: Fundamentals and Applications, 2nd Edition*; John Wiley & Sons, 2000.
6. Liu, F.; Lai, Y.; Liu, J.; Wang, B.; Kuang, S.; Zhang, Z.; Li, J.; Liu, Y., *J. Alloys Compd.* **2010**, *493*, 305.
7. Shah, A.; Torres, P.; Tscharnner, R.; Wyrsh, N.; Keppner, H., *Science* **1999**, *285*, 692.

Abstract A – Copyrights



RightsLink®

Home

Create Account

Help



Title: Controlling Cu₂ZnSnS₄ photocatalytic ability through alterations in sulfur availability

Author: Matthew J. Turnbull, Saghar Khoshmashrab, Zhiqiang Wang, Robert Harbottle, Tsun-Kong Sham, Zhifeng Ding

Publication: Catalysis Today

Publisher: Elsevier

Date: 1 February 2016

Copyright © 2015 Elsevier B.V. All rights reserved.

LOGIN

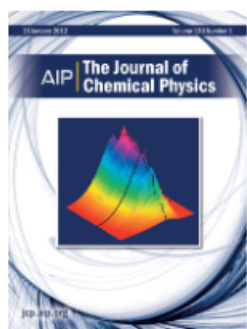
If you're a **copyright.com user**, you can login to RightsLink using your copyright.com credentials. Already a **RightsLink user** or want to [learn more?](#)

Please note that, as the author of this Elsevier article, you retain the right to include it in a thesis or dissertation, provided it is not published commercially. Permission is not required, but please ensure that you reference the journal as the original source. For more information on this and on your other retained rights, please visit: <https://www.elsevier.com/about/our-business/policies/copyright#Author-rights>

BACK

CLOSE WINDOW

Copyright © 2018 Copyright Clearance Center, Inc. All Rights Reserved. [Privacy statement](#). [Terms and Conditions](#). Comments? We would like to hear from you. E-mail us at customercare@copyright.com



Thank you for your order!

Dear Mr. Matthew Turnbull,

Thank you for placing your order through Copyright Clearance Center's RightsLink® service.

Order Summary

Licensee: Mr. Matthew Turnbull
Order Date: Aug 13, 2018
Order Number: 4407220507577
Publication: Journal of Chemical Physics
Title: Identifying barriers to charge-carriers in the bulk and surface regions of Cu₂ZnSnS₄ nanocrystal films by x-ray absorption fine structures (XAFSs)
Type of Use: Thesis/Dissertation
Order Total: 0.00 CAD

View or print complete [details](#) of your order and the publisher's terms and conditions.

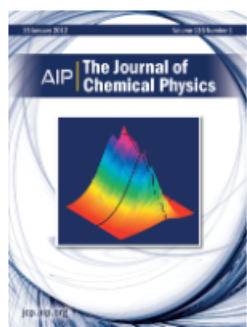
Sincerely,

Copyright Clearance Center

Tel: +1-855-239-3415 / +1-978-646-2777
customercare@copyright.com
<https://myaccount.copyright.com>



RightsLink®



Thank you for your order!

Dear Mr. Matthew Turnbull,

Thank you for placing your order through Copyright Clearance Center's RightsLink[®] service.

Order Summary

Licensee: Mr. Matthew Turnbull
Order Date: Aug 13, 2018
Order Number: 4407220416455
Publication: Journal of Chemical Physics
Title: Probing the CZTS/CdS heterojunction utilizing photoelectrochemistry and x-ray absorption spectroscopy
Type of Use: Thesis/Dissertation
Order Total: 0.00 CAD

View or print complete [details](#) of your order and the publisher's terms and conditions.

Sincerely,

Copyright Clearance Center

Tel: +1-855-239-3415 / +1-978-646-2777
customercare@copyright.com
<https://myaccount.copyright.com>



RightsLink[®]

Subscriber access provided by University of Western Ontario

Login Register Shibboleth Mobile Cart

Advanced Search

All Journals Search

Home About Us Journals Books Compilations Open Access Authors Librarians Societies Blog Contact Français

[Home](#) > Open Access Options- Meet your funding agency requirements

Open Access

- » OA Options
- » OpenArticle
- » How to Deposit to Tspace or Another Institutional Repository
- » How to Deposit to PubMed Central

Open Access at Canadian Science Publishing

Our liberal [authors' rights](#) ensure that NRC Research Press and Canadian Science Publishing journals are compliant with the open access policies of all major research funding agencies:

- Authors who publish in NRC Research Press or Canadian Science Publishing journals have the option of a free automatic deposit of their accepted manuscript into the [ISpace repository](#). Contact the editorial office of your journal for more information.
- NRC Research Press journals offer an [OpenArticle](#) service to authors who wish to purchase open access for their published article. This option is a fee-based mechanism for individual authors or their research funding agencies to sponsor the open availability of their articles. Read more about [OpenArticle](#).
- All authors who publish in NRC Research Press or Canadian Science Publishing journals may at any time in the publication process self-archive their submitted and/or accepted manuscript on their institution's Web site or in an open-access repository such as [PubMed Central](#).
- Authors may submit to an open access journal such as [Arctic Science](#), [FACETS](#), [Anthropocene Coasts](#), or a journal with a 12 month embargo such as the [Canadian Journal of Animal Science](#), [Canadian Journal of Plant Science](#) and the [Canadian Journal of Soil Science](#).

Empowered by Science

Canadian Science Publishing's 2018-2022 Strategic Plan envisions a world where everyone is empowered with scientific knowledge.

[Explore Our Plan](#)

Scientific knowledge is powerful.

We ensure it's empowering.

Curriculum Vitae

- Name:** Matthew J. Turnbull
- Education:** The University of Western Ontario
London, Ontario, Canada
2007-2013 B.Sc.
- The University of Western Ontario
London, Ontario, Canada
2013-2018 Ph.D.
- Honours and Awards:** Queen Elizabeth II Graduate Scholarship in Science and Technology
2017-2018
- N. Stewart McIntyre Award in Surface Science
2017
- Related Work Experience:** Head Teaching Assistant
The University of Western Ontario
2017
- Teaching Assistant
The University of Western Ontario
2013-2017
- Publications:**
9. **Turnbull, M.J.;** Gupta, J.; Goldman, M.; Yiu, Y.M.; Ding, Z. Layer-by-Layer Construction Strategies towards CZTS-Based Solar Cell Devices. *Manuscript ready for submission.*
 8. **Turnbull, M.J.;** Yiu, Y.M.; Goldman, M.; Sham, T.K.; Ding, Z. Favorable Bond and Band Structure of $\text{Cu}_2\text{ZnSnS}_4$ and CdS Films and Their Photovoltaic Junctions. *Manuscript ready for submission.*
 7. Tapley, A.; **Turnbull, M.J.;** Swick, K.; Ding, Z. Electrochemical Deposition of Light-Absorbing CuInSe_2 for use in Solar Cells. *Manuscript in preparation.*
 6. **Turnbull, M.J.;** Vaccarello, D.; Wong, J.; Yiu, Y.M.; Sham, T.K.; Ding, Z. Probing the CZTS/CdS Heterojunction Utilizing

Photoelectrochemistry and X-ray Absorption Spectroscopy. *J. Chem. Phys.*, (2018), 148, 134702-9.

5. **Turnbull, M.J.**; Khoshmashrab, S.; Yiu, Y.M.; Ding, Z. Resolving the Effects of Compositional Change on Structures in $\text{Cu}_2\text{ZnSnS}_4$ Nanocrystals by X-ray Absorption Fine Structure. *Can. J. Chem.*, (2018), 96, 785-794.
4. He, S.; **Turnbull, M.J.**; Nie, Y.; Sun, X.; Ding, Z. Band Structure of Blue Luminescent Nitrogen-Doped Graphene Quantum Dots by Synchrotron-Based XPS. *Surf. Sci.*, (2018), 676, 51-55.
3. **Turnbull, M.J.**; Vaccarello, D.; Yiu, Y.M.; Sham, T.K.; Ding, Z. Identifying Barriers to Charge-Carriers in the Bulk and Surface Regions of $\text{Cu}_2\text{ZnSnS}_4$ Nanocrystal Films by X-ray Absorption Fine Structure (XAFS). *J. Chem. Phys.*, (2016), 145, 204702-12.
2. **Turnbull, M.J.**; Khoshmashrab, S.; Wang, Z.; Harbottle, R.; Sham, T.K.; Ding, Z. Controlling $\text{Cu}_2\text{ZnSnS}_4$ Photocatalytic Ability Through Alterations in Sulfur Availability. *Catal. Today*, (2016), 260, 119-125.
1. Khoshmashrab, S.; **Turnbull, M.J.**; Vaccarello, D.; Martin, S.; Ding, Z. Effects of Cu Content on the Photoelectrochemistry of $\text{Cu}_2\text{ZnSnS}_4$ Nanocrystal Thin Films. *Electrochim. Acta*, (2015), 162, 176-184.

Oral Presentations:

2. **Turnbull, M.J.**; Ding, Z. (2017) Synchrotron-Based X-ray Absorption Fine Structure (XAFS) and Interfacial Studies of $\text{Cu}_2\text{ZnSnS}_4$ Solar Cells. 6th Georgian Bay International Conference on Bioinorganic Chemistry, Parry Sound, Ontario, Canada.
1. **Turnbull, M.J.**; Khoshmashrab, S.; Ding, Z. (2014) Optimization of $\text{Cu}_2\text{ZnSnS}_4$ Nanocrystal-Based Films for use in Photovoltaic Devices. Canadian Society for Chemistry Conference, Vancouver, British Columbia, Canada.